This meeting will be co-sponsored
by The Electrochemical Society

BRNO
UNIVERSITY
OF TECHNOLOGY

FACULTY
OF ELECTRICAL
ENGINEERING
AND COMMUNICATION

ÚACh
Institute
of Inorganic
Chemistry
AS CR

10th ABAF

BRNO 2009

Advanced Batteries, Accumulators and Fuel Cells

INTERNATIONAL CONFERENCE

August 30th - September 2nd 2009

Organised by:

Department of Electrotechnology,
Faculty of Electrical Engineering and Communication,
Brno University of Technology

Institute of Inorganic Chemistry,
Academy of Science of Czech Republic, Řež near Prague

Organizing committee:
Jiří Vondrák
Marie Sedlaříková

ISBN 978-80-214-3943-6

Conference is sponsored by:

NOVA-LAB

AUTOLAB Electrochemical Instruments

Bochemie®

HYtest®

This meeting will be co-sponsored
by The Electrochemical Society

ECS

We would like to express our thanks to the Brno University of Technology, Faculty of Electrical Engineering and Communication and to the Institute of Inorganic Chemistry AS CR for support and help with organising 10th ABAF conference.

Honourary Scientific Committee:

Stefan Koller
Doron Aurbach
John R. Owen
Raisa Apostolova
Petr Vanýsek
Libuše Trnková
Jana Bludská
Jiří Kazelle
Josef Jirák
Jiří Vondrák
Marie Sedlaříková

Organisation Committee:

Jiří Vondrák
Marie Sedlaříková
Vítězslav Novák
Peter Barath
Jiří Vognar
Jiří Vrbický
Tibor Jirák
Michal Macalík
Kristýna Jandová
Jaromír Makovička

Program Committee:

Jiří Vondrák
Marie Sedlaříková
Jiří Kazelle
Vítězslav Novák
Peter Barath
Petr Špičák
Jiří Špinka
Helena Polsterová
Zdenka Rozsívalová
Edita Hejátková

Contents

Nanosized or layered materials

Solid and polymeric conductors

Intercalation materials

Special electrochemical components

Accumulators

Methods

Fuel cells

:-)

Sponsors

Nominal

10th

ABAF

BRNO 2009

Advanced Batteries, Accumulators and Fuel Cells

Nanosized or layered materials

ELECTROCHEMICAL DEPOSITION OF HYDROXYAPATITE AND HYDROXYAPATITE/Ag COMPOSITE COATINGS ON TITANIUM ALLOY SURFACE

J. Kadlec[1], Z. Joska[1], Z. Studeny[1], M. Dvorak[2], M. Jelinek[3] and T. Kocourek[3]

[1] Depth. of Mechanical Engineering, University of Defence in Brno, Kounicova 65, 662 10, Brno, Czech Republic
[2] Depth. of Mechanical Technology, Faculty of Mechanical Engineering, Brno University of Technology, Technicka 2, 616 69 Brno, Czech Republic
[3] Institute of Physics, Na Slovance 2, 182 21 Prague 8, Czech Republic

Corresponding author: Jaromír Kadlec (kadlecjara@yahoo.com)
Phone +420 973 442 355

Experimental

Hydroxyapatite (HA) $Ca_{10}(PO_4)_6(OH)_2$ can be prepared by various of methods e.g. electrochemical deposition [1,2,3], pulsed laser deposition (PLD) or hybrid laser-magnetron deposition (PLDMS) [4,5] and quite a few of other technologies. In this case hydroxyapatite $Ca_{10}(PO_4)_6(OH)_2$ and hydroxyapatite $Ca_{10}(PO_4)_6(OH)_2$ / Ag composite coatings were prepared by electrochemical deposition from water solution of $Ca(NO_3)_2.4H_2O$, $NH_4H_2PO_4$ and $AgNO_3$ according to parameters in Table 1 on the Ti6Al4V/TiON surfaces, whereas TiON thin film was deposited by long-time thermal annealing in atmosphere of pure N_2 at 500°C.

***Table 1** Parameters of electrochemical deposition of $Ca_{10}(PO_4)_6(OH)_2$ / Ag structures*

Compound	Concentration	Temperature	Current density	Duration time
$Ca(NO_3)_2.4H_2O$	0,042 M	65 ± 2 °C	1,5 - 4 mA.cm^{-2}	35 - 120 min
$NH_4H_2PO_4$	0,025 M			
$AgNO_3$*	150-500 mg.l^{-1}		1 mA.cm^{-2}	30 - 120 min

** In the case of HA/Ag composite. Ag can be deposited either during (see Fig. 4-5) or after (see Fig. 6) deposition of HA.*

Results and Discussion

Properties of subsequently deposited HA coatings with defined chemical composition (Ca-P ratio) and proper structure depend on process parameters, i.e. electrolyte chemical composition, temperature, current density and last but not least pH. Chemical composition and structure of the system substrate/coating were studied by GDOES, SEM and EDS methods on the SA2000 spectrometer Leco and SEM Vega 5135 with Noran system Six, respectively.

Conclusions

Described technology has made possible to create HA nanostructures of various morphology (see e.g. Fig. 1-3) and to create HA nanostructures with Ag particles of various shape, size and frequency (see e.g. Fig. 4-6). For practical use these HA and HA/Ag structures could/should be reinforced by either organic or inorganic carbon based structures or both.

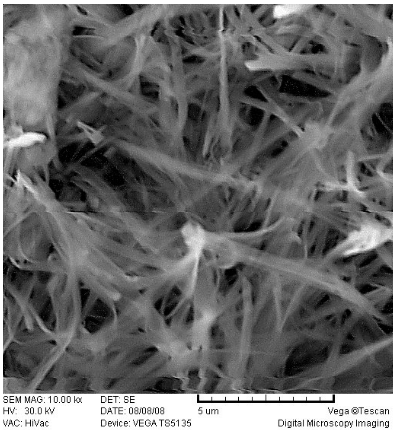

Fig.1 *HA nanostructure, Ca/P = 1,74 (10 kx, SE) [Magnification in relation to the area of 150x150 mm]*

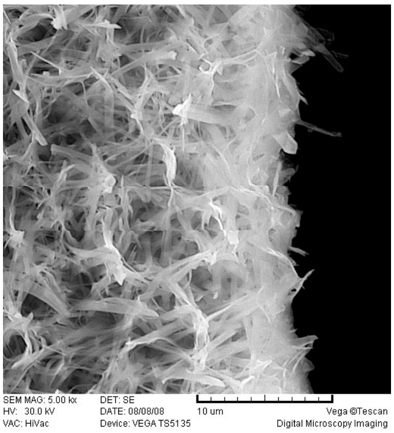

Fig.2 *HA nanostructure (5 kx, SE)*

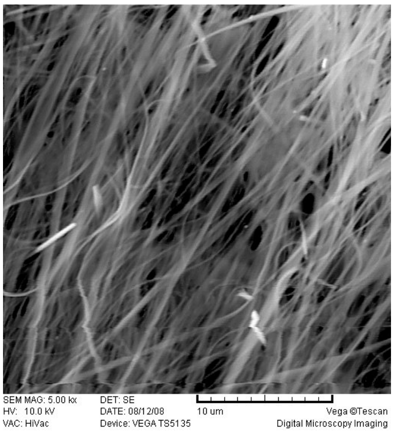

Fig.3 *HA nanostructure/nanofibers (5 kx, SE)*

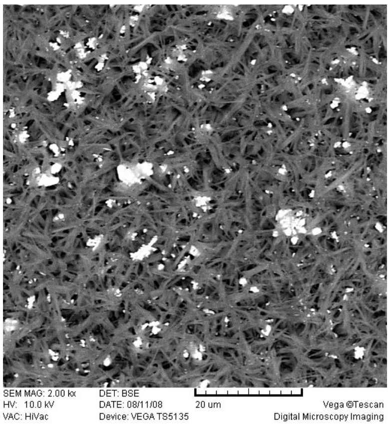

Fig.4 *HA nanostructure with Ag pseudoglobular particles (2kx, BSE)*

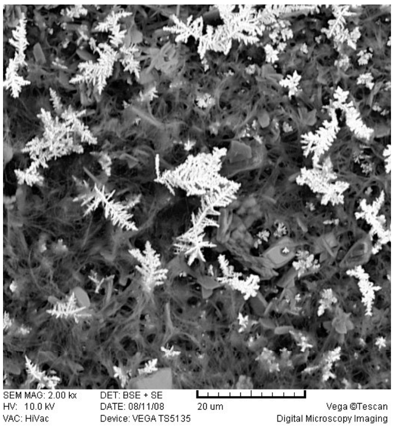

Fig.5 *HA nanostructure with Ag dendritic particles (2kx, BSE+SE)*

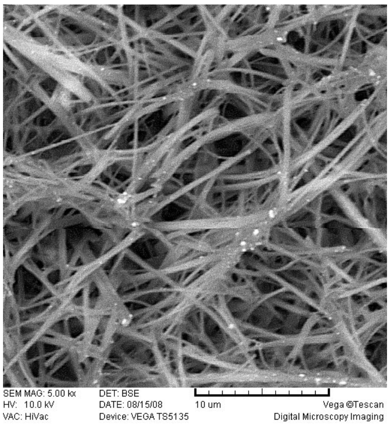

Fig.6 *HA nanostructure with Ag globular particles on the surface of HA fibers (5 kx, BSE)*

Acknowledgements

The research was supported by the Grant Agency of the Czech Republic, project no. 106/08/1243 and by Ministry of Defence of the Czech Republic, project FVT 0000404.

References

1. M.C. Kuo, S.K. Yen: Materials Science and Engineering C 20 (2002) 153.
2. Y. Zhang, J. Tao, Y. Pang, W. Wang, T. Wang: Transactions of Nonferrous Metals Society of China 16 (2006) 633.
3. Z. Studeny: Doctoral thesis, University of Defence Brno (2009).
4. M. Jelinek, T. Kocourek, J. Kadlec, J. Zemek: Laser Physics 19 (2009) 149.
5. T. Kocourek, M. Jelinek, J. Kadlec, C. Popov, A. Santoni: Plasma Proc. Polym. 4 (2007) S651.

PLASMA NITRIDED AND SUBSEQUENTLY TiCN COATED X12CrNi 18 8 STEEL SURFACE

Z. Joska[1], J. Kadlec[1], V. Hrubý[1]

[1] University of Defence Brno, Kounicova 65, Brno, Czech Republic

Corresponding author: Joska Zdenek (joska.zdenek@unob.cz)
Phone: +420 723 668 071

Introduction

This article described surface treatment of austenitic stainless steel X12 CrNi 18 8. Combination of both plasma nitriding and PVD coating TiCN as a surface treatment were used to improve material hardness, wear resistance. GDOES, SEM, microhardness, indentation test were used to investigate the chemical composition, surface morphology, adhesion and hardness of the deposited duplex coating.

Tab.1 *Chemical composition of stainless steel*

Chemical composition (%)							
	C	Mn	Cr	Ni	Si	P	S
DIN standard	≤ 0,12	≤ 2,00	17 - 19	8 – 10	≤ 1,00	≤0,045	≤0,03
GDOES/Bulk	0,045	1, 78	18,6	8,60	0,45	0,027	0,002
Parameters of GDOES/Bulk analysis: U =800 V, I = 30m A, pAr = 314 Pa							

Experimental

Austenitic stainless steel X12CrNi 18 8 is very attractive material due to excellent corrosion resistance in various environments, superior cryogenic properties, good high-temperature strength and sufficient biocompatibility, for this properties is used in the food and chemical industry and in medicine for surgical cutting tools. Unfortunately poor hardness, low wear resistance limit their applications. Duplex surface system was applied to improve surface and subsurface properties without losing main property – corrosion resistance. We used combination of both plasma nitriding and subsequent thin film TiCN.

Tab.3 *Summary of samples treatment*

Sample	*Plasma Nitriding*	*TiCN Coating*
1.3	*XX*	*5 µm*
1.6	*XX*	*1,5 µm*
1.9		*1,5 µm*
1.10		*5 µm*

Chemical composition was determined by GDOES method, result is shown in Table.1. Plasma nitriding process was carried out on the PN 60/60 equipment parameters are described in Table.2 Subsequent TiN coating was deposited by PVD process conditions are summarized in Table 2. For experiment were used 4 samples, parameters of their treatment are shown in Tab. 3.

Chemical composition of substrate material was measured by GDOES/Bulk method (SA 2000 spectrometer) depth profiles was evaluated by GDOES/QDP. Calibration of nitrogen: JK41-1N and NSC4A standards. Microstructure and surface morphology was evaluated by electron (Vega TS 5135 electron microscope) and light microscopy (Neophot 32 light microscope), surface microhardness was measured by Vickers indentation method (M400 microhardness tester), adhesion was measured by indentation test (Rockwell C). Relations among chemical composition, structure and diffusion layer properties were briefly discussed.

Tab.2 *Main treatment parameters*

Plasma nitriding process		
Parameter	Value	
	Plasma cleaning	Plasma nitriding
Temperature (^{0}C)	520	550
Time/Duration (min, h)	30 min	8 h
Flow H_2 (l/min)	20	8
Flow N_2 (l/min)	2	32
Flow CH_4 (l/h)	0	1,5
Voltage (V)	800	530
Pulse length (μs)	100	100
Pressure (Pa)	80	280

PVD TiCN coating		
Parameter	Value	
	TiCN 1.5 μm	TiCN 5 μm
Bias Voltage (V)	100	100
Substrate temperature(^{0}C)	450	450
Cathode-substrate distance (mm)	150 mm	150 mm
Deposition time	1 h 20 min	4 h
N_2 +C_2H_2 pressure (mbar)	0,0037	0,0037

Results and Discussion

Depth profiles of plasma nitrided layer for carbon and nitrogen replied to the proposed plasma treatment regime is shown Figure 2 and 3. they decrease along the depth layer. There is for carbon carbon concentration maximum 1300 s. Depth profiles of TiCN coatings are shown in Figures 4 and 5 that content of both nitrogen and carbon on plasma nitrided surface is higher than on the untreated surfaces. Nitrogen layer is decreased and chromium layer is increased more slowly. In depth 7 μm is carbon content 5 atomic percent and nitrogen content about 10 atomic percent. Adhesion was measured by Rockwell C indentation test, load was 1470 N, and matches to (HF1 – HF3) Figs. 6, 7, 8. Surface microhardness was measured in range of load 0,1N to 9,81N in Figure 1 are shown results for all types of treatment. The highest values have samples with duplex surface treatment.

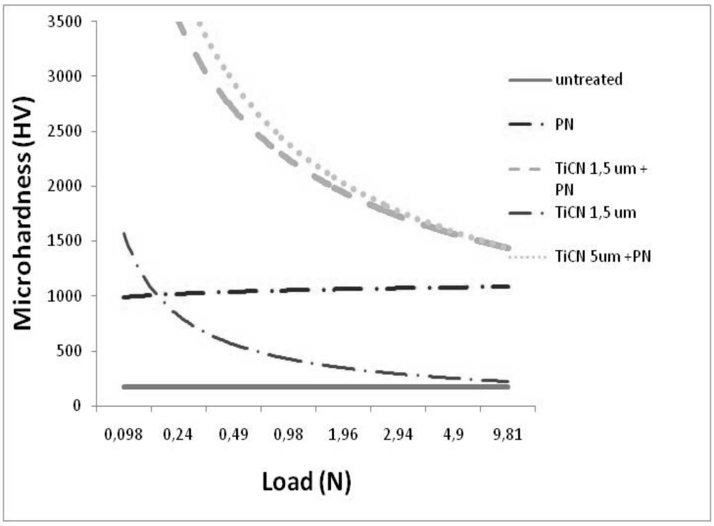

Fig.1 *Surface microhardness*

Conclusions

Duplex surface treatment on the steel X12CrNi 18 8 surface was investigated. The aim of the research was found the relation between chemical composition, structure and properties of duplex system. This system improved the hardness differences between the coating and substrate. Results from indentation test are shown that both of duplex system has very similar adhesion. Around the indentation we can see symmetric scratches and delaminated coating. The highest values of microhardness has duplex system of sample 1.3 (Plasma nitrided + TiCN 5 µm). To conclude, it can be said that a precisely controlled duplex surface treatment provides superior tribological and load bearing properties to X12 CrNi 18 8 stainless steels, which cannot be obtained by individual treatments.

Acknowledgements

The work was supported by research project by Ministry of Defence of the Czech Republic, project No. MO0FVT 0000404, and Grand Agency of the Czech Republic No. 106/08/1243.

References

1. K.H.Lo,et al., *Materials Science and Engineering R (2009)*doi: 10.1016/ j.mser.2009.03.001
2. J. Kadlec, V. Hruby, and M. Novak, Vacuum, **41**, 2226 (1990)

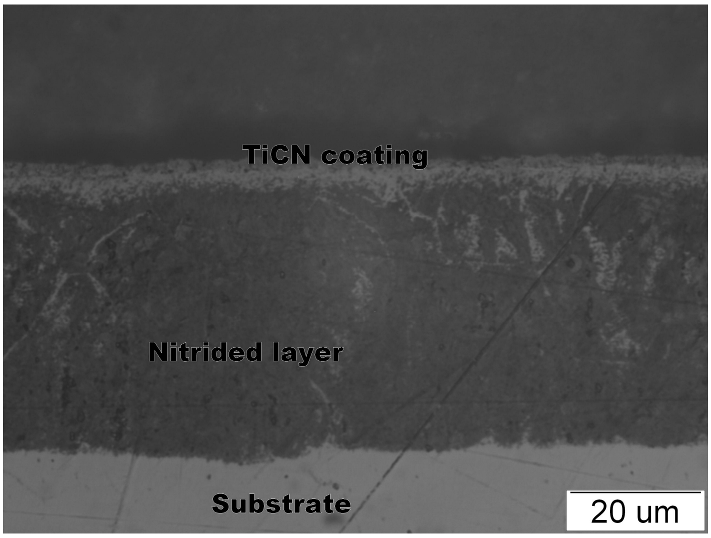

Fig.2 *Microstructure of sample 1.3*

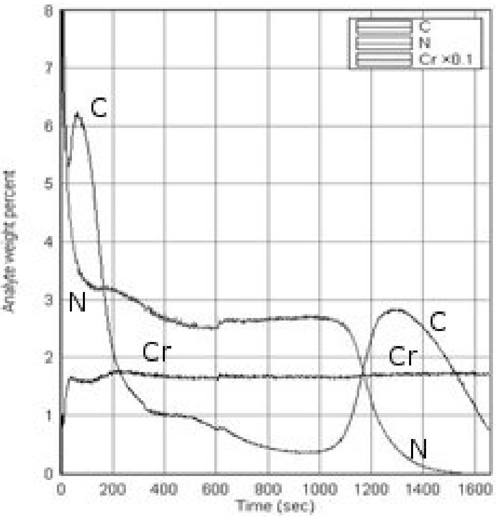

Fig.3 *Chemical composition of nitrided layer*

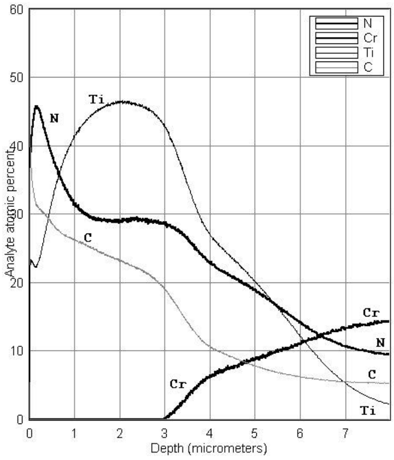

Fig.4 *Chemical composition (sample 1.2) TiN 1,5 µm on plasma nitrided surface*

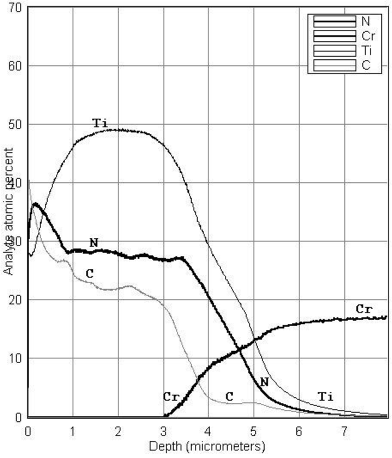

Fig.5 *Chemical composition (sample 1.1) TiN 5 µm on untreated surface*

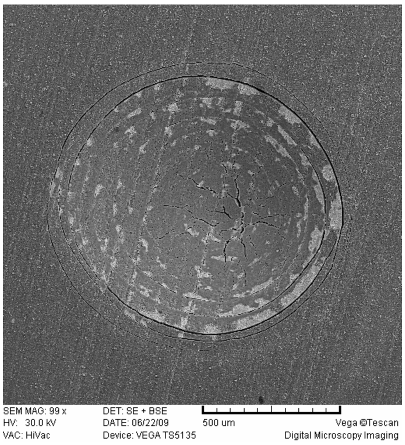

Fig.6 *Indentation adhesion test of sample 1.3 (Plasma nitrided + TiCN 5 µm)*

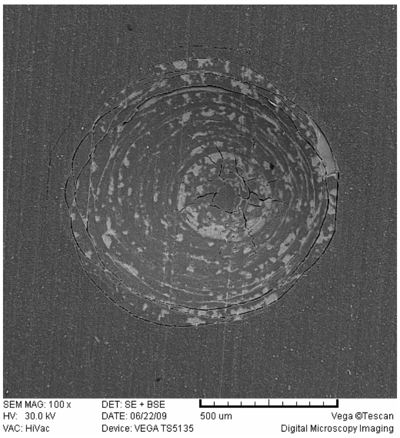

Fig.7 *Indentation adhesion test of sample 1.6 (Plasma Nitrided + TiCN 1,5um)*

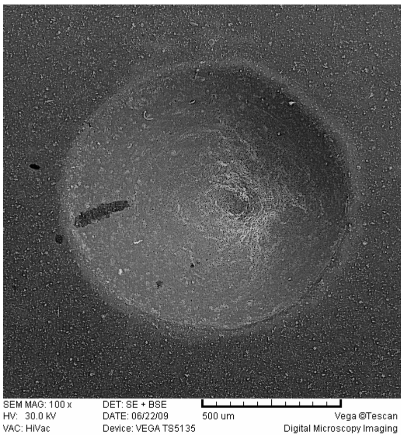

Fig.8 *Indentation adhesion test of sample 1.1 (TiCN 1,5um)*

ELECTROLYTIC IRON SULFIDES COATED WITH THE FILM OF SOLID ELECTROLYTE BASED ON Li_2O-LiF-P_2O_5 IN THE MODEL OF LITHIUM ACCUMULATOR WITH LIQUID ELECTROLYTE

A. Tron[1], *R. Apostolova*[1], *A. Baskevich*[1], *A. Nosenko*[1], *E. Shembel*[1,2]

[1]*Ukrainian State Chemical Technology University, Dnepropetrovsk,*
[2] *Enerize Corporation, Coral Springs, Fl, USA*

Corresponding author: E.Shembel (shembel@onil.dp.ua)
Phone, Fax::+380562 470391

Introduction

As a result of chemical and electrochemical interaction with Li^+-comprising liquid-phase aprotic electrolytes, cathode and anode materials are usually coated with the surface films (SEI - solid electrolyte interface) playing a key part in the transformation of lithium and lithium-ion batteries [1]. Reduction of battery irreversible capacity is promoted by modification of surface films with the additives introduced either into electrolyte or directly on the active material that involves changing the morphology and chemical composition of the electrode material/electrolyte interface [1, 2].

Electrolytic iron sulfides with the symbolic notation (e-Fe_xS_y), which are interesting for thin layer electrodes of the lithium accumulators operational at ambient temperature, lose their discharge capacity to the extent of cycling because of a number of reasons [3].

In the work for increasing electrolytic iron sulfide cycling efficiency, surface of (e-Fe_xS_y)– electrode was coated with the thin layer of solid glassy electrolyte. The results of (e-Fe_xS_y)-electrode electrochemical transformation are compared with those having thin - layer solid electrolyte in the models of lithium accumulator depending on the interval of discharge-charge voltage.

Experimental

Electrolytic iron sulfides, produced in accordance with [4] on aluminum substrate (e-Fe_xS_y/Al), were investigated within the 2.8-1.1 voltage range as the cathode materials for lithium accumulators; sulfides deposited on the stainless steel 18H12X9T (e-Fe_xS_y/SS) were investigated in a series of 2.80-0.05 V as the anode materials for lithium-ion system.

In the investigations there were used a solid electrolyte comprising Li_2O-LiF-P_2O_5 [5]. It was applied on the (e-Fe_xS_y)- electrode surface of 5-20 μm layer.

For determination of (e-Fe_xS_y)– deposits morphology their photographic recording was carried out with the Optical microscope NU-2, Carl Zeiss at 312,5 magnification.

Phase composition of the deposits was determined on the DRON-2.0 diffractometer using LiF monocrystal as a monochromator in CoK_α-radiation.

Electrochemical characteristics of e-Fe_xS_y were investigated in the model of disk 2325 cell with lithium counter electrode as well as in a three-electrode cell with lithium auxiliary electrode and Li/Li^+- reference electrode at room temperature. Galvanostatic cycling of the models was carried out on a test desk. Registration of cyclic voltamperograms was carried out on the analytical radiometer VoltaLab PJZ 301.

Results and discussion

Physical - chemical, structural and electrochemical characteristics of e-Fe_xS_y depend on the technological parameters of synthesis, the nature of a substrate and iron-sulfide mass in a thin layer electrode.

Comparison of the morphology of (e-Fe_xS_y)-deposits produced in this work on stainless steel and aluminum shows the insignificant difference in the size of forming them spheroid micrometric grains (4-8 µm).

The X-ray phase analysis has detected availability of the iron-sulfide phases of FeS mackinawite (15-37) and Fe_3S_4 in the composition of e-Fe_xS_y, deposited on a stainless steel and aluminum substrate. Fe_3S_4 structure depends on a substrate structure. In composition of the deposits obtained on a stainless steel the Fe_3S_4 phase with a smythite hexagonal structure predominates (10-437), whereas, in the deposit on aluminum the cubic structure of greigite (23-1123) is the prevalent structure of Fe_3S_4 phase. Size of deposit crystallites on aluminum substrate, determined by the reflection indexes of Fe_3S_4 phase (311), is equal to 32 nm, and in the deposit on a stainless steel the crystallite size is two times less.

At comparison of the electrochemical characteristics of initial (e-Fe_xS_y/Al)- electrodes and those coated with solid electrolyte it has been established that sulfide material coating does not change the discharge-charge profile of lithium accumulator models within the 2.8-1.1 voltage range. The values of the primary discharge capacity of initial (e-Fe_xS_y/Al)-electrode and the electrode coated with a solid electrolyte are practically the same. The irreversible capacity of (e-Fe_xS_y/Al) – electrode is 25-30% relatively the primary one. Specific discharge capacity of (e-Fe_xS_y, 5-6 $mg.cm^{-2}$) /Al)- electrode coated with a solid electrolyte (0.5 $mg.cm^{-2}$), stabilizes at the level of ~240 $mAh.g^{-1}$ (Fig.1). Solid electrolyte increases e-Fe_xS_y adhesion to aluminum substrate. Discharge capacity drop of the iron-sulfide electrode without coating is (1.3-1.5) % / a cycle, and that coated with solid electrolyte is (0.3-0.4) % / a cycle during 60-80 cycles at 0.06 $mA.cm^{-2}$ discharge current density.

The obtained data confirm that a solid electrolyte does not electrochemically react with the materials of (e-Fe_xS_y/Al)-electrode within the range of 2.8 - 1.1 V and stimulates its efficient cycling in lithium accumulator.

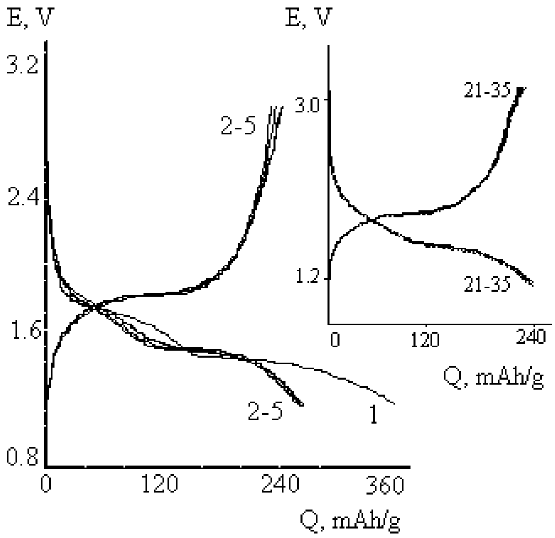

Fig.1 *Discharge-charge curves of the system (FeS, Fe_3S_4/Al – solid electrolyte) / EC DMC, 1M $LiClO_4$ /Li. I_{charge}=0.05 mA.cm^{-2}, $I_{discharge}$=0.06 mA·cm^{-2}. Figures near curves – cycle numbers.*

Discharge-charge characteristics of the initial (e-Fe_xS_y/SS)–electrode and that with the film of solid electrolyte within the 2.80-0.05 voltage range are different. The primary discharge capacity can reach for the initial (e-Fe_xS_y/SS)-electrode 800 mAh.g^{-1} (Fig.2a) and more, for (e-Fe_xS_y/SS-electrode) with the film of solid electrolyte it is significantly less (Fig.2b). In the cycling process capacity for (e-Fe_xS_y/SS)-electrode without film drops to the level of 500 mAh.g^{-1} (Fig.2a), for the (e-Fe_xS_y/SS)-electrode with a film its value is below this level (Fig.2b).

The cathode processes proceeding at the potentials below 1.0 V depend on the catalytic possibility of electrode materials for electrolyte decomposition. It is known that the cathode processes proceeding in the reactions of transient metal sulfides and oxides with lithium in liquid aprotic electrolytes within the 0.90-0.01 V range are connected with the electrochemical interaction of these compounds with electrolyte resulting in polymer film (SEI) formation on the surface of electrode material which can be repeatedly electrochemically transformed [6-8].

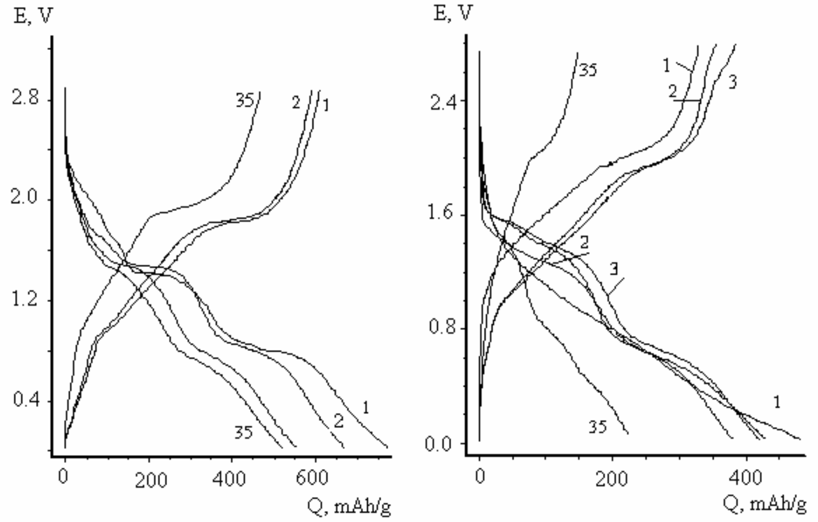

Fig.2 *Discharge-charge curves (FeS, Fe_3S_4/(SS) / EC, DMC, 1M $LiClO_4$ /Li: left-electrode with film, right- electrode without film. i_{charge}=0.05 mA.cm^{-2}, i_{disch} =0.06 mA·cm^{-2}*

The process of polymer film formation in the case of FeS, Fe_3S_4 /EC,DMC, 1M $LiClO_4$/Li system is only partially reversible. By the data of cyclic voltammetry, in the first discharge process for the (e-Fe_xS_y)–electrode coated with a solid electrolyte, the typical stages for the initial iron-sulfide electrodes at 1.65-1.70 and 1.40-1.45 V are absent, and the beginning of reduction process corresponds to 1.25-1.30 V. The all special cathode processes are displaced into the anode region. In the next 2-4 cycles their displacement takes place into the return direction toward the potentials specific for the initial (e-Fe_xS_y /SS)-electrode. Such a behavior can be explained as follows. In the first cycle the low value of discharge voltage is connected with a potential drop in the layer of solid electrolyte, which conductivity is lower than the liquid one and is ~10^{-7} Cm cm^{-1} [5]. In the further cycling the conductivity of solid electrolyte changes due to its electrochemical activity showing itself at low potentials. At cycling during 35 cycles the discharge capacity of (e-Fe_xS_y/SS) – electrode with coating gradually decreases that, to a certain extent, is determined by the electrochemical activity of solid electrolyte in the region of low potentials.

Conclusions

It has been established, that the solid electrolyte comprising Li_2O-LiF-P_2O_5 (Li_2O content ≥ 40 mol.%) is electrochemically stable on the surface of electrolytic FeS, Fe_3S_4 sulfides, deposited on aluminum at their interaction with lithium within the 2.8-1.1 voltage range in alkyl carbonate electrolyte of lithium perchlorate. The mentioned solid electrolyte may be recommended as the thin-layer coating for adhesion stabilization of electrolytic metal-sulfide cathode materials and increasing their cycling efficiency in lithium liquid-phase accumulators. In contract to this, at the potentials below 1V vs Li/Li^+ solid electrolyte takes part in the electrochemical irreversible process on (FeS, Fe_3S_4)-electrode as well as on the stainless steel, which is the constructional electrode material. Discharge characteristics of (FeS, Fe_3S_4)-electrode deteriorate due to the electrochemical activity of solid electrolyte at low potentials. Therefore it can not be useful as the coating of metal sulfide compounds used as the anode materials in lithium-ion systems.

References

1. L.El Quatani, R. Debryvère, C. Siret, P. Biensan, S. Reynaud, P. Iratçabal, and D. Gonbeau // J. Electrochem. Soc. 156. (2009) A103 - A113.
2. Yu-Chan Yen, Sung-Chieh Chao, Hung-Chun Wu, and Nae-Lih Wu. // J. Electrochem. Soc. 156. (2009) A95-A102.
3. V.M. Nagirny, R.D. Apostolova, E.M. Shembel. Synthesis and electrochemical characteristics of electrolytic metal-oxide and metal-sulfide materials for lithium accumulator systems. Dnepropetrovsk: USCTU. 2008. P. 260.
4. E. Shembel, R. Apostolova, V. Nagirny, A. Baskevich., P. Litvin. Elektrokhimiya 40.
1. (2004) 843-851. (In Russian).
5. A.V Tron, A.V Nosenko, E.M. Shembel // Russian Journal of Electrochemistry (Engl. Transl.). 45. (2009) 527-532.
6. G. Gireaud, S. Grugeon, S. Laruelle, S. Pillard, J.-M. Tarascon // J. Electrochem. Soc. 152. (2005) A850-A857.

7. P. Novák, A. Würsig, H. Buqa, M. Holzapfel, M. Hahn, R. Kotz // Lithium Batteries Discussions - Electrode materials. Arcachon. France. 22-27 May 2005. P. 178.
8. R. Apostolova, E. Shembel, Y. Talyosef, J. Grinblat, B. Markovsky, D. Aurbach // Russian Journal of Electrochemistry (Engl. Transl.). 45. (2009) 311-319.

ELECTROLYTIC IRON SULFIDES IN MODEL OF LITHIUM - ION POWER SOURCE

R. Apostolova[1], O. Kolomoyets[1], S. Chivikov[1], E.Shembel[1, 2]

[1]Ukrainian State Chemical Technology University, Dnepropetrovsk,
[2] Enerize Corporation, Coral Springs, Fl, USA

Corresponding author: E.Shembel (shembel@onil.dp.ua)
Phone, Fax:+380562 470391

Introduction

Me-sulfides (Me=Fe, Co, Ni, Mo), produced by electrolysis using the technology [1] is of certain interest for thin-layer lithium accumulator production. Electrolytic iron sulfides from a series of Fe_4S_3, Fe_2S_3, FeS, Fe_3S_4, FeS_2 are, to a different extent, electrochemically active in the reaction with lithium in lithium accumulator system with liquid–phase as well as with polymer electrolyte with PVdF-matrix within the voltage range 2.8 – 1.1 V [2, 3]. In this work it is shown the effective repeated transformation of electrolytic iron sulfide e-Fe_xS_y within the range of 2.8-0.02 V in the negative electrodes of lithium-ion system.

Experimental

Iron sulfides have been produced on stainless steel foil (10x10, mm) by the cathode reduction of aqueous electrolytes at the component ratio in the deposition electrolyte Fe:Ni:Cu:S=10:1.5:0.5:3.5, $T_{electrolysis}$=20°C. T_{drying}= 20°C [2]. Charge-discharge cycling of as-prepared Fe-sulfide electrodes was carried out at room temperature by galvanostatic method using lithium as an anode and also together with $LiCoO_2$ cathode. Positive composite electrode includes (%): $LiCoO_2$ - 80, acetylene black - 10, binder F4 - 10. $LiCoO_2$ is synthesized by thermal method, sintering stoichiometric mixture Li_2CO_3 and Co_3O_4. $LiCoO_2$-electrode with the active component mass 9 $mg.cm^{-2}$ produced by traditional spread method on aluminum current collector. Discharge capacity of $LiCoO_2$ is 130 mA $h.g^{-1}$ during the 5th cycle.

1 M $LiClO_4$ («Iodobrom», Ukraine) / 1:1 (vol) EC:DMC (Merck) was used as an electrolyte in power source model. Galvanostatic cycling of the models was carried out within the 2.8-0.02 V potential range on a test bench with computer ensuring with 0.05 $mA.cm^{-2}$ current density. Structure of the synthesized compounds was examined by X-ray diffraction analysis (DRON-2).

Results and Discussion

e-Fe_xS_y, consisting mainly of iron sulfide with the Fe_3S_4 structure having FeS admixture (Fig.1) has shown the cycleability within the 2.8-0.02 V range as it is shown in Fig.2. Differential capacity curves of such sulfide (Fig. 3) indicate availability of some stages in the interaction reaction with lithium taking place at the potentials of 2.0; 1.4; 0.8 V in reduction process and 1.0; 1.4; 2.0; 2.4 V in oxidation one. The reversible part of electrochemical transformation is 75-80%, whereas 20-25% is related to the side irreversible process connected with electrolyte decomposition.

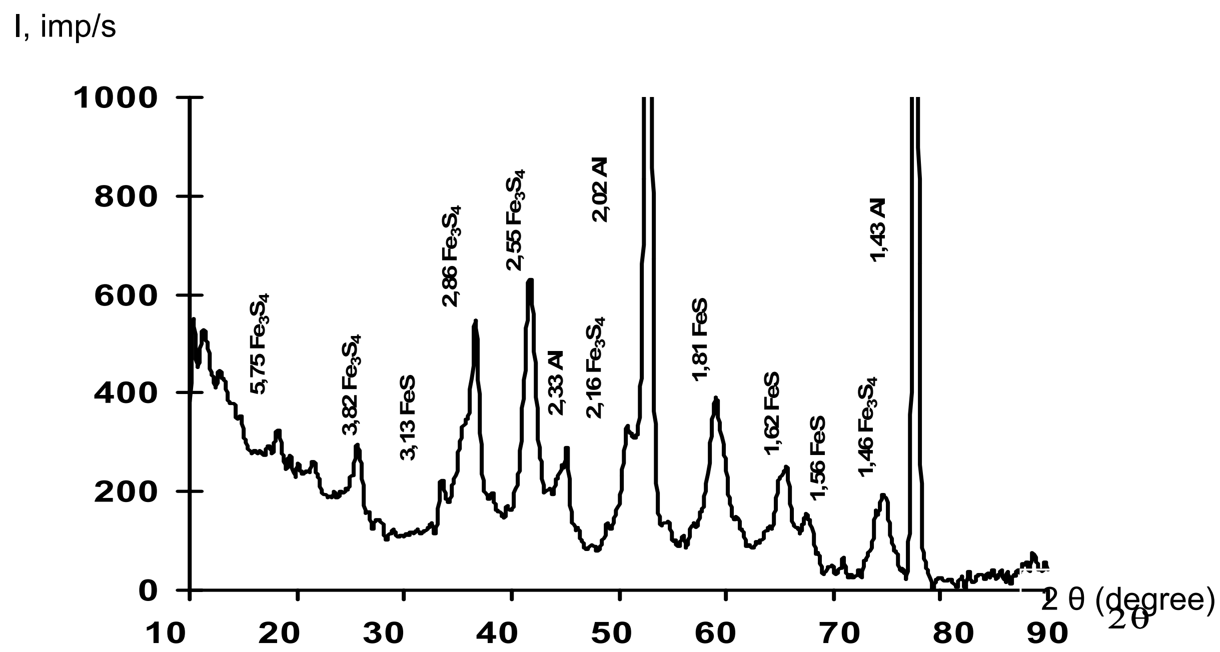

Fig. 1 X-ray pattern of electrolytic Fe_xS_y deposit. *Co-K_α radiation.*

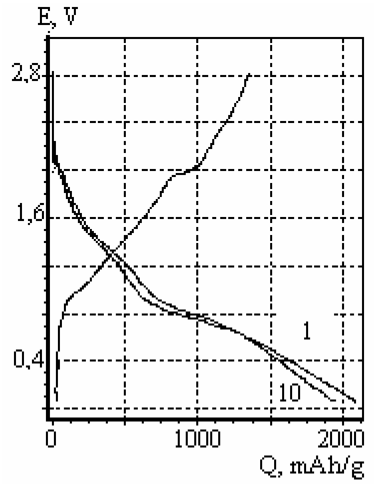

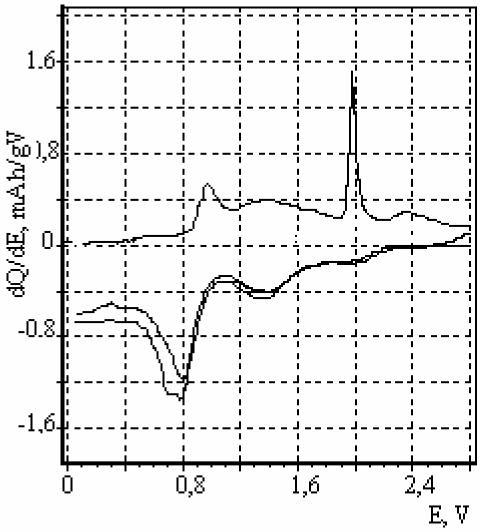

Fig. 2 *(left) - Discharge-charge characteristics of e-Fe_xS_y (1.5 mg/cm^2) in the model of lithium CPS.*

Fig. 3 *(right) - Curves of differential capacity in the function of e-Fe_xS_y potential.*

Discharge – charge profiles of $LiCoO_2$-Fe_xS_y system based on the electrodes with the presented characteristics is shown in Fig.4.

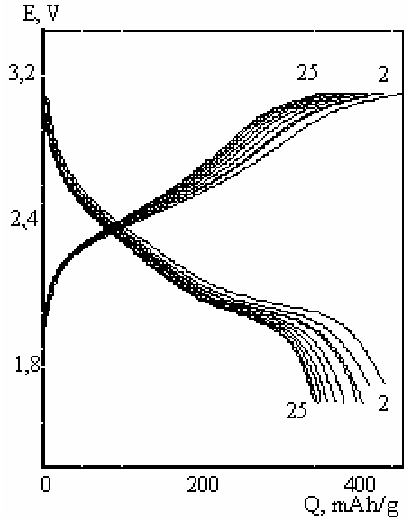

Fig.4 *Discharge-charge curves of e-Fe_xS_y / $LiCoO_2$ system. Numerals near curves – cycle numbers.*

As evident, the system represents the 2-volt power source, electrochemically transformed within the 3.1-1.4 V range. In the first discharge process the discharge capacity of 450 mAh /g e-Fe_xS_y stabilizes at the level of 350 -370 mAh/g after the 15th cycle.

Conclusions

The capacity of electrolytic iron sulfides for electrochemical transformation in the models of lithium –ion system of e-Fe_xS_y / $LiCoO_2$ within the 2.8-0.02 V range with the efficiency of 350-400 mAh /g e-Fe_xS_y during more than 50 cycles has been determined. As it is known, in traditional lithium-ion system ($LiMn_2O_4$) or ($LiCoO_2$)/ C (carbon material), the theoretical discharge capacity of graphite (C) is equal to 372 mAh/g. Thus, electrolytic iron sulfides can be considered as the promising ones for thin-layer negative electrodes of lithium-ion systems.

Acknowledgements

The authors acknowledge with thanks the financial support provided by the Ministry of Education and Science of Ukraine *(Contract 42070390).*

References

1. V.M.Nagirny*, R.D. Apostolova, E.M. Shembel* Synthesis and electrochemical characteristics of electrolytic metal-oxide and metal-sulfide materials for lithium accumulator systems, USCTU, Dnepropetrovsk, 2008. p. 260.
2. E.M. Shembel, R.D.Apostolova, V.M. Nagirny*, A.S. Baskevich, P.M. Litvin. //* Elektrochimiya (In Russian), **40** (2004). 843-851.
3. R.D. Apostolova*, L.I. Neduzhko, E.M. Shembel //* Zhurnal prikladnoy khimii (In Russian). **81** (2008). 939-944.

10th
ABAF
BRNO 2009
Advanced Batteries, Accumulators
and Fuel Cells

Solid and polymeric conductors

SYNTHESIS AND CHARACTERISTICS OF HYPERBRANCHED POLYMER ELECTROLYTE MEMBRANES FOR HIGH TEMPERATURE FUEL CELLS

Takahito Itoh[1], Takahiro Sakakibara[1], Yuki Takagi[1], Keita Hirai[1], Takahiro Uno[1], Masataka Kubo[1], and Yuichi Aihara[2]

[1]Division of Chemistry for Materials, Graduate School of Engineering, Mie University
1577 Kurima Machiya-cho, Tsu-shi, Mie 514-8507, JAPAN
[2]Samsung Yokohama Research Institute
2-7 Sugasawa-cho, Tsurumi-ku, Yokohama 230-0027, JAPAN

Corresponding author: Takahito Itoh (itoh@chem.mie-u.ac.jp)
Phone(Fax): +81-59-231-9410

Introduction

Polymer electrolyte fuel cells (PEFCs) are the most promising candidates for electric vehicles and portable electrical power sources because of their high energy efficiency and environmentally benign technology. The present PEFCs are used at a relatively low temperature, around 80 ^oC, because the proton conducting membranes used for fuel cell lose rapidly the proton conductivity at higher temperatures than 100 ^oC. In order to improve their performance and avoid the problem of catalyst poisoning by CO and reduce their cost, the operation of the PEFCs at higher temperatures than 100 ^oC is strongly desired. Recently, we prepared the interpenetrated-type proton conducting membranes based on the hyperbranched polymer with a sulfonic acid group at the periphery [1]. However, this interpenetrated-type membrane had a problem of leakage of the hyperbranched polymer with a sulfonic acid group at high temperature. In this work, the hyperbranched polymers with both a phosphonic acid group as a functional group and an acryloyl group as a cross-linker (**HBP-PA-Ac**), and with both a sulfonic acid group and an acryloyl group (**HBP-SA-Ac**) at the periphery were synthesized, and the ionic conductivities of their cross-linked membranes (**CL-HBP-PA**, **CL-HBP-SA**) under dry condition, their thermal properties, and fuel cell performance were investigated.

Experimental

The hyperbranched polymers with both a phosphonic acid and an acryloyl group (**HBP-PA-Ac**) were synthesized by the reactions of hyperbranched polymers with a OH group at terminals (**HBP-OH**, M_n=4,200 and 11,000) with acrylic acid, and with 4-(diethoxyphosphorylmethyl)benzoic acid, followed by hydrolysis with trimethylsilyl bromide and methanol. The hyperbranched polymers with both a sulfonic acid and an acryloyl group (**HBP-SA-Ac**) were synthesized by the reactions of **HBP-OH** (M_n=4,500) with acrylic acid, and with 4-sulfobenzoic acid monopotassium salt, followed by ion exchange reaction (**Scheme 1**). The membranes were prepared by a cast procedure. The fuel cell experiment was carried out with a single membrane electrode assembly (MEA) cell. Gas diffusion electrodes with 20 wt% Pt loading (1 mg/cm^{2}Pt, Pt/Vulcan XC-72, Electrochem. Inc.) was used to prepare to the MEA. I-V performances were determined under a flow of dry H_2 (100 ml/min)/O_2 (100 ml/min).

Results and Discussion

Addition of 5-10wt% SiO_2 as a thickener in the polymerizations of **HBP-PA-Ac** and **HBP-SA-Ac** with BPO was effective to form the cross-linked polymer electrolyte membranes (**CL-HBP-PA**, **CL-HBP-SA**) suitable for fuel cell experiments.

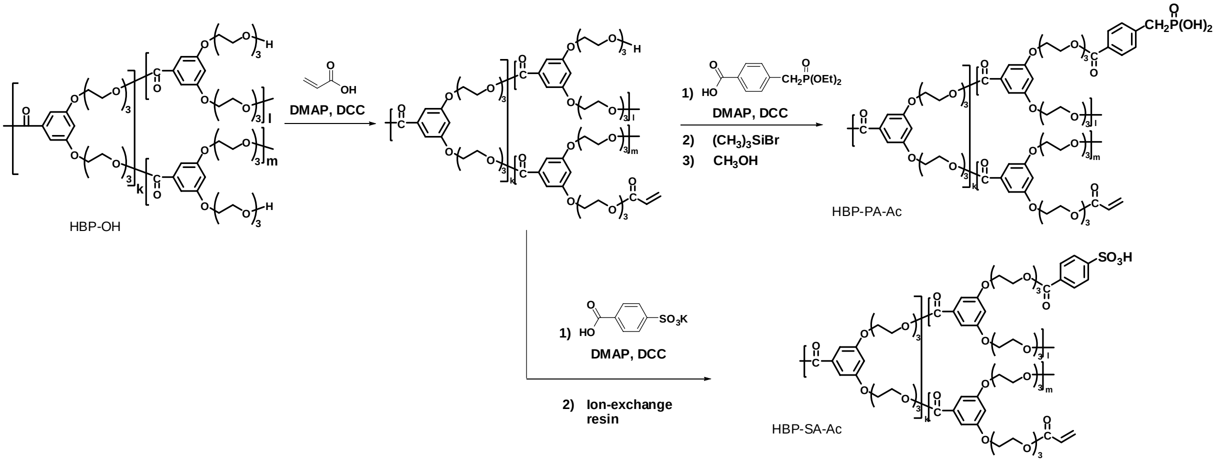

Scheme 1 *Synthesis route of hyperbranched polymers with functional groups at the periphery.*

The temperature dependence of ionic conductivities for the **CL-HBP-PA** and **CL-HBP-SA** membranes at 80-150 °C showed the VTF-type behavior (**Figs. 1** and **2**) and the ionic conductivities were found to be $1.2\mathrm{x}10^{-5}$ S/cm for the **CL-HBP-PA** (M_n=4,200) and $2.6\mathrm{x}10^{-6}$ S/cm for the **CL-HBP-PA** (M_n=11,000), respectively, at 150 °C.

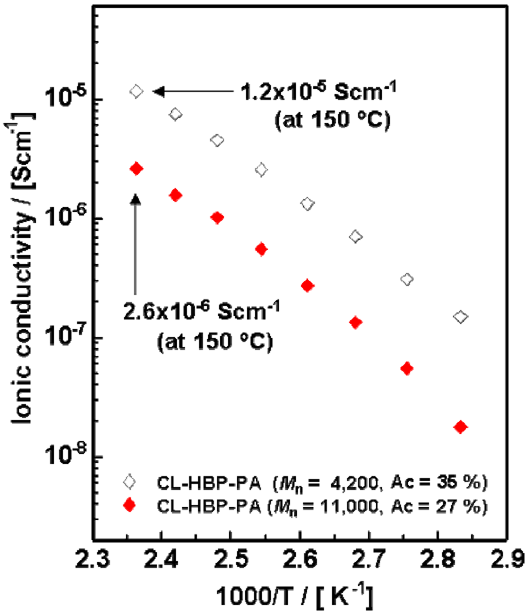

Fig. 1 *Arrhenius plots of the ionic conductivity for the **CL-HBP-PA** (M_n=4,200) and **CL-HBP-PA** (M_n=11,000).*

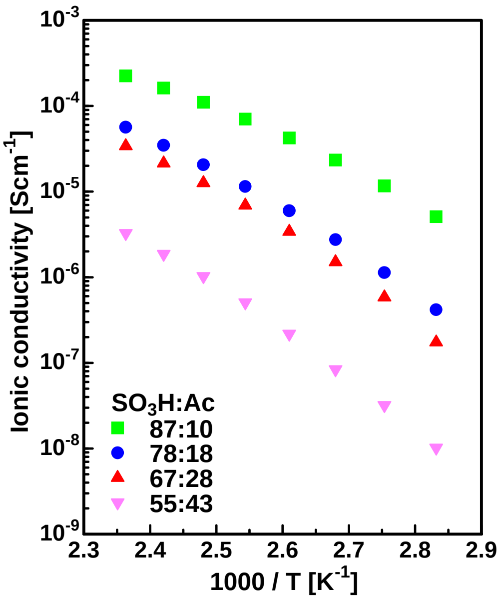

Fig. 2 *Arrhenius plots of the ionic conductivity for the* ***CL-HBP-SA*** *with various* SO_3H *contents.*

The glass transition temperatures (T_g) of the **CL-HBP-PA** (M_n=4,200) and **CL-HBP-PA** (M_n=11,000) membranes were determined by DSC measurement to be 26.8 ^oC and 38.8 ^oC, respectively. Both membranes did not show weight loss until 300 ^oC by TG/DTA measurement, indicating that they have excellent thermal stability for the fuel cell applications. Ionic conductivity of the **CL-HBP-SA** (M_n=4,500) membranes increased with an increase in the SO_3H unit and it was found to be 2.2×10^{-4} S/cm for the **CL-HBP-SA** with a 87%SO_3H/10%Ac ratio. The T_g of the membrane was 36.5 ^oC, and the membrane was stable until 260 ^oC.

Fuel cell measurement was carried out at 150 ^oC with **CL-HBP-PA** and **CL-HBP-SA** membranes using dry H_2 and O_2 gas under non-humidified conditions (**Figs. 3** and **4**). The open circuit voltages (OCV) were observed to be 0.76 V for the **CL-HBP-PA** (M_n=4,200), 0.53 V for the **CL-HBP-PA** (M_n=11,000), and 0.73 V for **CL-HBP-SA** (M_n=4,500) with a 78%SO_3H/18%Ac ratio, respectively. This indicates that electric power generation by the fuel cell using the present membranes under non-humidified conditions is possible.

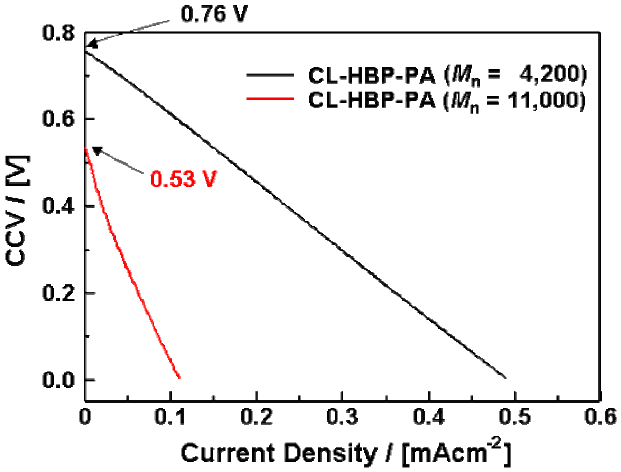

Fig. 3 *I-V characteristics of test fuel cells at 150 ^oC using CL-HBP-PA membranes as electrolytes. Sweep rate: 20mV/sec.*

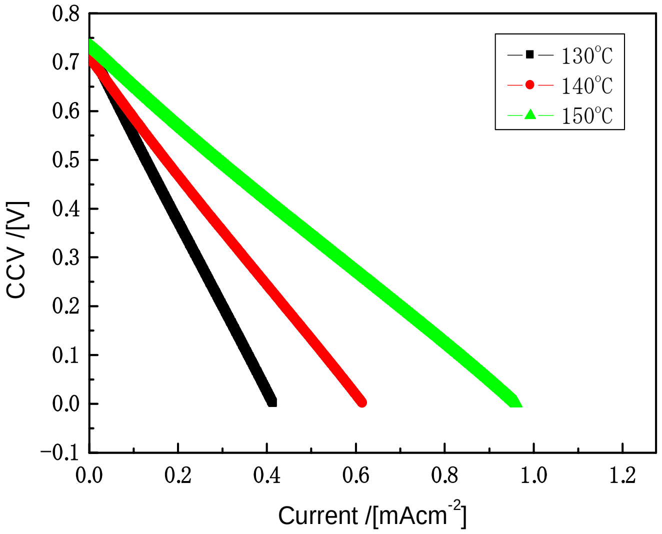

***Fig. 4** I-V characteristics of test fuel cell using the **CL-HBP-SA** membrane as electrolyte. Sweep rate: 20mV/sec.*

References

1. T. Itoh, T. Hamaguchi, T. Uno, M. Kubo, Y. Aihara, A. Sonai: Solid State Ionics **177** (2006) 185.

DESIGN OF SOLID POLYMER ELECTROLYTES BASED ON POLYESTERDIACRYLATES WITH Li^+ CONDUCTIVITY

K.G. Khatmullina, O.V. Yarmolenko, L.M. Bogdanova

Institute of Problems of Chemical Physics Russian Academy of Sciences, Academician Semenov avenue-1, Chernogolovka, Moscow region, 142432, Russia

Corresponding author: Khatmullina K.G. (kynsyly@icp.ac.ru)
Phone: +7(496)5225625

Introduction

Polymer electrolytes are used in various electrochemical devices (solar batteries, super capacitors, power sources), including electrochromic devices (e.g., «smart windows»). One of the most promising areas of application is the solid-state lithium batteries, which in the case of replacing of the liquid electrolyte on the polymer electrolyte are much safer. In addition, the working area of the temperature of the batteries is expanding that are most actually for their application in hybrid electric vehicles, which are highly heat. Solid polymer electrolytes (SPE) constitute «limit searchings» in terms of desired properties of the batteries, because they allow to create a completely solid state device with simple production process. It is possible to obtain the device of any form or size.

The aim of this work is to develop new solid polymer electrolyte based on polyesterdiacrylate and $LiClO_4$ for solid state lithium battery used in electric vehicles at temperatures up to 100 °C. The developed systems should be differed fire and explosion safety, so far as the organic solvent is excluded.

Experimental

For the synthesis of polymer matrices were used following initial components:

1) diacrylate based on polyethylene glycol (DAc-PEG), M_n=430:

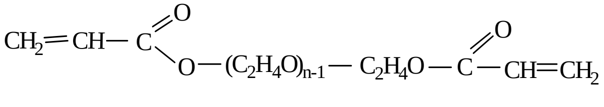

2) polyesterdiacrylate based on oligohydroxyethylacrylate (DAc-OHEA), M_n=2500:

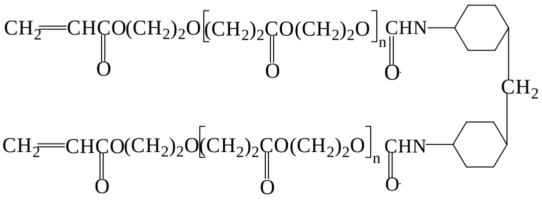

The polymer electrolyte was synthesized in the form of films with thickness d = 0.011–0.015 cm according to the reaction of radical polymerization of polyesterdiacrylates containing $LiClO_4$ in the presence of benzoyl peroxide (BP) as the initiator in stepwise heating:T_1= 80 ºC (5 h), T_2= 140 ºC (2 h).

The equivalent circuit (Fig. 1) includes the geometric capacitance shunting the electrolyte resistance and electrode impedance. The C_{DL} and CPE elements characterize the double layer charging at the electrode/electrolyte interface.

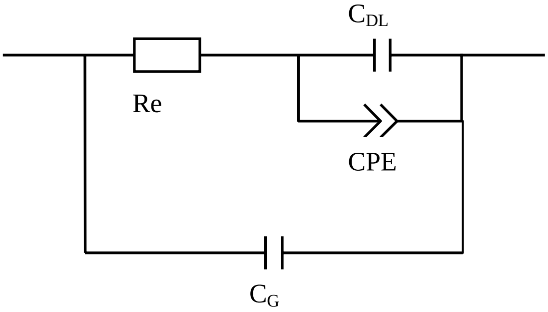

Fig. 1 *Equivalent circuit of the SS/SPE/SS cell: Re is the electrolyte resistance;* C_G *is the geometric capacitance;* C_{DL} *is the double layer capacitance; CPE is the constant phase element.*

Result and Discussion

SPE based on DAc-PEG with different concentrations of $LiClO_4$: 10, 15, 20, 25 wt.% were synthesized and studied. Glass transition temperatures of SPE all composition were measured by differential scanning calorimeter (DSC). The results are shown in Table 1. Fig. 2 shows a typical DSC diagram by example of SPE with 20 wt.% $LiClO_4$. Table 1 shows, that at addition of $LiClO_4$ glass transition temperature of SPE increases, which indicates the formation of intermolecular bonds of polymer - salt.

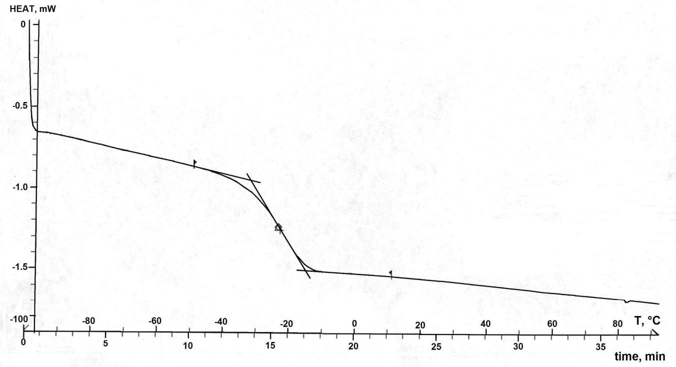

Fig. 2 *DSC diagram of SPE with 20%* $LiClO_4$ *(the y-axis corresponds to the heat generated; the x-axis corresponds to temperature and time). The glass point of the SPE with 20%* $LiClO_4$ *is -23.25 °C.*

Table 1 *Dependence of glass transition temperature of SPE on concentration of* $LiClO_4$

$[LiClO_4]$, wt.%	0	10	15	20	25
T_g, °C	-30,0	-27,0	-23,4	-21,0	-20,5

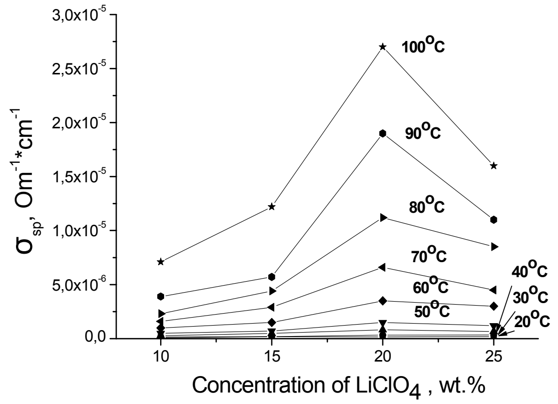

Fig. 3 *The dependence of conductivity of SPE based on DAc-PEG on concentration of* $LiClO_4$ *at different temperatures.*

Specific conductivities (σ_{sp}) of SPE all composition were measured by impedance spectroscopy. The results presented in Fig. 3. Fig. 3 shows that the highest conductivity in the temperature range 50 ÷ 100 ° C has a polymer electrolyte with the introduction of 20 wt.% $LiClO_4$. This concentration was chosen for further studies.

SPE based on mixtures of DAc-OHEA and DAc-PEG at their different molar ratio are synthesized. Compositions of SPE are given in Table. 2.

Table 2 *Composition of SPE*[*]*.*

№ SPE	DAc-OHEA	DAc-PEG	$LiClO_4$	BP	σ (30°C)	σ (100°C)
1	–	79,2	20	0,8	$2,88\times10^{-7}$	$2,69\times10^{-5}$
2	79,2	–	20	0,8	$4,78\times10^{-7}$	$5,25\times10^{-5}$
3	39,6	39,6	20	0,8	$3,15\times10^{-7}$	$1,93\times10^{-5}$
4	26,4	52,8	20	0,8	$7,74\times10^{-7}$	$4,07\times10^{-5}$
5	19,8	59,4	20	0,8	$3,41\times10^{-8}$	$1,97\times10^{-5}$
6	13,2	66,0	20	0,8	$7,88\times10^{-8}$	$2,93\times10^{-5}$
7	7,2	72,0	20	0,8	$2,05\times10^{-7}$	$3,67\times10^{-5}$
8	52,8	26,4	20	0,8	$8,64\times10^{-8}$	$2,96\times10^{-5}$
9	59,4	19,8	20	0,8	$4,02\times10^{-8}$	$9,23\times10^{-6}$
10	66,0	13,2	20	0,8	$1,53\times10^{-8}$	$1,80\times10^{-5}$
11	72,0	7,2	20	0,8	$9,59\times10^{-9}$	$1,34\times10^{-5}$

[*] - compositions are presented in mass percentage.

The conductivity of SPE based on mixtures of DAc-OHEA and DAc-PEG at their different molar ratio was investigated. The results presented in Fig. 4.

To increase of ionic conductivity in composition of SPE № 5 (Table 2) was introduced nanocomposite TiO_2 (60 nm) in number of 1 and 5%. The results presented in Fig. 5.

Fig. 5 shows that ionic conductivity of the SPE is increased throughout temperature range (20 ÷ 100)°C: the maximal effect is observed at 30°C (5.6 times compared with SPE without additives).

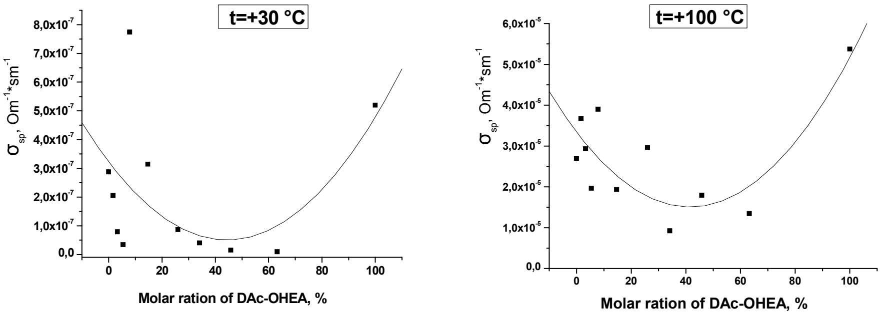

Fig. 4 *The dependence of SPE conductivity on the molar content of DAc-OHEA in the system of DAc-OHEA–DAc-PEG.*

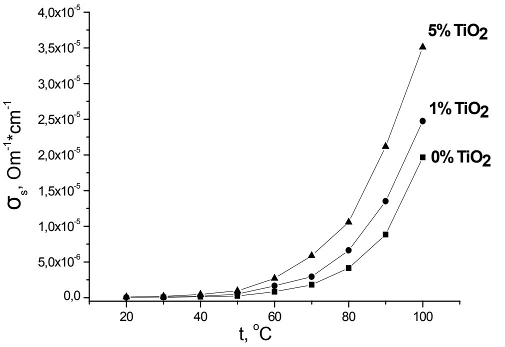

Fig. 5 *The dependence of SPE conductivity on temperature at different contents of TiO_2 (1, 5 wt.%).*

From literature data [1-4] it is known, that the addition of nanocomposite increases the mechanical strength of obtained thin film electrolyte, which was observed in our experiment too – the film became more stable and elastic.

Conclusion

Thus, new solid polymer electrolytes based on polyesterdiacrylates one of which contains blocks of polyethylene, and salt $LiClO_4$ were synthesized and studied by the method of radical polymerization. Concentration of $LiClO_4$ in SPE based on DAc-PEG was optimized. Found that the maximum conductivity in the range of 20 - 100 °C has the SPE with the introduction of 20 wt. % $LiClO_4$. We studied the composition of the polymer matrix based on DAc-OHEA and DAc-PEG at their various ratios: DAc-OHEA:DAc-PEG (1:59) (1:29) (1:17) (1:12), (1:6), (1:3) (1:2) (1:1), (2:1). The best conductivity 7.7×10^{-7} S/cm at 30 °C in SPE based DAc-OHEA:DAc-PEG (1:12), and at 100 °C conductivity of lithium ions most increases in the matrix of pure DAc-OHEA and reaches 5.4×10^{-5} S/cm. The influence of additives of TiO_2 nanocomposites on ion conductivity of SPE at temperatures 20 ÷ 100 °C was studied. Ionic conductivity of the SPE increases throughout the temperature range and at 30 °C increases in 5,6 times in comparison with SPE without additives.

References

1. B. Scrosati, F. Croce and L. Persi: J. Electrochem. Soc. **147** (2000) 1718–1721.
2. B. Kumar and L.G. Scanlon: Solid State Ionics, **124** (1999) 239–254.
3. G.B. Appetecchi, F. Croce, L. Persi, F. Ronci, B. Scrosati: Electrochim.Acta, **45** (2000) 1481.
4. A.S. Best, J. Adebahr, P. Jacobsson, D.R. MacFarlane, M. Forsyth: Macromolecules, **34** (2001) 4549.

APPLICATION OF CHITOSAN/IOTA-CARRAGEENAN POLYMER ELECTROLYTES IN ELECTRICAL DOUBLE LAYER CAPACITOR (EDLC)

N. E. A. Shuhaimi, N. A. Alias, M. Z. Kufian, S. R. Majid and A. K. Arof

Center for Ionics, University of Malaya, 50603, Kuala Lumpur, Malaysia

Corresponding author: A. K. Arof (akarof@um.edu.my)
Phone No.: +603-79674085
Fax No.: +603-79674146

In this work, the use of chitosan/iota-carrageenan electrolyte as a separator in electrical double layer capacitor was studied. The separator is in solid form. The solid electrolyte was prepared by using solution casting technique. The source of proton was orthophosphoric acid (H_3PO_4) and polyethylene glycol (PEG 200) as plasticizer. A set of samples with different ratios of PEG and H_3PO_4 were prepared to see the effects of the proton donor and plasticizer on the conductivity. The best conducting sample was used as separator in EDLC. The discharge capacitance of over 25 cycles is 30 F g^{-1}.

PROPERTIES OF COMPOSITE POLYMER ELECTROLYTE USING HYPERBRANCHED POLYETHER

Takahiro Uno, Hiroki Sano, Masataka Kubo, and Takahito Itoh

Division of Chemistry for Materials, Graduate School of Engineering, Mie University,
1577 Kurimamachiya-cho, Tsu, Mie 514-8507, Japan

Corresponding author: Takahiro Uno (uno@chem.mie-u.ac.jp)
Phone: +81-59-231-9411, Fax: +81-59-231-9410

Introduction

Solid polymer electrolytes composed of poly(ethylene oxide) (PEO) and lithium salt have been widely studied as an electrolyte material for all solid lithium secondary batteries because of its high ionic conductivity at high temperature, but the practical use of PEO-based solid polymer electrolytes is often hindered due to their low ionic conductivity at room temperature and poor mechanical properties. Recently, we have investigated the polymer electrolyte based on hyperbranched polymer (HBP) which is completely amorphous and has large number of branch end with highly segmental motion ability. We have reported that the composite polymer electrolytes composed of PEO, lithium salt and hyperbranched polyester, poly[(bis(triethylene glycol)benzoate)] capped with acetyl groups, (**HBP-1a**) as a plasticizer show high ionic conductivity over the wide temperature range because of the effective suppression of crystallization of PEO by addition of **HBP-1a** [1]. Furthermore, we found that the use of hyperbranched polyester with terminal acryloyl groups (**HBP-1b**) instead of **HBP-1a** could improve the mechanical property of the composite polymer electrolytes by the introduction of cross-linking [2]. However, those hyperbranched polyesters were formed by ester-linkage which is relatively weak chemical bond, and there were some problems on their chemical stability. In this work, we synthesized novel hyperbranched polymer formed by ether-linkage (**HBP-2**), and investigated the properties, such as ionic conductivity, thermal stability, electrochemical stability, mechanical strength and chemical stability, of composite polymer electrolyte composed of PEO, lithium salt and **HBP-2**.

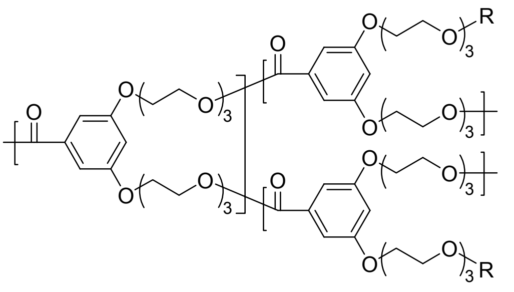

R = $CH_3-\underset{O}{\underset{\|}{C}}-$: **HBP-1a**

$CH_2=CH-\underset{O}{\underset{\|}{C}}-$: **HBP-1b**

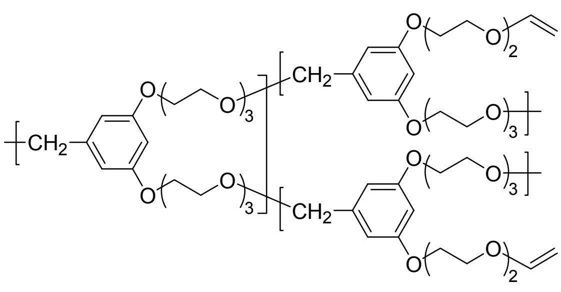

HBP-2

Experimental

Novel hyperbranched polyether (**HBP-2**) was synthesized by polycondensation of AB_2-type monomer with one hydroxy group and two bromo groups (**2**), which derived from previously reported AB_2-type monomer (**1**) by two step reactions (**Scheme 1**). The composite polymer electrolyte films were prepared by solvent casting method of the mixture of PEO (80 wt%), **HBP-2** (20 wt%) and $LiN(SO_2CF_3)_2$ at various compositions, and then cross-linked by heating.

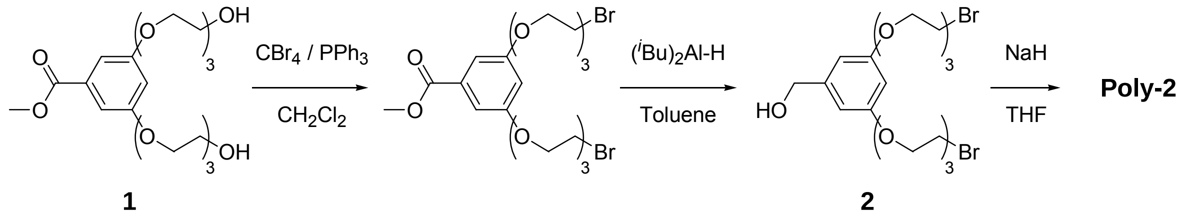

***Scheme 1** Synthesis route of hyperbranched polyether (**poly-2**).*

Results and Discussion

The effect of the lithium salt concentration on the ionic conductivity for the cross-linked composite polymer electrolyte using **HBP-2** was investigated at four different lithium salt concentrations ([Li]/[O] ratios of 1/8, 1/12, 1/16, and 1/20). The temperature dependence of ionic conductivities of their composite polymer electrolytes was shown in **Fig. 1**. The ionic conductivity increased with increasing lithium salt concentration, reached the maximum value at [Li]/[O] ratio of 1/12, and then decreased. This behavior is similar to the composite polymer electrolytes using hyperbranched polyester previously reported.

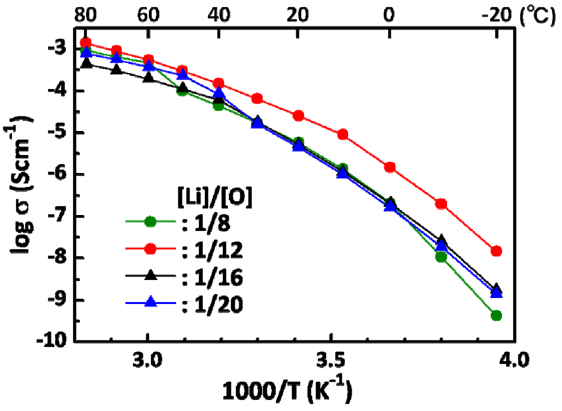

***Fig. 1** Temperature dependence of the ionic conductivities for the cross-linked composite polymer electrolytes using **HBP-2** at the different [Li]/[O] ratios.*

The effect of the HBP structure on the ionic conductivity for the composite polymer electrolytes at fixed [Li]/[O] ratio of 1/12 was investigated using three different HBPs (**HBP-1a**, **HBP-1b**, and **HBP-2**), and the results were shown in **Fig. 2**. The ionic conductivity of the cross-linked composite polymer electrolyte using **HBP-1b** was lower than that of the none-cross-linked composite polymer electrolyte using **HBP-1a**. This indicates that the segmental motion of polymer chains, which plays an important role on ion transport, was restricted by cross-linking. On the other hand, the cross-linked composite polymer electrolyte using **HBP-2** showed the higher ionic conductivity than that of non-cross-linked composite polymer electrolyte using **HBP-1a**. This result suggests that the segmental motion of polymer chains in the composite polymer electrolyte was improved by the alteration of HBP structure from ester-linkage to ether-linkage.

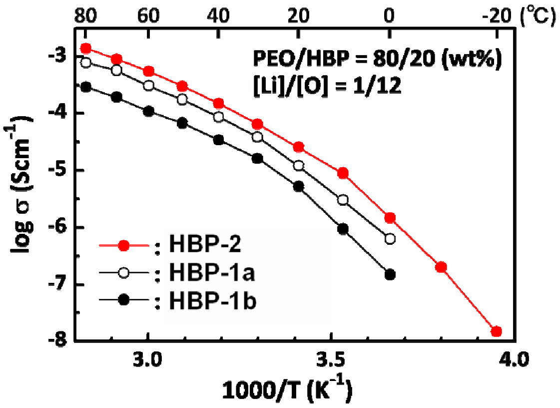

Fig. 2 *Temperature dependence of the ionic conductivities for the composite polymer electrolytes using various hyperbranched polymers.*

Thermal property, electrochemical stability and mechanical property for the composite polymer electrolytes using three different HBPs were summarized in **Table 1**. All composite polymer electrolytes showed almost same glass transition temperature, 5 wt% loss temperature and breakdown voltage, indicating that the HBP structure did not affect significantly the thermal property and electrochemical stability of the composite polymer electrolytes. The cross-linked composite polymer electrolyte using **HBP-2** showed about one-third tensile strength of the cross-linked composite polymer electrolyte using **HBP-1b**, but it has twice as high tensile strength as the non-cross-linked composite polymer electrolyte using **Poly-1a**. The molecular weight of **Poly-1a** decreased gradually in the presence of lithium hydroxide, while the molecular weight of **Poly-2** did not change. This indicates that **Poly-2** formed by ether-linkage possesses high chemical stability against hydrolysis.

Table 1 *Thermal property, electrochemical stability and mechanical property of the composite polymer electrolytes using three different HBPs.*

HBP in Composite Polymer Electrolyte	Glass Transition Temperature (T_g) (°C)	5 wt% Loss Temperature (T_{d5}) (°C)	Breakdown Voltage (V)	Tensile Strength (MPa)
HBP-2	−45	378	4.2	0.67
HBP-1a	−40	360	4.3	0.37
HBP-1b	−41	313	4.3	2.21

References

1. T. Itoh, Y. Ichikawa, T. Uno, M. Kubo, O. Yamamoto: Solid State Ionics. **156** (2003) 393.
2. T. Itoh, S. Gotoh, S. Horii, S. Hashimoto, T. Uno, M. Kubo, T. Fujinami, O. Yamamoto: J. Power Sources. **146** (2005) 371.

NEWS CONCERNING GEL POLYMER ELECTROLYTES

M. Sedlaříková[1], J. Vondrák[2], M. Macalík[1]

*[1] Faculty of Electrical Engineering and Communication, Department of Electrotechnology,
Údolní 53, 602 00 Brno, Czech Republic
[2] Department of Inorganic Chemistry, Academy of Science, Husinec, Řež near Praque,
Czech Republic*

Corresponding author: Jiří Vondrák (vodrakj@iic.cas.cz)
Phone: +420 607 285 434
Fax: +420 541 146 147

Gel polymer electrolytes based on PMMA and aprotic solvents have been studied for a long time in our laboratory. Generally, the gels are prepared by the polymerization of MMA with the solvent (PC, usually) by action of either a commercial polymerization catalyst SUPERACRYL® (Spofa-Dental Co., Czechia) or the agent ABIN (azo bis iso butyronitrile) activated by heat.

It was shown already that ABIN polymerized gels exhibit lower specific conductivity. Similarly, the apparent diffusion coefficient of the ferrocene redox couple is lower in ABIN polymerized gels. The difference between them was investigated using NMR spectrometry of ^{7}Li ions as shown in Fig. 1 where the process of their formation was monitored. Apparently, ABIN formed gels undergo deeper decrease of ^{7}Li mobility that these formed by SUPERACRYL®. This indicates that solid particles of the activator SUPERACRY:L remain in the mass and the intergranular space is filled by quasi liquid solution of Li salts. Moreover, it was impossible to remove the residuum of polymerization catalyst. Therefore we have limited further investigation to ABIN formed gels only.

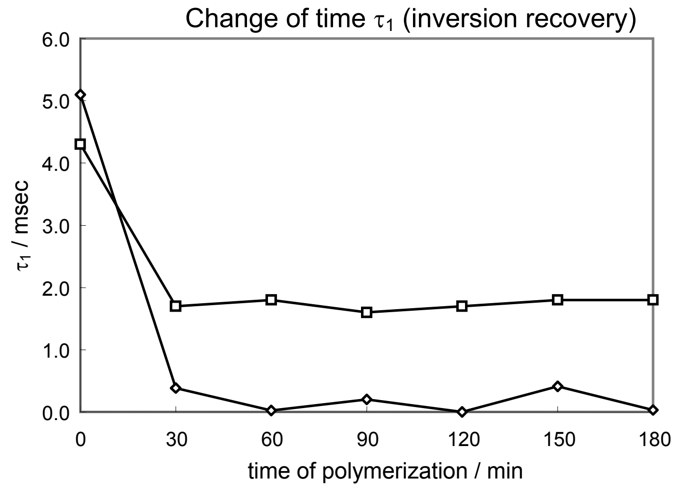

***Fig. 1** Decrease of relaxation time τ_1 in the process of film ageing at +80°C. Squares: SUPERAKRYL formel gels, diamonds: ABIN formel gels.*

Considering the gel containing $LiClO_4$ to be strong electrolyte, its conductivity should be expressed as equivalent (molar for electrolyte 1:1), i.e. as $\Lambda = \sigma / (1000 \cdot c)$ from specific conductivity σ and concentration *c.* This quantity should slowly and linearly decrease with increasing ionic strength (according to Kolrausch, Debye, Hückel and Onsager theories expressed as $c^{1/2}$).

Molar conductivity Λ at temperatures below room temperature to -20°C is shown in Fig. 2. It is apparent that the quantity Λ passes through a maximum which cannot be simply explained by ion association.

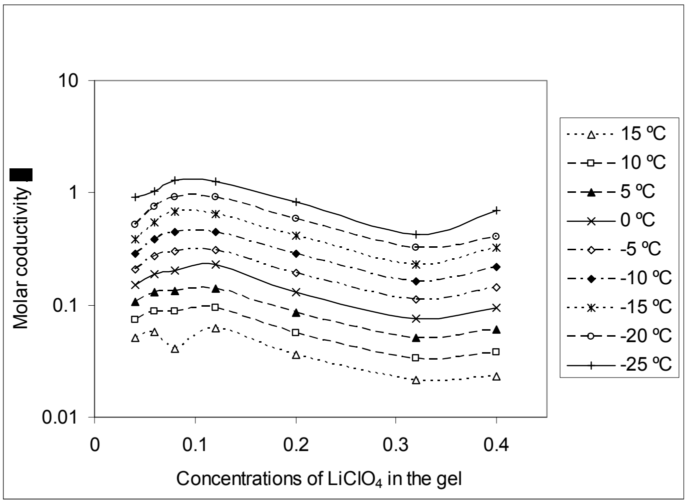

Fig. 2 *Equivalence molar coductivity Λ(in logarithmic scale) for various concentrations of $LiClO_4$ in the gel. From top to down: from temperature -25°C up by 5°C to +15°C.*

Fig 3 shows the Young module E for samples in the range of concentrations. This value exhibits a monotonous increase. We must expect that the presence of salt (Li perchlorate) increases the solidity of the gel and that this change changes the rheology of the gel and as a result also the specific conductivity.

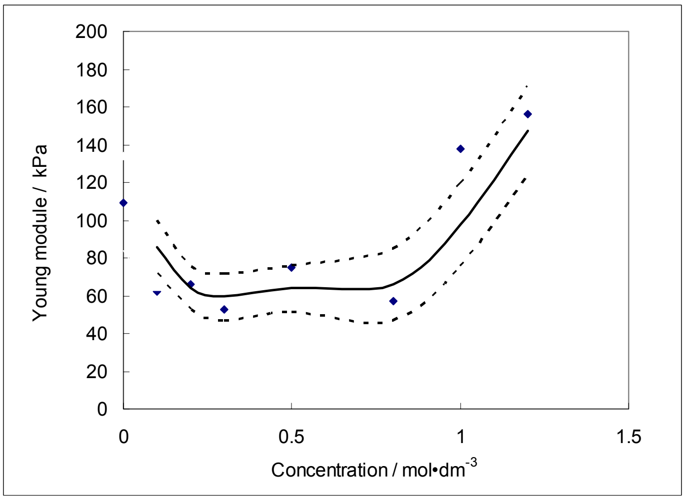

Fig. 3 *Influenc e of $LiClO_4$ concentration on Young module of PMMA-PC gel. Dotted lines: statistic estimations of reliabilities*

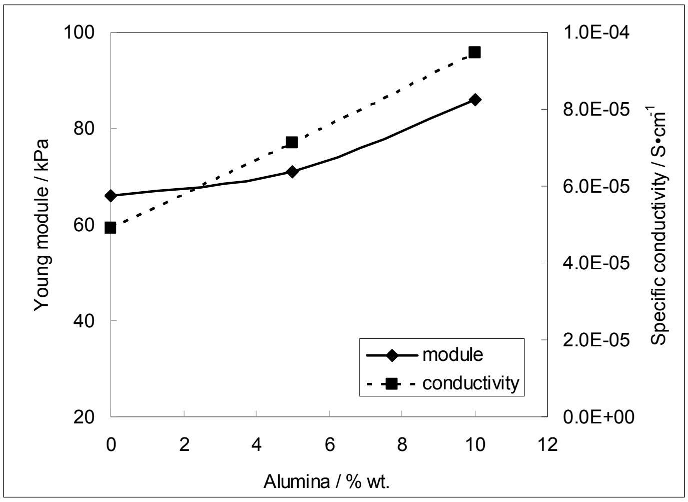

***Fig. 4** The addition of nano-alumina. (left, solid) Young module, kPa, (right, dotted) specific conductivity, S/cm, Horizontal: Addition of nano-alumina, % wt.*

Following Fig. 4 shows how both Young module and specific conductivity increases in gels to which nano-alumina was added. Also this fact emphasizes the influence of rheologic properties of gel polymer electrolytes. This fact is supported by the Walden theory according which the product $\Lambda.\eta$should be pore or less constant.

References

Krejza, O; Velická, J; Sedlaříková, M, et al., *J. Power Sources* **178** (2008) 774

Acknowledgment

Ministry of Education of Czech Republic, Project MSM002130516
Academy of Sciences, Research Plan AV/ 0Z403 0502
The Grant Agency of the Academy of Sciences of the CR, project KJB208130902.

THERMAL PROPERTIES OF SULFOLANE

M. Sedlaříková[1], *J. Vondrák*[2], *M. Zatloukal*[1]

[1] *Faculty of Electrical Engineering and Communication, Department of Electrotechnology, Údolní 53, 602 00 Brno, Czech Republic*
[2] *Department of Inorganic Chemistry, Academy of Science, Husinec, Řež near Praque, Czech Republic*

Corresponding author: Jiří Vondrák (vodrakj@iic.cas.cz)
Phone: +420 607 285 434
Fax: +420 541 146 147

Introduction

The thermal properties of sulfolane (tetrahydrothiofendioxide) $C_4H_8O_2S$ (further abbreviated as SL) is a compound rather similar to aprotic strongly polar solvent propylene carbonate (PC) or ethylene carbonate (EC) by many of its properties as well as structure formulas:

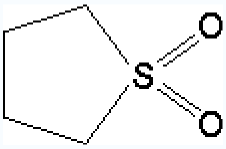

SL

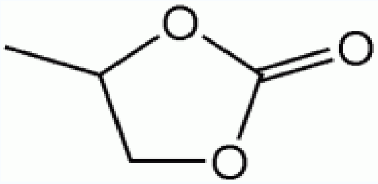

PC

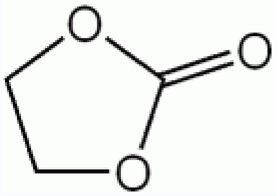

EC

We decided to investigate some of its thermal properties both alone and in mixture with propylene carbonate.

Melting point

Rather high melting point would be great disadvantage in technical applications (similarly as EC). We have measured freezing curves of SL, solutions of $LiClO_4$ and mixtures SL-PC. Some results are given in Fig. 1. Marked super cooling is visible on the temperature profile and proper value appears after the super cooling is passed over. In the presence of Li salt however the profile changes and the solidification starts rather lower. The cryoscopic constad and heat of fusion were estimated in this way. On contrary to this, an addition of PC does not exhibit the cooling profile of the same type and formation of solid solutions should be expected. Both data show the way how the unpleasant high melting (freezing) point of SL can be bypassed.

Flash point

The flash point of SL-PC mixtures is given in Fig.1. Apparently, the increase of flash point is in accordance to lower vapor pressure of SL.
Thermal stability of gel polymer electrolytes containing SL

Gels prepared by polymerization of MMA containing a solution LiClO4 in SL were exposed to heating in a DTA –GTA device. The device is enabled by mass spectrometric identification of decomposition products. An example of results is presented in Fig2. As we see, the gel prepared from SL does not undergo any heat emitting reaction up to temperature close to 250°C. The composition of gaseous products is also shown in the figure. Typical products are SO_2, CO_2 and water.

Conclusion

The properties of CL as aprotic and highly polar solvent are promising for many applications.

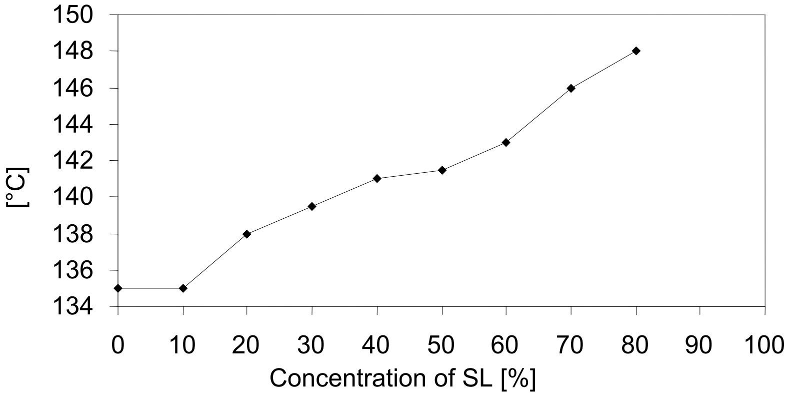

Fig. 1 *Flash point of mixtures LS-PC (wt. %)*

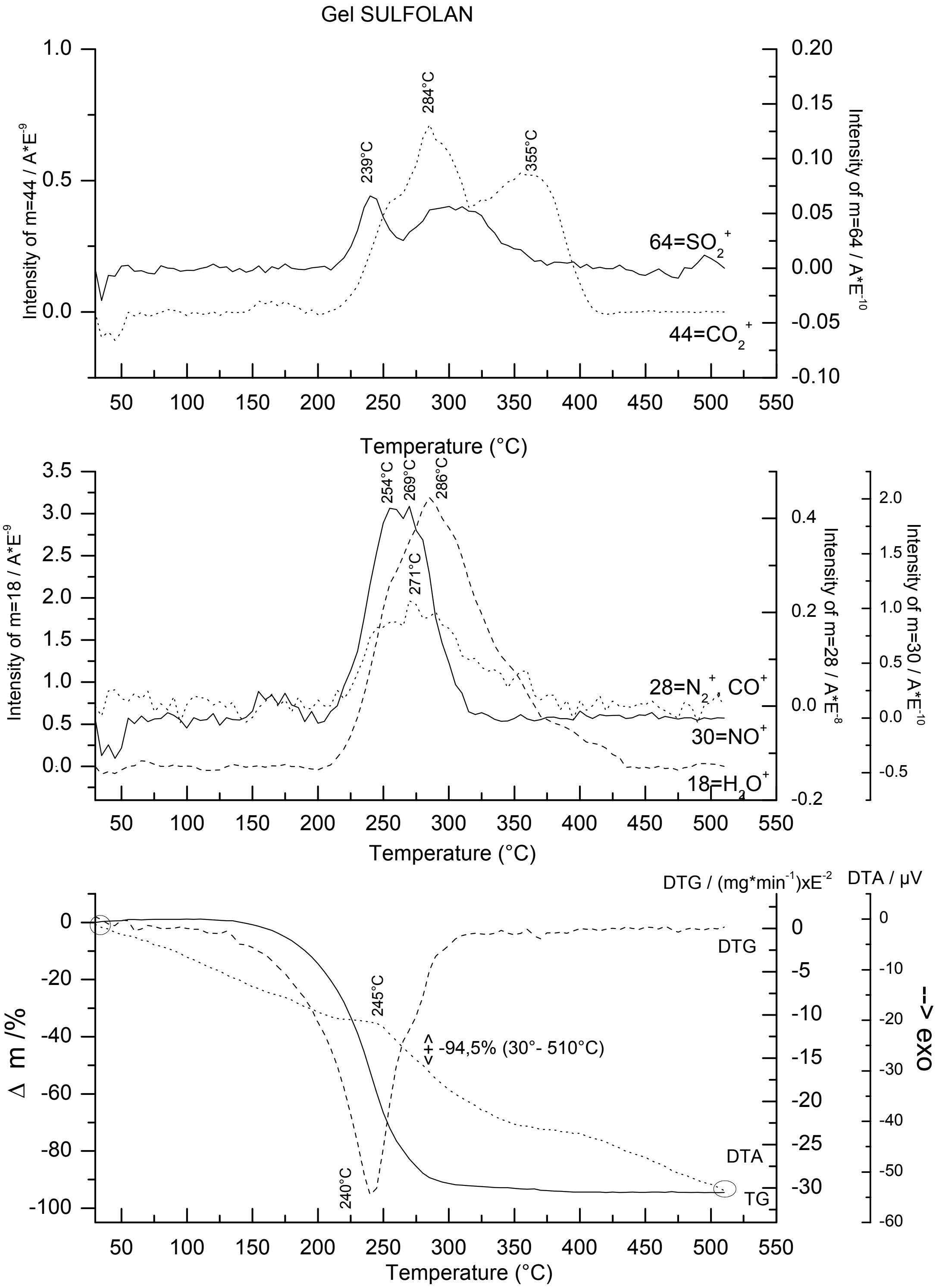

Fig. 2 DTA-GTA test of PMMA-sulfolane gel. (above: mass spectrometry of decomposition products)

Acknowledgment

Ministry of Education of Czech Republic, Project MSM002130516
Academy of Sciences, Research Plan AV/ 0Z403 0502

NMR TRANSPORT MEASUREMENTS OF PMMA/LITHIUM SALT-BASED POLYMER ELECTROLYTES

S. Abbrent[a], S. Khatun[b], S.G. Greenbaum[b], J.Vondrak[c], M Sedlarikova [c]

[a]Faculty of Science, University of South Bohemia, Branišovská 31, 370 05 České Budějovice, Czech Republic
[b]Dept. of Physics and Astronomy, Hunter College of CUNY, 695 Park Avenue, New York, NY 10065 USA
[c] Brno University of Technology, Faculty od Electrical Engineering and Communication, Department of Technology

Corresponding author: Sabina Abbrent-Nováková (abbrent@seznam.cz)

Abstract

NMR pulsed field gradient diffusion and spin-lattice relaxation measurements have been conducted on two polymer systems consisting of lithium perchlorate dissolved in propylene carbonate and PMMA polymer or crosslinked PMMA polymer. The differences between these systems, namely the effects of crosslinking, and lithium salt concentration have been studied as a function of temperature. Using both ^1H and ^7Li NMR allows the investigation of the mobility of solvent, polymer chains, and Li^+ ions.

10th
ABAF
BRNO 2009
Advanced Batteries, Accumulators
and Fuel Cells

Intercalation materials

SODIUM USED INSTEAD OF LITHIUM IN THE ELECTROCHROMIC DEVICES

*V. Svoboda, J. Kazelle, *J. Vondrák, M. Sedlaříková*

Institute of Electrotechnology
Faculty of Electrical Engineering and Communication
Brno University of Technology, Czech Republic
**Institute of Inorganic Chemistry, Academy of Sciences of Czech Republic*

Corresponding author: Vít Svoboda (xsvobo39@stud.feec.vutbr.cz)

Abstract

The mass of thin layer can be observed by the EQCM method. This method is based on the changes of the resonance frequency of a quartz crystal resonator. The investigated substance is deposited on the surface of the resonator. Various metals (Pt, Au, Ag) and their compounds should be plated on the resonator. Most frequently, the resonators for the frequency 5,0 MHz are used. This frequency change is used for the detection of chemical changes of the electrode surface and is very sensitive.

Keywords: Quartz crystal microbalance, intercalation processes, mass changes

Introduction

The possibility of using quartz crystal resonators as quantitative mass measuring devices was first explored by Sauerbrey. The decrease of the resonant frequency of a thickness shear vibrating quartz crystal resonator, having AT or BT cut, was found to be proportional to the added mass of the deposited film:

$$\Delta f = -\frac{f_q^2 \cdot m_f}{N \cdot \rho_q \cdot S} = -C_f \cdot m_f \qquad (1)$$

where fq is the fundamental resonant frequency of the quartz, N the frequency constant of the specific crystal cut, ρ_q = 2.65 kg/dm^3 the quartz density and S is the surface area of the deposited film, the mass of which is $m_{f,}$ C_f is calibration constant. [1].

Intercalation

Tungsten trioxide is a well-known electrochemical material due to its ability to change its optical properties under the intercalation/deintercalation process. Similar intercalation is used in lithium ion batteries. Mass change of battery electrodes due to intercalation/deintercalation follows changes of capacity.

The knowledge of transport kinetics parameters in thin solid films is of great importance to understand the behavior of these films during insertion/extraction processes. The response time of the electrochemical process of the films is determined by the rate of charge transfer and mass transport.

Experimental

Electrochemical instrumentation:

Measurements were conducted using a Maxtek quartz crystal analyzer (model PM 710), an AUTOLAB potentiostat (model PGSTAT 100) and GPES electrochemical software.

Electrodes:

We used an electrode from Maxtek (plano – plano) as a working electrode. This electrode has a resonant frequency of ~ 5MHz with gold or platinum electrodes on both sides. These electrodes had a flat surface with little roughness.

- The crystal is placed in a special teflon holder.
- A Pt electrode was used as a counter and a Ag/AgCl electrode as a reference electrode.
- The intercalation of cations into vacuum deposited layers of WO_3 was performed from 0,1 M $LiClO_4$ 0,1M $NaClO_4$ (in propylene carbonate PC).
- The layers of WO_3 were vacuum deposited on the crystals

Results and discussion

Crystal calibration

The electrochemical reaction involved in the copper electrodeposition - electrodissolution is simply:

$$Cu^{2+} + 2e^{-} \longleftrightarrow Cu \qquad (2)$$

where Cu^{2+} is the hydrated ion. Using Faraday's second law:

$$C_f = \frac{M_{Cu}}{zF}\frac{\Delta q}{\Delta f} \qquad (3)$$

Where z is the number of electrons transferred in the electrochemical reaction (Eq. 2) and in the case of Cu deposition z =2

The calibration constant for our measurement is a 56 ng mass change for every 1Hz change.

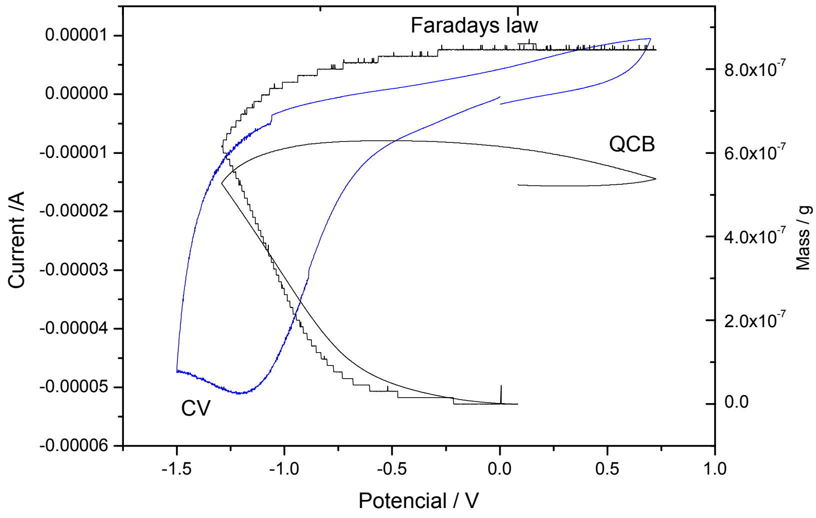

Fig. 1 *Intercalation Li to the WO_3 layer in the $LiClO_4$ + PC vs Ag/AgCl electrode, Cyclic voltametry, 0.1 M $LiClO_4$, the mass changes of Li in to the WO_3 layers*

Figure 1 displays the Lithium intercalation to the WO_3 layer. This intercalation starts and stops at the - 0,5V potential. During this intercalation we can see the optical changes of the WO_3 structure. This structure turned blue at about -1.25 V and then changes back to its normal color when we apply a positive potential.

The aim of our work was to investigate whether we can use sodium instead of lithium as an intercalation element in the electrochromic devices with WO_3 layer. This answer is given in Figure 2. Sodium is able to intercalate to the WO_3 layer. The sodium started intercalation to the WO_3 at the same potential as lithium. The color again turned blue at about -1 V potential.

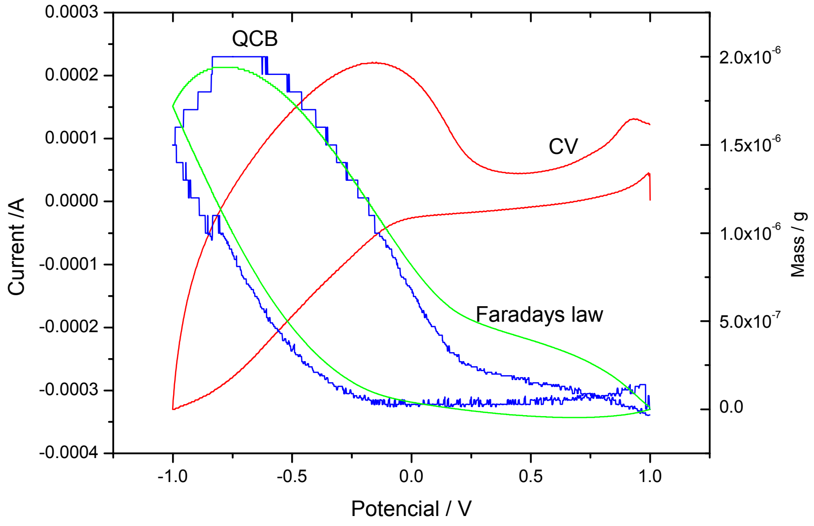

Fig. 2 *Intercalation Na to the WO_3 layer in the $NaClO_4$ + PC vs Ag/AgCl electrode, Cyclic voltametry, 0.1 M $NaClO_4$, the mass changes of Na in to the WO_3 layers*

Conclusion

The QCM technique shows us the opportunity for using sodium instead of lithium in the electrochromic devices. During our measurements, we observed that the amount of intercalated material is slightly more than when lithium was used. I think that this is very good news for electrochromic devices and for an industry that is concerned with electrochromic devices as well.

References

1. Mecea, V. M.: Sensors and Actuators A 128 (2006) 270–277
2. Špičák, P.: Diploma thesis, Institute of Electrotechnology BUT, Brno 2006
3. Svoboda, V.: Diploma thesis, Institute of Electrotechnology BUT, Brno 2006
4. Vatankhah, J. Lessard, G. Jerkiewitz: Electrochimica Acta 48 (2003) 1613-1622

Acknowledgements

This work was supported by:
Ministry of Education MSM0021630516

HIGH EFFICIENCY CATHODE BASED ON LITHIUM MANGANESE SPINEL FOR Li-ION BATTERIES

I. Maksyuta[1], L. Neduzhko[1], V. Maslov[2], V. Pisny[2], E. Shembel[1,2]

[1]Ukrainian State Chemical Technology University, Dnepropetrovsk
[2] Enerize Corporation, Coral Springs, Fl, USA

Corresponding author: Elena Shembel (shembel@onil.dp.ua)
Phone, Fax: +380562 470391

Introduction

$LiMn_2O_4$ – spinel is widely used in industrial scale for the production of lithium-ion batteries. The theoretical specific discharge capacity of $LiMn_2O_4$ (148 Ah/kg) is lower than that of cobalt ($LiCoO_2$) and nickel ($LiNiO_2$) compounds. Nevertheless, interest in the lithium-manganese spinel as cathode material for Li-ion battery is increased. This because $LiMn_2O_4$ has a relatively low toxicity, availability and significantly lower cost.

The high efficiency cathode was obtained using a lithium manganese spinel which was synthesized according newly developed method. Step-by-step process of heat treatment of spinel in the process of synthesis can adjust the structure of the final material and provides the active material with high electronic conductivity and high bulk density. [1]

Using the electrode mass with maximum percentage of the active substance can improve specific characteristics of the source current. However, even in the case of active materials which have relatively high conductivity, such as spinel presented in this article, the electro conductive additives (graphite, carbon black) must be entered in the electrode mass.

Thus, the performance characteristics of lithium-ion battery to a large extent depend not only on the properties of the active electrode material, but also other components which make up electrode mass of the cathode.

In order to improve the charge - discharge characteristics of lithium ion battery the researches to determine the optimal percentage of the active substance $LiMn_2O_4$, electrically conductive additive and binder have been conducted. The goal was to provide the high specific discharge capacity of positive electrode, coulomb efficiency of the electrode process and a high stability of discharge capacity during the cycling.

Experimental

MnO_2 with high tap density and high electronic conductivity was used as the starting material for the $LiMn_2O_4$ synthesis. The initial MnO_2 and method of this oxide synthesis have been developed by the author of the paper presented here [2].

Production technology of lithium-manganese spinel was carried out by two technologies which can be in common described by the following equations:

$4MnO_2 + 2LiOH \rightarrow 2LiMn_2O_4 + H_2O + 1/2O_2\uparrow$
$4MnO_2 + Li_2CO_3 \rightarrow 2LiMn_2O_4 + CO_2 + 1/2O_2\uparrow$

Spinel synthesized samples were analyzed in the following main characteristics: bulk density (g/cm3) before compaction and after compaction; type of structural modification; crystallite dimensions; manganese dioxide percentage in the final product; fractional composition; electrochemical characteristics. The following analyses were performed: chemical, thermo gravimetric, X-ray phase, electrochemical including volt-ampere characteristic; galvanostatic cycling and impedance spectroscopy.

Electrochemical tests positive electrodes based on $LiMn_2O_4$ have been conducted in three electrodes cell and coin cells Li-$LiMn_2O_4$. Size of the coin cell was 2325. Operating range of the potential was from 3.0 V up to 4.3.V. Current of the charge was 1C; current of the discharge was 1C and 2C. Electrode mass included LiMn2O4, graphite, black and binder. As electrolyte the solution of 1M $LiClO_4$ in EC: DMC (1:1) was used.

Results and Discussion

The results of electrochemical tests showed that the performance characteristics of electrodes which are based on spinel depend on the conditions of spinel synthesis, including the molar ratio Li : Mn in the reaction mixture, heat treatment and the nature of initial components. The important factor is ration of the components (spinel, graphite, black, binder) in the electrode mass.

Technology based on lithium hydroxide using as Li-comprising raw material show better results as compared with technology based on lithium carbonate raw material.
In the case of hydroxyl technology the bulk density of the samples of spinels in 1.5 times higher than for the carbonate technology and is 1, 75-1, 84 g/cm^3 without compaction and 2, 4-2, 66 g/cm^3 with compaction.

Charge - discharge curves for electrodes which are based on the synthesized samples spinels have two playground with potentials 4.1V and 4.25 V (charging branch), and 4.1V and 3.9V (discharge branch) (Fig. 1). This shows the course of two-stage process for intercalation and for de intercalation of lithium ion in the matrix structure of spinel. These processes are accompanied by reversible oxidation - reduction transition $Mn^{+4} \leftrightarrow Mn^{+3}$ [3].

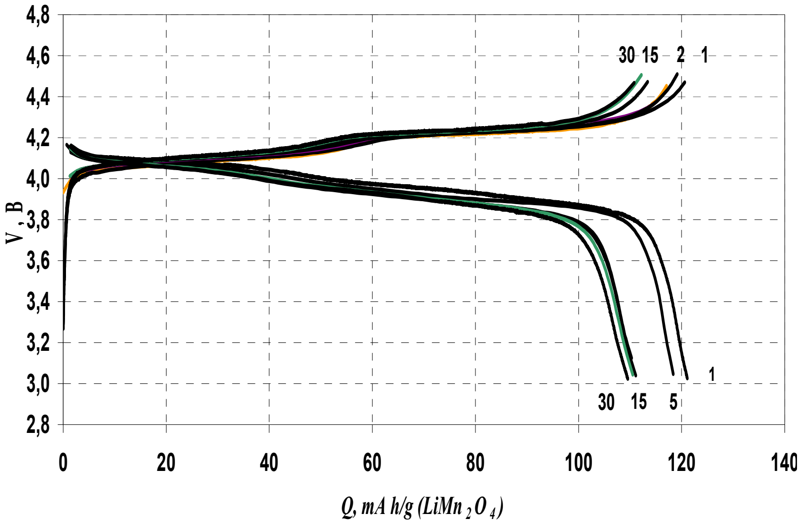

Fig.1 *Charge - discharge curves LiMn2O4- electrode Ich=Idch=1C.*

The results of electrochemical testing of cells Li - LiMn2O4 with the different composition of the cathode mass presented in Table 1 and in Fig. 2 for two values of the discharge currents: 1C and 2C. The results presented there show that the influence of active mass composition on the electrochemical characteristics of positive electrodes depends on the discharge current. When the discharge current is 1C (100mA /g or 0,995 mA/cm^2) the reversible discharge capacity of the electrodes with the composition in the range of 85% $LiMn_2O_4$ > 80% $LiMn_2O_4$ > 90% $LiMn_2O_4$ decreases. Under these conditions the degradation of the discharge capacity during cycling of the electrodes with the compositions in the range 85% $LiMn_2O_4$ < 80% $LiMn_2O_4$ < 90% $LiMn_2O_4$ increased.

As we can see here not obvious effect is manifested: the best performance performances seen for electrodes with the content of spinel electrodes equal 85%. When the content of spinel increases (90% $LiMn_2O_4$) or decreases (80% $LiMn_2O_4$) the characteristics of the electrodes to deteriorate. This effect is due to the influence of the kinetics and macro kinetics of the electrochemical process. Kinetics is determined by the properties of spinel when macro kinetics is determined by the macrostructure of the electrode and the conductivity of its components.

With the increasing the discharge current up to 2C (current density 200 mA / g) reversible discharge capacity of the electrode with the composition in the range of 80% LiMn2O4> 85% LiMn2O4> 90% LiMn2O4 decreases. This is because at high discharge currents, the process of electrochemical intercalation / de intercalation of lithium ions proceeds to a greater extent on the electrode surface. At this conditions the degree of penetration of the electrochemical process on the thickness of the electrode and the utilization of active material decreases. In addition when the content of active material increases the number of electrically conductive additive is reduced, which in turn leads to increasing the electrical resistance to solid-phase electrode, increasing the polarization resistance and decreasing the voltage during discharge of the electrode.

Comparison of characteristics of electrodes which were based on spinels obtained by hydroxyl technology and carbonate technology showed that under currents up to 1C the characteristics of the electrodes practically do not differ. However, with increasing the discharge current for example up to 2C or 5C in the case of spinel obtained by hydroxyl technology the discharge capacity of electrodes and stability of electrodes performance during cycling are significantly better than in the case of the spinel obtained by carbonate technology.

Table.1 *The results of electrochemical testing LiMn2O4-electrodes with different composition of the active mass. Electrolyte: 1M LiClO4, EC, DMC (1:1)*

# cell	Composition cathodic mass	Quantity of spinel, g	Idch, C	Q,mA.h/g						
				Number cycle						
				1	5	10	30	50	80	100
1586	$LiMn_2O_4$ -80%; graphite-5%; black - 5%; binder- 10%	0,0179	1C	112.8	106.3	100.9	98.6	92.7	83.4	80.3
1587		0,0215	2C	109.6	108.7	103.4	99.4	96.5	87.7	84.4
1588	$LiMn_2O_4$ -85% Graphite-1%; black- 10%; binder- 4%	0.0199	1C	116.1	112.1	108.8	105.1	100.5	94.0	91.7
1589		0.0231	2C	106.3	103.7	103.4	96.8	91.8	81.7	78.3
1590	$LiMn_2O_4$ -90%; graphite-5%; black - 5%; binder- 4%	0.0261	1C	106.2	105.6	104.5	94.4	81.4	67.0	62.0
1591		0.0256	2C	104.1	102.4	97.3	88.0	79.3	67.7	60.6

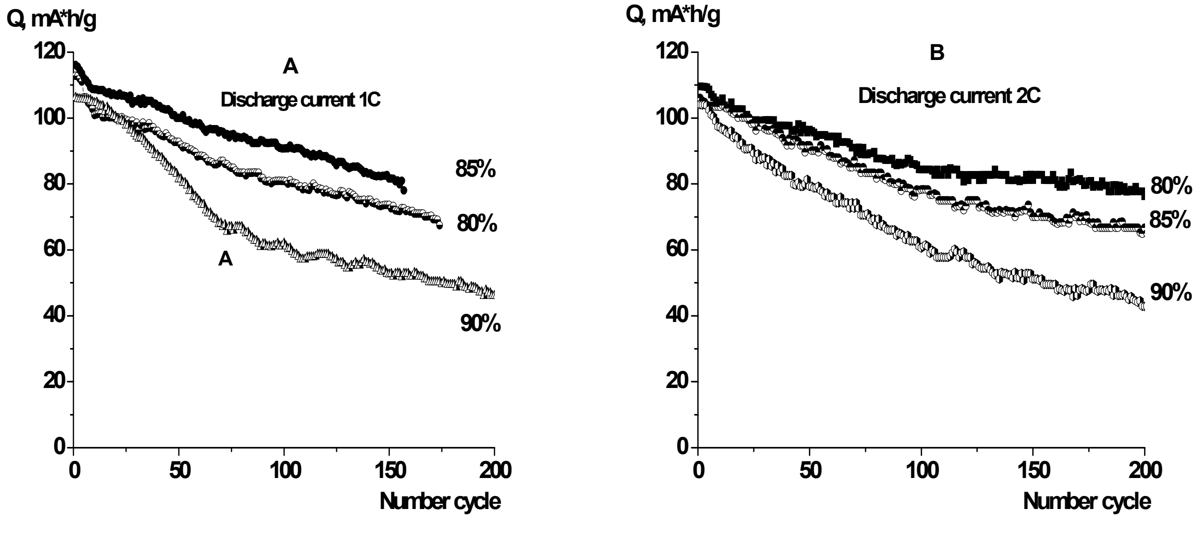

Fig. 2 *Dependence of discharge capacity LiMn2O4 electrode of the number of cycles. Electrolyte: 1M $LiClO_4$, EC, DMC (1:1); Charge current 1C.*
Active mass composition:
$LiMn_2O_4$-80%; graphite -5%; black - 5%; binder – 10% (composition 1)
$LiMn_2O_4$-85%; graphite -1%; black - 10%; binder – 4% (composition 3)
$LiMn_2O_4$-90%; graphite -1%; black - 5%; binder -4% (composition 4)

Conclusions

Investigation the electrochemical properties of the lithium manganese spinel ($LiMn_2O_4$) which was synthesized using newly developed solid state method of synthesis was conducted. The special type of chemical manganese oxide with high tap density and high electronic conductivity was used as initial material. The developed spinel has a high tap density, conductivity and discharge capacity under high discharge current. It was found that the main control parameters of obtaining lithium-manganese spinels are the duration and mode of heat treatment and the ratio of Li: Mn in the initial reaction mass. Spinel synthesized using LiOH has a higher performance characteristics than the spinel synthesized using Li_2CO_3. The influence the composite material of positive electrode: spinel, graphite, black and binder on the characteristics of the electrode was investigated. The ways of optimization of the composite material of the positive electrode for high values of specific discharge capacity in a wide range of discharge currents and high coulomb efficiency of the electrode process in the cycling have been substantiated.

Acknowledgements

These development and investigation were conducted based in funding provided by the Ministry of Education and Science of Ukraine *(Contract DZ/279-2008)* and the company Enerize Corporation (*Contract* 03/Y/2007).

References

1. US Patent Application No. 12/287,396 Manganese lithium spinel and method for
2. production thereof.
3. US Patent Application No. **10/583,886.** Oxide of the manganese for lithium battery cathode.
4. D.Kellerman, V. Gorshkovв: J. Elektrokhimiya 37 (2001) 1413-1420. (In Russian).

INTERCALATION OF Li IONS INTO ELECTRODEPOSITED WO_3 FILM

M. Macalik[1], *M. Sedlarikova*[1], *J. Vondrak*[1,2]

[1] *Department of Electrotechnology, FEEC, BUT, Údolní 53, 602 00 Brno, Czech Republic*
[2] *Institute of Inorganic Chemistry of the ASCR,v.v.i., 250 68 Řež near Prague, Czech Republic*

Corresponding author: Michal Macalik (michal.macalik@seznam.cz)
Phone: +420 5 4114 6170

Introduction

Amorphous tungsten oxide is the most frequently used and best-known material for electrochromic devices. Its main advantage is high coloration efficiency and acceptable cycling stability. Intercalation of hydrogen, lithium or sodium ions into WO_3 leads to complex structural changes. Tungsten oxide can be prepared by a number of methods. The direct cathodic electrodeposition of WO_3 from a peroxytungstate solution was first reported by Yamanaka [1].

Experimental

Starting solution for the deposition of WO_3 was created by dissolving 6.5g of tungsten powder (Sigma-Aldrich, 99.9%) in 40ml of hydrogen peroxide (30%, Penta, p.a.). The solution must be placed at a low temperature (5-10°C) and continuously stirred. Low temperature prevents the formation of precipitates. After 24 hours the solution is filtered to remove insoluble residues. The 40 ml of glacial acetic acid was added into peroxotungstid acid solution [2], which is ideal for low carbon content, good burnout properties and chemical compatibility. This solution was heat for 3 hours, which leads to decompose off ecces H_2O_2 and to acetylation of peroxotungstid acid. The resulting pale greenish-yellow solution is diluted in the volume ratio 1:1 with pure ethanol to increase wettability.

Electrodeposition of the WO_3 from this solution was carried out under the conditions laid down for example, according to lit [3] using the μAutolab (Ecochemie, Netherlands). The reference electrode was used Ag/AgCl electrode and the platinum plate like counterelectrode. Deposition potential of working electrode consisting of a FTO layer (Flabeg, Germany, 35Ω/□, surface 2x3cm) was U_{dep} = -0.45 V against the reference electrode at room temperature. Time of deposition was 5, 8, 10, 12 and 15 minutes. The layers of each thickness were annealed at temperatures 60, 120 and 200°C for one hour, one of the sample of each thickness was left at room temperature (RT marked).

Results and Discussion

The layer thickness was measured by profilometer Talysurf CLI 1000. As can be seen from Fig. 1, film thickness linearly increases with time of deposition.

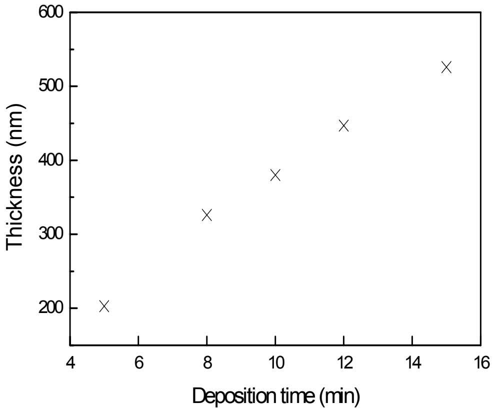

Fig. 1 *Thickness of electrodeposited WO_3 layer according the deposition time.*

Layers have been analyzed using the SEM VEGA TESCAN 3135 in terms of surface structure. It appeared that the layers without annealing and annealed at 60°C are much more porous than the layers annealed at 120°C, resulting in a clear loss of porosity. It seems on the contrary that annealing at 60°C slightly increases the porosity. The width of the pore is approximately 10μm.

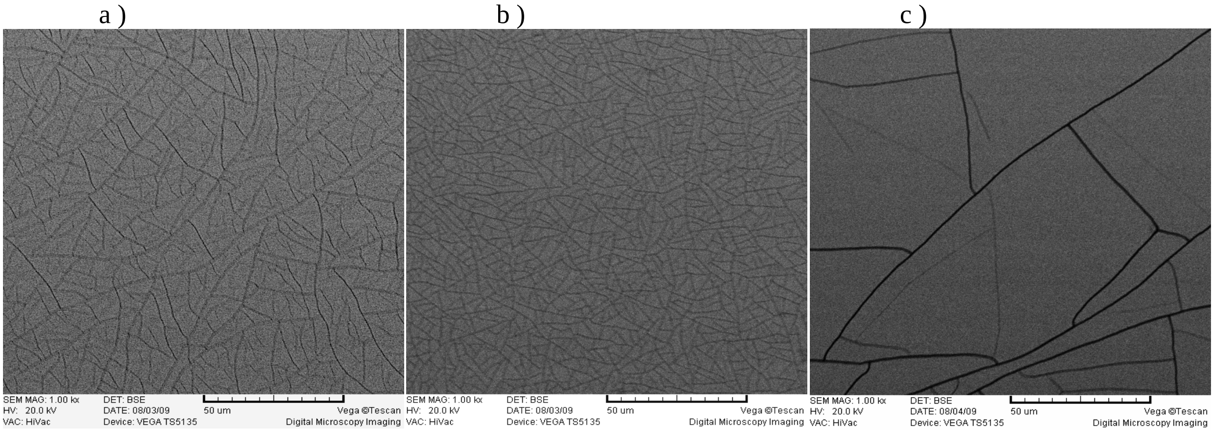

Fig. 2 *Surface structure of WO_3 layer deposited 10min obtained using SEM, witnout annealing (a), annealed at 60°C (b) and at 120°C (c).*

The optical and electrochemical properties were measured in 0,5M $LiClO_4$/PC electrolite. Potentials have been defined using the μAutolab device and Cd/Cd^{2+} reference electrode [4], platinum plate was used as counterelectrode. Polarization limits of the working electrode were seted from -0.5V to 1.5V. Optical properties were measured by spectrophotometer Unicam Helios δ.

The optical transmittance was measured for all the samples in the wavelength range 325-900nm. For the state of "colored" was the WO_3 electrode layer polarized at -0.5V, the state of "bleached" at 1.5V, while measurements of optical spectra was initiated after a period of 1 minute. The figure 4 shows clear reduction in the transmission by the negative polarization potential. Higher transmission in the wavelength range 350-500nm is caused by the blue color layers. Annealing the layer at a temperature of 60°C brings very positive effect on low-transmission by intercalation of Li^+ ions. This phenomenon occurred in all samples.

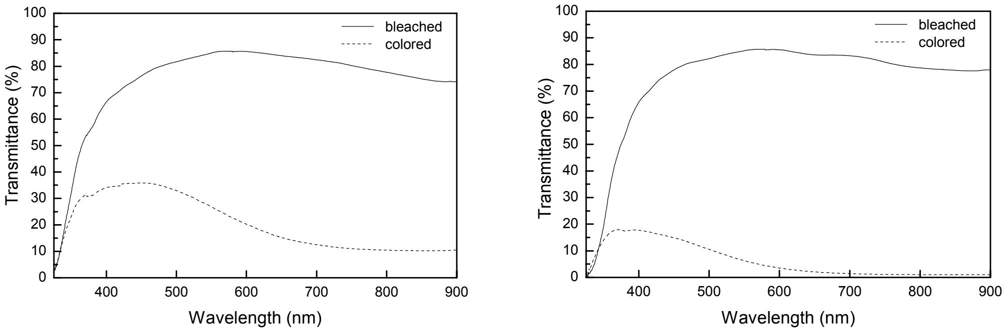

Fig. 3 *Optical properties of WO_3 layers deposited 10min, measured in 0.5M $LiClO_4$/PC electrolyte. Non-annealed (left) and annealed at 60°C (right).*

The colouring and bleachin times measured at constant wavelength 550nm are very short and they are less then 10s for the non-annealed samples and samples annealed at 60°C. Annealing samples at 120°C and 200°C extends the times of coloring and bleachnig on the units to tens of minutes, Fig. 4.

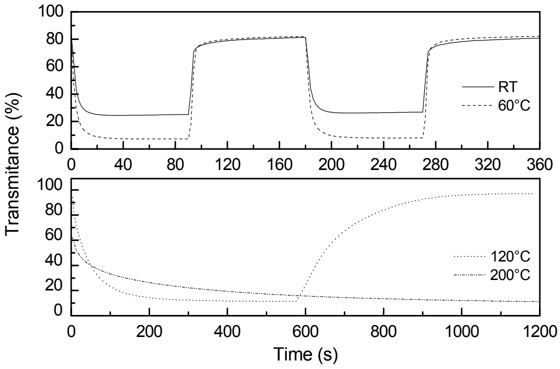

Fig. 4 *The speed of system response to the change of polarization WO_3 layer deposited 10 minutes and annealed at different temperatures.*

Table 1 *Coloring and bleaching transmittance, optical density, ion storage capacity and coloration efficiency measured at 550nm.*

Deposition time (s)	Annealing (°C)	T_b (%)	T_c (%)	ΔT (%)	ΔOD (-)	ISC (mC/cm^2)	CE (cm^2/C)
5	RT	76,2	38,4	37,8	0,30	12,3	24,1
	60	88,8	38,1	50,7	0,37	7,7	47,9
8	RT	77,3	32,6	44,7	0,38	10,5	35,7
	60	86,5	19,2	**67,3**	0,65	11,2	**58,5**
	120	87,0	20,4	**66,6**	0,63	14,5	43,4
10	RT	81,3	25,6	55,7	0,50	11,2	44,9
	60	82,1	7,3	**74,8**	**1,05**	15,7	**67,1**
	120	86,9	11,4	**75,5**	**0,88**	15,8	**55,7**
12	RT	69,2	10,2	59,0	**0,83**	21,3	39,0
	60	45,8	3,9	41,9	**1,07**	18,3	**58,4**
15	RT	38,9	8,9	30,0	0,64	7,8	81,8
	60	64,2	3,6	60,6	**1,25**	19,5	**64,2**

From these measurements can be very well calculated evaluation criteria for determining quality of electrochromic films. One of them is the optical density (ΔOD), another criterion is ion storage capacity (ISC) and finally coloration efficiency (CE):

$$CE = \frac{\Delta OD}{ISC} = \frac{\log \frac{T_c}{T_b}}{\frac{Q}{A}} [cm^2 / C],$$

where T_b and T_c are the transmittances of the film in the bleached and colored states.

It is very apparent that the modulation of the transmission obtained at a wavelength of 550nm is approximately 75% of the samples deposited ten minutes and annealed at 60°C and 120°C. In view of the optical density the highest level of coloration was achieved on samples deposited 10, 12 and 15 minutes, but samples deposited 12 and 15 minutes show the low value of T_b. The calculated values of electrochromic efficiency are for samples annealed at 60°C higher than non-annealed.

From the graph below is clearly evident the impact of temperature on the electrochemical properties. Curve surface of layers annealed at 60°C is broader than non-annealed samples, while surface of samples annealed at 120°C and 200°C is much smaller, which corresponds to very poor results from measurements of optical spectra.

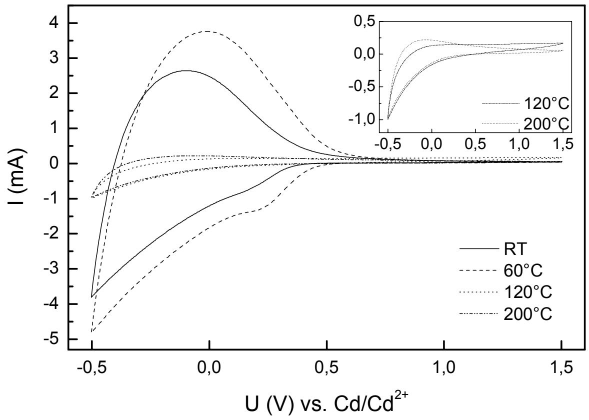

Fig. 5 *Cyclic voltammetry measurement of WO_3 layer deposited 10 minutes, data from the 10th scan, electrolyte 0,5M $LiClO_4$/PC, scan rate 20 mV/s.*

Conclusions

Different thickness WO_3 layers were prepared and the influence of different annealing temperatures was monitored. The best optical and electrochemical properties were found for the sample deposited ten minutes and annealed at 60°C. The sufrace structure of this sample is mostly porous.

Acknowledgements

This work was supported by the Ministry of Education, Youth and Sports (project MSM0021630516) and by the Grant Agency of the Academy of Sciences of the Czech Republic (project KJB208130902).

References

1. K. Yamanaka: Jpn. J. Appl. Phys. 26 (1987) 1884.
2. M. Deepa, K. Saxena, D.P. Singh, K.N. Sood, S.A. Agnihotry: Electrochim. Acta 51 (2006) 1974
3. G. Leftheriotis, P. Yianoulis: Solid State Ionics 179 (2008) 2192
4. J. Reiter, J. Vondrak, Z. Micka: Solid State Ionics 177 (2007) 3501

HIGH ENERGY DENSITY SILICON-CARBON COMPOSITE FOR LIB ANODIC APPLICATION

T. Stankulov, W. Obretenov, A. Momchilov, B. Banov, A.Trifonova

Institute of Electrochemistry and Energy Systems (IEES), Acad. G. Bonchev str., bl. 10,
Bulgarian Academy of Sciences, 1113 Sofia, Bulgaria

Corresponding author: Atanaska Trifonova (trifonova@bas.bg)
Phone: +359 2 979 2741
Fax: +359 2 872 2544

Introduction

Silicon is an attractive anode material for lithium ion battery due to its very large lithium insertion capacity - up to 4000 mAh/g. The commercial use of Si powder is, however, still hindered because of some problems. In general, the failure modes of Si composite anodes may be attributed to three basic features: (i) severe volume change in the Si particles upon cycling; (ii) lack of elasticity of the electrode layer; (iii) poor conductivity of the Si and lithiated Si particles.

To overcome the above problems we tried to coat the silicon particles with carbon using multi-steps process. It is expected that the carbon layer should reduce the volume expansion of the Si particles and simultaneously should compensate for the poor conductivity. Moreover, carbon is also an active material for the intercalation of lithium.

The electrochemical behaviour of such electrodes will be reported. Cyclic voltammometry and cycling with different protocols are coupled with electrochemical impedance spectroscopy for the characterization of the electrodes.

Experimental

For the preparation of the composite, equal portions (weight ratio) of nano-sized silicon and graphite powders (Nanostructured and Amorphous Materials, Inc. USA) were consequently dispersed in an organic precursor solution, containing methacryloxypropyltrimethoxysilane (Merck, Germany). The silane induces the formation of chemical bonds between the silicon and graphite particles, resulting in a more effective coating. The mixture was sonicated in order to perform uniform dispersion. Finally, the obtained powder was annealed at 700°C under inert atmosphere.

The electrode composition contained 85 % (w/o) active material (Si:C - 50:50), 2 wt. % conductive additive (Super P carbon black, Timcal, Switzerland) and 13 wt. % binder (CMC). The formed slurry was spread on copper foil and vacuum dried. The active material loading was typically ~ 2.0 ± 0.1 mg/cm^2 for 12 mm electrode diameter.

Galvanostatic tests were carried out in a three-electrode laboratory type metallic cell (prototype of 2032 button cell), using a metallic Li foil as both counter and reference electrode and LP40 electrolyte. The applied constant current correspond to 0.1 C-rate and the potential range was 5 -1500 mV vs. Li/Li$^+$.

We have used a CC-CV regime as conditioning step during the first charging: the cell was charged with constant current (0,1 C) from OCP to 5 mV. This potential was maintained until the current dropped to 10% of C-rate and then the cell was discharged. The subsequent cycles 2-30 were performed without such a potentiostatic step.

Cyclic voltammograms were measured at a scan rate of 30 µVs^{-1} in the same potential range.

Electrochemical impedance spectroscopy was performed with an IM6 impedance station (Zahner, Germany), coupled with microprocessor controlled electrochemical research station to control the cycling. Data were obtained in series measuring at ac frequency from 10 mHz to 100 kHz in the potential region given above.

Results and Discussion

Cyclic voltammogram curves for the first three cycles are displayed in Fig. 1. A distinctive wave can be seen for the first cycle at potentials between 0.9 and 0.7 V, but it disappears during the next cycle. It is associated with the SEI formation process.

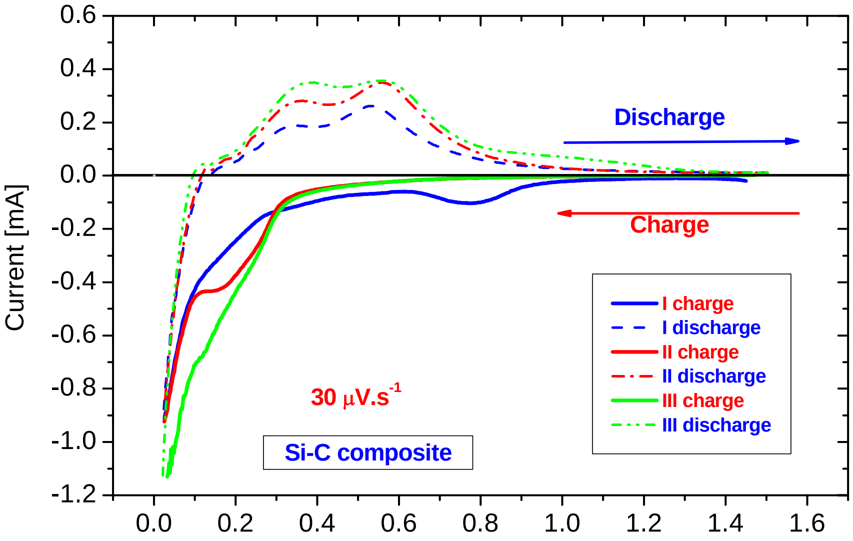

Fig. 1 *Cyclic voltammogram of Si-C composite electrode in LP40 electrolyte. Potential range: 5 mV – 1.5 V; scan rate 30 µV /s.*

Furthermore, the cathodic current is relatively constant up to 0.33 V, after that it increases and reaches the value of 0.85 mA.cm^{-2}. Eventually, Li_2Si is formed with the beginning of Li intercalation (~ 0.33 V). A sharp peak is visible in the low voltage region (below 0.1 V), that correspond to the initial lithiation of crystalline silicon and lithiated amorphous silicon, Li_xSi is also formed [1, 2]. Moreover, this peak increases during the following two cycles (the cathodic current also increases), which suggests that more and more crystalline silicon is lithiated. The two-phase region results in two plateaus during the removal process (at ca. 0.35V and 0.55 V) where de-lithiated amorphous silicon is formed. If this phase is then again lithiated, the voltage curve forms two sloping plateaus, indicative of single-phase regions (cycles 2, 3 in Fig. 1-cathodic part).

We chose to test the electrochemical performance of our material by complete lithiation, i.e. to make more amorphous silicon available. At complete lithiation the particles are in electrical contact with one another. However, during the de-lithiation, they may get isolated. In this case, the carbon coating (and the binder as well) should provide the electrical contact between the particles. In our case (1:1 ratio) it is not obvious whether the percolation threshold has been reached. Anyway, the electrode works quite well definitely (see Table 1). This suggests that the electrode composition is capable of accommodating a certain amount of volume expansion during cycling. The discharge capacities and the appropriate efficiencies for the both cycling protocols are listed in Table 1.

Table 1 *Summary of the cycling data, obtained from both testing regimes: constant current cycling and constant current-constant voltage. The capacity values are normalized to the first discharge capacity (for CCC-1533 mAh/g; for CCCV- 1789 mAh/g).*

Cycle	CCCV mode		CCC mode	
Nº	Dch cap %	Eff %	Dch cap %	Eff %
1	100	93.08	100	93.3
3	99	98.8	101	98.5
6	100	98.8	99	98.6
9	100	98.6	99	98.5
12	100	98.4	98	98.1
15	99	97.9	98	97.7
18	98	97.6	97	97
21	98	97.06	96	96.5
24	97	96.9	95	95.4
27	96	96.5	95	94.9
30	96	95.9	94	95.1

This “conditioning step” was used only during the first charging so that the initial capacity cannot be exceed, ensuring that the complete lithiation of the electrode has been achieved during the formation. The potentiostatic step may allow the material enough time to release the mechanical strain and adapt to the increasing volume by particle rearrangement (thermodynamic phase stability). It is interesting to note that since the second cycle, which is the first at normal current density, the coulombic efficiency is higher than that for a control electrode cycled at standard conditions. Moreover, the slow suppressing hysteresis between charge and discharge (the curves are not given here) may be related to the graphite coating and suggests that the interfacial contact between graphite and silicon could be a key factor influencing the cycling stability.

Looking at the actual EIS data, we can see that in all charged states, the spectras form depressed semicircles located in the high frequency range. The linear Warburg-like part is also present. However, the slope of this line is substantially higher than 45°. The depressed semi-circular shape may be attributed to roughness, porosity and/or polycrystalline state, which results in hindering the frequency dispersion within the interface. It is very interesting to note that the conductivity of the composite electrode is not affected by the increasing volume during charge, resulting in a constant ohmic resistance of the cell.

Conclusions

We presented a silicon-carbon composite, prepared by multi-steps process. The possible advantages of this material are: a) electrode preparation technique common to the industry, b) higher than the usual conductivity, c) both phases are active towards Li^+, i.e., no inert mass is involved with the electrode.

This composite material allows maintaining a good electronic contact between all active particles (silicon and graphite) and the current collector. Obviously, in the case of the complex CC-CV mode the discharge capacity and the stability of composite test electrode are enhanced.

Acknowledgements

This work was funded by NATO via EAP.RIG.982531.
T. Stankulov would like to acknowledge the World Federation of Scientists, Switzerland for the national scholarship.

References

1. Jing Li, J. R. Dahn, J. Electrochem. Soc., **154** (3), (2007) A156
2. M. N. Obrovac, I. J. Krause, J. Electrochem. Soc., **154** (2), (2007) A103

10th ABAF

BRNO 2009

Advanced Batteries, Accumulators
and Fuel Cells

Special electrochemical components

ELECTRONIC SENSOR BASED ON Nb_2O_5 ELECTROCHROMIC THIN FILMS

L. Skatkov[1]*, V. Gomozov*[2]*, S. Deribo*[2]

[1] *PCB "Argo", 4/23 Shaul ha-Melekh Str., 84797 Beer Sheva,ISRAEL*
[2]*NTU "KhPI",21 Frunze Str., 61002 Kharkov, UKRAINE*

Corresponding author: Leonid Skatkov (sf_lskatkov@bezeqint.net)

In the present work the technique for generation of electrochrome effect (ECE) in Nb_2O_5 amorphous anodic oxide films (AOF) is proposed. We have also found that when AOF is polarized by the packages of microsecond pulses, initial potential of gasemission can be increased three- to fivefold, which promotes significant increase in current density on film electrode, and, thus, raises the ECE.

Until the present time electrochromism has been observed and studied in Nb_2O_5 polycrystalline anode layers which, unlike amorphous ones, demonstrate pronounced electrochrome properties [1].

These differing (from the electrochrome effect viewpoint) properties of Nb_2O_5 amorphous and polycrystalline anode films make us turn our attention to the surface morphology of oxide layers, since the volumetric properties of amorphous Nb_2O_5 are known to be favorable for electrochromism. The comparison of Nb_2O_5 amorphous and polycrystalline layers reveal multipores surface in polycrystalline oxides, and highly unbroken surface in amorphous ones.

The technique for generation of anode layers with highly developed surface has been devised to examine the realization of potential electrochromism in Nb_2O_5 amorphous anodic films by surface development in these films. It is known [2] that in aluminium, AOF can be obtained with porous surface in oxide-etching electrolytes. Hence, oxide layers, obtained in etching component-containing- hydrofluoric acid (HF) – electrolyte were our object of study.

Niobium as a foil annealed under 2200 K in a vacuum not less that 10^{-5} Torr was oxidized in electrolyte, containing 25 ml of orthophosporic acid (H_3PO_4)) 25 ml of pure HF per 1 liter of water, by alternate asymmetrical current with 5:1 ratio of cathode half-period amplitude to anode one, by two stages: first, under fixed current density j = 5-7 mA/cm^2 (halvanostatic mode) up to the voltage of 40-50 V, and then under fixed voltage U=10 V (voltstatic mode) for 20 to 30 min.

The films obtained had uniform light gray color. Oxide layer thickness was dependable on the oxidizing conditions, and varied from 0.2 – 0.3 nm under above specified conditions, to 30 nm upon 1-hour exposure under 50 V voltage.. The anode oxide thickness was determined by the weight technique of [2].

The anodic films obtained by this technique are amorphous, which is evidenced by haloes on electron diffraction patterns. Also generated niobium pentoxide films posses typical electrochrome properties.

It should be emphasized that despite the fact that the metal-semiconductor phase transition with absorption jump-including ECE scenario, reported in [3], relates to polycrystalline Nb_2O_5 AOF, it is rather probable that in obtained amorphous AOF of niobium pentoxide, the ECE mechanism is also similar to above described model.

We would notice that, as was shown in [4], the absence of distant order in amorphous structure, generated during anodic oxide growth, does not result in the suppression of such phase transition as we have considered above, in AOF.

An alternative was found to the ECE, and it is the process of recombination of hydrogen atoms emitted on the surface of AOF and their subsequent evacuation as gas bubbles, which considerably limits the ECE rate.

A number of papers discuss the emergence of states differing in their life times and emergence of states differing in their life times and emergence nature on AOF surfaces. Thus, slow surface states (SSS) generated by the electrolyte chemosorbed ions participate in adsorption and even initiate it [5].

It is found that ECE can take place similarly to the catalytic mechanism of dissociated chemosorption [6]. Kinetic factors of such mechanism can be taken into account upon examination of diffusion equation [7]. The equation first term contains Θ parameter, characterizing the extent of surface filling during adsorption. It is possible that Θ parameter, constant for normal conditions, can grow by the superposition of packages of microsecond-duration pulses, i.e. electroadsorption effect is realized.

The Θ growth accelerates ionization of hydrogen atoms and their subsequent diffusion to the AOF solid phase, and prevents the development of rivaling recombination and gas emission processes.

It has been shown earlier [8], that the pulses of transverse electric field, applied to the sample, result in the accumulation of positive charge in SSS associated with water adsorption, whivh has no time to resolve in the interpulse period. The “accumulation effect” was explained by electroadsorption.

In our case, it is also evident that polarization of pulses with period-to-pulse duration ratio smaller than the SSS life times results in the increase of surface concentration of OH^{+}_{3} – groups, caused by the accumulation effect, and in subsequent discharge of hydrogen atoms.

In other words, the application of pulse polarization by the packages of microsecond pulses with low period-to-pulse duration ratio promotes significant increase of ECE rate in Nb_2O_5 at the expence of added filling of AOF surface by hydrogen ions.

References:

1. Skatkov L.I. Abstr. Int. Meet. On Electrochromism, IME-4 (Uppsala, Sweden, 2000) – P. 74.
2. Young L. Anodic Oxide Films. – Academic Press. – L.-N.Y., 1960.
3. Bayrachny B.I., Liashok L.V., Gomozov V.P., and Skatkov L.I. // Phys.Stat.Sol.(a). – 1989. – V.115. – P. 207.
4. Malinenko V.P., Stefanovich G.B., Chudnovskiy F. A.// Pis'ma v Z. Tech. Fiz. – 1983. – n. 9. – P. 754.
5. Kao K.C., Hwang W. Electrical Transport in Solids. – Pergamon Press. – Oxford-N-Y. – 1984.
6. Palatnik L. S., Maluk Yu.I., Belozerov V.V. // DAN SSSR. – 1974.- V.215. – P. 1182.
7. Reichman B., Bard A., Laser D. // J. Electrochem. Soc. – 1980. – V. 127. – P. 647.
8. Skatkov L. I. Abstr. 9th Europ. Conf. ECASIA'01 (Avignon, France, 2001). – P. 308.

10th ABAF

BRNO 2009

Advanced Batteries, Accumulators and Fuel Cells

Accumulators

$LiMnPO_4$ CATHODE MATERIAL FOR HIGH PERFORMANCE Li ION BATTERY

I. Exnar, A. Kay , G. Deghenghi, T. Drezen, J. Miners

High Power Lithium HPL SA, PSE-B, EPFL, 1015 Lausanne, Switzerland

Corresponding author: Ivan Exnar (i.exnar@highpowerlithium.com)
Phone: +41216938683
Fax:+41216938684

Lithium Metal Phosphates have recently attracted attention as potential Li-ion battery cathode materials due to their lower cost, lower toxicity, and better electrochemical and thermal stability, when compared to the currently used $LiCoO_2$ [1].

The durability, chemical- and thermal-stability of Olivine Metal Phosphate is due to its rigid three-dimensional structure that stabilized by strong covalent bonds between oxygen and the Phosphorous ions [1].

$LiMnPO_4$ has an ideal redox potential of 4.1 V vs. Li metal [1]. This is considered to be the optimum voltage: high enough to maximize energy density yet within the stability limits of electrolytes.

HPL demonstrated that particle size reduction is essential to improve the rate performance of the $LiMnPO_4$ material. Smaller particles reduce the diffusion path length for electrons and lithium ions in the cathode material [2], there by overcoming the low intrinsic electronic conductivity and slow lithium diffusion kinetics within the material.

In this presentation the performance of $LiMnPO_4$ and doped $LiMnPO_4$ synthesized by different preparation methods and will be discussed. A special emphasis will be devoted to safety and stability of $LiMnPO_4$ cathode material and the application in large size Li Ion batteries.

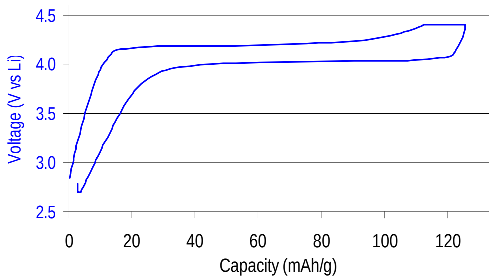

***Fig. 1** Voltage profile of $LiMnPO_4$ CCCV charge andD/10 discharge*

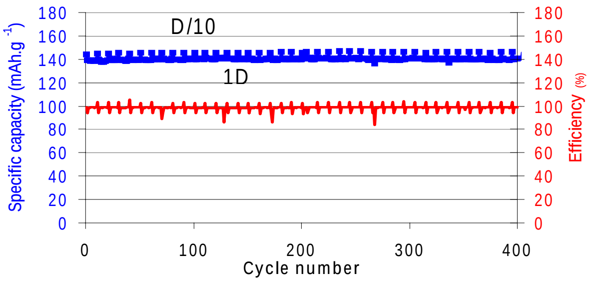

***Fig. 2** Cycle life of $LiMnPO_4$ cathode at D/10 and 1D discharge rate*

References

1. K. Padhi, K. S. Nanjundaswamy, and J. B. Goodenough, *J. Electrochem. Soc.* 144, (4), 1188-1194 (1997).
2. Nam-Hee Kwon, Thierry Drezen, Ivan Exnar, Ivo Teerlinck, Motoshi Isono and Michael Graetzel, *Electrochemical and Solid-State Letters,* 9**,** (6), A277-A280 (2006)
3. Deyu Wang, Hilmi Buqa, Michael Crouzet, Gianluca Deghenghi, Thierry Drezen, Ivan Exnar, Nam-Hee Kwon, James H. Miners, Laetitia Poletto, Michael Grätzel, *IMLB14, Journal of Power Sources,* 189,624,(2009)

PREPARATION AND PROPERTIES OF MANGANESE DIOXIDE STUDIED BY EQCM

P. Špičák[a], *V. Novák*[a], *P. Barath*[a], *J. Vondrák*[b], *J. Kazelle*[a]

[a] *Department of Electrical and Electronic Technology, Brno University of Technology,*
602 00 Brno
[b] *Institute of Inorganic Chemistry of the AS CR, v.v.i., 250 68 Řež near Prague*

Corresponding author: Vítězslav Novák (novakv@feec.vutbr.cz)
Phone: +420 541 146 121
Fax: +420 541 146 147

Introduction

Manganese dioxide is active material widely used in batteries as positive electrodeThe only type of manganese dioxide used in commercial cells is electrolytic manganese dioxide (EMD, γ-MnO2).The electrochemical redox reaction of this secondary cell system is commonly formulated according to the scheme:

$$MnOOH + OH^- \leftrightarrow MnO_2 + H_2O + e^- \qquad (1)$$

All forms prepared at low temperatures contain quite high amount of water. This water must removed for their use in lithium batteries carefully enough to prevent the conversion to the inactive β - phase, for example, by heating over 300°C and many procedures of it are protected by patents. Most of the roduction is now based on electrochemical oxidation of manganous salts.Therefore the uptake and/or removal of water in the course of their formation or cycling in a battery are rather important.The use of Electrochemical Quartz Crystal Microbalance (EQCM) can help to clarify its formation by electrodeposition from manganous salts, the mass changes during cycling (charging and discharging) and to determine the nature of involved species its formation by electrodeposition from manganous salts and , the mass changes during cycling.

Experimental

The EQCM device QCM200 from SRS was used for both sample deposition and investigation together with potentiostat/galvanostat Autolab PGSTAT 12, EcoChemie, The Nederland.
The exposed area of the active electrode (platinum) in contact with the electrolyte is 1.37 cm^2 (the displacement area between the two circular electodes is $0.4 cm^2$). The resonant frequency of crystal is 5 MHz and its sensitivity factor C_f is 56.6 Hz μg^{-1} cm^2)

The samples were prepared by electrodeposition from a 0.1 M solution of $MnSO_4$ in distilled water. The investigation itself proceeded in 1M KOH deaerated by nitrogen. Potentials are related to a Hg/HgO reference electrode.

Results

Deposition of MnO_2 layers

An example of manganese oxide deposition is plotted in Fig. 1.

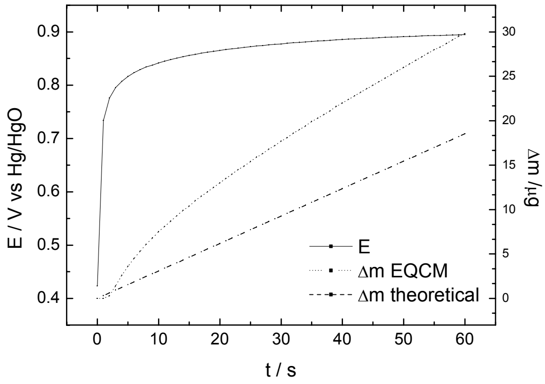

Fig. 1 *MnO_2 electrodeposition, potential (full line), measured (broken line) mass dependence, theoretical (punctuated line)*

The deposition current density was 0.5 mA.cm^{-2}. At the end, the charge passed corresponded to 18.2μg of deposited layer MnO_2. On contrary, the mass increase about 30 μg was estimated from the output of the EQCM device, which is by 11.2 μg more. The simultaneous incorporation of water seems to be evidenced by our experiments. The molar ratio between MnO_2 and water is then 1 : 3 approximately, and the sorption of water seems to be very strong.

Following Fig. 2 shows the cathodic charging at -0.3 V vs. Hg/HgO and its opposite process at -0.05 V by using cyclic voltammetry.

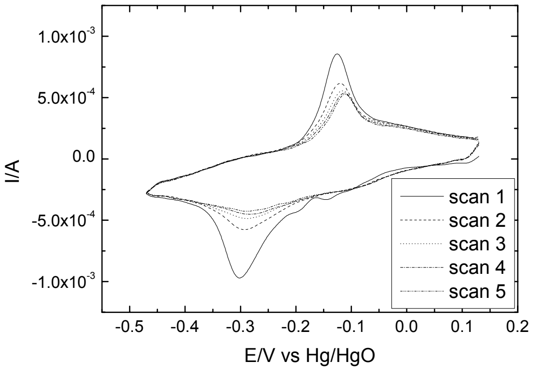

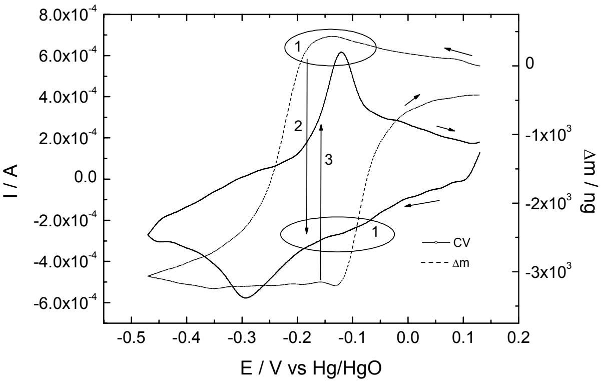

Fig. 2 (left) *Cyclic voltammetry, electrodeposited MnO_2 in 1M KOH, scan rate 10 mV/s, N_2 bubbled.*
Fig. 3 (right) *Cyclic voltammetry and massogram, comparison of electrodeposited MnO_2 in 1M KOH, scan rate 10 mV/s, N_2 bubbled, scan nr. 2*

Moreover, the progressive fading of the process in subsequent cycles is clearly indicated there. The scan rates of 0,1mV/s to 50 mV/s were employed.

The behavior of another electrode during first cycle is shown in Fig. 3.

We can see distinct mass changes in potential range of both anodic and cathodic voltammetric peaks. Apparently, the reduction is accompanied by mass loss and the oxidation (*i.e,* charging) is bound to mass increase.
The comparison of mass computed from charge passed through the system and the output of the EQCM are compared in Fig. 4.

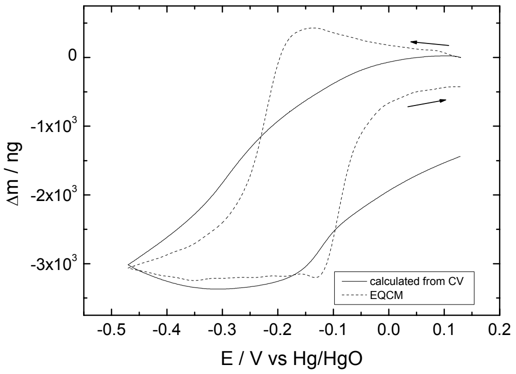

Fig. 4 *Theoretical (full line) and mesassured (broken line) mass flow in electrodeposited MnO2 in 1M KOH, scan rate 10 mV/s,* N_2 *bubbled, scan nr. 2*

The mass from the charge is compared under assumption of one molecule of water per one atom of Mn^{4+} changed to Mn^{3+}. Again we see that the material releases water in the process of reduction in an amount higher than 1 molecule to 1 atom of manganese. It should be noted that the massogram (the Δm versus potential) is almost closed. This indicates almost reversible sorption and desorption of water.

Conclusion

We can see a steady decrease both of the depth of the changes in one cycle and the total mass of the electrode, which indicates the termination of the life of the system perhaps due to slow dissolution of manganese oxide layer in the electrolyte. The incorporation of water into the manganese oxide (presumably, γ-MnO_2) plays an important role.

Acknowledgment

Ministry of Education of Czech Republic, Project MSM002130516

References

1. Torresi, S. at. All, J.Electrochem. Soc., 148, 10 A1179-A1184, 2001
2. Corrigan, D., Bendert, R., J. Electrochem. Soc., Vol. 136, No. 3, 1989
3. Meccea, V., Analytical Letters, 38: 753–767, 2005
4. Zhao, Y.L., Wang, J.M., Chen, H., Pan, T., Zhang, J.Q., Cao, C.N., Electrochimica Acta 50 (2004) 91–98
5. Klapste, B.,Vondrak, J., Velicka, J., Electrochimica Acta 47 (2002) 2365– 2369

6. P. Bezdička, T. Grygar, B. Klápšťě, J. Vondrák, Electrochimica Acta, 45, 913 (1999)
7. M. P. Owen, G. A. Lawrance, S. W. Donne, Electrochimica Acta 52 (2007) 4630–4639
8. S. Deabate, F. Henn, S. Devautour, J.C. Giuntini, J. Electrochem. Soc. 150 (2003), J23
9. Cartwright, R.L. Paul, in: B. Schumm, H.M. Joseph, A. Kozawa (Eds.), Proceedings of the MnO_2 Symposium, vol. 2, Tokyo, 1980, 290
10. R.L. Paul, A. Cartwright, J. Electroanal. Chem. 201 (1986) 113

DETERMINATION OF LEAD ACID BATTERY STATE OF CHARGE (SOC)

P. Křivík

Department of Electrotechnology, Faculty of Electrical Engineering and Communication Technologies, Technical University of Brno, Czech republic

Corresponding author: Petr Křivík (krivak@feec.vutbr.cz)
Phone: +420 541 146 189
Fax: +420 541 146 147

Introduction

An accumulator state of charge (SOC) is becoming an increasingly important information in many applications using accumulators as sources of electric energy. Previous strategies were only focused on limitation of accumulator voltage targeted at protection against deep discharge or overcharge. Now, this approach is changing, and the key factor for an improved check of accumulator state is as precise and fast as possible determination of the state of charge of a battery.

Experimental

Following the recent efforts to reduce emissions of greenhouse gases and attain sustainable growth, automotive industry, for example, has focused on the transition type of vehicle between the one with the conventional combustion drive and electromobile – the hybrid electric vehicle (HEV). This vehicle, driven by an electromotor, supplied (contrary to the conventional electromobile) by a relatively small array of accumulators, permanently charged by a combustion motor with a relatively low output, working in the mode of optimal revolutions with minimal exhalations. This type of vehicle is optimal mainly in city traffic where it considerably reduces pollution, and also fuel consumption is reduced.

One of the possible sources of current for the hybrid electric vehicle seems to be the economical lead acid acumulator, which is much cheaper than other systems that might be used for electric energy accumulation. To make the accumulators for hybrid electric vehicles able to receive electric charge also at relatively high rates of charge (e.g. in regenerative braking), they have to work in the partial state of charge. When this mode is applied to the lead acid accumulator, a new undesirable phenomenon appears resulting in loss of charging ability connected with irreversible sulphatation of negative electrodes. This undesirable effect can be overcome by using new types of additives into negative active substances different from the commonly used expanders (acting against the undesirable growth of large crystals of lead sulphate at the expense of the small ones), as well as optimization of current collector (distribution of flags) and down-pressure [1-4]. In this mode, it is highly desirable to know the current state of accumulator charge (i.e. its residual capacity) to prevent problems connected with discharge or even charge of this accumulator. At the same time, the method of SOC determination should be fast, relatively accurate and not very costly.

Extensive research has been done in this field. Approaches to the determination of the state of charge vary in accordance with the operating state of accumulators, some prefer photovoltaic applications, hybrid electric vehicles, communications, etc.

Among the methods for measurement of the state of accumulator charge are, for example, a discharge test, measurement of electrolyte concentration, measurement of unloaded battery voltage, impedance spectroscopy, measurement of internal resistance [5]. Most of these methods have disadvantages – they are not too precise and they are usable only in some types of accumulators.

The causes of the end of lifetime in testing cells can be different. The most common causes are sulphatation of plates, corrossion of positive electrode lattice, falling active substance in positive electrodes, short-cut or a combination of these factors. Experiments show that resistance values depend on formation and dissolution of $PbSO_4$ crystals in active substance, of mainly positive electrode, which is mostly restrictive (because of its lower capacity as compared with the negative electrode). Its resistance is an order higher as compared with that of the negative electrode, in both the state of charge and the state of discharge. This is also affected by the rate of discharge or charge as this parameter affects the shape, size and distribution of originating or in active substance dissolving $PbSO_4$ crystals.

An optimal method seems to be the method of change measurement after a short-term current loading (for both the charging and the discharging current). An accumulator at a high degree of charge should exhibit, after charging current application, a more substantial change of voltage than a battery at a lower degree of charge. Similarly, discharging current pulses would more accurately determine the state of batteries with a lower state of charge.

At the same time the changes of battery voltage after curent pulse application reflect the reaction processes in the electrode double layer at the boundary active substance-electrolyte, and also the diffusion processes inside the battery. All these reactions indicate the current state of charge, and also the lead acid accumulator lifetime.

Results and Discussion

Measuring and cycling software was developed for cycling of testing cells, setting of the accurate state of charge in regard to the previous capacity, application of a precisely determined current pulse (both discharging and charging) and finally continuous monitoring of voltage (potential) values of cells in situ at a rate of 100x per second.

Experimental cell was created, implemented and set in operation for experiments. Then the initial tests were performed. Voltage values in electrodes were recorded after application of current pulse (charging and discharging), during the pulse and after it to find the optimal magnitude and length of pulse for accurate determination of the degree of charge. The values were recorded at various states of charge. Experiments are only at the beginning and they will continue.

Resulting graphic dependencies of voltage courses of cell with capacity of 0,4Ah are presented on fig. 1, 2 and 3.

From fig. 1, 2 and 3 it is seen an evident difference in cell voltage courses, that depends on state of charge and magnitude of used current. When state of charge is 100%, measured voltage at the end of charge and discharge current pulse is higher compared with state of charge 50% (see fig. 1 and 2). When used current is 0,5A, measured voltage at the end of charge is lower and at the end discharge is higher compared with used current 1A (see fig. 2 and 3). It is in good accordance with theoretical expectations. Length of the pulses is not so important. It seems that 1,5s is sufficient for good determination of state of charge.

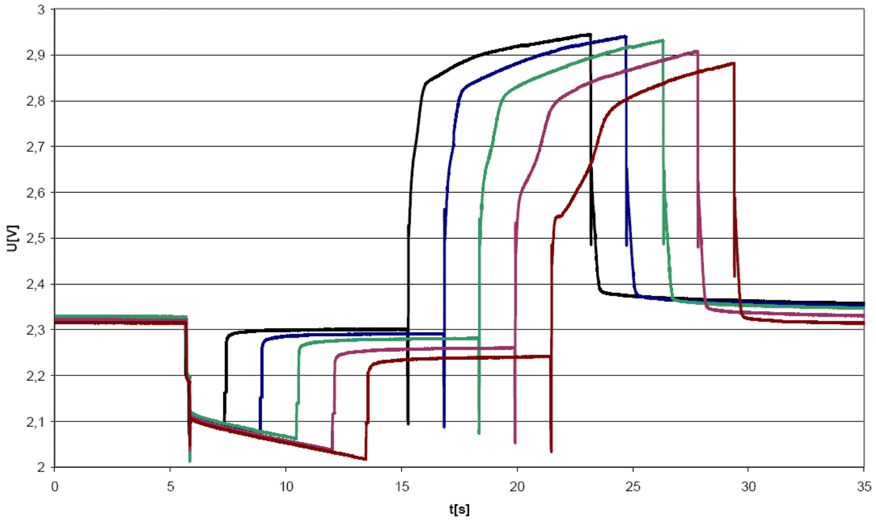

***Fig. 1** Time courses of cell voltage; discharge 1,5-7,5s; standing 7,5s; charge 7,5s; I=0,5A; 100% of charge*

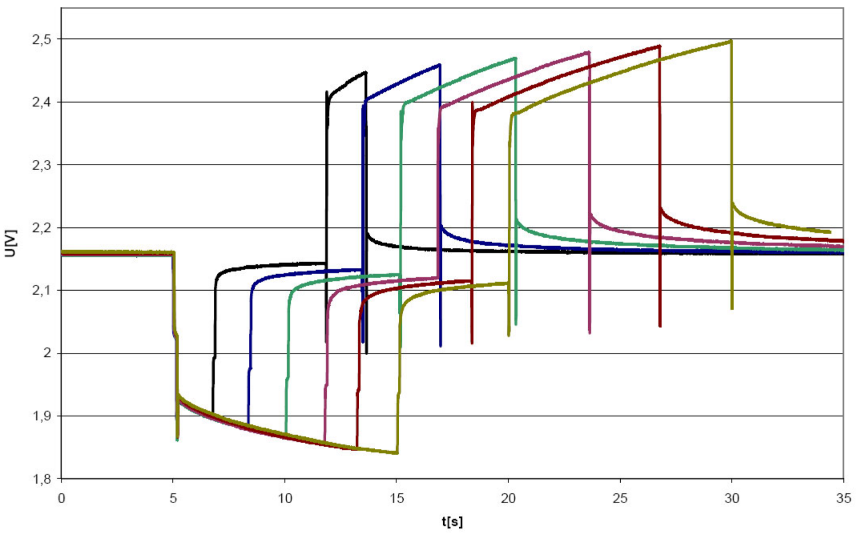

***Fig. 2** Time courses of cell voltage; discharge 1,5-9s; standing 4,5s; charge 1,5-9s; I=0,5A; 50% of charge*

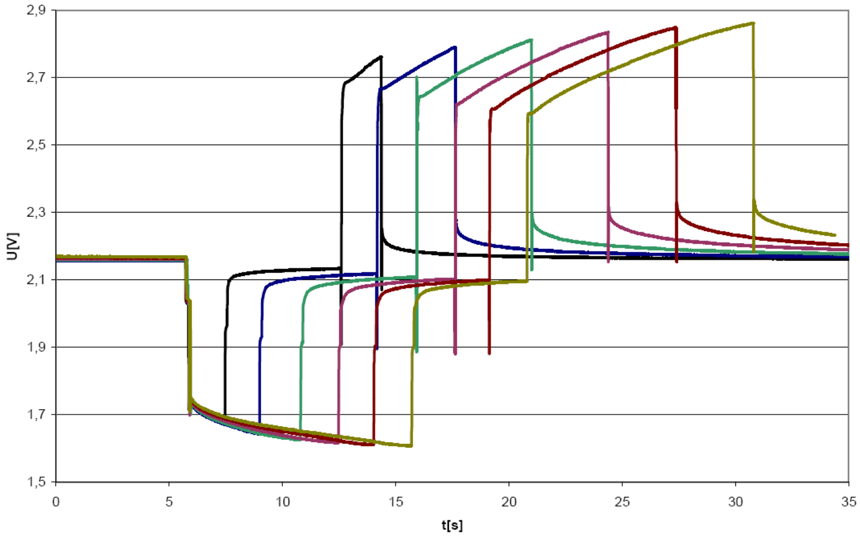

Fig. 3 *Time courses of cell voltage; discharge 1,5-9s; standing 4,5s; charge 1,5-9s; I=1A; 50% of charge*

Conclusions

Changes in voltage courses during voltage measurements in current pulse regime reflect state of charge of lead acid battery cells. There plays an important role especially magnitude of current during charge and discharge pulses.

Acknowledgements

This work was sponsored by grant No. MSM0021630516.

References

1. Nakamura K., Shiomi M., Takahashi K., Tsubota M., *Failure modes of valve-regulated lead/acid batteries*, J. Power Sources **59**, 153 (1996).
2. Shiomi M., Takayuki F., Nakamura K., Takahashi K., Tsubota M., *Effects of carbon in negative plates on cycle-life performance of valve-regulated lead/acid batteries*, J. Power Sources **64**, 147 (1997).
3. Trinidad F., Gimeno C., Guttiérez J., Ruiz R., Sainz J., Valenciano J., *The VRLA modular wound design for 42 V mild hybrid systems*, J. Power Sources **116**, 128 (2003).
4. Cooper A., Moseley P.T., *Progress in overcoming failure modes peculiar to VRLA batteries*, J. Power Sources **113**, 200 (2003).
5. S. Piller, M. Perrin, A. Jossen, *Methods for state-of-charge determination and their applications*, J. Power Sources **96**, 113 (2001).
6. Huet F.: *A review of impedance measurements for determination of the state-of-charge or state-of –health of secondary batteries*, J. Power Sources **70**, 59 (1998)
7. Huet F, Nogueira R.P, Torcheux L.: *Simultaneous real-time measurements of potential and high-frequency resistance of a lab cell*, J. Power Sources **113**, 414 (2003)

MEASUREMENT OF THE POSITIVE AND NEGATIVE ELECTRODE OF LEAD-ACID ACCUMULATOR USING ELECTROCHEMICAL IMPEDANCE SPECTROSCOPY ON EXPERIMENTAL ELECTRODE WITH SYSTEM OF NON-CONTINUOUS PARALLEL RIBS

P. Abraham, P. Bača

Department of Electrotechnology, Technical University, 602 00 Brno, Czech Republic

Corresponding author. Pavel Abraham (xabrah02@stud.feec.vutbr.cz)
Phone: +420 541 146 189
Fax: +420 541 146 147

Abstract

This article shows our ongoing development introduced in our article last year. It deals with possibilities of corrosion properties measurement of lead alloys used in acid mediums of lead-acid accumulators. At department of electrotechnology a new method was developed. This method makes possible to write down changes of corrosion impedance of interphase electrode/electrolyte. This method is based on electrochemical impedance spectroscopy of experimental electrode with non-continuous system of parallel ribs. [1,2]

Keywords: EIS, corrosion layer, active-mass, PAM, NAM

Introduction

Detailed description of measuring apparatus and circuitry is shown in article [3]. Experimental electrode with system of non-continual ribs is used, pasted with positive or negative active mass. Equivalent circuit of this electrode with detailed description is shown at [3]. Zm means impedance of active mass between single ribs of collector, Zk means impedance of interphase collector/active mass.

Experimental

Experimental electrodes was made from low-antimony lead alloy Pb Sb1.68 Sn0.05 (wt%). Individual ribs of electrode had dimensions 20x1 mm. Distance between ribs was 5.5 mm. Before we start with experiment we made experimental cell, that contained excess of electrolyte. Positive and negative electrode were pasted by commercially made active mass from company AKUMA Mladá Boleslav.

Two positive electrodes were placed on both sides from negative electrode. 1.8 mm thick AGM separators of the type BG-280GB180 (Hollingsworth&Vose) was used. Cell was put into operation and 100 cycles was done on it.

To interpret dependencies of real and imaginary part of impedance we used poteciostat BioLogic VSP. Dependencies were made for frequencies form 200 kHz to 0.1 Hz. Maximal voltage response was set to 30 mV, stabilizing time was set half of period.

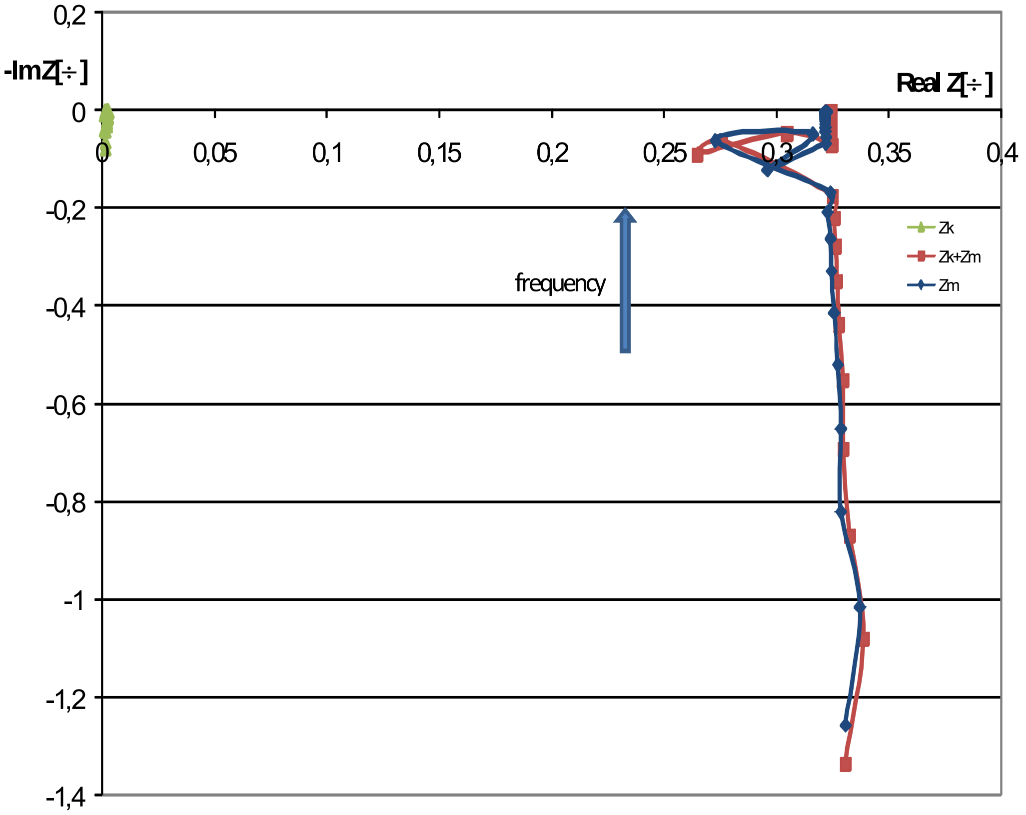

Fig. 1 *Dependency of imaginary and real part of impedance for negative electrode. Progression of Zm corresponds with impedance of negative active mass, progression Zk corresponds with calculated impedance of corrosion layer at interphase collecotor/active mass of negative electrode*

Measured and calculated dependencies of negative electrode impedance are shown at Fig. 1. Measured impedance (Zm and Zk+Zm) show only inductive properties, with increasing frequency imaginary part of impedance also increases. This inductive property of impedance is caused by parasite inductance of measure circuit wiring. In frequency range 10 kHz – 20 kHz anomaly occurs, that apparently means achieving of resonance frequency of wiring. In progression of calculated impedance of corrosion layer at interphase collector/negative mass Zk three values close to resonance frequency are skipped. Parasite component of wiring is in progression of Zk markedly muffled.

From Fig. 1 is evident that active mass of interphase collector/active mass of negative electrode has only ohmic nature, that corresponds with theory, because negative active mass consists of sponge lead and negative potential of electrode is lower then oxidation potential of lead, so corrosion and dissolution of negative electrode collector cannot be expected.

Progression of impedance Zm of positive electrode is shown at Fig. 2, 3 and 4. All three figures was obtained on electrodes without current during 30 minutes. Fig. 3 shows that low frequency of measurement was decreased to 1 mHz. Fig. 4 shows repeat of experiment shown at Fig. 2. with stabilizing time of 6 period.

From compare of Fig. 2. 3. and 4 it is evident that, equivalent scheme consists of two RC networks with different time constant, that differs at least of one digit value. First RC network almost did not change its parameters, the second one is apparently different – we assume that during first run charging of electrode double layer occurred and it does not return to starting state.

This statement is supported by Fig. 4 where longer stabilizing time was used and progression of second RC network was lowered. Diffusion occurs at frequencies lower then 6 mHz as shown at Fig. 3. We again assume that positive values of impedance at highest frequencies are caused by inductive element of of measure wiring.

At Fig. 5 total progressions are shown for impedance of positive active mass. Zm impedance of corrosion layer at collector/active mass Zk and their addition. These progressions are influenced by stabilizing time before measurement and apparently also by voltage respond during measurement. Methodology of positive electrode measurement needs further development and validating.

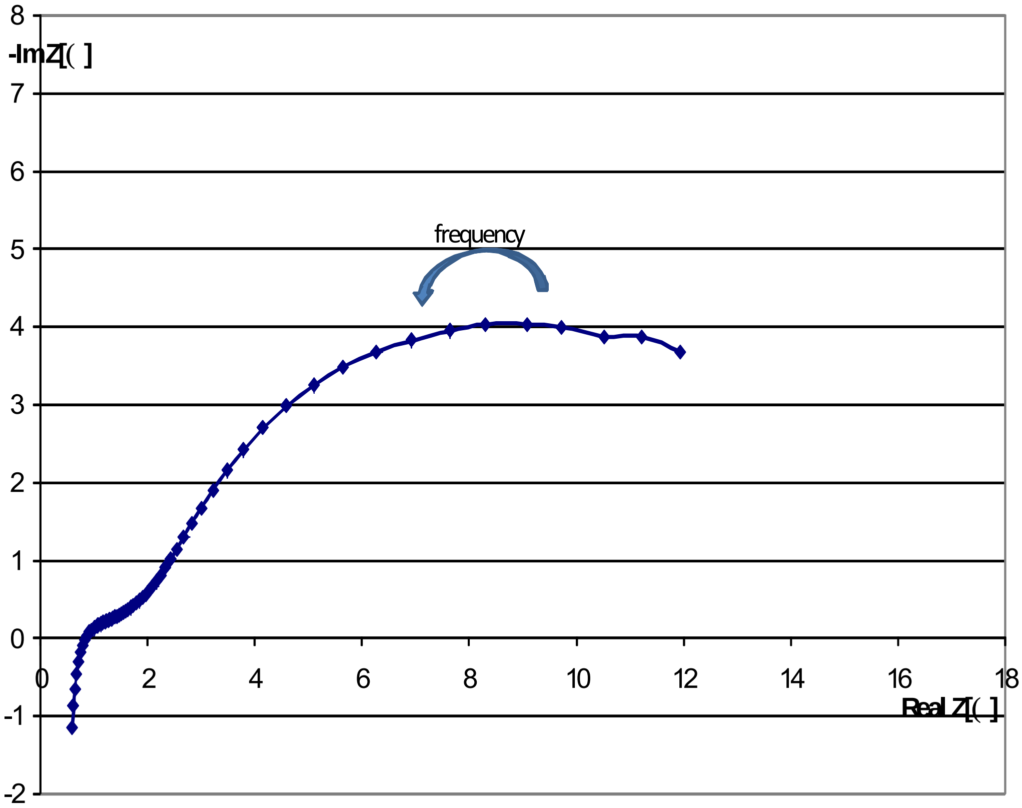

***Fig. 2** Dependency of imaginary and real part of impedance of active mass of positive electrode. First run.*

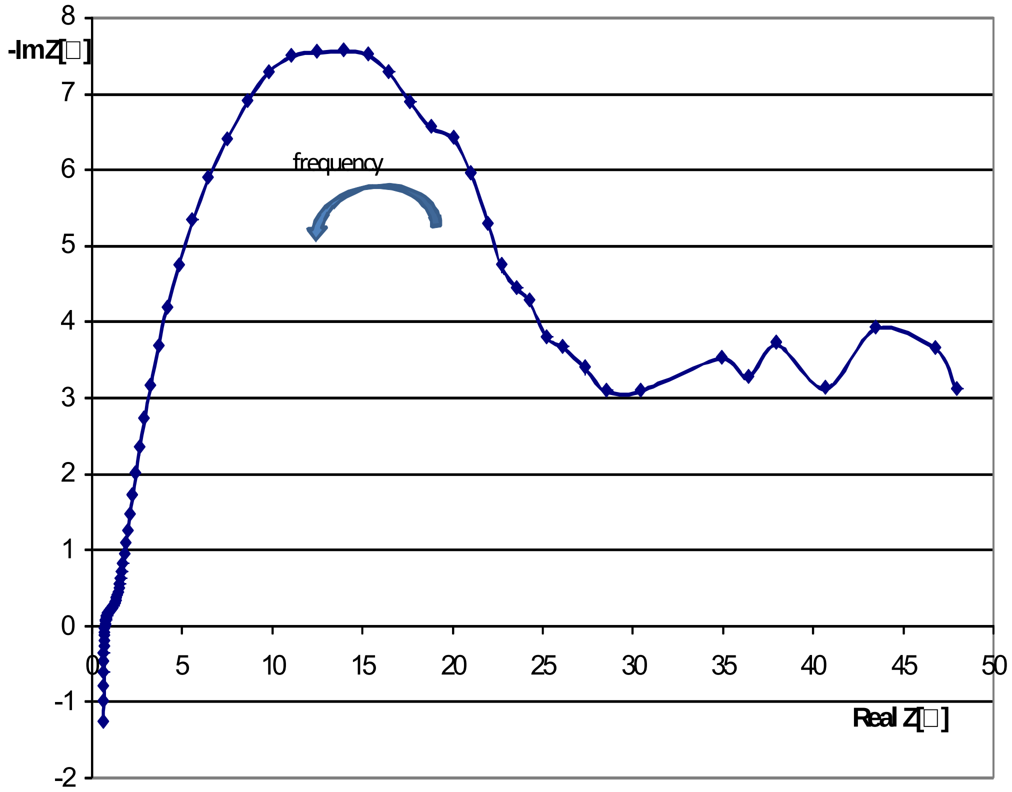

Fig. 3 *Dependency of imaginary and real part of impedance of active mass of positive electrode. Second run, measured with frequencies 200 kHz – 1 mHz.*

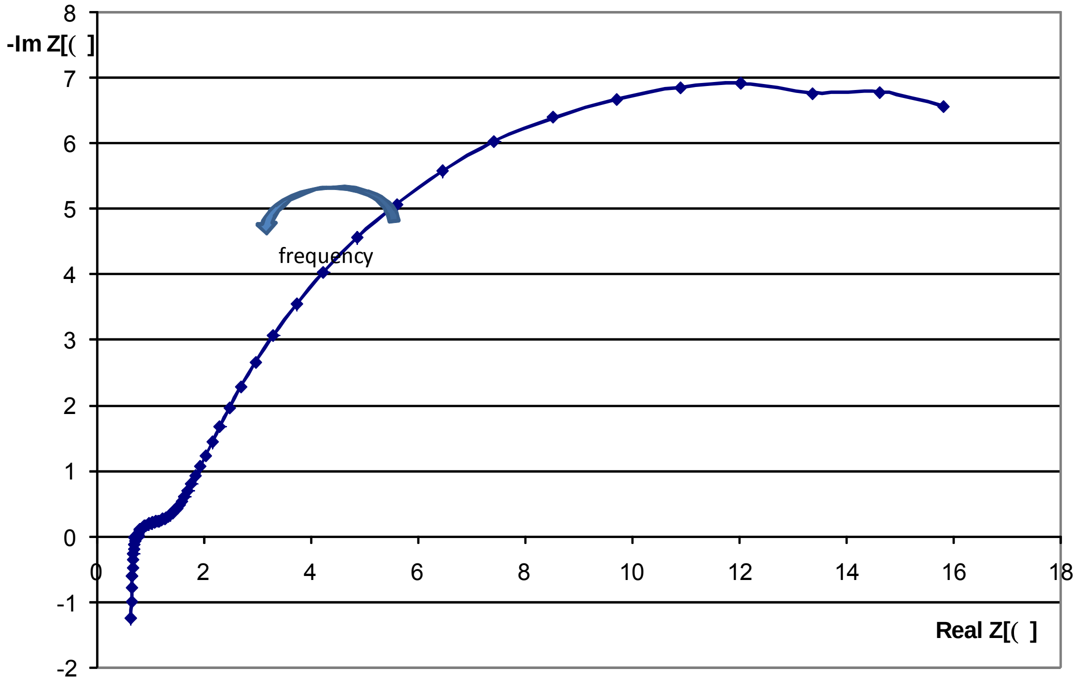

Fig. 4 *Dependency of imaginary and real part of impedance of active mass of positive electrode. Third run, stabilizing time 6 period.*

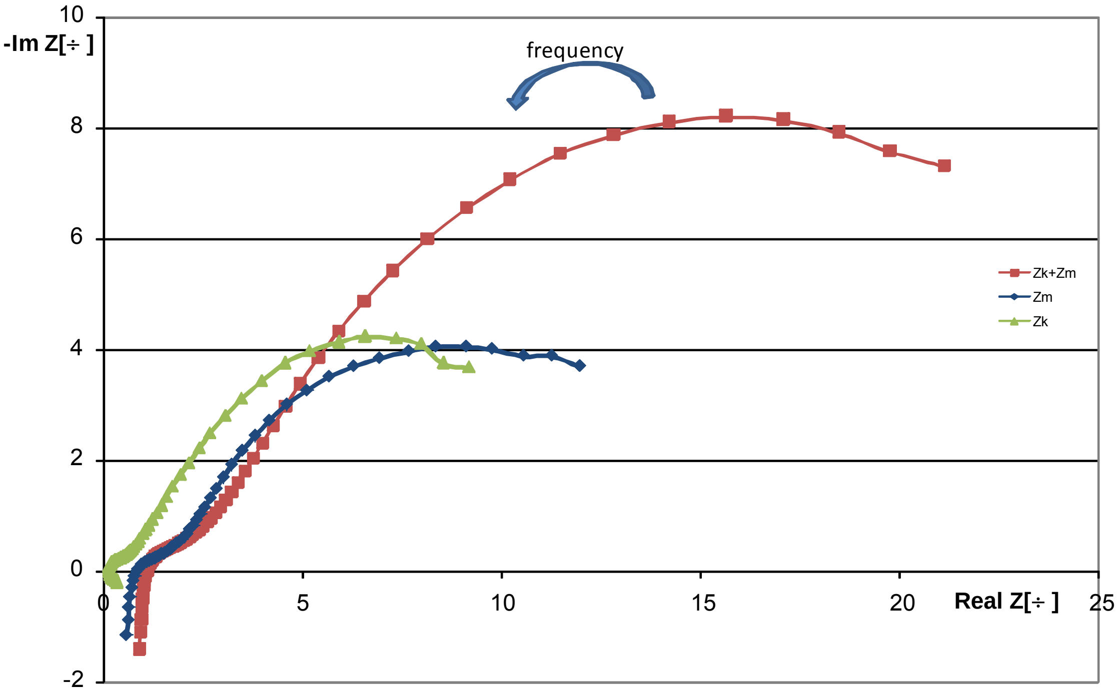

Fig. 5 *Dependency of imaginary and real part of impedance of active mass of positive electrode. Progression of Zm corresponds with impedance of negative active mass, progression of Zk corresponds with calculated impedance of corrosion layer at collector/positive electrode active mass. Stabilizing time 6 period.*

Results and discussion

From compare of graphical progressions of impedance of negative and positive electrode is evident that impedance of negative active mass is ohmic nature only. This corresponds with theory. At positive electrode corrosion layer origins at interphase collector/ active mass. This layer is ohmic and capacity nature and can give us important information about state of corrosion and whole electrode.

References

1. BAČA, P. Modified Conductometric Method. In Advanced Batteries and Accumulators - 9th ABA. Brno: TIMEART agency, 2008. s. 153-155. ISBN: 978-80-214-3659- 6
2. P. ABRAHAM: Measurement of the corrosive layer resistance of lead alloys using modified conductometric method, In Advanced Batteries and Accumulators - 9th ABA. Brno: TIMEART agency, 2008. s. 161-164. ISBN: 978-80-214-3659- 6
3. Bača, P. Abraham, P.: Measurement of the corrosive layer resistance of lead alloys using method derived from electrochemical impedance spectroscopy, 10th International Conference Advanced batteries and accumulators, 2009

MEASUREMENT OF THE CORROSIVE LAYER RESISTANCE OF LEAD ALLOYS USING METHOD DERIVED FROM ELECTROCHEMICAL IMPEDANCE SPECTROSCOPY

P. Bača, *P. Abraham*

Department of Electrotechnology, Technical University, 602 00 Brno, Czech Republic

Corresponding author. Petr Bača (baca@feec.vutbr.cz)
Phone: +420 541 146 189
Fax: +420 541 146 147

Abstract

This article shows our ongoing development introduced in our article last year. It deals with possibilities of corrosion properties measurement of lead alloys used in acid mediums of lead-acid accumulators.

At department of electrotechnology a new method was developed. This method makes possible to write down changes of corrosion impedance of interphase electrode/electrolyte. This method is based on electrochemical impedance spectroscopy of experimental electrode with non-continuous system of parallel ribs. [1,2]

Keywords: Corrosion layer, Modified conductometric method, Conductometry

Introduction

Measurement takes place at experimental electrode with system of non-continuous ribs (fig. 1). Ribs made out of led alloys are fixed between two strips of epoxy resin. To each rib one voltage and one current leading wire is connected to make possible to measure by four-point method.

Equivalent diagram of experimental electrode is at fig. 2. Rp means wire resistance that was measured before experiment begins, Zk means corrosion impedance of interphase electrode/electrolyte, Zm means impedance of electrolyte.

Measurement proceeds in two steps, frequency dependency is measured between ribs 5-6. During first step current flows between ribs 4-7 and in second step the current flows between ribs 5-7. In first step we theoretically measure only impedance of electrolyte Zm and in second step we measure compounded impedance Zm+Zk. When we substract these two values we get impedance of corrosion layer.

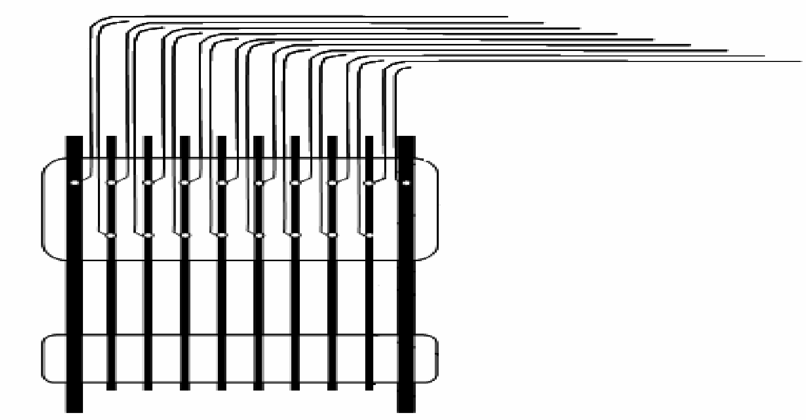

Fig. 1 *Electrode with system of non-continuous parallel ribs*

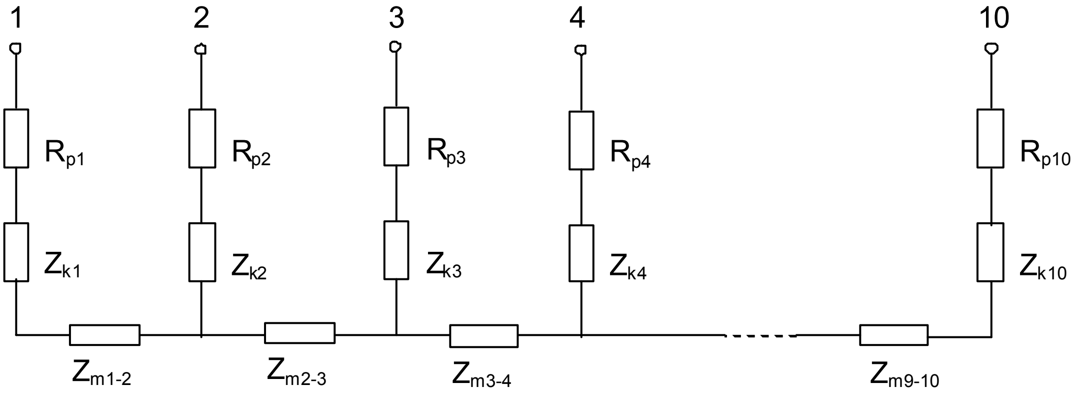

Fig.2 *Equivalent diagram*

Experimental

Experimental electrode was made from low-antimony lead alloy Pb Sb1.68 Sn0.05 (wt%). Individual ribs of electrode had dimensions 20x1 mm. Distance between ribs was 5.5 mm. Before we start with experiment we made experimental cell, that contained excess of electrolyte and negative active material from industry produced negative electrode of starting battery from AKUMA a.s. Mladá Boleslav. Negative electrodes were placed on both sides 2.5 mm far from experimental positive electrode. No separator was used. For creation of corrosion layer we charged the electrode with 0.2 A for 120 hours.

To interpret dependencies of real and imaginary part of impedance we used poteciostat BioLogic VSP. Dependencies were made for frequencies form 200 kHz to 0.1 Hz. Maximal voltage response was set to 30 mV, stabilizing time was set half of period.

Results of our measurement are presented at fig 3. Highest frequencies shows positive values of imaginary part of impedance, this we assume is because of inductance of circuit.

Blue progression in fig 3. represents first step of measurement, theoretically electrolyte impedance Zm. From graph is evident that progression is influenced by capacity of double layer and that diffusion occurs at lowest frequencies.

We can apply one RC network with Warburg's impedance called Randels equivalent diagram [3] shown at fig. 4. R corresponds with electrolyte resistance, Cdl means capacity of double layer, Rct is charge –transfer resistance that slows distribution of electrons between electrode and ions of electrolyte, Zw – Warburg's impedance)

Red progression in fig 3. represents second measure step, theoretically compound of impedance of electrolyte Zm and corrosion layer Zk. From graph is evident that we can apply two RC networks and their time constant differs at least by one digit place.

Diffusion represented by Warburg's impedance occurs again for low frequencies. First two progressions in graph are a bit flat that means that capacity in equivalent diagram should be replaced by capacity element with constant phase.

Green progression in fig. 3 is final dependency of corrosion layer Rk. This progression is represented only by RC network. Progression shows half of circle from highest frequencies to aprox. 12 Hz, where diffusion occurs.

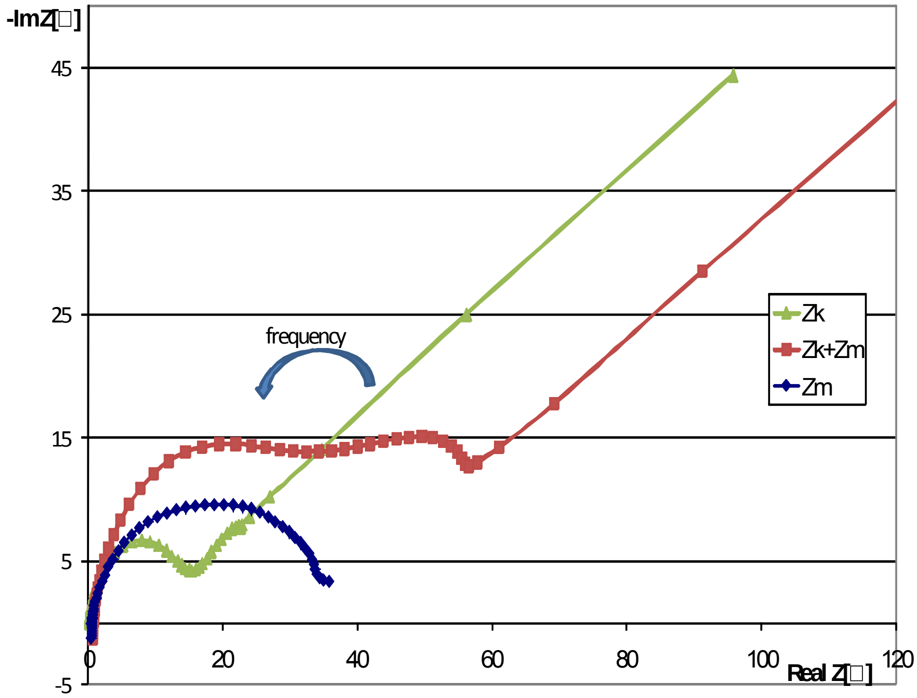

Fig. 3 *Dependency of imaginary part on real part of impedance for each step of measurement*

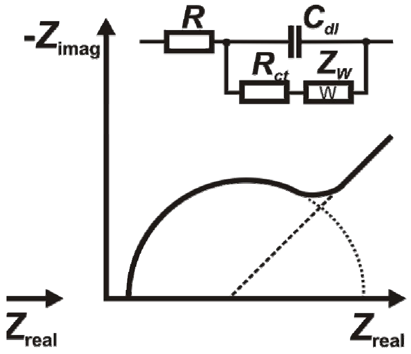

Fig.4 *Randles equivalent circuit*

When we repeated the experiment by step 2, we get a bit different results as shown at fig. 5. From graph is evident that first RC network did not change its parameters, but second one increased its capacity. We assume that during first measurement some changes occurs at electrode double layer. To overcome this problem it will be needed to lower voltage response during measurement and increase stabilizing time before next measurement.

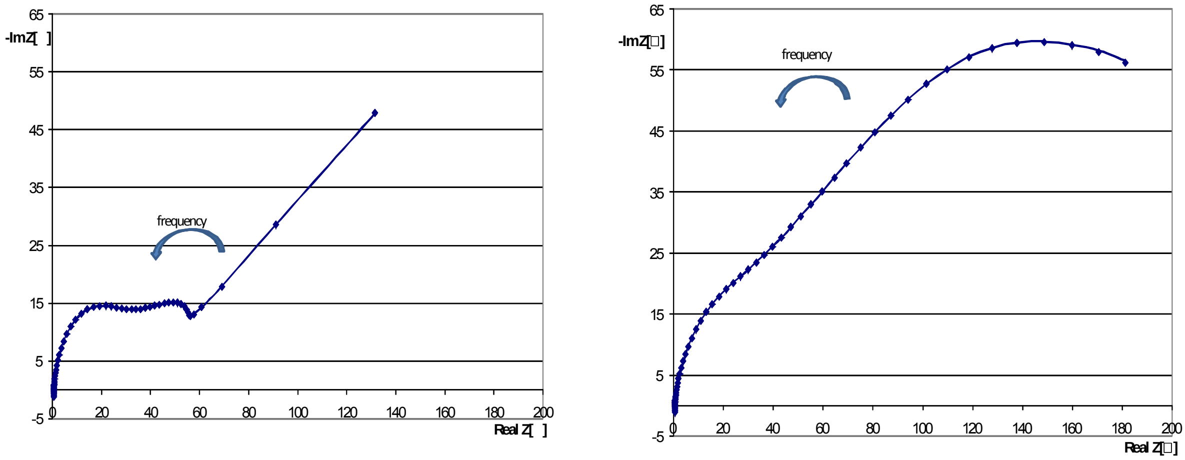

Fig.5 *Comparsion of first and second measurement at the same electrode*

Results and discussion

Our preliminary experiments shows that EIS method is acceptable for resistance of corrosion layer measurement at interface electrode/electrolyte and it can be used as comparative method for measuring of various collector alloys to find out corrosion rate of that alloy.

References

1. BAČA, P. Modified Conductometric Method. In Advanced Batteries and Accumulators - 9th ABA. Brno: TIMEART agency, 2008. s. 153-155. ISBN: 978-80-214-3659- 6
2. P. ABRAHAM: Measurement of the corrosive layer resistance of lead alloys using modified conductometric method, In Advanced Batteries and Accumulators - 9th ABA. Brno: TIMEART agency, 2008. s. 161-164. ISBN: 978-80-214-3659- 6
3. Prof. RNDr. František Opekar, CSc. : Učební texty na Př.f. UK

PREPARATION AND CHARACTERIZATION OF PPy/PEG-$LiFePO_4$ CATHODE MATERIAL FOR Li-ION BATTERIES

A. Fedorková[1], *R. Oriňáková*[2], *A. Oriňák*[2], *H.-D. Wiemhöfer*[3], *D. Kaniansky*[1]

[1]*Department of Analytical Chemistry, Faculty of Science, Comenius University, Mlynská Dolina,SK-842 15 Bratislava 4, Slovak Republic*
[2] *Department of Physical Chemistry, Faculty of Science, P.J. Šafárik University, Moyzesova 11, SK-04154 Košice, Slovak Republic*
[3] *Department of Inorganic and Analytical Chemistry, Westfälische Wilhelms University, Correnssstrase 30, 481 49 Münster, Germany*

Corresponding author, Andrea Fedorková (address: fedorkova@fns.uniba.sk)
Phone: +421-55-2342327
Fax: +421-55-6222124

Introduction

Rechargeable lithium batteries are now used extensively for a wide variety of applications, from portable electronic devices to hybrid and electric vehicles. The performance and cost of the batteries are often decided by the properties of the cathode material. Lithium cobalt oxide is the most successful commercial cathode material in batteries for portable devices, but it is limited by cobalt resources scarcity and its unsafety during overcharge. During the past few years, $LiFePO_4$ has received growing attention as a promising cathode material for lithium ion batteries. This compound has a theoretical capacity of 170 mAh/g and a constant open-circuit voltage of 3.4 V vs. Li/Li^+ that is matched to polymer electrolytes [1]. Bare $LiFePO_4$ is an insulator with electrical conductivity of about $\sim 10^{-11}$ S/cm. One of the approaches to increase electrical conductivity of $LiFePO_4$ is coating with conducting polymers [2,3]. Electroactive conducting polymers (ECPs) are conjugated polymers that exhibit electronic conduction when partially oxidized or reduced and are capable of undergoing oxidation/reduction reactions [4]. Examples of ECPs include polypyrrole (PPy), polyaniline, polytiophene and polyphenylenevinylene. Polypyrrole is a polymer which also acts as a host material for Li^+-ion insertion/extraction in the voltage range of 2.0 – 4.5 V versus Li/Li^+, with a theoretical capacity of 72 mAh/g [5]. Therefore, PPy additives can be used as both conductive agents and cathode materials. The principal problems with a practical utilization of conducting polymers like polypyrrole include its poor mechanical properties like brittleness and low processibility. Blending insulating polymers is an attractive route to improve their mechanical properties without loosing their conductivity [6,7]. The advantageous properties observed for PPy coated $LiFePO_4$ with PEG admixture may partially be explained by the increased salt solubility of the PPy/PEG composites as PEG is known as a very good solvent for lithium salts. We report the synthesis and characterization of $LiFePO_4$ prepared by a solvothermal method. To improve conductivity, capacity and battery performance, the $LiFePO_4$ particles were coated with polypyrrole or with composite polymer PPy/PEG. We report the synthesis and characterization of $LiFePO_4$ prepared by a solvothermal method. To improve conductivity, capacity and battery performance, the $LiFePO_4$ particles were coated with polypyrrole or with composite polymer PPy/PEG.

Experimental

Synthesis of $LiFePO_4$ particles: carbon-free $LiFePO_4$ sample was prepared by solvothermal method. Stoichiometric amounts of $Li(CH_3COO)\cdot H_2O$, $Fe(CH_3COO)_2$ and H_3PO_4 were dissolved in 70 ml of ethylene glycol. A liquid reaction mixture was placed in a round-bottom flask open only at the top. This flask was connected to a condenser and refluxed vigorously for 72 h at 200°C. The remaining product was filtered off, washed several times with distilled water and ethanol. The sample was initially preheated at 60°C for 5 hours and then sintered at 700 °C for 5 h under nitrogen atmosphere. As reference material for comparison with our $LiFePO_4$ was used $LiFePO_4$ with carbon coating from Südchemie.

Preparation of $LiFePO_4$ polymer composites: 1.5 g of pyrrole (Aldrich Chemicals Co.) monomer and 1 g of as described above synthesized $LiFePO_4$ were placed in a 100 ml round-bottom flask. 1.42 g $FeCl_3$ (99.9 % Aldrich) as oxidation agent was dispersed in aqueous solution (50 ml) of 0.1 mol/l HCl and was added to the flask. The reaction was allowed to proceed for further 7 h. The mixture was kept at ~ 4 °C and stirred vigorously. A black precipitate formed progressively during the reaction. The resulting polypyrrole-$LiFePO_4$ (PPy-$LiFePO_4$) powder was recovered by filtration, washed with water and acetone and dried in the oven (~70 °C) up to a constant weight. For preparation of PPy/PEG-$LiFePO_4$ samples polyethylene glycol (PEG 1000) was used at the beginning of polymerization (with a weight ratio PPy:PEG = 33:1).

Materials characterization: A slurry was made by mixing the PPy-$LiFePO_4$ as the active material with poly(vinylidene fluoride) (PVDF). PVDF was dissolved in N-methyl-2-pyrrolidone (NMP). A weight ratio of active material and PVDF was 90:10. The slurry was then coated onto aluminum foil as current collector using the doctor-blade technique and subsequently dried in a vacuum oven at 80°C for 18 h (NMP was than evaporated). Circular samples with 12 mm diameter were cut out. Test cells were assembled using these cathodes in a Swagelok T-cell together with a counter and a reference electrode made from lithium metal foil and a separator layer (SEPARION® and fiber glass separator Wattman GF/D). All handling was done in an argon filled dry glove box (MBraun, Unilab, Germany). The electrolyte consisted of 1 mol/l $LiPF_6$ in ethylene carbonate/ethylmethyl carbonate (EC/EMC, volume ratio 1:1).Cyclic voltammetry (CV) measurements were performed on the test cells using an EG & G scanning potentiostat (Mod. 273) in the voltage range 2.8-4.2 V and with a scannig rate of 0.05 mV/s. AC impedance measurements were carried out in the frequency range 10^5 Hz to 0.1 Hz with amplitudes of ±10 mV.

Results and discussion

We investigated the influence of PPy on the conductivity of the PPy-$LiFePO_4$ based electrodes by cyclic voltammetry and electrochemical impedance spectroscopy. Figure 1 shows the cyclic voltammograms of electrodes from PPy-$LiFePO_4$ (carbon-free $LiFePO_4$

prepared by synthesis) and PPy-$LiFePO_4$ ($LiFePO_4$ + 4% carbon – Südchemie) measured at room temperature. The voltammograms indicated that only a single electrochemical reaction occured during the charge and discharge of our samples. It can be clearly seen that the PPy-$LiFePO_4$ electrode prepared from carbonated $LiFePO_4$ (Südchemie) is more active. Higher electrochemical activity is result of carbon coating. The peaks of the carbon-free PPy-$LiFePO_4$ electrodes are thin and sharp, lithium insertion/extraction is more efficient as in case of carbonated $LiFePO_4$ sample. The peaks are slightly unsymmetric as the cathodic peak height is somewhat smaller than that of the anodic reaction.

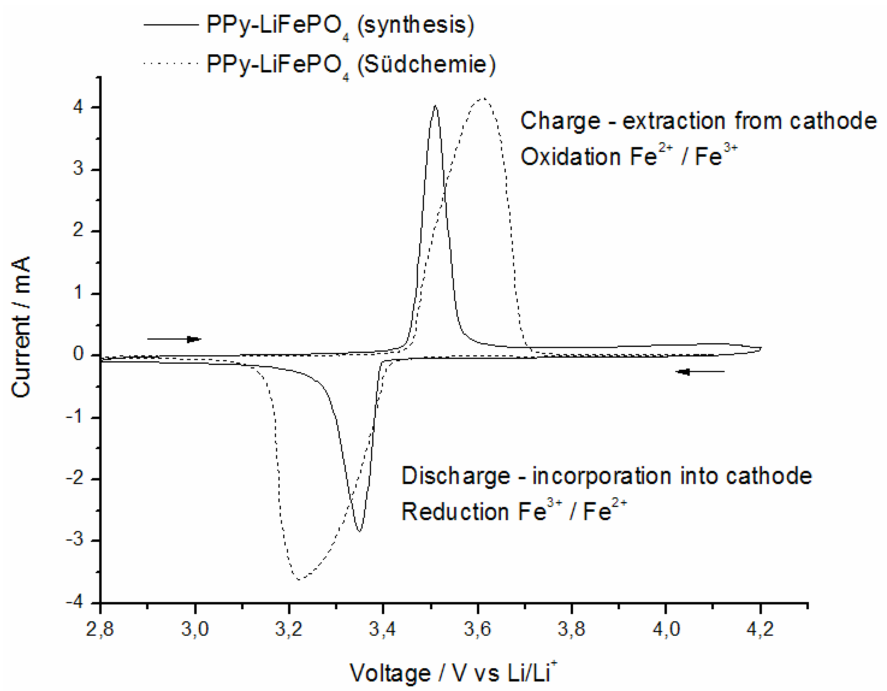

Fig. 1 *Cyclic voltammograms (3rd cycle) of PPy-$LiFePO_4$ (carbon-free $LiFePO_4$ prepared by synthesis) and PPy-$LiFePO_4$ ($LiFePO_4$ + 4% carbon – Südchemie) measured at 23 °C and with a sweep rate of 50 µV/s.*

AC impedance measurements were performed with the PPy-$LiFePO_4$ and with the PPy/PEG-$LiFePO_4$ composite electrodes. Fig. 2 shows typical Nyquist plots for our samples. Impedance on the Z´ at high frequency region represents the ohmic resistance – the resistance of the electrolyte and electrode. Impedance of the semicircle represents the migration of the Li^+ ions at the electrode/electrolyte interface through the SEI layer (high frequency) and charge transfer process (middle frequency). The resistance of electrolyte/electrode (R) is very similar because of adding Super P (carbon black) into the slurry which enables good conductivity of the electrodes. The charge transfer resistance (R_{CT}) is much lower for PPy/PEG-$LiFePO_4$ sample. The PPy/PEG coating increased the electrical conductivity between $LiFePO_4$ particles and promotes charge-transfer reaction in electrodes.

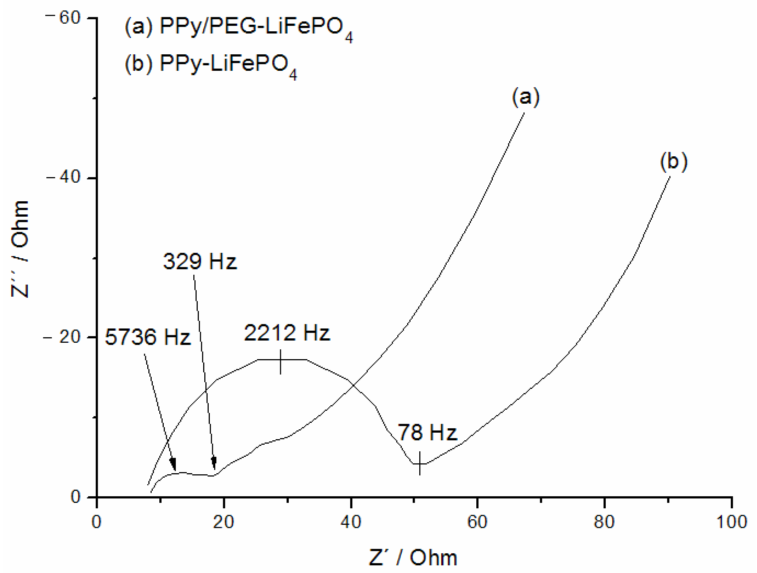

***Fig. 2** AC impedance spectra of (a) PPy/PEG-LiFePO$_4$ and (b) PPy-LiFePO$_4$ electrodes. Frequency range 10^5 Hz – 0.1 Hz.*

Conclusions

The PPy coating can improve conductivity of LiFePO$_4$ and increases specific surface area of electrodes. PPy/PEG coating allows easier access of ions and electrons to deeper lying of LiFePO$_4$ structure. AC impedance and cyclic voltammetry measurements confirmed that PPy/PEG composite polymer improved electrochemical activity and charge-transfer reaction of PPy/PEG-LiFePO$_4$ cathodes.

Acknowledgements

We acknowledge the financial support from DAAD (grant No. 03042007/SMS) and Slovak Grant Agency VEGA (grant No. 1/0043/08).

References

1. N. Ravet, Y. Chouinard, J.F. Magnan, S. Besner, M. Gauthier, M. Armand: J. Power Sources **503** (2001) 97.
2. S. Kuwabata, S. Masui, H. Yoneyama: Electrochim Acta **44** (1999) 4593.
3. G.X. Wang, L. Yang, Y. Chen, J.Z. Wang, S. Bewlay, H.K. Liu: Electrochim Acta **50** (2005) 4649.
4. D.E. Tallman, C. Vang, G.G. Wallace, G.P. Bierwagen: J. Electrochem. Soc. **149** (3) (2002) C173.
5. T. Osaka, T. Momma, K. Nishimura, S. Kakuda, T. Ishii: J. Electrochem. Soc. **141** (1994) 1994.
6. Kassim, H.N.M. Ekarmul Mahmud, L.M. Yee, N. Hanipah: Pacific J. Sci. Technol. **7** (2) (2006) 103.
7. Fedorková, H.D. Wiemhöfer, R. Oriňáková, A. Oriňák, M.C. Stan, M. Winter, D. Kaniansky, A.N. Alejos: J. Solid State Electrochem. In press (2008) DOI: 10.1007/s10008-008-0756-3.

IONIC LIQUIDS FOR SAFER LITHIUM-ION BATTERIES – ALUMINIUM CORROSION IN TFSI-BASED ILs

M. Nádherná[1], R. Dominko[2], M. Gaberšček[2], J. Reiter[1]

[1] Institute of Inorganic Chemistry of the ASCR, v. v. i., 250 68 Řež near Prague, Czech Republic
[2] National Institute of Chemistry, Hajdrihova 19, SI - 1000 Ljubljana, Slovenia

Corresponding author: Jakub Reiter (reiter@iic.cas.cz)
Phone: +420 266 172 198
Fax: +420 220 941 502

Introduction

Recently used and developed lithium-ion batteries usually contain electrolyte consisting of a mixture of organic carbonates (e.g. ethylene, diethyl and dimethyl carbonate) with dissolved lithium hexafluorophosphate or lithium bis(oxalato)borate. The presence of volatile and flammable organic solvents together with environmentally controversial $LiPF_6$ is a serious problem mainly for large-scale batteries, e.g. in the automotive industry. In this context, due to their physical properties, room temperature ionic liquids (RTILs) are a possible choice to improve safety.

Our recent work is aimed at the investigation of ionic liquids with a group of new cathode materials based on Li_2MSiO_4 (M=Fe and/or Mn) [1, 2] and graphite serving as the anode. Employing ionic liquids can overcome some drawbacks due to their main advantages:

- improved thermal stability (up to 250 – 400 °C);
- nonflammability;
- minimal vapour tension;
- minimised aluminium current collector corrosion [3].

Fig. 1 *Structures of studied ionic liquids BMMI TFSI (left) and PYR_{14}TFSI (right).*

Two ionic liquids, 1–butyl–2,3–dimethylimidazolium bis(trifluoromethanesulfonyl)imide BMMI TFSI and 1–butyl–1–methylpyrrolidinium bis(trifluoromethanesulfonyl)imide PYR_{14}TFSI (see fig. 1) with 0.7m LiTFSI or 0.5m $LiPF_6$ were successfully tested as electrolytes for Li_2FeSiO_4 cathodes operating at elevated temperature of 60°C (ref. [4]). Our interest was aimed also at the study of reactivity of ionic liquids towards aluminium current collector and blank electrodes (only binder and carbon black on the aluminium current collector). Recently these and similar electrolytes are been studied with various carbonaceous materials.

Experimental

Considering the environmental requirements, the method of ionic liquid preparation is based on direct synthesis eliminating the use of either large excess of alkylbromide or halogenated solvents in both synthetic steps. The method of preparation is based on a two–step synthesis, when bromide (BMMI Br or $PYR_{14}Br$) is prepared in high yields by direct alkylation of 1,2–dimethylimidazole or 1–methylpyrrolidine with a stoichiometric amount of alkylbromide and then the anion is substituted by bis(trifluoromethanesulfonyl)imide in aqueous solution, where these ionic liquids are insoluble.

Li_2FeSiO_4 cathode material was prepared by an optimised hydrothermal synthesis - very similar to the one described recently [5], graphite SLP-30 and SFG-6 was obtained from Timcal (Switzerland).

The initial electrochemical investigation of prepared ionic liquids and electrolytes was performed in a three–electrode arrangement with a gold or platinum (both from BASi, 1.6 mm in diameter) working electrode and a lithium counter and reference electrode. The electrochemical characteristics of half batteries were measured in vacuum–sealed triplex foil (coffee bag foil) at 60°C. All electrochemical experiments were performed in a glove box (MBraun, USA) using Autolab (EcoChemie, The Netherlands) or VMP3 (Bio–Logic, France) potentiogalvanostats.

Results and Discussions

Initially the potential limits of studied electrolytes were estimated. The measurements showed high anodic stability up to ca. 5 V vs. Li/Li^+, where the limiting factor for both BMMI TFSI and $PYR_{14}TFSI$ is the stability of the anion. The results are presented in fig. 2. In both cases, the addition of LiTFSI to neat ionic liquid enhances the stability of the ionic liquid against oxidation, consistently with previous observations by Saint [6] for lithium salts in various RTILs.

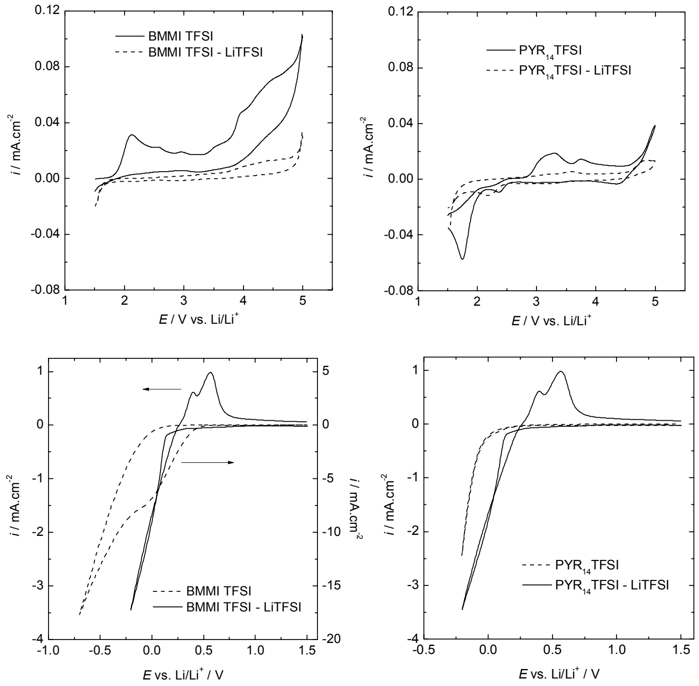

Fig. 2 *Cyclic voltammograms (1st cycle) of neat ionic liquids and IL–LiTFSI electrolyte on gold electrode at 10 mV.s*$^{-1}$ *at 20°C.*

At low potentials, reversible lithium plating and stripping was observed in both electrolytes. Used ionic liquids are chemically stable towards lithium.

The main electrochemical parameters of studied electrolytes are summarised in Table 1, when the obtained parameters allow the application of electrolytes in lithium ion batteries operating at elevated temperatures, e.g. at 60°C.

Table 1 *Specific conductivities (at 20 and 60 °C), apparent activation energy* E_A *and ideal glass transition temperature* T_0 *from the fit by VTF equation, the glass transition temperatures determined by DSC (*T_g*) and the start decomposition temperatures (*T_{dec}*) determined by TGA of studied ionic liquids and their lithium salt electrolytes.*

Electrolyte	σ (20°C) [S.cm^{-1}]	σ (60°C) [S.cm^{-1}]	E_A [kJ.mol^{-1}]	T_0 [°C]	T_g [°C]	T_{dec} [°C]
BMMI TFSI	1.6×10^{-3}	7.4×10^{-3}	6.2	–98	–81	405
BMMI TFSI – 0.7m LiTFSI	6.1×10^{-4}	4.0×10^{-3}	6.4	–88	–71	395
BMMI TFSI – 0.5m $LiPF_6$	6.7×10^{-4}	4.4×10^{-3}	7.0	–93	–70	315
$PYR_{14}TFSI$	2.1×10^{-3}	8.3×10^{-3}	6.9	–113	–90	385
$PYR_{14}TFSI$ – 0.7m LiTFSI	4.6×10^{-4}	3.3×10^{-3}	6.7	–88	–90	390
$PYR_{14}TFSI$ – 0.5m $LiPF_6$	7.5×10^{-4}	4.5×10^{-3}	10.0	–123	–88	255

The stability of Al current collector was tested at an elevated temperature of 60°C in four different electrolytes based on the present ionic liquids. As reference electrolytes, we used two conventional electrolytes with organic solvents (1M $LiPF_6$ or 1M LiTFSI in DEC:EC). To evaluate the practical use of ionic liquids with cathode materials, we first determined the electrochemical stability of aluminium current collector (Fig. 3a) and the stability of blank electrodes (Al current collector covered with carbon black (CB) / ethylene propylene diene terpolymer (EPDM) composite (Fig. 3b) in all six electrolytes.

Figure 3a shows the CV behaviour in the first cycle for all six electrolyte solutions. In the case of 1M LiTFSI solution the corrosion current was by ca. two orders of magnitude higher that in the other electrolyte solutions. The results confirm a good compatibility of RTIL-based electrolytes with the Al current collector at potentials higher than 4 V vs. Li/Li^+, even though the electrolyte solutions contained the LiTFSI salt or generally the $TFSI^-$ anion.

Testing of blank electrodes (electrodes without active material) in ionic liquids based electrolytes is not common in research reports. With the aim to evaluate possible oxidation reactions occurring on the surface of additives (binder and CB), we decided to evaluate separately the compatibility of ionic liquids based electrolyte solutions with electrodes that were prepared only from inactive additives (CB and EPDM binder in our case) pressed on the surface of Al current collector. Figure 3b shows CV behaviour in the first cycle for all six electrolyte solutions used in this study. Comparison of stability between ionic liquids electrolytes and 1M $LiPF_6$ in DEC:EC electrolyte with CB/EPDM composite shows that, at elevated temperature, the ionic liquids are much more stable in the presence of CB/EPDM composite at the potentials above 4 V vs. Li/Li^+. At potentials up to 4 V we did not detect any increase in oxidation currents in CVs with electrolyte solutions based on ionic liquids and DEC:EC 1M $LiPF_6$ electrolyte. And exactly stable voltage range from 2 V up to 3.9 V is the electrochemical window for electrochemical exploration of Li_2FeSiO_4 cathode material.

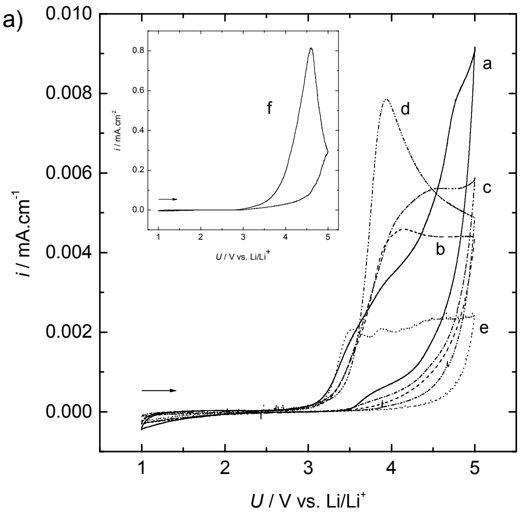

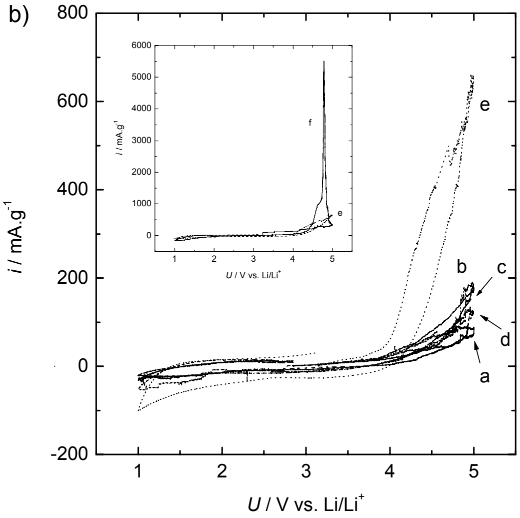

Fig. 3a *(left) Cyclic voltammograms (1st cycle) of the aluminium current collector in the six different electrolytes at 0.5* $mV.s^{-1}$ *scan rate. The current densities are normalized per surface area of Al current collector.*

Fig. 3b *(right) Cyclic voltammogram (1st cycle) of the aluminium current collector covered with CB/EPDM composite in the six different electrolytes at 0.5* $mV.s^{-1}$ *scan rate. The current densities are normalized per mass of CB/EPDM composite.*

Electrolytes: $PYR_{14}TFSI–LiTFSI$ *(a),* $PYR_{14}TFSI–LiPF_6$ *(b), BMMITFSI–LiTFSI (c), BMMITFSI–*$LiPF_6$ *(d), 1M* $LiPF_6$ *in EC–DEC (e), and 1M LiTFSI in EC–DEC (f; inset).*

Conclusions

We compared the electrochemical properties of the electrolytes based on ionic liquids Li_2FeSiO_4 with conventional organic electrolytes. The typical temperature for electrochemical testing was 60°C. The electrochemical tests against aluminium current collector showed slightly higher corrosion of Al when the ionic liquids were used, if compared to DEC:EC – 1M $LiPF_6$ electrolyte solution; however, the corrosion currents in DEC:EC – 1M LiTFSI were 100 times higher. The electrolytes based on ionic liquids were more compatible with electrode additives (a combination of Al, CB, and EPDM binder) than the conventional electrolytes.

We successfully tested the Li_2FeSiO_4 cathode material with ionic liquid-based electrolytes and achieve an excellent cycling stability at C/10 and C/2 rate with capacities of 110 $mAh.g^{-1}$ to 130 $mAh.g^{-1}$ were achieved at a C/10 cycling rate.

Acknowledgements

This work was supported by the Grant Agency of the Academy of Sciences of Czech Republic (KJB400320701), the Ministry of Education, Youth and Sports, Czech Republic (LC523 and MEB090806) and by the Academy of Sciences (Research Plan AV0Z40320502).

References

1. R. Dominko: J. Power Sources **184** (2008) 462.
2. A. Nyten, S. Kamali, L. Hänggstrom, T. Gustafsson, J.O. Thomas: J. Mater. Chem. **16** (2006) 2266.
3. B. Garcia, M. Armand: J. Power Sources **132** (2004) 206.
4. M. Nadherna, R. Dominko, D. Hanzel, J. Reiter, M. Gaberscek: J. Electrochem. Soc. **156** (2009) A619.
5. R. Dominko, D.E. Conte, D. Hanzel, M. Gaberscek, J. Jamnik: J. Power Sources **178** (2008) 842.
6. J. Saint, A.S. Best, A.F. Hollenkamp, J. Kerr, J.–H. Shin, M.M. Doeff: J. Electrochem. Soc. **155** (2008) A172.

THE LiOH AND COBALT INFLUENCE IN $Ni(OH)_2$

P. Spicak[1], T. Maca[3], M. Sedlarikova[1], J. Vondrak[2], J. Kazelle[1]

[1] Department of Electrical and electronic technology, Faculty of Electrical Engineering and Communication Technologies, Brno University of Technology
Udolní 53, 602 00 Brno, Czech Republic
[2]Institute of Inorganic Chemistry of the ASCR, v.v.i., 250 68 Řež near Prague, Czech Republic
[3]Bochemie a.s., Lidická 326, 735 95 Bohumín, Czech Republic

Corresponding author: Petr Spicak (petrspicak@seznam.cz)

Introduction

The Nickel hydroxide is an active material for positive electrode in various Ni-based rechargeable accumulators such as Ni-Cd, Ni-Zn and Ni-MH, they could be called alkaline. We were investigated the influence of cobalt or cobalt hydroxide and lithium hydroxide in electrolyte with use of Electrochemical Quartz Crystal Microbalance (EQCM) on electrochemical parameters.

Using EQCM together with potentiostat, much information can be obtained, as both the electrochemical response and accompanying mass changes can be measured simultaneously. EQCM was extensively used to investigate the effect of the conditions on the formation of the $Ni(OH)_2$ depends on $Co(OH)_2$ addition.

Nickel hydroxide $Ni(OH)_2$ is an active material widely used in batteries as the positive electrode. There is still many issues to investigate concerning the alpha phase and its transformation (ageing) during cycling. The electrochemical redox reaction of this secondary cell system is formulated according to:

$$Ni(OH)_2 + OH^- \leftrightarrow NiOOH + H_2O + e^- \quad E^0 = +0{,}490\ V/SHE \qquad (1)$$

But this is a simplified notation for a typical β/β system. The reality is much more complicated.
Bode plot shows that $Ni(OH)_2$ and the oxidized compound NiOOH can both exist in two different polymorph structures. Differing in both the organization and the inter-slab distance (distance between NiO layers).

$$\begin{tikzcd} \beta\text{-}Ni(OH)_2 \arrow[r, leftrightarrow] & \beta\text{-}NiOOH + H^+ + e^- \arrow[d, "\text{overcharging}"] \\ \alpha\text{-}Ni(OH)_2 \arrow[u, "\text{ageing, degradation}"] \arrow[r, leftrightarrow] & \gamma\text{-}NiOOH + H^+ + e^- \end{tikzcd}$$

***Fig. 1** Simplified phase diagram of nickel hydroxide*

β-$Ni(OH)_2$ has very organized structure inter-slab distance of 4,6 Å, compared to disorganized (turbostratic character) α-$Ni(OH)_2$, which has base parameter c = 8 – 9 Å depending of type and amount of intercalated anions (cations from electrolyte) and water between the layers. Oxidized compounds α and $\tilde{\gamma}$ NiOOH (oxohydroxides) has c = 4,8 Å and 7 Å, respectively. Conversion from β-NiOOH to γ occurs during overcharging and there is a problem with mechanical damaging of the electrode because of the increased inter-slab distance due to intercalated compounds and water. These mechanical changes can be avoided using α/γ couple, where the c parameter is very similar.

Cobalt hydroxide in active mass transform to CoOOH during the first (activation) charging, which supplies a conductive network for the positive electrode. Also, the addition of cobalt in $Ni(OH)_2$ lattice has been shown to increase the oxygen evolution potential, which has second beneficial effect to life of the electrode.

Nickel hydroxide in typical electrolyte which is water solution of KOH incorporated KOH on oxidation. When the LiOH is added, there is little LiOH uptake and the mass change was due to proton expulsion. Correlation of mass and charge responses as functions of LiOH concentration suggests that oxidation is accompanied by lithium ion expulsion and solvent transfer. The final effect should be higher stability during cycling.

The quartz crystal microbalance (QCM) technique is based on the inverse piezoelectric effect in which an electric field applied across a piezoelectric material (quartz crystal) induces a mechanical strain in that material. Mathematically is described by the Sauerbrey equation.

In the electrochemical application (EQCM), one electrode of the crystal also serves as the working electrode in the electrochemical cell. For thin rigid film, the change in the resonant frequency of the oscillating crystal (Δf) is proportional to the change in mass (Δm) per unit area (A).

$$\Delta f = -\frac{2 * \Delta m * f_0^2}{A * (\mu\rho)^{1/2}} \qquad (2)$$

where, f_0 is the resonant frequency of the crystal and μ is the shear modulus (2.947*1011 $g.cm^{-1}.\ s^{-2}$) and ρ is the density of quartz (2.648 $g\ .cm^{-3}$).

Experimental

The electrochemical cell consisted of EQCM (QCM200 SRS Inc.) with 5 MHz nominal resonant frequency of the crystal unit and potentiostat in three electrode connection. Working electrode was quartz resonator with deposited active material on the surface, counter electrode was platinum wire and referent electrode was Hg/HgO/1M KOH. The supporting electrolyte was 1M and 6M MOH, where M = K, Na and Li in distilled water.

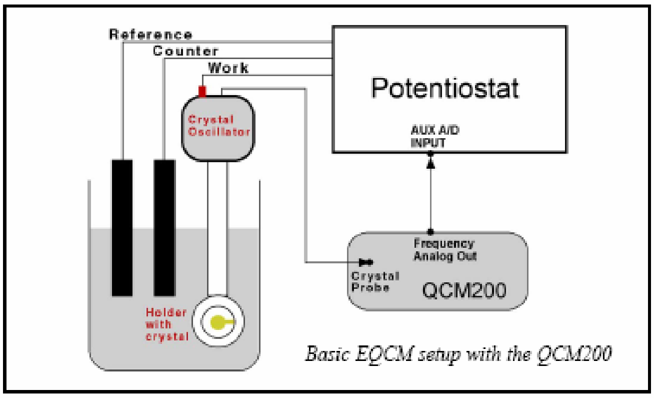

Fig. 2 *Electrochemical cell connection diagram, EQCM and potenciostat Biologic VSP*

Results and Discussion

The mass of surface film and the charge change were used to calculate molecular weight (Mw) parameter. Mw is relative mass of exchanged species between electrode and electrolyte. It indicates relative mass of exchanged species between electrode and solution.

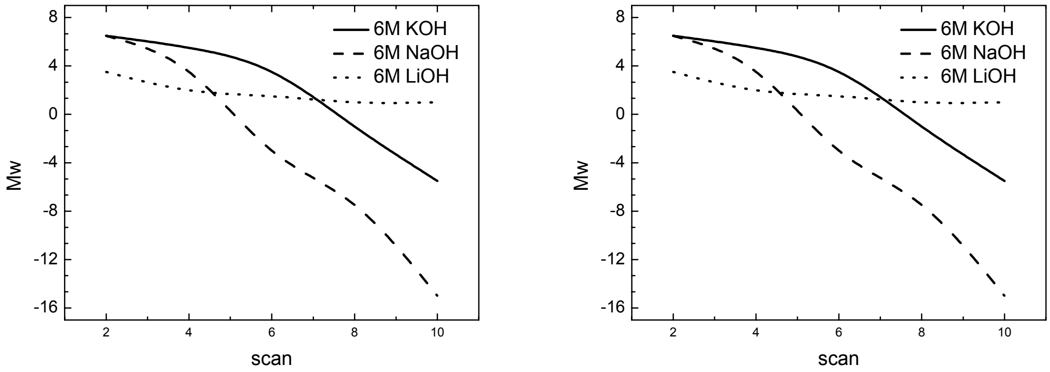

Fig. 3 *Electrodeposited $Ni(OH)_2$ from 0.1M $Ni(NO_3)_2$, in 6M electrolytes, dependence of Mw on cycle number (left), Electrodeposited $Ni(OH)_2$ from mixed Ni/Co 9/1 nitrate salt, in 6M electrolytes, dependence of Mw on cycle number (right)*

Lithium hydroxide has beneficial effect on stability of molecular weight Mw. This effect supports cobalt influence in active mass. In the case of pure nickel hydroxide, Mw decrease from 1.5 to 0.5 in the first ten cycles, in mixed layer Mw acquire values from 3.5 to 1 in the first ten cycles.

The cyclic voltammograms in dependence on added amount of cobalt salt $Co(NO_3)_2$ in mother solution describes figure 4:

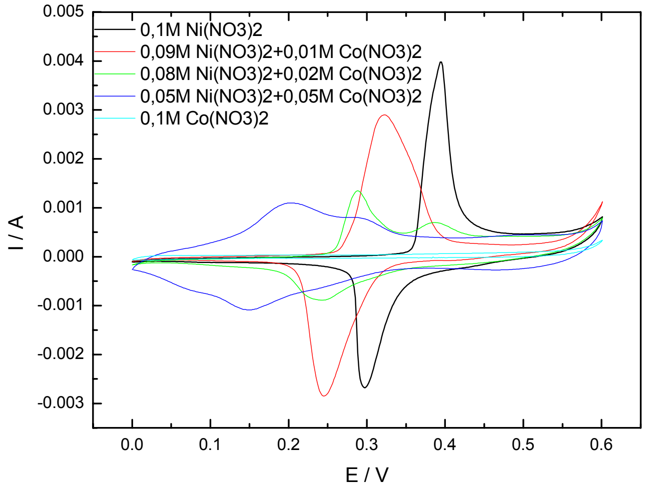

Fig. 4 *CV, different addition of cobalt nitrate*

In the case of nickel hydroxide with different addition of cobalt nitrate there is a strong dependence of position of both cathodic and anodic peak. Cobalt hydroxide moves redox potential (both peaks) into more negative values, peaks are sharper when no cobalt is added.

The mass of surface film and the charge change were used to calculate following equations:

$$M_W = F\Delta m_{film}(\Delta Q) \tag{3}$$

$$\Delta Q = \int_{t1}^{t2} i dt \tag{4}$$

where F stands for the Faraday constant (96500 C mol^{-1}), and t1 and t2 defined the integration time interval (between two successive data acquisitions), Q is charge (C). Comparing these two formulas a quantity Mw can be obtained. Molecular weight Mw represents the relative weight of mass exchanged between electrode and electrolyte. The individual components of this Mw are very difficult to separate and mathematically describe. We can consider hydrogen cations H^+, hydroxide anion OH^- or water H_2O, alkaline cations from electrolyte M^+ (where M= K, Na or Li) and anion from precipitation, usually $(CO_3)^{2-}$ or NO^{3-}.

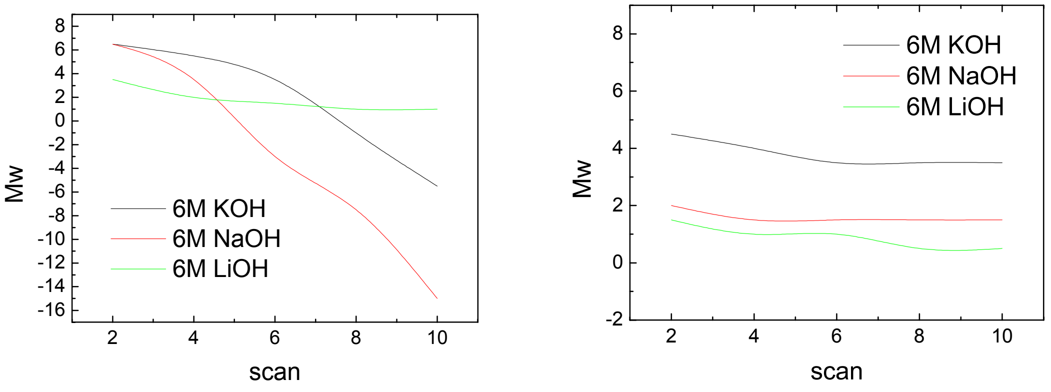

Fig. 5 *Mw in 6M KOH in first 10 cycles, mother solution 0,1M Ni(NO$_3$)$_2$ (left) and 0,09M Ni(NO$_3$)$_2$ + 0,01M Co(NO$_3$)$_2$ (right)*

Figure 5 shows dependence of Mw during cycling of $Ni(OH)_2$ in 6 M KOH. There is a difference in characteristics. When cobalt nitrate (10 molar %) is added into solution (fig. 5 right), Mw has stable value in first 10 cycles, when no cobalt is added, Mw decreasing more rapidly (fig. 5 left). This decrease indicates, that structure of α-$Ni(OH)_2$ is quite unstable in strong alkaline medium and transform into beta phase.

Conclusions

The addition of cobalt in active mass in nickel positive electrode has significant influence on electrochemical characteristics. Improved electrical conductivity and higher stability in alkaline solution (6M) was observed. Molecular weight Mw is more stable, this indicates that mass exchange between electrode and electrolyte is stable and phase transformation is slower. Lithium hydroxide has a beneficial effect on stability of molecular weight Mw. This effect support cobalt influence in active mass. In the case of pure nickel hydroxide.

Acknowledgements

Grant Agency of Czech Republic (grant No. MSM0021630516)
Bochemie, a.s.

References

1. P. Bernard, C. Gabrielli, M. Keddam, H. Takenouti, J. Leonardi, P. Blanchard, Electrochim. Acta 36 (1991) 743
2. M. Wehrens-Dijksma: Electrochimica Acta 51 (2006) 3609–3621
3. T. Ohligschlager, G. Schwitzgebel: Phys. Chem. Chem. Phys., 2001, 3, 5290-5296
4. ŠPIČÁK, P.; VONDRÁK, J.; SEDLAŘÍKOVÁ, M.; SVOBODA, V. Coinsertion of Water and Hydrogen in Transition Metal Oxides and Hydroxides Studied by QCM. In 213th Meeting (c) 2008 The Electrochemical Society isbn 9781605601816. Phoenix, USA: ECS, 2008. s. 127 (1 s.).
5. VONDRÁK, J.; SEDLAŘÍKOVÁ, M.; VELICKÁ, J.; ŠPIČÁK, P.; SVOBODA, V.; KAZELLE, J. Insertion of cations into WO3 investigated by QCM techniques. Journal of Solid State Electrochemistry, 2007, roč. 11, č. 10, s. 1459-1462. ISSN: 1432-8488.

STABILIZATION EFFECT OF MAGNESIUM ADITIVES IN NICKEL HYDROXIDE

J.Vrbický[1], *J. Vondrák*[2], *M. Sedlaříková*[1]

[1] *Institute of Electrotechnology, Technical University of Brno, 602 00 Brno*
[2] *Institute of Inorganic Chemistry AS CR, 250 68 Řež, Prague*

Corresponding author: Jiří Vrbický (xvrbic00@stud.feec.vutbr.cz)
Phone: +420541146112
Fax: +420541146147

Introduction

Nickel hydroxide is the basic material for positive electrode of alkaline accumulators as Ni-Cd, Ni-MH and Ni-Fe. The three modification of nickel hydroxide is known, alpha, beta and gama.

The α-form has large interlayer space of 0,76nm, whereas β-form offers layers which are just apart by 0,46nm. Upon oxidation the a-nickel hydroxide converts to γ-nickel oxyhydroxide and β-nickel hydroxide to β-nickel oxyhydroxide. The theoretical specific capacity of α-γ couple is 456 mAhg−1 as compared to 289 mAhg−1 for β-β. It is based on 1.6 and 1.0 electron reversibly exchanged during the redox reactions.

Alpha nickel hydroxide is stable in normal conditions, but in alkaline electrolytes is unstable and turns into β- $Ni(OH)_2$. When β- $Ni(OH)_2$ is overcharged to γ- NiOOH, the volume expansion is increasing so it occurs many construction and durability problems, it also solves the electrode made of α- $Ni(OH)_2$.

Possibility to prepare α- $Ni(OH)_2$ more stable in strong alkaline media is to add some other metals such as Al, Fe, Mn, Co and others. The aluminium doped α- $Ni(OH)_2$ was tested in various KOH electrolyte concentrations.

Experimental

The samples of α-form nickel hydroxide were deposited on nickel substrate. The nickel substrate was cleared by nitric acid with hydrogen peroxide. The cleaning process ensures constant quality of surface, so the electrochemical changes of nickel hydroxide can be observed.

The solution for electrodeposition consists 0,1M Ni(NO3)2. The solution with magnesium consists 0,05 M Ni(NO3)2 and 0,05 M Mg(NO3)2. Electrodeposition was preformed by current 1mA for 300s.

The electrolyte for testing was 6M KOH.

The samples were measured by cyclic voltammetry. Voltammetric measurements were performed vith Pt counter electrode and Hg/HgO reference electrode. For each sample were taken 60 scans.

Results and discussion

The charging and discharging of nickel hydroxide substitued by magnesium is very similar to charging and discharging of pure nickel hydroxide.

Pure nickel hydroxide degrades from α modification to β modification completely after 60 cycles (see Fig.1).

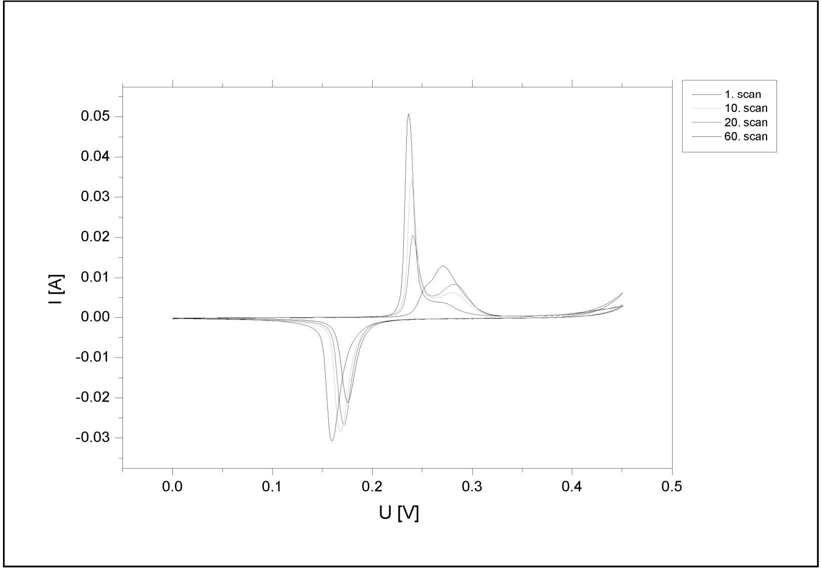

***Fig.1**: Voltammograms of pure Ni(OH)$_2$*

Nickel hydroxide with magnesium aditive degrades from α modification to β modification little slowly, and after 60 cycles is not yet fully changed to β (see Fig.2). Magnesium aditive has very small effect on nickel hydroxide stability.

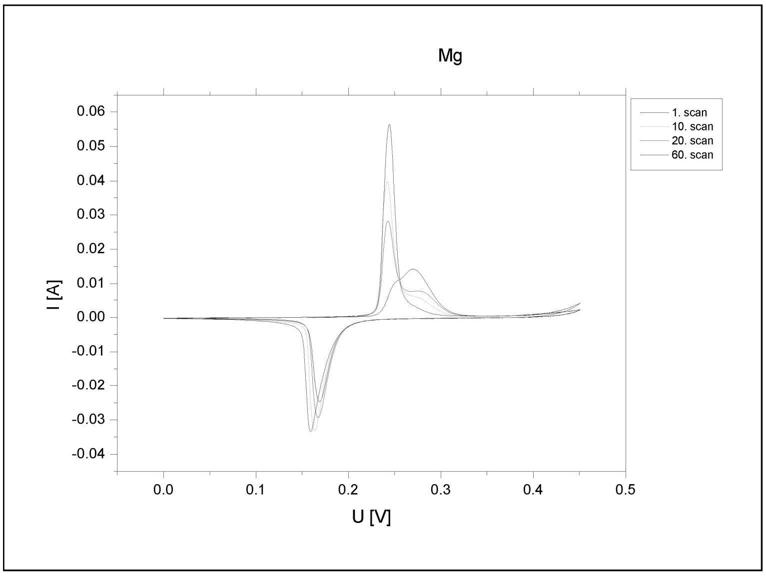

***Fig.2**: Voltammograms of Ni(OH)$_2$ with Mg aditive*

Conclusion

The capacity and stability of magnesium substituted α- $Ni(OH)_2$ were investigated. Magnesium has no effect on nickel hydroxide electrochemical capacity. The effect of magnesium on stability is very low, the magnesium improves stability a little, but not more than 10 percent. This effects are not useable in commerce production.

Acknowledgment

The investigations were supported by:
Ministry of Education of Czech Republic, Project MSM0021630516

References

1. M.A. Fetcenko , S.R. Ovshinsky, B. Reichman, K. Young, C. Fierro, J. Koch, A. Zallen, W. Mays, T. Ouch: *Recent advances in NiMH battery technology,* Journal of Power Sources *165 (2007) 544–551*
2. Rand, D.A.J., Woods, R, Dell, R.M.: *Batteries for electric vehicles* – Tauton, Somerset, England, Research studies press, 1998
3. Falk, S.U., Salkind, A.J.: *Alkaline storage Batteries* - New York, The electrochemical society INC., 1969
4. GANESH-KUMAR, V., BAET,S. W., LEE, J. S., NAM, K. W., KIM, K. B., Contraction of Alpha-nickel hydroxide Layers by Excess Coulombic Attraction of Anions

UTILIZATION OF ALPHA NICKEL HYDROXIDE IN ALKALINE ACCUMULATORS

T.Máca[1], L.Nezgoda[1], V. Špachman[1], J.Vondrák[2], M.Sedlaříková[3], P.Barath[3], J.Vrbický[3], P.Špičák[3], T.Jirák[3]

[1] Bochemie Inc., R&D Department
[2] Institute of Inorganic Chemistry AS CR, 250 68 Řež near Prag
[3] Institute of Electrotechnology, Technical University of Brno, 602 00 Brno

Corresponding author: Tomáš Máca (tomas.maca@bochemie.cz)

Introduction

Nickel hydroxide is used as an electrochemically active component of accumulator masses for positive electrode of Ni-Cd, Ni-MH and Ni-Zn alkaline accumulators.

From morphological point of view there are two basic versions of nickel hydroxide known as crystallographic modifications, alpha phase and beta phase. The latter having regularly arranged structure of brucite type (with basal lattice parameter c = 4,6 Å and density 3,85 $g.cm^{-3}$) is in substance pure simple $Ni(OH)_2$. Compactness of perfectly crystallized pure beta $Ni(OH)_2$ interferes its electrochemical activity. Hence, the lattice must always involve a failure rate. Strongly defective crystals formed from faulty nucleus growth will induce significantly facilitated H^+ protons diffusion during cycling process. Such particles are signed as badly crystallized beta hydroxide. In accordance with Bode´s diagram , intensive overcharging of beta systems leads to „low-density“ gamma phase which includes even hydrated oxides of tetravalent nickel. However, presence of such compounds is very temporal because of their enormous instability and easy decomposition tendency accompanied by oxygen evolution. This issue is reflected in discharge curves as rapid initial cell voltage falling after finished charging without any capacity contribution.

Alpha nickel hydroxide attains superior performance compared to commonly produced beta hydroxides in consequence its transition ability to nickel in tetravalent state (although partially) in stabilized forms and thereby gain higher capacity from the same nickel content.

Alpha nickel hydroxide is rather more complicated intercalate compound comprising of variable stages of hydration. Compound with idealized composition and simplified formula $3Ni(OH)_2 .2H_2O$ (specific weight is about 2,5 $g.cm^{-3}$) is quite unstable in alkaline medium and easily transforms to β-$Ni(OH)_2$. Therefore, it is necessary to find solution of structure stabilization. Hence, wide group of layered double hydroxides (LDH) with partially substituted nickelous ions by suitable trivalent stabilizing cations (most often Al^{3+}) is considered to be alpha nickel hydroxide. Addition of aluminium just seems to be just most frequent doping according to most of published reports. Gamma phase formed by charging of alpha nickel hydroxide represents a mixture of trivalent and tetravalent nickel as hydrated oxides where contained tetravalent nickel is stabilized by corresponding amount of intercalated anions (including OH^- anions from the electrolyte) to ensure charge equilibrium. For that reason, electrochemical reactivity of alpha nickel hydroxide should overcome that of β-$Ni(OH)_2$.

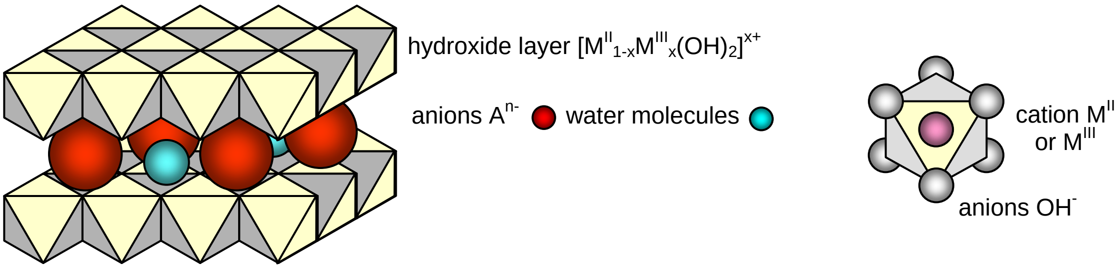

Fig.1 *Layered structure of hydrotalcite type compounds*

The unquestionable advantage of the „α/γ“systems is that material can be electrochemically cycled without having perceptible volumetric changes. The outstanding feature is the effectual overcharging tolerance as well. It is caused by very close lattice constants for both of the redox couple components. Despite all of the advantages which are potentially offered by using of alpha nickel hydroxide in alkaline accumulators there is a fundamental problem if is this system able to provide such parameters in the long term condititions. There is obvious inclination that there is a crystal-phase transformation toward more stable and termodynamically preferable beta form in general alpha phase definition according to Bode´s diagram.

Experimental

Different methods can be used to synthetize alpha nickel hydroxide. We have examined several ways of preparation. Significant differences have been proved in achieved performances of obtained samples although all of them represent structure of alpha phase according to recorded XRD patterns.

The electrochemical test of $Ni(OH)_2$ electrodes

The electrochemical behavior of the synthesized alpha nickel hydroxides in Ni-Cd cells in 6M KOH electrolyte was studied. For the investigations on all of nickel hydroxide samples, pressed electrodes were used in pocket version. The electrodes were constituted of an activated mixture of nickel hydroxide and graphite which gives improved electronic conductivity. Such active material using β_{bc}-$Ni(OH)_2$ produced by Bochemie Inc. represents its commercial accumulator mass with trade name „NICOL G“ and it has served as a comparative mass/reference sample in carried out tests.

The cycling process at the 0,17 C rate is typically used in our laboratory for testing of the type of accumulator mass. It consists in galvanostatically charging and discharging continuously the cell with short relaxation between the various steps. At the very beginning of the cycling, four cycles of "formation" of the electrode are performed at the same rate (0,17 C), including strong overcharging of the cell in the first cycle (20 h successfully). The overcharging corresponds to 200% of the theoretical capacity for common accumulator mass NICOL G.

Results and Discussion

Electrochemical measurements of discharge capacity

Al-substituted alpha nickel hydroxide

Maximal discharge capacity provided by active materials based on Ni-Al LDH is apparent in cycle life records for our prepared and evaluated types of alpha nickel hydroxide. However, having been attained during formation period the discharge capacity began to drop rapidly.

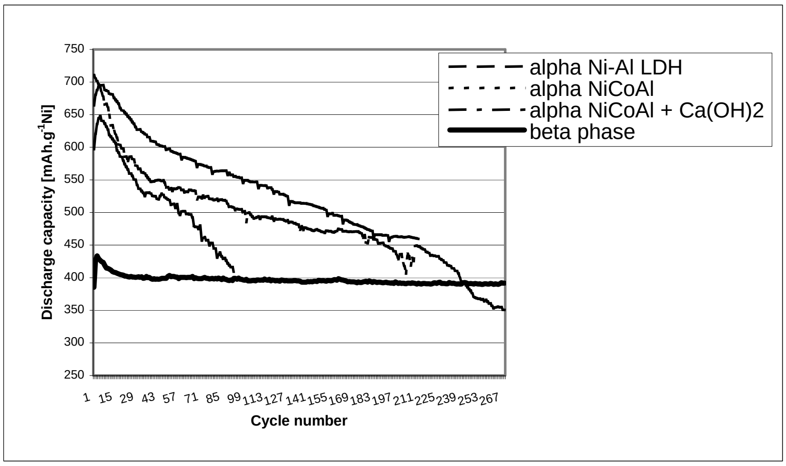

Fig. 2 *Performance of Ni-Al LDH type of alpha nickel hydroxide related to nickel content*

Mn-substituted alpha nickel hydroxide

On the other hand, discharge capacity of active materials based on Ni-Mn LDH in dependence on cycle numbers fast faded immediately after cycling process had been started. The performance loss was early stopped and kept steady values (corresponding to the beta hydroxide) in relatively long time.

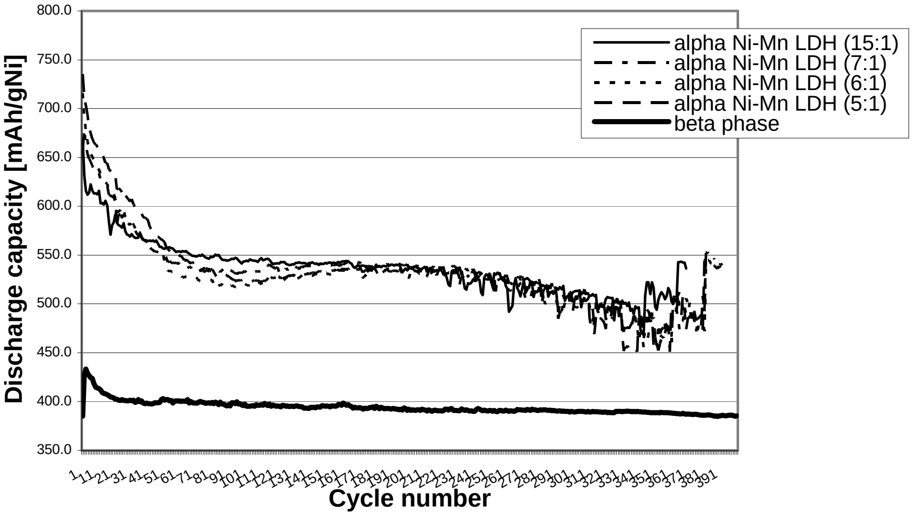

Fig. 3 *Performance of Ni-Mn LDH type of alpha nickel hydroxide related to nickel content*

EQCM measurement for Ni-Al LDH

Very good reversibility of the electrode processes including cycled Al-substituted alpha nickel hydroxide is observed from the beginning. However, the material participation in redox reactions occuring in cycled cell drastically decreses with increasing cycles. The residual participating indicates that best part of Al-substituted alpha nickel hydroxide (about 90%) remains inactive.

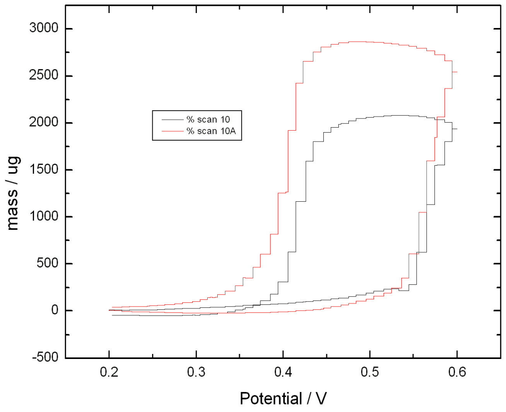

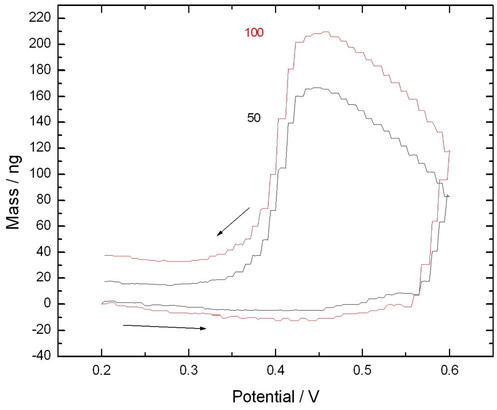

Fig. 4 (left) *Massogram for scan 10*
Fig. 5 (right) *Massogram for scans 50 and 100*

Conclusion

All prepared samples of nickel hydroxide have been proved to be alpha modification in this work. Electrochemical tests of the samples have been made. Despite most of the papers regarding the alpha nickel hydroxide we haven´t obtained any results like the published ones. We have disclosed causes, why the capacity of the measured samples faded, but we haven´t found yet, how to prevent from this phenomenon.
sDisclosed reasons of performance falling:

Ni-Al LDH

Passivation of higher-valent nickel fast occurs without being transformed to the beta phase. Material becomes isolated in charged state and thereby can not be completely discharged. The effect accelerates in several initial cycles. We have not elucidated exact mechanism of the passivation yet and our work on solving that continues.

Ni-Mn LDH

Phase separation – beta nickel hydroxide is formed from initial alpha structure. The transformation is also considerably sped. The active material becomes better reversible and behaves as common beta phase.

References

1. Y.L. Zhao, J.M. Wang, H. Chen, , T. Pan, J.Q. Zhang, C.N. Cao, International Journal of Hydrogen Energy 29 (2004) 889 – 896; Electrochimica Acta 50 (2004) 91–98
2. Mufit Akinc, Nathalie Jongen, Jacques Lemaitre and Heinrich Hofmann, Journal of the European Ceramic Society 18 (1998) I559- I564
3. Jinxiang Dai, Sam F.Y. Li , T. Danny Xiao, Donald M. Wang, David E. Reisner, Journal of Power Sources 89_2000.40–45
4. Yueming Li, Weiyang Li, Shulei Chou, Jun Chen, Journal of Alloys and Compounds xxx (2007) xxx–xxx
5. R. Acharya, T. Subbaiah, S. Anand, R.P. Das, Materials Chemistry and Physics 81 (2003) 45–49
6. V. Ganesh Kumar, N. Munichandraiah, P. Vishnu Kamath , A.K. Shukla, Journal of Power Sources 56. (1995) 1 I l-l 14
7. Wei-Kang Hu, Xue-Ping Gao, Dag Noréus, Trygve Burchardt, Nils K. Nakstad, Journal of Power Sources 160 (2006) 704–710
8. Susana I. Co´rdoba de Torresi, Kellie Provazi, Marcos Malta, and Roberto M.Torresi, *Journal of The Electrochemical Society*, 148 (10) A1179-A1184 (2001)
9. Michael Rajamathi, P. Vishnu Kamath, Journal of Power Sources 70 (1998) 118–121
10. Xian-Zhu Fu, Xing Wang, Qing-Chi Xu, Jun Li, Jeff-Qiang Xu, Jing-Dong Lin, Dai-Wei Liao, Electrochimica Acta 52 (2007) 2109–2115
11. C.Y. Wang, S. Zhong, K. Konstantinov, G. Walter, H.K. Liu, Solid State Ionics 148 (2002) 503– 508

10th ABAF

BRNO 2009

Advanced Batteries, Accumulators
and Fuel Cells

Methods

SURFACE TEXTURES AND THEIR ANALYSIS

E. Svoboda, K. Maňas, R. Dvořáková

Department of Mechanical Engineering, University of Defence in Brno, Kounicova 65,
662 10 Brno, Czech Republic

Corresponding author: Karel Maňas (karel.manas@unob.cz)
Phone: +420 973443325

Abstract: This contribution describes 2D and 3D systems surface texture analyses, compares and assesses 3D system used in research and production practice.

Keywords: *Surface analysis, 2D surface profile, 3D surface topography, surface structure*

Introduction

Current development trends in surface shape or texture analysis are focussed on a wider use of 3D measuring system. The acquisition of the spatial characteristics of engineered surfaces is based on the parameters measured on the series of surface profiles, presenting new possibilities in the texture analysis, unobtainable in 2D measurement methods. This detailed spatial surface profiling appears valuable.
Measurement results have proved that 3D surface profiling system provides more objective surface characteristics, allowing detection and description of the component texture variations, but also showing difference in the values of parameters obtained from the area and from the profile. This article contributes to the above problems by comparing selected roughness parameters of some specific 2D and 3D surfaces.

Experimental

Considering the practice of developing engineered surfaces and their resultant performance, the spatial surface texture characteristics are very important. The spatial data may be useful in checking the surface texture development statuses and production conditions. The 3D surface analysis allows a substantially wider data set on the texture, enabling thus to assess also defects in the surface that are not available in 2D measurement mode.

The assessment capabilities of a defined and applied surface texture in terms of the current measurement trends have the following distinctive features:
- 2D surface – the assessment of parameters on the profile
- 3D surface – the assessment of parameters on the area.

Surface texture measurement conditions

The roughness measurements were carried out on roughness standards (standards were machined by grinding, roughness nominal value Ra 0.05 μm, 0.1 μm, and 0.2 μm; lathe turning, roughness nominal value Ra 0.2 μm a 0.4 μm), and on three assorted planes on real components machined by milling and grinding.

A Talysurf CLI 1000 was used for the surface analysis (3D), and an inductive scanning instrument with 522μm range and 8nm response to check the absolute roughness (2D), a Surtronic 25 profiler for the roughness checking method (2D) with an inductive scanning of 10μm or 100μm range.

An area of 4.5mm x 2.5mm stepped by 0.5 μm in both the measuring axes was used for the 3D surface analysis. A roughness absolute method (2D) was carried out on 3 profiles chosen at random on the surface being measured and analysed. 3 individual profiles in parallel were measured by a relative method on a surface corresponding to that used for 3D system measurement.

A Talymap Platinum (3D) or a Talyprofile Platinum (2D) was used for the assessment of the roughness data from the measured profiles by a programme based on standard methods with the following steps: level and align the surface or profile, remove the shape, select the apparatus sensitivity (zones), use a filter between non-filtered surface or profile, visualize 3D surface or 2D profile and calculate the area or profile parameters.

Different parameters were applied in the surface analysis according to [2] and [3], of which only the following are dealt with in this contribution:

Sa – the surface mean deviation;
Sa_P – the basic surface mean deviation – after levelling and removing the shape;
Sa_R – the surface roughness mean deviation – after filtering (roughness designate cut-offs – 0.25mm or 0.8mm), i.e. the basic surface against surface roughness and waviness;
Ra – the profile roughness mean deviation;
Ra_{abs} – the profile roughness mean deviation – measured by the absolute method;
Ra_{rel} – the profile roughness mean deviation – measured by the relative method.

Parameters on the surface roughness profile agree with Standard ČSN EN ISO 4287.

Results and Discussion

As the measurement duration of the parameters in 3D surface (3D analysis) Sa is for hours, they were measured only once. The Ra parameters were measured on the same surface, but at least on three cut-offs in parallel, and an average value and standard deviation was calculated from them.

***Table 1** Results of the roughness standard measurement*

Roughness standard		**Surface roughness values**			
Method	Nominal value	Sa_P [μm]	Sa_R [μm]	Ra_{abs} [μm]	Ra_{rel} [μm]
Grinding	0.05 μm	0.377	0.295	0.070 ± 0.003	0.053 ± 0.010
	0.1μm	0.417	0.322	0.129 ± 0.007	0.135 ± 0.032
	0.2 μm	0.388	0.293	0.172 ± 0.003	0.184 ± 0.013
Lathe turning	0.2 μm	0.481	0.364	0.203 ± 0.005	0.212 ± 0.010
	0.4 μm	0.502	0.429	0.357 ± 0.010	0.415 ± 0.004

Parameters Sa in all the textures have higher values than Ra parameters. The values of roughness parameters Ra of the standard by the absolute method are lower than those attained by the relative method except for the standard with Ra=0.05 μm (Table 1). But this thesis is void in measuring real surfaces (Table 2); the values are either lower (grinding) or vary (milling), as the surface texture type may be.

Table 2 *Results of the roughness measurement on the specimen surface textures*

Surface texture		**Surface roughness values**			
Production method	Specimen	Sa_P [μm]	Sa_R [μm]	Ra_{abs} [μm]	Ra_{rel} [μm]
Grinding	1 and 2	0.626/0.623	0.431/0.371	0.207 ± 0.016/ 0.249 ± 0.063	0.219 ± 0.011/ 0.348 ± 0.052
Face milling and re-grinding	1 and 2	0.675/0.513	0.483/0.417	0.256 ± 0.014/ 0.234 ± 0.008	0.216 ± 0.007/ 0.314 ± 0.006
	1 and 2	0.464/0.465	0.371/0.402	0.271 ± 0.005/ 0.234 ± 0.008	0.252 ± 0.068/ 0.265 ± 0.027

The current measurement technology allows surface texture measurements stepped from 0.5 μm, what may be the cause of differences in 2D roughness values, because a smaller scanning step will definitely result in higher profile peaks and valleys, causing higher value of Ra, and of course even Sa in the roughness measurement.

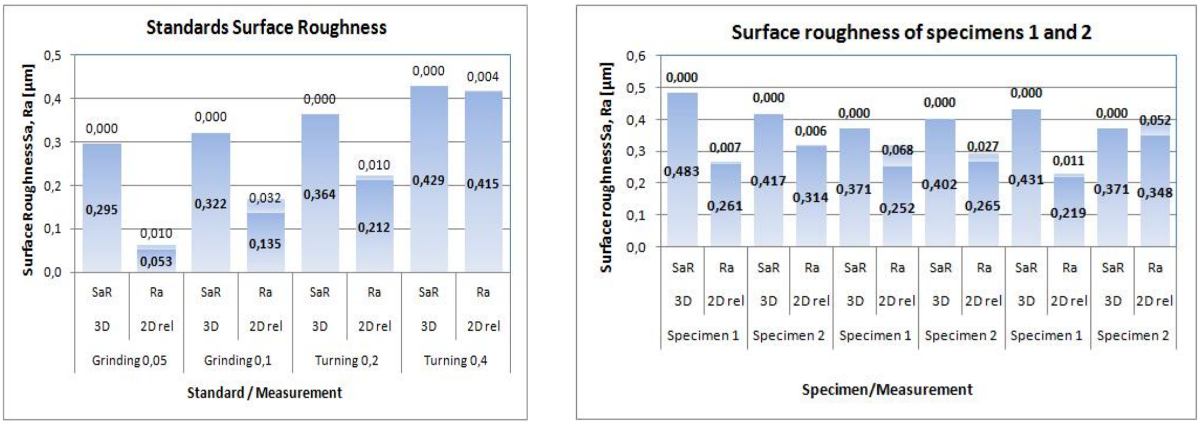

Fig. 1 *Roughness Sa and Ra on standards and specimens 1 and 2*

It follows from 2D and 3D comparison above that Sa roughness parameters have attained higher values, evidently in all the cases. These differences are even more apparent with the roughness standards than with the specimens. Reference [1] gives relation between 2D and 3D surface roughness parameters as:

$$\mathbf{Sa = (0.79 \div 1.21)\ Ra} \qquad [1]$$

This relation obtained by a classic relative profiler from the measurement of 50 profiles in parallel, spaced by 50μm on the surface with single discrete points stepped by 5μm was not approved in these results.

The standard/specimen roughness measurements results give the relation between Sa_R and Ra parameters in the following form:

$$\mathbf{Sa_R = (1.20 - 4.20)\ Ra \quad / \quad Sa_R = (1.07 - 2.08)\ Ra} \text{(See Fig. 2)} \qquad [2, 3]$$

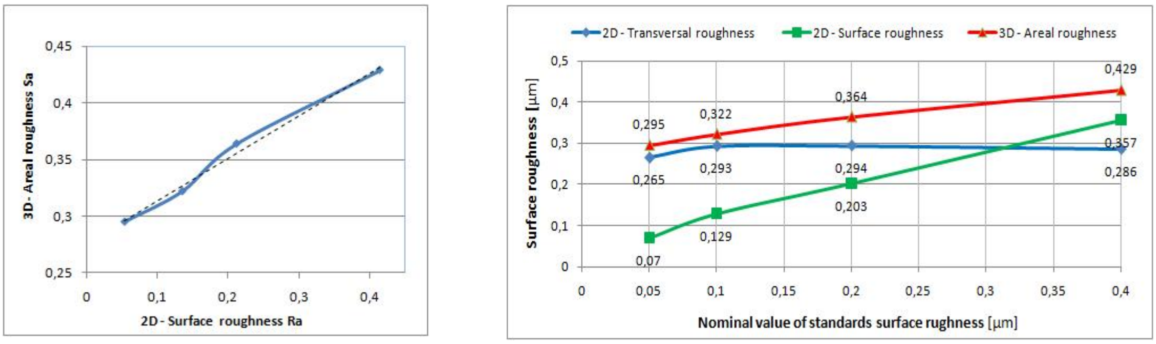

Relation between Ra and Sa_r *Relations between roughness standards*

Fig. 2 *Relations between the individual roughness parameters*

It is generally assumed that lower conversion factor values are applied to higher roughness values, and higher conversion factor values are used to lower hardness values Ra. See relations [2, 3].

In conversion relations [2, 3] the factors in the standards are higher than those in specimen surfaces. The higher factor values may have resulted from the value of roughness standards, which is lower. However, standards should have their factor values higher also due to the transversal roughness (in the cutting tool direction), ranging from Ra = 0.265µm up to 0.294µm, i.e. higher in roughness standards than in the nominal roughness. Therefore the transversal roughness values contribute to higher values of the area roughness in all standards below Ra = 0.2µm.

Conclusions

The 3D surface topography has significantly enhanced assessment capabilities of engineered surfaces. It provides a primary view of the relation between 2D and 3D parameters (Sa and Ra) for the frequently used parameters. Theoretically, it may be assumed that the planar surface parameters will attain higher values, however the 3D surface topography data will enhance their functional performance assessment. The above conversion relations offer new approach to a more detailed specification of surface texture acquired with the up-to-date tools in their assessment.

Acknowledgements

This contribution was developed for the research intent UO FVT 0000404 "Research and development of modern materials and technologies for the military equipment applications" and SV K216 "Application of surface technologies in the production of special equipment", and forms a detail issue in these research activities.

References

1. Novák Zdeněk, Mikrogeometrie povrchu – 3. část (Surface Micro-geometry – Part 3). MM Průmyslové spektrum, 1999, No. 11, pp. 46 -47. ISSN 1212-2572
2. ČSN EN ISO 4287 – Geometrical Product Specifications (GPS) – Surface Texture: Profile Method – Terms, Definitions and Surface Texture Parameters
3. ČSN EN ISO 4288 – Geometrical Product Specifications (GPS) – Surface Texture: Profile Method – Rules and Procedures for the Assessment of Surface Texture

AUTOMATIC DETECTION OF DEFECT IN SOLAR CELLS

J. Vanek, A. Vesely, J. Stencel, J. Dolensky

Department of Electrotechnology, Brno University of Technology,
Faculty of Electrical Engineering and Communication
Udolni 53, 602 00 Brno, Czech Republic

Corresponding author Jiri Vanek (vanekji@feec.vutbr.cz)
Phone: +420541146122
Fax: +420541146147

Introduction

The output data of defect detection method like LBIC or elecroluminiscence image contains lots of information about contacts structure and about the defects in the area of solar cell. This data can be analyzed by operator in image form or can be analyzed by computer system in row form.

Image Analyzing - Thresholding

The method used to preparing analyzed data for comparing in image processor is thresholding used for image analyzing. During the thresholding process, individual data's point (pixel in an image) are marked as "object" pixels if their value is greater than some threshold value (assuming an object to be brighter than the background) and as "background" pixels otherwise. This convention is known as threshold above. Variants include threshold below, which is opposite of threshold above; threshold inside, where a pixel is labeled "object" if its value is between two thresholds; and threshold outside, which is the opposite of threshold inside. Typically, an object pixel is given a value of "1" while a background pixel is given a value of "0." Finally, a binary image is created by coloring each pixel white or black, depending on a pixel's label.

Adaptive Thresholding

Thresholding is called adaptive thresholding when a different threshold is used for different regions in the image. This may also be known as local or dynamic thresholding .

The key parameter in the thresholding process is the choice of the threshold value (or values, as mentioned earlier). Several different methods for choosing a threshold exist; users can manually choose a threshold value, or a thresholding algorithm can compute a value automatically, which is known as automatic thresholding (Shapiro, et al. 2001:83). A simple method would be to choose the mean or median value, the rationale being that if the object pixels are brighter than the background, they should also be brighter than the average. In a noiseless image with uniform background and object values, the mean or median will work well as the threshold, however, this will generally not be the case. A more sophisticated approach might be to create a histogram of the image pixel intensities and use the valley point as the threshold. The histogram approach assumes that there is some average value for the background and object pixels, but that the actual pixel values have some variation around these average values. However, this may be computationally expensive, and image histograms may not have clearly defined valley points, often making the selection of an accurate threshold difficult. One method that is relatively simple, does not require much specific knowledge of the image, and is robust against image noise, is the following iterative method:

1. An initial threshold (T) is chosen, this can be done randomly or according to any other method desired.
2. The image is segmented into object and background pixels as described above, creating two sets:
   i. $G_1 = \{f(m,n):f(m,n)>T\}$ (object pixels)
   ii. $G_2 = \{f(m,n):f(m,n)<= T\}$ (background pixels) (note, f(m,n) is the value of the pixel located in the m^{th} column, n^{th} row)
3. The average of each set is computed.
   i. m_1 = average value of G_1
   ii. m_2 = average value of G_2
4. A new threshold is created that is the average of m_1 and m_2
5. T' = (m1 + m2)/2
6. Go back to step two, now using the new threshold computed in step four, keep repeating until the new threshold matches the one before it (i.e. until convergence has been reached).

Fig. 1 *Usage of threshodling for image preparation for analyzing.*

This iterative algorithm is a special one-dimensional case of the k-means clustering algorithm, which has been proven to converge at a local minimum—meaning that a different initial threshold may give a different final result.

Solar cells image analyzing

The output data of defect detection method like LBIC or elecroluminiscence image contains lots of information about contacts structure and about the defects in the area of solar cell. This data can be analyzed by operator in image form or can be analyzed by computer system in row form. It is important to analyze data only which are contain information about defects. So in first stem must be made differential image of the new image and reference image. This process masks the structure of contacts which is no more analyzed.

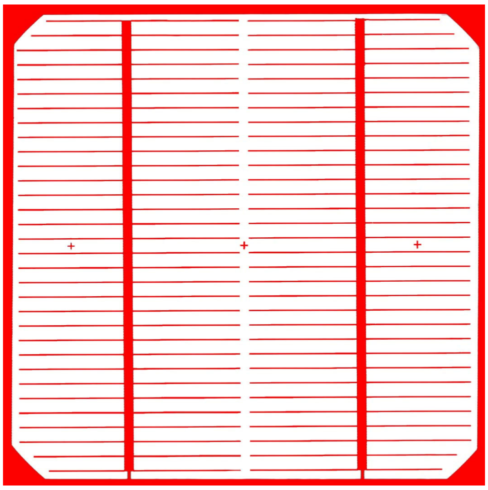

Fig. 2 *Data applied on the images to mask contact grid*

Then on the image is applied the thresholding and the defects are analyzed by image processor and compared with known defects shape and characters.

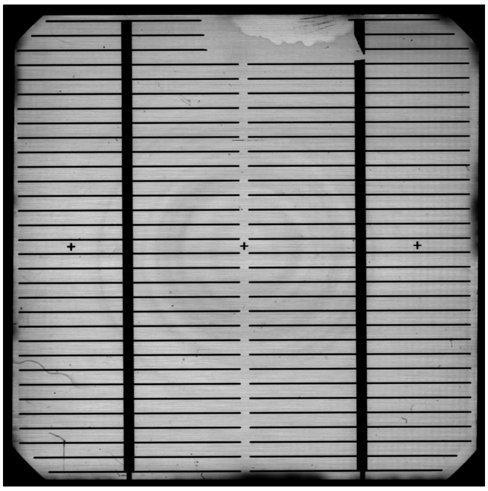

Fig. 3 *Analyzed LBIC images (displayed in 256 gray-scale)*

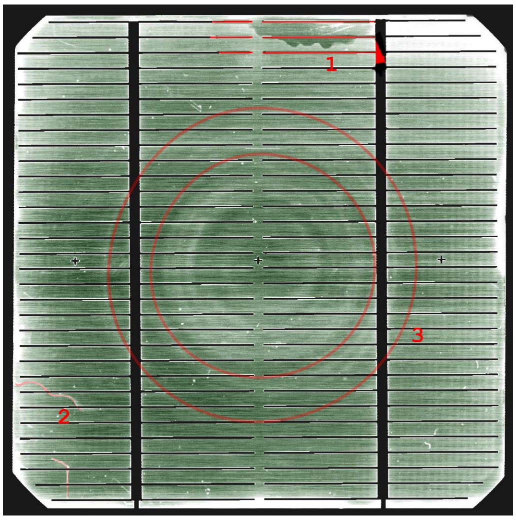

Fig. 4 *Illustration of detected defects – 1. missing contacts, 2. a random curves (scratches and dust), 3. a circles (Oxide in swirl defect)*

The image processor compare the know defects shapes and structures with gained images. We are able to detect missing contacts, random curves which represents scratches and dust and regular shapes like circles which represents swirl defects.

Conclusions

The computer data analyses of LBIC image were done. There is possible to detect missing contacts, scratches and dust traces and swirl defects. For more defects detection is important to make large catalog of defect shape and character to be able detect.

Acknowledgments

This research has been subsidized by VZ MSM 21630516 Project and by the Grant Agency of the Czech Republic, grant No. 102/09/0859.

References

1. JANDOVÁ K.: *Katalog defektů, VUT Brno, 2007*
2. HLAVÁČ, V; ŠONKA, M. *Počítačové vidění.* Praha: Grada, 1992. 272 s. ISBN 80-85424-67-3
3. Horak P., *Počítačové vidění.* P.pdf dostupný na Q:/vyuka/horak
4. *The MathWorks Accelerating the pace of engineering and science* URL:<http://www.mathworks.com/access/helpdesk/help/toolbox/images/index.html?/access/helpdesk/help/toolbox/images/imrotate>.

USING BACKLIGHTING IN THE PHOTOLUMINESCENCE IMAGING

A. Vesely, J. Vanek, J. Dolensky

[1] *Faculty of Electrical Engineering and Communication*
Brno University of Technology, Udolni 53, 602 00 Brno

Corresponding author: Ales Vesely (ales.vesely@phd.feec.vutbr.cz)

Introduction

Photoluminescence

Photoluminescence is a kind of luminescence evoked by energy of incident electromagnetic radiation. According to Stoke's law have an excited radiation of light always higher value of wave length (lower of energy value) than exciting radiation. That is why the luminescence can be only rarely evocate by the visible radiation. Usually it is necessary to use an ultraviolet or X-ray radiation. Photoluminescence spectroscopy is being used to investigate defects and localized band tail states within the band gap of silicon wafers. From the comparison of band-edge photoluminescence intensity and minority carrier lifetime, we confirmed that low photoluminescence intensity regions corresponded to short lifetime regions.

Backlighting photoluminescence

The method of backlighting photoluminescence is getting on from same presumptions and laws like standard method photoluminescence described in previous chapter.

Difference is only in placing source of short-wave exciting light radiation. At classic method photoluminescence the source is set on same the side solar cell like CCD camera. On the other hand at transmission photoluminescence is the source set on the opposite side solar cell than is the CCD camera. Supposed advantage of this method is that we might see more distinctly structure respectively defects hidden in greater depth from front side of solar cell.

Experimental

Description of measuring workplace

On the Figure 1 there is a scheme of measuring workplace of experimental photoluminescence diagnostic method with transillumination lighting at look to the internal part.

Measuring box, which is exploited also by others diagnostic methods, was necessary to modify for purposes of metering by means of transillumination lighting. Appearance to that in special illuminant box with matt surface glass owing to halogen lamps happens at illumination to temperature increase, to be necessary this space ventilation and that is why into the side of structure measuring box had to be bored two vents. First vent with diameter 50 mm is determined to supply ventilating into box and second vent with diameter 40 mm for drain off hot air out of box. Vents farther was necessary equip with bushings which make for gripping ventilating tubing plus eventually to obstruction of these vents.

Result of measurement

On the figures 2, 3, 4 and 5, 6, 7 are step by step captured three solar cells by methods photoluminescence and backlighting photoluminescence so that couple forms always same cell measured by those methods. On the Figures 5, 6 and 7, captured through the usage of classical method photoluminescence, there are visible bright dots guiding spot caused by inhomogeneity of material. On the Figure 4 there is in middle part good visible defect inhomogeneity diffusive layer. On Figures 2, 3 and 4 are same three cells measured using by backlighting photoluminescence. There are obviously visible surface defects, grid of backside contacts, mild inhomogeneity of silicon wafer and diamond-shaped phenomenon in the middle which come up in some our measuring solar cells and which come through caused by either strange reflection from matt surface glass or by structure in use source of light. This method thus relatively well discovers surface defects silicon solar cells, indeed there are not expressive visible inner defects such as for example swirl defect. Some account swirl defect placed in the middle of measured solar cell sample A, but isn't too objective. Well visible is there back grid of solar cell consist of silver (Ag) with addition aluminum (Al). To be possible to see inner defects it requirements through functioning light source change depth of penetrating radiation of light into solar cell. Cells are manufactured in thickness to the 300 µm. Ideal depth of penetrating lights for detection inner defects would be about 100 – 150 µm.

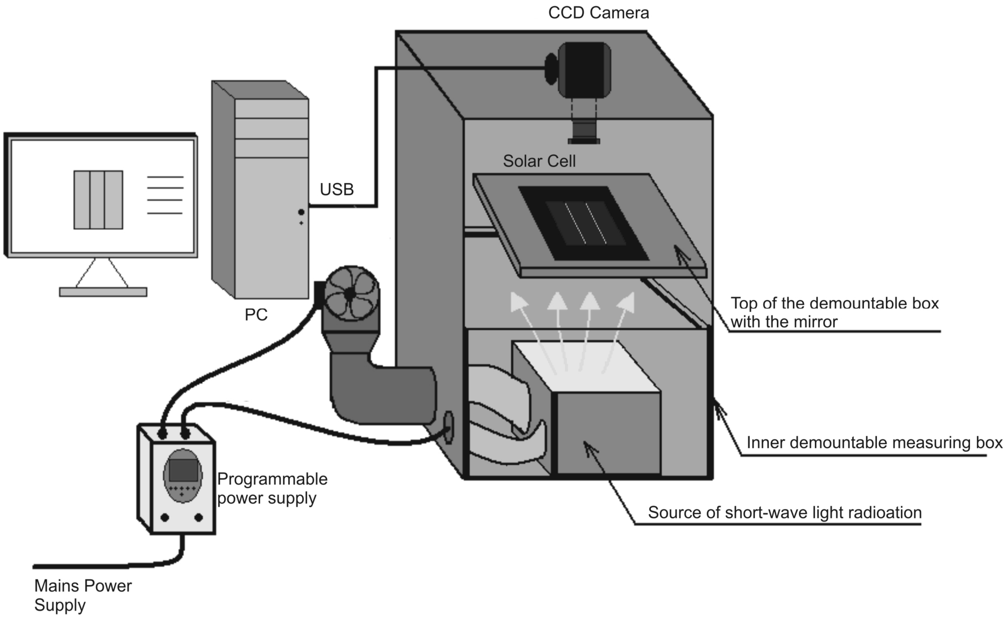

Fig. 1 *Scheme of measuring workplace*

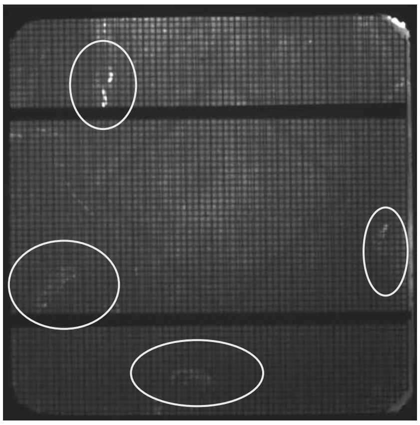
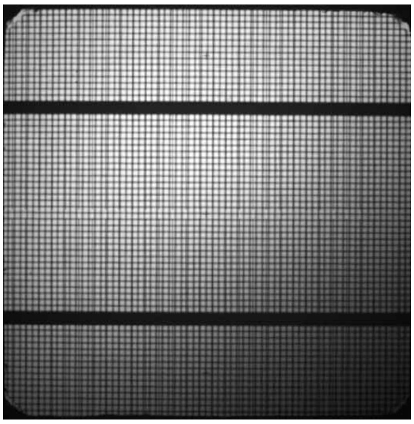
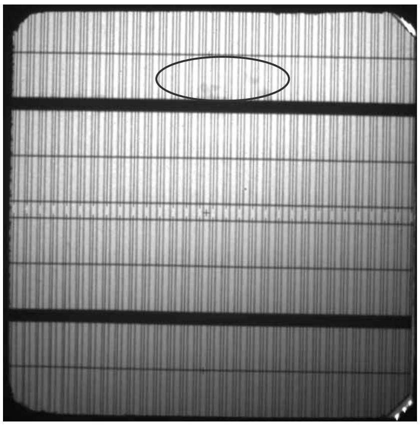

Fig. 2 *(left) Transillumination PL Sample A*
Fig. 3 *(middle) Transillumination PL Sample B*
Fig. 4 *(right)Transillumination PL Sample C*

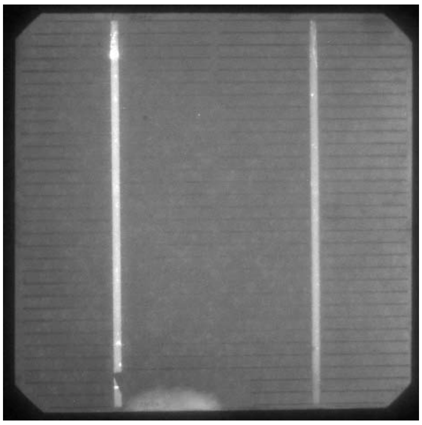
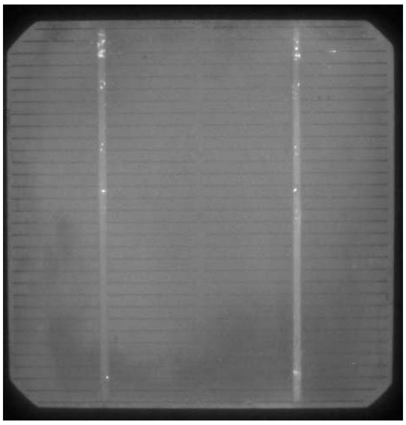
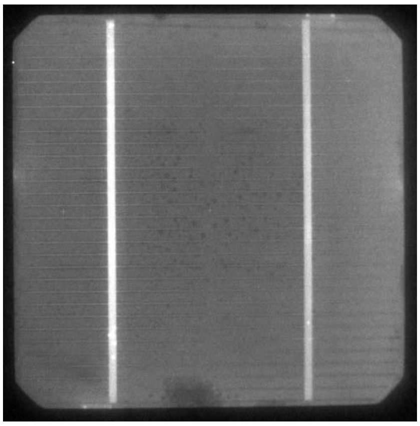

Fig. 5 *(left) Photoluminescence Sample A*
Fig. 6 *(middle) Photoluminescence Sample B*
Fig. 7 *(right) Photoluminescence Sample C*

Conclusions

This method discovers relatively well surface defects of silicon solar cells however there are not expressive visible inner defects such as for example the swirl defect. Ours expectation unfortunately didn't acknowledge. To be possible to see inner defects, it requirements through functioning light source change depth of penetrating radiation of light into solar cell. The other problem was that ours source of ultra-violet light radiates in infra-red spectrum, too. This infrared radiation passes through solar cell block out infra-red light emitted by the photoluminescence. To future development will be necessary this infra-red radiation filtered off or provide such source of light, which would in this spectrum not radiate.

Acknowledgements

This research has been subsidized by VZ MSM 21630516 Project and by the Grant Agency of the Czech Republic, grant No. 102/09/0859.

References

1. Vesely A.; Vanek J.; JANDOVA K. Analysis of back side contact imaging phenomenon in LBIC. In Proceedings of the 15.th conference Student EEICT, volume 3. Brno: NOVPRESS s.r.o., 2009. s. 223-226. ISBN: 978-80-214-3870-5.
2. Vesely A.; Vanek J. Použití fotoluminiscence při analýze fotovoltaických článků. In 3. Česká fotovoltaická konference, Sborník příspěvků. Rožnov pod Radhoštěm: Czech RE Agency, o.p.s, 2008. s. 155-156. ISBN: 978-80-254-3528-1.
3. Vanek J.; Jandova K.; Kazelle J.; Barinka R. Nedestruktivní detekční metody pro charakterizaci solárních článků. In 3. Česká fotovoltaická konference - Sborník příspěvků. Rožnov p.R.: 2008. s. 106-110. ISBN: 978-80-254-3528-1.
4. Jandova K.; Vanek J. Detekce defektů solárních článků. In 29. Nekonvenční zdroje elektrické energie. Brno: Česká elektrotechnická společnost, 2008. s. 29-33. ISBN: 978-80-02-02058-5.H. Strehlow: *Electrode Potentials in Non-aqueous Solvents;* in: *The Chemistry of Non-aqueous Solvents, Vol. 1* (J.J. Legowski, ed.). Academic Press, New York 166, page 157.

METHOD OF DETECTION MICROPLASMA IN SOLAR CELL

J. Dolenský, A. Veselý, J. Vaněk, J. Kazelle

Brno University of Technology, Faculty of Electrical Engineering and Communication,
Department of Electrical and Electronic Technology, Údolní 53, 602 00 Brno

Corresponding author: Jan Dolenský (jan.dolensky@phd.feec.vutbr.cz)
Phone: + 420 5 4114 6168
Fax: + 420 5 4114 6147

Introduction

One of the negative factors the technical civilization is never ending increase of power consumption. Due this factor is required highly usage of alternative electric power sources. One of the “green energy” sources is photovoltaic system which could cover high level of demand of consumption. The flagrant necessity for massive use of the solar system in praxis is increasing the solar cell efficiency. For the efficiency increasing is a selective process needed. One of the parts this process is observation and analyzing microplasma in the solar cell.

Let us count that a diode having a single microplasma region in the PN junction. When the reverse voltage is low, it is a stable state and there are no avalanche breakdowns. So the current on the diode is constant. If reverse voltage is increased, very-low-frequency short-time current impulses will start appearing. Next voltage increase results in increasing both the impulse frequency and width (Fig. 1). After a definite voltage is passed over, the plasma will be ionized solidly and the stable state will be obtained again. If there are a few of microplasma regions in the diode, the above process may occur several times if the voltage is further increased.

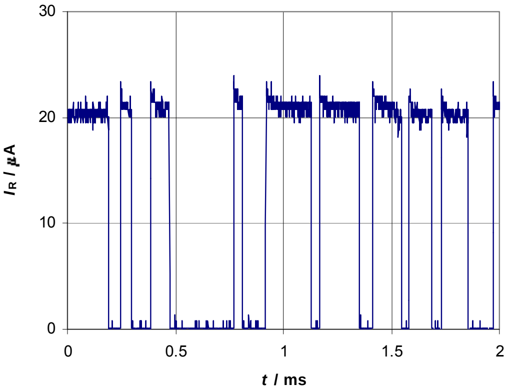

Fig. 1 *Example of two-level noise vs. time plot.*

This theoretically describe of microplasma time behaviour in the PN junction is applicable on large-area Si PN junction. If is named PN junction as large-area it is area much bigger than tenth of square millimetres. In this application is observed area of PN junction approximately 100 square centimetres.

Microplasma can originate in whole solar cell. The origination of microplasma can be cause by several factors. The first of factor is dislocation in crystal grid. In this case is microplasma observable with the increasing reversed biased voltage. In time scale microplasma is more evident with increasing reversed biased voltage.

Second factor of microplasma origin is mechanical damage such as damaged pyramid in PN junction, which can be caused by bad manipulation during production. Other possible sign of mechanical damage is bad treatment of solar cell edges. Passivated edges of solar cell are often damaged. Scratches originated during produce are other possible damage. Defects caused by mechanical damage are stable in time and reversed biased voltage and their quantity is still almost the same. They can be seen already with low reversed voltage. Mechanical defect can be categorized as process defects and can be minimalized by increase of produce quality.

Microplasma that originated at mechanically damaged places is critical, because the defects are usually bigger. By that ability to recombination at PN junction is decreased significantly, and total efficiency is also decreased.

If more contacts are damaged then influence of total efficiency is more significant. Influence of local defects in crystal grid that is more significant with increasing reversed biased voltage, does not decrease total efficiency solar cell. They influence on is in summary only few of percent of total solar cell area.

Experimental

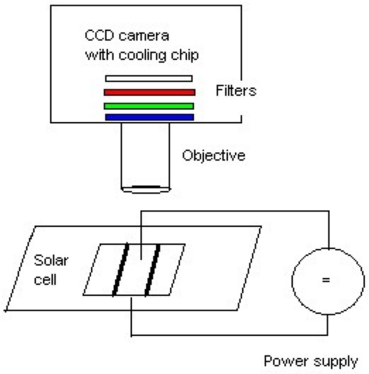

Fig. 2 *Microplasma method workplace*

Considering that microplasma emitted light in visible spectrum it is possible observed the process with a special CCD camera in a dark cryogenic box. The apparatus for the method (fig. 2) contains highly sensitive low-noise CCD camera G2-3200 with CCD chip by Kodak KAF – 3200ME. It can be cooled up to -20° C. Camera contains set of light filters, special objectives and equipment for contacting solar cells. Solar cell is connected to reverse bias DC power source. Signal form CCD camera is analyzed by PC computer. The contact area is placed on dish with LN2. The temperature of underside area is -21°C. Due to the cooling is possible to observe the smallest defects in solar cell.

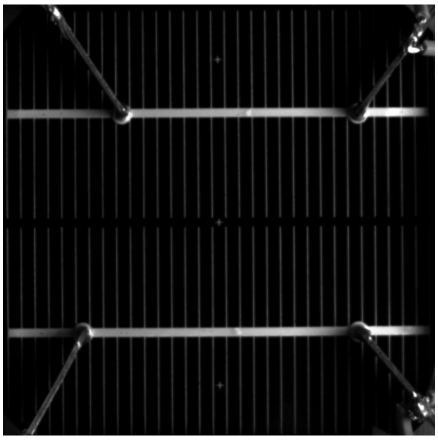

Fig. 3 *Tested solar cell*

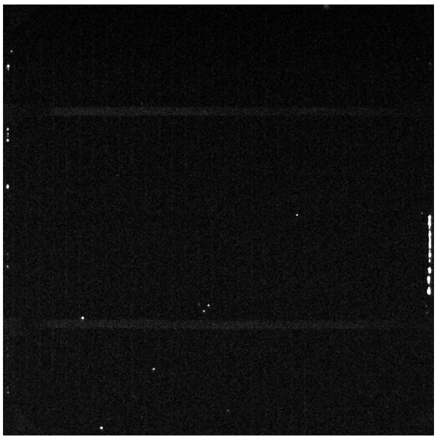

Fig. 4 *First bigger detection of microplasma sources - right edge and a few of local microplasma on solar cell;* $R_{BV} = 4$ *V,* $I = 0{,}13$ *A*

The number of the visible defects in solar cell depends on connected reversed biased voltage (RBV). During increasing reverse biased voltage it is possible to observe more shining points (Fig. 4 - Fig. 5.). It was measured with exposure time 20 sec, clear light filter and the CCD chip was cooled into -20° C.

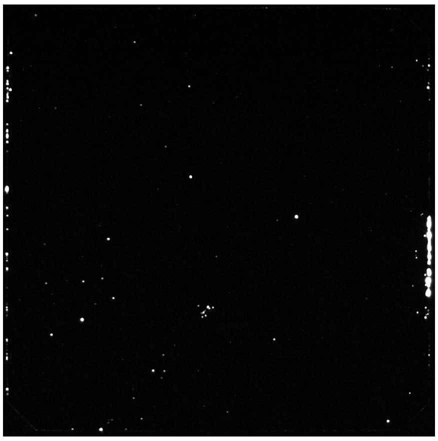

Fig. 5 *Fully developed areas of microplasma sources – left and right edges and much more local microplasma on solar cell;* $R_{BV} = 10$ *V,* $I = 0{,}34$ *A*

As we can see on figures 4 and 5 during increasing reverse biased voltage it is possible to recognize more local microplasma sources. Counts of microplasma sources are highly depending on reversed biased voltage. It is necessary to control reverse current values.

High values can create avalanche breakdown in the PN junction and damaged or destroyed solar cell.

For Comparison this analyzing method is following picture taken by another method, using electroluminescence analysis (Fig. 6). It contains visible swirl defect. The dark areas on figure are places with low current density.

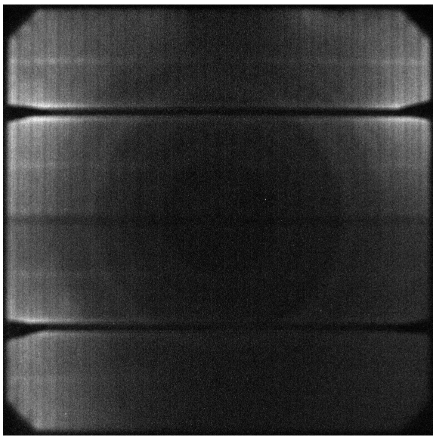

Fig. 6 *Electroluminescence method –* $I_F = 1$ *A, t = - 20 °C*

Conclusions

Behaviour microplasma sources in the solar cell dependent on connected reversed biased voltage and reason of originate. Counts of microplasma caused by defects in crystal grid increase with connected reversed voltage. A count of microplasma on edges is not depending on reversed voltage. Only the intensity of emitting light is growing up.

In contrast with figure taken by electroluminescence method screens of microplasma do not contain visible marks of swirl defect.

Acknowledgements

This paper is based on the research supported by the Grant Agency of the Czech Republic, grant No. 102/09/0859, FRVS 2197/G1/2009 and the project VZ MSM0021630516.

References

1. P. Koktavý, J. Šikula, Reverse Biased P-N Junction Noise in GaAsP Diodes with Avalanche Breakdown Induced Microplasmas. Fluctuation and Noise Letters, ISSN 0219-4775, 2002, roč. 2, č. 2, s. L65 – L70.
2. RJ. McINTYRE, Theory of Microplasma Instability in Silicon. J. Appl. Phys., June 1961, vol. 32, no. 4, p. 983-995.
3. V. Benda, J. Salinger, Z. Macháček The effects of lattice imperfections on the electrical properties of solar cells, In 3rd IWTPV. Prag, IEE. 2006. p. 107 - 108. ISBN 80-01-03467-4.
4. Z. Chobola, Impulse noise in silicon solar cells. Microelectronics Journal, Vol.32/9 (2001), ISSN 0026-2692, pp.707-711.

TESTING QUALITY OF NEW SOLAR CELLS DESIGNED FOR CONCENTRATORS SYSTEM BY NOISE SPECTROSCOPY

J. Vanek[1], Z. Chobola[2], M. Lunak[2], J. Dolenský[1]

[1] Brno University of Technology, Faculty of Electrical Engineering and Communication Technologies, Department of Electrotechnology, Udolni 53, 602 00 Brno, Czech Republic
[2] 1Brno University of Technology, Faculty of Civil Engineering, Department of Physics ,
Veveri 95, 602 00 Brno, Czech Republic

Corresponding author: Jiri Vanek (vanekji@feec.vutbr.cz)
Phone: +420541146122
Fax: +420541146147

Introduction

The need for increasing the solar cell efficiency implies the application of selective processes within the framework of their structure preparation technology. Under the term selective processes, we understand such processes, in the course of which the solar cell structure is formed within an exactly predefined region. This process includes, as a rule, the formation of two different structure regions at the front and rear side, or, within one of the sides.

The starting point in the solar cell optimization process consists in defining a process structure, which is as simple as possible, containing as few process steps as possible. The input-stage substrate is a single-crystal silicon wafer of a thickness of about 300 μm, which has been made from an ingot by means of a wire cutter. A damaged sub-surface layer containing a number of defects, is given rise during the wire cutting process, which is assisted by a cutting emulsion supply. The defective layer is to be removed by etching in an alkali solution. The double-sided-etched silicon wafer with a nearly defect-less surface has to be subjected to another etching process in order to minimize the reflected light intensity. Randomly localized pyramids of various sizes (as a rule up to 15 μm at the pyramid base) arise during the etching process.

The above described initial technology makes a limiting factor for the resulting solar cell efficiency, mainly due to a large area of the cell rear side additionally increased by a textured surface and to an inappropriate floating N^+ layer structure of the of the thick-film contacts at the rear side. What matters is the rear side face properties, from the minority charge carrier surface recombination point of view. Present technologies use silicon wafers, whose thickness is being reduced permanently, so that the effect of the wafer surface on the resulting solar cell parameters is more pronounced.

Diagnostic methods have been applied to examine the process steps intended to eliminate or at least reduce the above mentioned structure imperfections. They include the following: acid-etch-based surface structuring and single-side etching of the rear side, aimed at removing the excessive N^+ layer and finishing the surface. In addition, the effect of the silicon oxide thin film located under the silicon nitride cover layer, particularly at the single side etched rear side, have been investigated.

Noise and transport characteristics have been measured in the framework of this study. An analysis of U-I characteristics is presented in this paper. The spectral power density versus frequency function allowed us to evaluate the different types of noise. On the basis of the behavior of particular spectral power densities versus forward voltage plots the quality of the different specimens can be evaluated [1-3].

Experiment results and their assessment

Three silicon solar cells of dimensions 80 x 80 mm labeled S1-25, S1-26 and S2-26 have been studied.

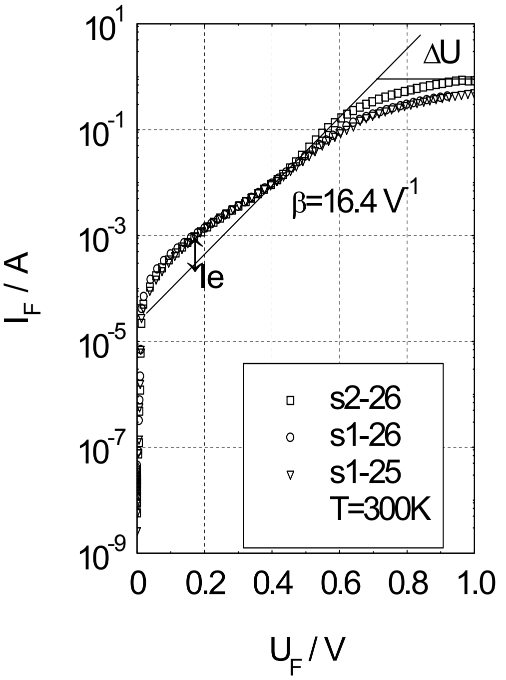

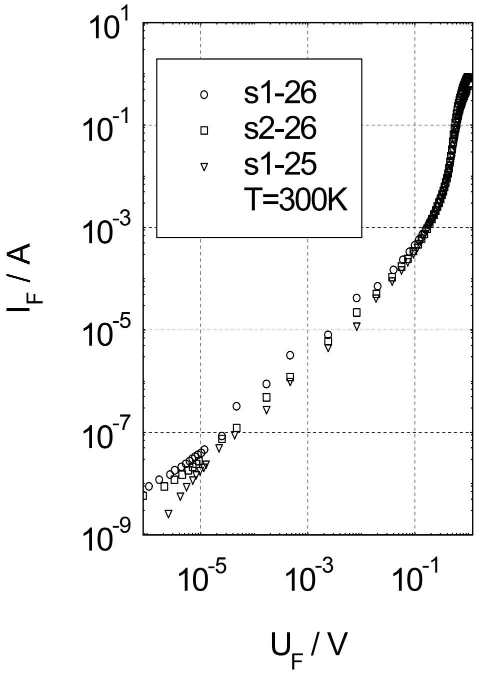

***Fig. 1** (left) I-V characteristic for solar cells No S1-25, S1 -26 and S2-26 in forward bias direction*
***Fig. 2** (right) Plot of log I versus log U for solar cells No S1-25, S1-26 and S2-26 in forward bias direction*

Fig. 1 shows a semilog chart of the U-I characteristics of these cells. All of the three specimens feature a marked excess current component Ie in the forward voltage region near 0.2 V. The slope β ranges from 16.2 V-1 for specimen No S1-26 up to β = 16.4 V-1 for specimen No S2-26.

A voltage drop across the specimen contacts is observed at voltages over 0.7 V. The least voltage drop is exhibited by specimen No S2-26 – the best contacts of the specimen set – and the highest voltage drop is observed in specimen No S1-25. The S2-26 specimen contact series resistance is 0.6 Ω, the S1-25 contact series resistance, about 3 Ω.

As is seen in Fig. 2, showing the log-log scale U-I characteristic, a straight-line section occurs in the characteristic at forward voltages of up to 0.1 V, giving evidence of a parallel resistance effectively shunting the PN junction. The shunt resistance is about 500 Ω and 200 Ω for S1-26 and S1-25 specimens, respectively.

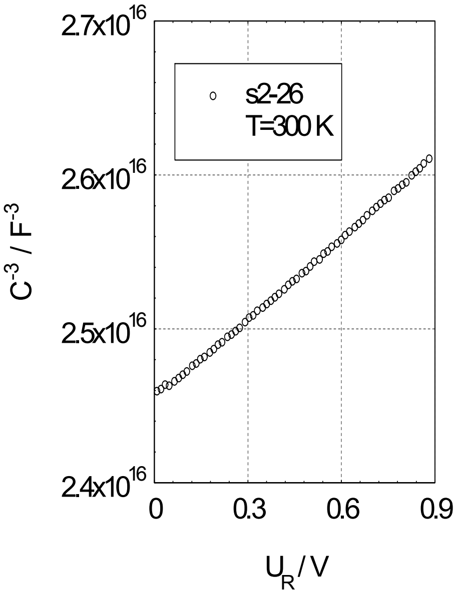

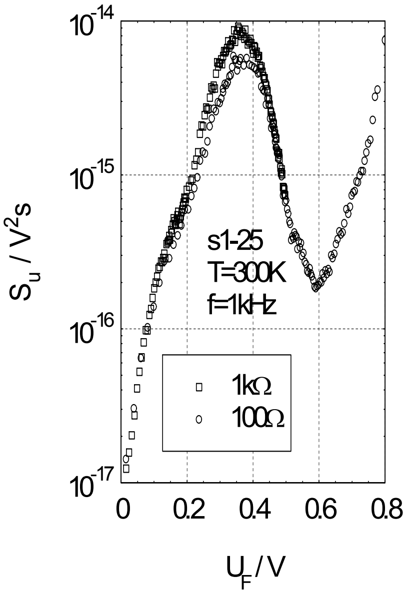

Fig. 3 *(left) C-V characteristic for solar cells No.S2-26*
Fig. 4 *(right)The noise spectral density as a function of forward voltage for solar cells No.S1-25*

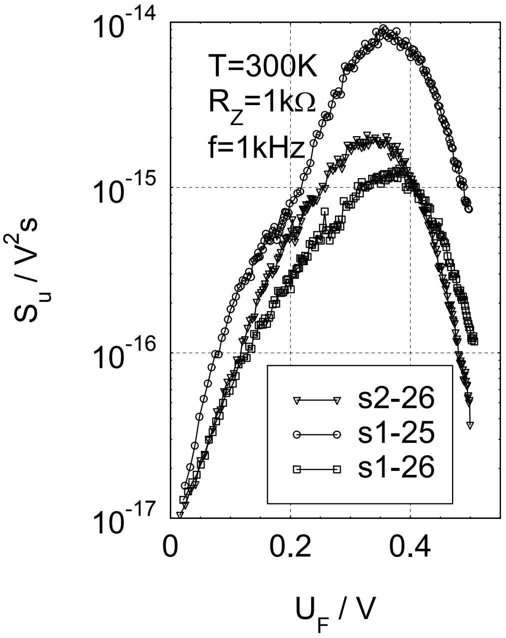

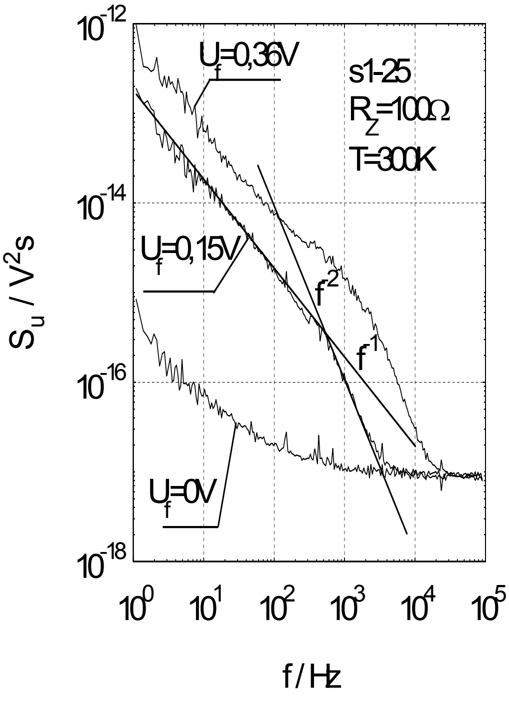

Fig. 5 *(left) The noise spectral density as a function of forward voltage and load resistors R_L=100Ω, for solar cells Nos.S1-25, S1-26 and S2-26*
Fig. 6 *(right) The noise spectral density versus frequency for solar cells No.S1-25, R_L = 100 Ω, at U_F = 0 V, U_F = 0.15 V and U_F = 0.36 V*

C-U characteristics have been measured, too. S2-26 specimen features a capacitance of 3.4 μF. Fig. 3 shows the function C = (U_n) resulting from our measurements. The function appears to be almost of the U1/3 type, which would suggest a linear type junction by Shockley.

Fig 4 shows a noise power spectral density versus DC forward voltage plots as picked up across a load resistance of R_L = 100 Ω and R_L = 1 kΩ for specimen No S1-25, at a mean frequency of 1 kHz and a bandwidth of 20 Hz.
A curve showing two peaks is observed. The first peak occurs at a voltage of U_{max1} = 0.15 V, whereas the second, at U_{max2} = 0.35 V.
The maximum noise voltage is observed in the case of the PN junction dynamic resistance matching the load resistance value. This makes us to suppose two different defects in the PN junction regions being connected in parallel to each other.

The behavior of the characteristic over 0.6 provides us with indications concerning the contact quality. A fast growth of excess noise in this region leads us to a conclusion that the contact duality is poor. Fig 5 shows the noise voltage power spectral density Su versus applied DC voltage plots for a load resistance R_L = 1 kΩ for all specimens under test. It is easily seen that the PN junction quality of S1-25 specimen is the poorest of the set, as Su_{max} = 1.10^{-14} V^2s and two excess current sources), as well as the poorest contact quality. At U_F = 0.7 V, the spectral density is = 7 x 10^{-16} V^2s.
S1-26 specimen features the best-quality PN junction, his noise power spectral density equaling Su_{max} = 1,05 x 10-15 V2s.
On the other hand, the best-quality contacts are shown by S2-26, as its noise spectral density Su_k = 8.10^{-17} V^2s at U_F = 0.7 V.

Fig 6 shows the noise voltage spectral density versus frequency plot for specimen No S1-25. The load resistance was RL = 100 Ω. The different characteristics have been measured at voltages: U_{F1} = 0 V characterizing the measuring setup background noise, U_{F2} = 0.15 V – the operating region of the first defect, and U_{F3} = 0.36 V – the operating region of the second defect. The excess noise appears to have two components. At frequencies below 1 kHz, noise of 1/f is predominating, whereas in the frequency range from 10^3 Hz to 10^4 Hz, noise of $1/f^2$ type is predominating. This behavior gives evidence of the generation-recombination noise being present. Taking into account the frequency at which the g-r noise drops to one half, the charge carrier life time $\tau = \frac{1}{2\pi f}$ can be deduced, resulting in $\tau_1 = 1.10^{-3}$ s at $f_{01} = 1,5.10^2$ Hz for the first defect and $\tau_2 = 5.10^{-5}$ s at $f_{02} = 3.10^3$ Hz for the second defect.

Conclusion

Quality of three specimens of silicon solar cells of dimensions 80 x 80 mm designed for concentrator systems has been investigated.
Based on the above analysis of transport and noise characteristics, we can conclude that specimen No S1-26 features the best-quality PN junction, whereas specimen No S1-25, the worst.
The best-quality contacts were observed in specimen S2 - 26, the worst, in specimen No S1-25.

Acknowledgements

This research has been subsidized by VZ MSM 21630516 Project and by the Grant Agency of the Czech Republic, grant No. 102/09/0859.

NUMERICAL MODEL LEAD-ACID ACCUMULATOR GRIDS

P. Fiala, Z. Szabó, Z. Roubal

Brno University of Technology, Faculty of Electrical Engineering and Communication,
Department of Theoretical and Experimental Electrical Engineering
Kolejni 2906/4, 612 00 Brno, Czech Republic

Corresponding author: P. Fiala (fialap@feec.vutbr.cz)

Introduction

The lead-acid battery uses lead dioxide as the active material of the positive electrode and metallic lead, in a high-surface-area porous structure, as the negative active material. Typically, a charged positive electrode contains both α-PbO_2 (orthorhombic) and β-PbO_2 (tetragonal). The equilibrium potential of the α-PbO_2 is more positive than that of β-PbO_2 by 0,01 V The α form also has a larger, more compact crystal morphology which is less active electrochemically and slightly lower in capacity per unit weight; it does, however, promote longer cycle life. Neither of the two forms is fully stoichiometric. Their composition can be represented by PbO_x, with *x* varying between 1,85 and 2,05. The introduction of antimony, even at low concentrations, in the preparation or cycling of these species leads to a considerable increase in their performance. The preparation of the active material precursor consists of a series of mixing and curing operations using leady lead oxide (PbO + Pb), sulfuric acid, and water. The ratios of the reactants and curing conditions (temperature, humidity, and time) affect the development of crystallinity and pore structure. The cured plate consists of lead sulfate, lead oxide, and some residual lead (<5%). The positive active material, which is formed electrochemically from the cured plate, is a major factor influencing the performance and life of the lead-acid battery. In general the negative, or lead, electrode controls cold-temperature performance (such as engine starting). The electrolyte is a sulfuric acid solution, typically about 1,28 specific gravity or 37% acid by weight in a fully charged condition. On the grids there are following reactions

NEGATIVE ELECTRODE

$$\mathrm{Pb} \underset{\text{charging}}{\overset{\text{discharging}}{\Leftrightarrow}} \mathrm{Pb}^{2+} + 2\mathrm{e}^- \quad (1) \qquad \mathrm{Pb}^{2+} + \mathrm{SO}_2^{\;2-} \underset{\text{charging}}{\overset{\text{discharging}}{\Leftrightarrow}} \mathrm{PbSO}_4 \quad (2)$$

POSITIVE ELECTRODE

$$\mathrm{PbO}_2 + 4\mathrm{H}^+ + 2\mathrm{e}^- \underset{\text{charging}}{\overset{\text{discharging}}{\Leftrightarrow}} \mathrm{Pb}^{2+} + 2\mathrm{H}_2\mathrm{O} \quad (3) \qquad \mathrm{Pb}^{2+} + \mathrm{SO}_4^{\;2-} \underset{\text{charging}}{\overset{\text{discharging}}{\Leftrightarrow}} \mathrm{PbSO}_4 \quad (4)$$

OVERALL REACTIONS

$$\mathrm{Pb} + \mathrm{PbO}_2 + 2\mathrm{H}_2\mathrm{SO}_4 \underset{\text{charging}}{\overset{\text{discharging}}{\Leftrightarrow}} 2\mathrm{PbSO}_4 + 2\mathrm{H}_2\mathrm{O} \quad (5)$$

Mathematical and numerical model

Electromagnetic part is derived from reduced Maxwell equations

$$rot\,\boldsymbol{H} = \boldsymbol{0}\,, \quad (6) \qquad div\,\boldsymbol{B} = 0\,, \quad (7)$$

where ***H*** is the vector of magnetic field intensity, ***B*** is magnetic field induction, ***J*** is vector of current density.

$rot\,\boldsymbol{E} = \boldsymbol{0}$, (8) $div\,\boldsymbol{J} = 0$, (9)

where ***E*** is the vector of electric field intensity. Vector functions of electric, magnetic field are expressed by means of a scalar potentials ϕ_e, ϕ_m, Final current density from (9) ***J*** is influenced by velocity ***v*** of the flowing ion solution and outer magnetic field

$$\boldsymbol{J} = \gamma\left(\boldsymbol{E} + \boldsymbol{v} \times \boldsymbol{B}\right). \tag{10}$$

If electrodes E_1 and E_2 have different electrical potentials then the current density ***J*** is created in the Ω area according to (10) and the current I_L flows in the ion solution

$$I_L = \iint_{S_e} \boldsymbol{J} \cdot d\,\boldsymbol{S} = \iint_{S_e} \gamma\left(\boldsymbol{E} + \boldsymbol{v} \times \boldsymbol{B}\right) \cdot d\,\boldsymbol{S} \cdot \tag{11}$$

where $\boldsymbol{S}_e$ is a directed area of electrodes E_1 and E_2 into space Ω. In equation (11) there is the electric field intensity ***E*** for ion solution much smaller than product of $\boldsymbol{v} \times \boldsymbol{B}$, so we ignore the influence of electric field intensity. The specific force ***f*** affects the moving charge *q* and the force ***F*** in whole Ω area is

$$\boldsymbol{F} = \iiint_{\Omega} \boldsymbol{J} \times \boldsymbol{B}\, dV \cdot \tag{12}$$

We obtain voltage between electrodes E_1, E_2 from

$$U_L = \int_{E_1}^{E_2} \frac{\boldsymbol{F}}{q} \cdot d\ell \cdot \tag{13}$$

where the electric field intensity is derived from the force ***F*** which affects a charge *q*. After modification voltage on electrodes is

$$U_L = \iiint_{\Omega} \left(\frac{\boldsymbol{J}(\boldsymbol{v})}{I_L} \times \boldsymbol{B} \right) \cdot \left(\boldsymbol{v} \ \right) dV\,. \tag{14}$$

The current density ***J***(***v***) depends on immediate ion velocity between E_1 and E_2. The magnetic field, which is expressed in (14) by the induction *B*, we gain from Biot-Savart law by means of different scalar magnetic potentials (DSP) [1]. We get discretization by means of an approximation of the scalar magnetic potential

$$\phi_m = \sum_{k=1}^{N_\phi} \varphi_{mk} W_k\left(x,y,z\right),\ \forall\left(x,y,z\right) \subset \Omega\ , \tag{15}$$

where φ_m is the nodal value of the scalar magnetic potential, *W* is base function, N_φ is number of mesh nodes. We obtain semidiscrete solution by means of the approximation (15) in the relation of Galerkin method

$$\sum_{j=1}^{N_\phi} -\int_{\Omega} \mu\, \boldsymbol{t}_j \cdot gradW_i + \mu\, grad\varphi_{mj} \cdot gradW_i\, d\Omega = 0\ \boldsymbol{,}\ i = 1,..,N_\varphi\,, \tag{16}$$

Where $\boldsymbol{t}_j$ is the nodal value of known magnetic field intensity. Equations (15) is possible to write briefly

$$-\left[k_{Tij}\right] + \left[k_{ij}\right]\left\{\varphi\right\} = 0\ i,\, j = 1,..,N_\varphi\,. \tag{17}$$

Coefficients for (17) are written as

$$k_{Tij}^{em} = -\int_{\Omega^e} \mu^e\, \boldsymbol{t}_j \cdot gradW_i d\Omega \quad i,j = 1,..,N_e \quad k_{ij}^{em} = -\int_{\Omega^e} \mu^e\, grad\,\varphi_j \cdot gradW_i\ d\Omega \tag{18}$$

where Ω^e is the area of the selected element of mesh, μ^e is the material permeability of the selected element, N_e is the number of elements of mesh. The equation system changes into relation

$$-\left[k_{Tij}^{em}\right] + \left[k_{ij}^{em}\right]\left\{\varphi\right\} = 0\ e = 1,..,N_e\,. \tag{19}$$

We can solve the equation system (19) by means of standard algorithms. The solution by means of DSP consists of two parts. Firstly, we express the distribution of magnetic field intensity ***T*** from current sources with the respect to boundary conditions and in the area Ω_{Pb}. Secondly, we have to find out the solution of the magnetic intensity ***H*** distribution from the previous step. The model of electrical or current field is formulated from previous equations

$$\gamma \, div \, grad \phi_e = 0 \,. \tag{20}$$

On the interface there are conditions

$\boldsymbol{n} \cdot \gamma \left(grad \phi_e \right) = 0$ on the boundary $\Gamma_{E\text{-}k}$, (21)

where ***n*** in the normal vector to the surface of the electrode. $\Gamma_{E\text{-}k}$ is the interface between liquid and an electrode. The continuity of tangential components of electrical field intensity on the interface is

$\boldsymbol{n} \times \left(grad \phi_e \right) = \boldsymbol{0}$ on the boundary $\Gamma_{E\text{-}k}$. (22)

We can do the approximation of the scalar electric potential in the similarly way like in the relation (15) and by means of (15), (20) and Galerkin method we get semidiscrete solution

$$\sum_{j=1}^{N_\phi} \; - \int_{\Omega} \gamma \; grad \varphi_{ej} \cdot grad W_i \, d\Omega = 0 \;, \; i = 1,..,N_\varphi \,, \tag{23}$$

where φ_{ej} is the nodal value of the scalar electric potential. We can rewrite the equation system (28) by the help of

$$\left[k^J{}_{ij} \right] \left\{ \varphi \right\} = 0 \;\; i, j = 1,..,N_\varphi \,. \tag{24}$$

$$k_{ij}^{Je} = - \int_{\Omega^e} \gamma^e \, grad \varphi_{ej} \cdot grad W_i \; d\Omega \,, \tag{25}$$

where Ω^e is the area of the selected element of mesh, γ^e is the specific conductivity of liquid in the static state of the selected element, N_e is the number of elements. The relation for a voltage drop during discharging $U(t) = U_0 - \Delta u$ is

$$\Delta u = \sqrt{ Z \left(\int_{\Omega} \frac{ \boldsymbol{J}_e{}^{-} q_e{}^{-} \cdot \boldsymbol{v}_e{}^{-} }{ \Delta V_e \gamma_e } \right) d\Omega + Z \int_{\Omega} \left(\boldsymbol{J}_e \times \boldsymbol{B}_e \right) \cdot \boldsymbol{v}_e{}^{-} d\Omega + Z \left(\int_{\Omega} \frac{ \boldsymbol{J}_e{}^{+} q_e{}^{+} \cdot \boldsymbol{v}_e{}^{+} }{ \Delta V_e \gamma_e } \right) d\Omega + Z \int_{\Omega} \left(\boldsymbol{J}_e \times \boldsymbol{B}_e \right) \cdot \boldsymbol{v}_e{}^{+} d\Omega } \tag{26}$$

where

$$\mathrm{v}_e^{+} = \frac{ \mathrm{E}_e \, \gamma }{ F_c \, \Delta V_e \sum_{k=1}^{N_{ion+}} c_k^{+} N_{\mathrm{k}}^{+ion} } \,, \; \mathrm{v}_e^{-} = \frac{ \mathrm{E}_e \, \gamma }{ F_c \, \Delta V_e \sum_{k=1}^{N_{ion-}} c_k^{-} N_{\mathrm{k}}^{-ion} } \,, \; q_e^{+} = F_c \, \Delta V_e \sum_{k=1}^{N_{ion+}} c_k^{+} N_{\mathrm{k}}^{+ion} \,, \; q_e^{-} = F_c \, \Delta V_e \sum_{k=1}^{N_{ion-}} c_k^{-} N_{\mathrm{k}}^{-ion} \tag{27}$$

Where F_c is the Faraday constant, F_c=96484 C.mol^{-1}, $\boldsymbol{E}_e$ the electric field intensity in direction of ions motion in an element of mesh, c^+ the positive ions concentration, c^- the negative ions concentration, ΔV_e is the element volume, N_k^{+ion} is the integer multiple of electron charge for specific positive ion, N_k^{-ion} is the integer multiple of electron charge for specific negative ion, q_e^- is the whole charge of negative ions in one element,, q_e^+ is the total charge of positive ions in one element, N_{ion+} is the number of different positive charge carriers (elements, compounds), N_{ion-} is the number of negative charge carriers. There are concentrations c_k in fluid

Positive ions	**Negative ions**
H^+ … 9,9193.10^2 mol.m^{-3}	SO_4^{2-}… 4,9597·10^3 mol.m^{-3}
Pb^{4+} … 2,2028·10^4 mol.m^{-3}	OH^- … 8,8110·10^4 mol.m^{-3}

Numerical solution

The numerical model was prepared by means of ANSYS tools [1]. In the Fig. 3 we can see distribution of current density module J on the grid surface and in the electrolyte between positive and negative electrode. For computation we used initial voltage was 2,3V, minimal voltage of discharged accumulator, supposed discharging time, and time period between steps of computation.

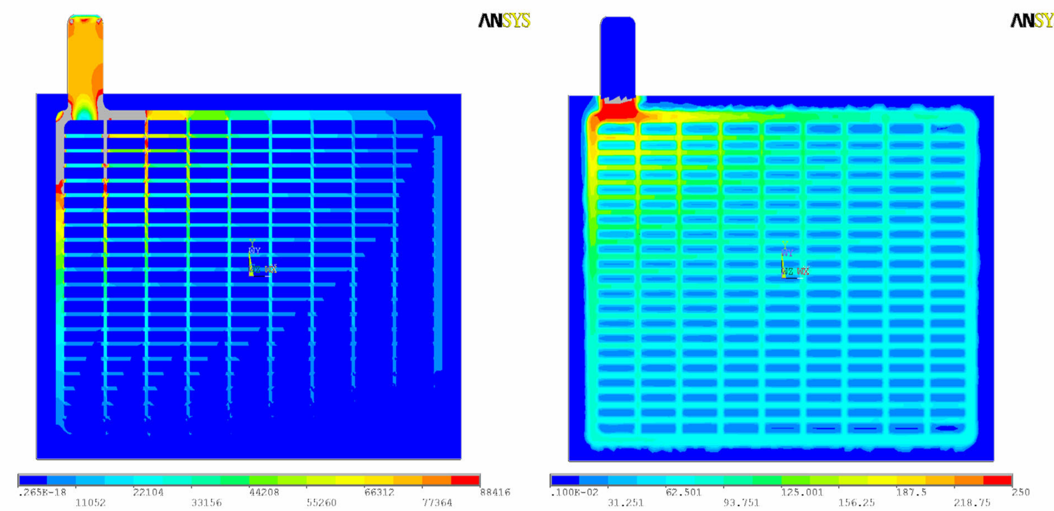

Fig. 1 *Current density distribution on the grid surface (left) and in the electrolyte between positive and negative electrode (right), charged state*

Conclusion

This work deals with chemical processes on electrodes and in an electrolyte of a lead-acid accumulator. There is mathematical and numerical description in the article and results of current density distribution in the electrodes area. Such analysis could be used for an optimization of grid geometry. The best shape we get if module of current density is constant on the electrode surface.

Acknowledgements

The paper was prepared within the framework of the research plan No. MSM 0021630516 of the Ministry of Education, Youth and Sports of the Czech Republic.

References

1. *Ansys User's Manual.* Huston (USA): SVANSON ANALYSYS SYSTEM, Inc., 2003.
2. SALKIND, A. J., CANNONE, A. G., TRUMBURE, F. A., *Handbook of batteries*. Boca Raton (Florida, USA): CRC Press, Inc., 2001.
3. BURIAN, I. DĚDEK, L. DĚDKOVÁ, J. *Analysis and optimization of an inductive flowmeter*. 8th International Symposium on theoretical electrical engineering, Thessaloniki, September 22-23,1995,p.506-509
4. FIALA,P *Model of Induction flowmeter DN100*. Research report no.2/01, Laboratoř modelování a optimalizace polí v elektromechanických systémech. FEI VUT BRNO, 21.6.2001, Brno, Czech Republic

MODELING OF AIR FLOW IN THE HEAT ACCUMULATOR LAYER

P. Fiala, *Z. Roubal*

Brno University of Technology, Faculty of Electrical Engineering and Communication,
Department of Theoretical and Experimental Electrical Engineering
Kolejni 2906/4, 612 00 Brno, Czech Republic

Corresponding author: P. Fiala (fialap@feec.vutbr.cz)

Introduction

Phase changes of materials are a perspective way of thermal energy storage. The application of PCM offers a lot of advantage. We can reach higher density of stored energy. Table 1 shows the calculation for classical materials and PCM. The initial temperature 20 C and final temperature 50 C at the end of heating are supposed. Next advantage is a possibility to store heat at low temperature. We don't need to have such good thermal insulation and solar collectors work with better efficiency so the demand for area of collectors decreases.

***Table 1** The comparison of classical materials and PCM*

material	density of storage energy [kWh.m^{-3}]
water	34,5
gravel	23,0
paraffine wax	62,4
$CaCl_2.6H_2O$	117,4
$Na_2CO_3.10H_2O$	131,7
$Na_2HPO_4.12H_2O$	134,7

Mathematical and numerical model of turbulence

The model of air velocity distribution is derived for incompressible fluid as

$$div\,\boldsymbol{v} = 0 \qquad (1)$$

for a stabile state of flow stands

$$div\ \rho\boldsymbol{v} = 0 \qquad (2)$$

from the energy conservation law. We suppose a turbulent flow

$$rot\ \boldsymbol{v} = 2\boldsymbol{\omega} \qquad (3)$$

where ω is the angular velocity of fluid. If we use the Stokes theorem, the Helmoholtz theorem for moving particle and continuity equation, we can formulate from the balance of forces the Navier-Stokes equation for the fluid element

$$\frac{\partial \boldsymbol{v}}{\partial t} + \boldsymbol{v}\cdot grad\boldsymbol{v} = \boldsymbol{A} - \frac{1}{\rho} grad\,p + \boldsymbol{\upsilon}\cdot\Delta\boldsymbol{v} \qquad (4)$$

where ***A*** is an external acceleration and υ kinematic viscosity. In the equation (4) we can substitute pressure losses, detailed described in [1]. We can prepare a discretization of equation (4) by means of the approximation of velocity ***v*** and acceleration ***a***.

$$\boldsymbol{v} = \sum_{k=1}^{N_{\varphi}} \boldsymbol{v}_{\mathrm{vk}} W_{\mathrm{k}}(x,y,z), \quad \forall (x,y,z) \subset \Omega,$$

$$\boldsymbol{a} = \sum_{k=1}^{N_{\varphi}} \boldsymbol{a}_{\mathrm{vk}} W_{\mathrm{k}}(x,y,z), \quad \forall (x,y,z) \subset \Omega, \tag{5}$$

where $\boldsymbol{v_v}$, $\boldsymbol{a_v}$ are immediate node values, *W* is a base function, N_φ is a number of mesh nodes. If we apply the approximation and Galerkin principle in , see [1], we get the semidiscrete solution

$$\begin{gathered}\int_{\Omega} W_{\mathrm{j}} \left[\rho \left(\sum_{i=1}^{N_{\mathrm{v}}} W_{\mathrm{i}} \frac{\partial \boldsymbol{v}_{\mathrm{vi}}}{\partial t} + \sum_{i=1}^{N_{\mathrm{v}}} W_{\mathrm{i}} \boldsymbol{v}_{\mathrm{vi}} \cdot grad \boldsymbol{v}_{\mathrm{vi}} \right) + \sum_{i=1}^{N_{\mathrm{v}}} W_{\mathrm{i}} grad\, p_{\mathrm{i}} - \rho \sum_{i=1}^{N_{\mathrm{v}}} W_{\mathrm{i}} \boldsymbol{A}_{\mathrm{vi}} - \sum_{i=1}^{N_{\mathrm{v}}} W_{\mathrm{i}} \sum_{l=1}^{N_{\mathrm{s}}} \boldsymbol{F}_{\mathrm{li}} \right] \mathrm{d}\Omega - \\ - \int_{\Omega} W_{\mathrm{j}} \left[\sum_{i=1}^{N_{\mathrm{v}}} W_{\mathrm{i}} div \boldsymbol{\upsilon} \cdot grad\, \boldsymbol{v}_{\mathrm{vi}} \right] \mathrm{d}\Omega - \int_{\Gamma} W_{\mathrm{j}} \left[\sum_{i=1}^{N_{\mathrm{v}}} W_{\mathrm{i}} \boldsymbol{X}_{\mathrm{i}} \right] \mathrm{d}\Gamma = 0, \quad j = 1,2 \ldots N_{\mathrm{v}}\end{gathered} \quad , \tag{6}$$

where *X* are the known conditions on the interface of area. We substitute pressure losses in (6) and we obtain the model of air flow

$$\begin{gathered}\rho \int_{\Omega} W_{\mathrm{j}} W_{\mathrm{i}} \mathrm{d}\Omega \frac{\mathrm{d}\boldsymbol{v}_{\mathrm{vi}}}{\mathrm{d}t} + \rho \int_{\Omega} W_{\mathrm{j}} \boldsymbol{v}_{\mathrm{vi}} \cdot \left(\frac{\mathrm{d}W_{\mathrm{i}}}{\mathrm{d}x} \boldsymbol{u}_{\mathrm{x}} + .. + \frac{\mathrm{d}W_{\mathrm{i}}}{\mathrm{d}z} \boldsymbol{u}_{\mathrm{z}} \right) \mathrm{d}\Omega \boldsymbol{v}_{\mathrm{vi}} + \int_{\Omega} W_{\mathrm{j}} \cdot \left(\frac{\mathrm{d}W_{\mathrm{i}}}{\mathrm{d}x} \boldsymbol{u}_{\mathrm{x}} + .. + \frac{\mathrm{d}W_{\mathrm{i}}}{\mathrm{d}z} \boldsymbol{u}_{\mathrm{z}} \right) \mathrm{d}\Omega\, p_{\mathrm{i}} - \\ - \rho \int_{\Omega} W_{\mathrm{j}} \mathrm{d}\Omega \boldsymbol{A}_{\mathrm{i}} - \int_{\Omega} W_{\mathrm{j}} \mathrm{d}\Omega \boldsymbol{F}_{\mathrm{li}} - \int_{\Omega} \left(\frac{\mathrm{d}W_{\mathrm{j}}}{\mathrm{d}x} + \frac{\mathrm{d}W_{\mathrm{j}}}{\mathrm{d}y} + \frac{\mathrm{d}W_{\mathrm{j}}}{\mathrm{d}z} \right) \boldsymbol{\upsilon}_{\mathrm{i}} \cdot \left(\frac{\mathrm{d}W_{\mathrm{i}}}{\mathrm{d}x} \boldsymbol{u}_{\mathrm{x}} + \frac{\mathrm{d}W_{\mathrm{i}}}{\mathrm{d}y} \boldsymbol{u}_{\mathrm{y}} + \frac{\mathrm{d}W_{\mathrm{i}}}{\mathrm{d}z} \boldsymbol{u}_{\mathrm{z}} \right) \mathrm{d}\Omega \boldsymbol{v}_{\mathrm{vi}} - \\ - \int_{\Gamma} W_{\mathrm{j}} \mathrm{d}\Gamma \boldsymbol{X}_{\mathrm{i}} = 0, \quad i, j = 1,2 \ldots N_{\mathrm{v}}.\end{gathered} \tag{7}$$

On the interface there are conditions

$$\boldsymbol{n} \cdot (\boldsymbol{v}) = 0 \tag{8}$$

on the border Γ_{vr1} where ***n*** is a normal vector to direction of air flow

$$\boldsymbol{n} \cdot (p) = 0 \tag{9}$$

on the border Γ_{vr2} where $\Gamma_{\mathrm{vr1}} \subset \Gamma_{\mathrm{vr2}}$ is the interface between the solid body and the liquid. We can write

$$\left[C_{\mathrm{ij}}^{\mathrm{f}}\right] \left\{ \frac{\mathrm{d}\boldsymbol{v}_{\mathrm{vi}}}{\mathrm{d}t} \right\} + \left[K_{\mathrm{ij}}^{\mathrm{sx}} - K_{\mathrm{ij}}^{\mathrm{Fx}}\right] \{\boldsymbol{v}_{\mathrm{vi}}\} + \left[K_{\mathrm{ij}}^{\mathrm{cx}}\right] p = \left[K_{\mathrm{ij}}^{\mathrm{gx}}\right] \{\boldsymbol{A}_{\mathrm{i}}\} + \left[F_{\mathrm{ij}}^{\mathrm{bx}}\right] \{\boldsymbol{F}_{\mathrm{li}}\} + \left[F_{\mathrm{ij}}^{\mathrm{sx}}\right] \{\boldsymbol{X}_{\mathrm{i}}\} \quad i, j = 1,2 \ldots N_{\mathrm{v}}. \tag{10}$$

Matrixes C_{ij}^{f}, K_{ij}^{sx}, K_{ij}^{Fx}, K_{ij}^{cx}, K_{ij}^{gx}, F_{ij}^{bx}, K_{ij}^{Fx}, F_{ij}^{sx} are related to coefficients of equations (14). We can rewrite a form for an element of mesh

$$\left[C_{\mathrm{e}}^{\mathrm{f}}\right] \left\{ \frac{\mathrm{d}\boldsymbol{v}_{\mathrm{vi}}}{\mathrm{d}t} \right\} + \left[K_{\mathrm{e}}^{\mathrm{sx}} - K_{\mathrm{e}}^{\mathrm{Fx}}\right] \{\boldsymbol{v}_{\mathrm{vi}}\} + \left[K_{\mathrm{e}}^{\mathrm{cx}}\right] p_{\mathrm{i}} = \left[K_{\mathrm{e}}^{\mathrm{gx}}\right] \{\boldsymbol{A}_{\mathrm{i}}\} + \left[F_{\mathrm{e}}^{\mathrm{bx}}\right] \{\boldsymbol{F}_{\mathrm{li}}\} + \left[F_{\mathrm{e}}^{\mathrm{sx}}\right] \{\boldsymbol{X}_{\mathrm{i}}\} \quad e = 1,2 \ldots N_{\mathrm{e}}. \tag{11}$$

For the solution we used the standard k-ε model, the standard k-ω model and the SST (Shear Stress Transport Model). The standard k-ε gives exact results and use two equations for turbulent kinetic energy and its dissipation. Model k-ω solves the equations for turbulent kinetic energy and its specific dissipation rate. This model gives better results in the nearness of wall but worse in the distance from wall. The SST model combines and switch between k-ε and k-ω model in order to get the best result in [4], [5] and [6].

Numerical model of heat accumulator layer

There is geometric model of one layer of accumulator in the Fig 1. It consists from 26 PVC pipes in the square configuration. Inside of pipes there are 9,36 liters of modified

$CaCl_2.6H_2O$. The air flows through the layer and transfers heat into pipes. Progress of numerical solution had two parts. First we solved turbulence model and got heat transfer film coefficients. These results were the input of solution for second part when thermal model was calculated. Time dependence of temperature distribution in the layer is final result.

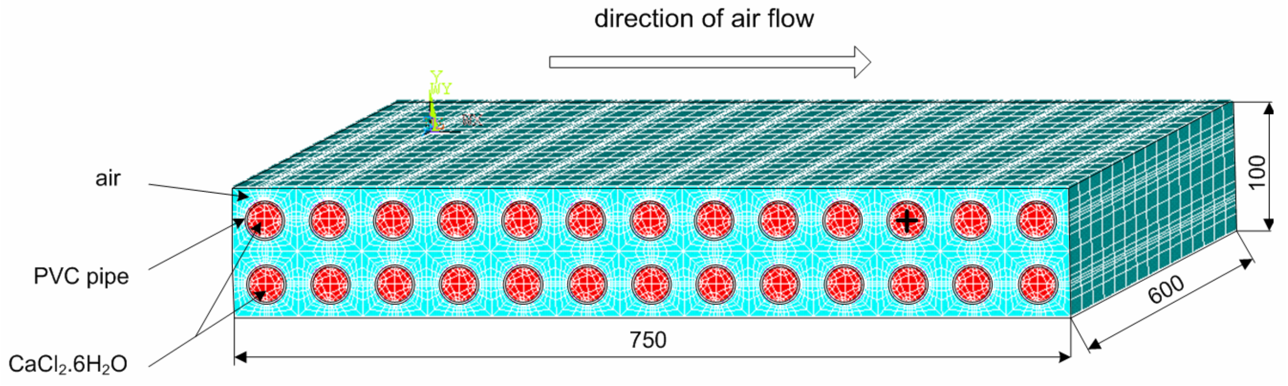

Fig. 1 *Geometric model of layer with mesh of elements*

Initial and boundary conditions: inlet temperature of the air is 50 °C, inlet velocity of the air is 0,4 $m.s^{-1}$, outlet pressure is 101,3 kPa + 10 Pa, initial temperature of the air, PVC and $CaCl_2.6H_2O$ is 20 °C

There are distributions of velocity in Fig. 2 and next results for distribution of the turbulent kinetic energy, dissipation, temperature, and pressure in following pictures.

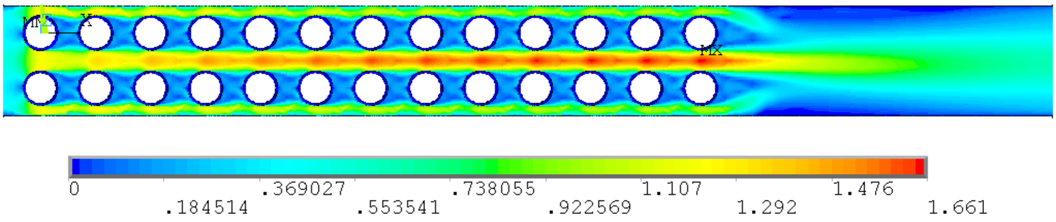

Fig. 2 *Velocity distribution of the air*

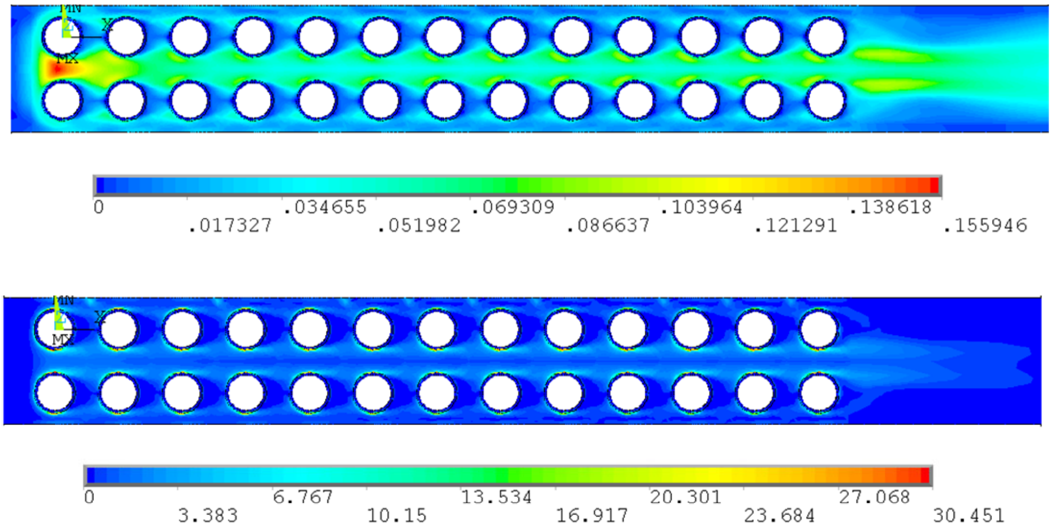

Fig. 3 *Distribution of kinetic energy, dissipation*

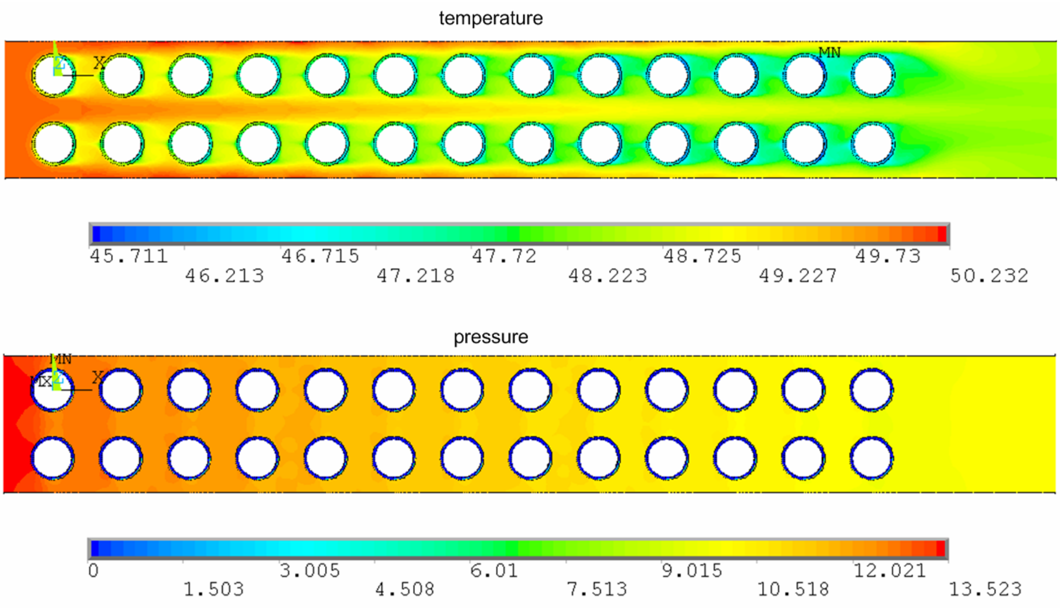

Fig. 4 *Distribution of temperature and pressure*

Conclusion

We presented a numerical model of one layer of heat accumulator. This heat accumulator exploits advantages and suppresses disadvantages of water and gravel accumulator. The numerical model was solved by means of FEM in ANSYS software. We solved coupled problem of air flow turbulence, heat transfer, conduction, convection, and also phase change. There are also problems with solution stability during iteration in ANSYS FLOTRAN. Finite element method (FLOTRAN) is not suitable for turbulence modeling. The application of finite volume method (e.g. ANSYS CFX, FLUENT) for more complicated tasks is necessary.

Acknowledgements

The paper was prepared within the framework of the research plan No. MSM 0021630516 of the Ministry of Education, Youth and Sports of the Czech Republic.

References

1. FIALA,P *Model of Induction flowmeter DN100*. Research report no.2/01, Laboratoř modelování a optimalizace polí v elektromechanických systémech. FEI VUT BRNO, 21.6.2001, Brno, Czech Republic
2. *Ansys User's Manual.* Huston (USA): SVANSON ANALYSYS SYSTEM, Inc., 2003.
3. SPECHT, B. Modellierung von beheizten laminaren und turbulenten Strömungen in Kanälen beliebigen Querschnitts. Braunschweig (Germany): Technische Universität Carolo-Wilhelmina., 2000.
4. PISZACHICH, W.S. Nonlinear Models of Flow, Diffusion and Turbulence. Leipzig (Germany): Teubner Verlagsgessellschaft, 1985.
5. WILCOX, D.C. Turbulence modeling for CFD. La Canada (California, USA): DCW Industries, Inc., 1994.
6. ZHANG, Y. Finite Elemente zur Berechnung instationärer Strömungen mit bewegten Wandungen. Stuttgart (Germany): Universität Stuttgart., 1996.

ELECTROLYZER FOR HYDROGEN PRODUCTION

M. Kunovjánek[1]*, J. Vondrák*[1, 2]*, M. Sedlaříková*[1]

[1] Department of Electrical and Electronic Technology, University of Technology Brno,
602 00 Brno, Czech Republic
[2] Institute of Inorganic Chemistry of the ASCR, v. v. i., 250 68 Řež near Prague,
Czech Republic

Corresponding author: Miroslav Kunovjánek (xkunov04@stud.feec.vutbr.cz)
Phone: +420 605 933 898

Abstract

The article is concerned with a production of hydrogen and oxygen through by the help of electrolytic process in a device called electrolyzer. The basis of the work is assurance of the best efficiency of this process by testing a variety of materials and surfaces of electrodes, and testing different types of alkalic electrolytes.

Introduction

Hydrogen is at the present time spoken as fuel of the future. Production of hydrogen by the help of electrolytic process is revealing as the most profitable method, because traditional methods of hydrogen production result from elaboration of earthy gas, where rising toxic and greenhouse gases during the reaction. Two laboratory electrolyzers, a big and a small, were proposed for these demands, where all measurings were proceeded. The basis of the work is assurance of the best efficiency of electrolytic process in electrolyzer. We are trying to achieve this, mainly, by testing on a variety of materials for electrodes and by making of new surfaces of electrodes with galvanic metallization.

Experimental

For measure on electrolyzer we will use 5 MOL KOH electrolyte, because this concentration of KOH electolyte has the biggest conductivity. At present, we solve the problem of electrolyzer membranes. Pristine membranes Ralex® from MEGA Company were found to be unusable. It was found that in long-term use they evoke degradation of electrolyte. There are currently successfully tested membranes from non-woven polypropylene textile. These membranes have excellent properties for the long-term use of elektrolyzer, but there are doubts about their gas proofness, especially when the pressure in elektrolyzer chambers is different.

The quality of the electrolyte has a major impact on the efficiency of electrolysis. Electrolyte is changing during the electrolysis (lose H2O). For this reason, the exchange of the electrolyte during the electrolysis has a major impact on its efficiency (see Figure 1).

During the measurement of electrolyte was completely replaced after 5 (10, 15, 20, 25, 35, 55) minutes.

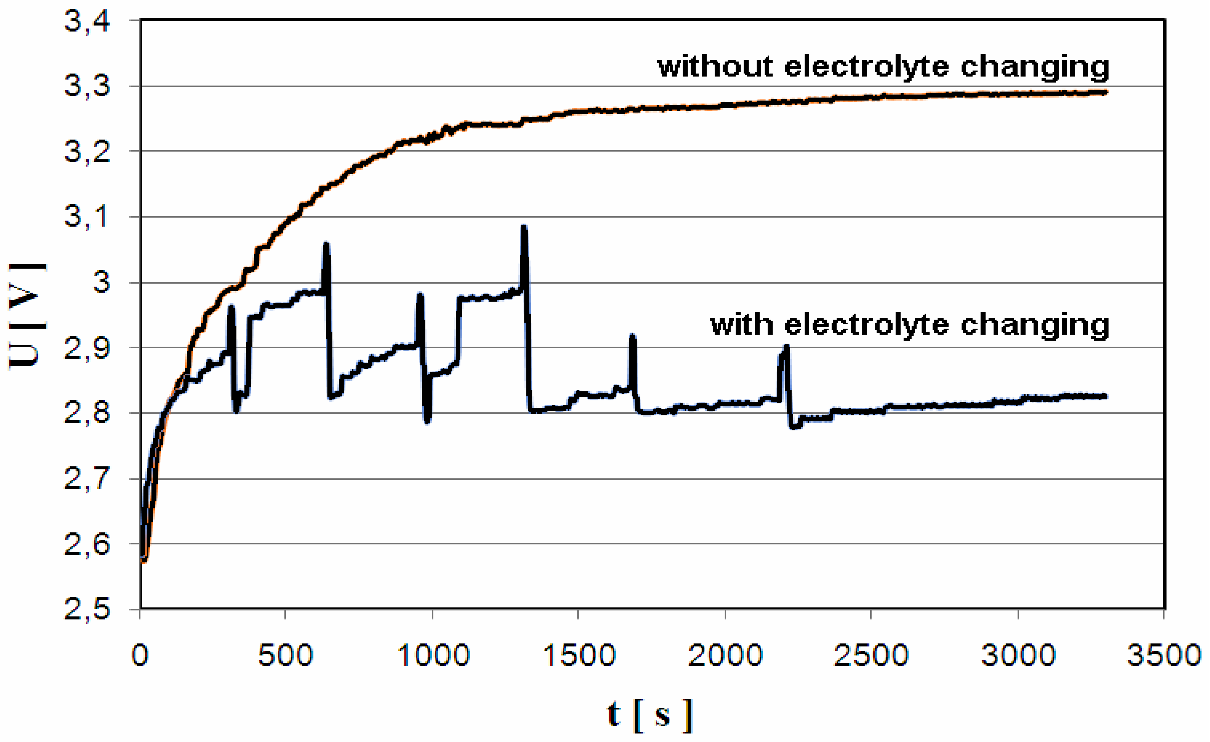

Fig. 1 *Measurements on elektrolyzer with and without electrolyte changing*

Other way to incrase efficiency of electrolyzer is extension of active surface of electrodes by the help of patent no. 125479 [2]. On surface of nickel or brass material we built-up Zn-Ni surface and sequentially we ate away redundant zinc. Four samples of electrodes was created for this experiment. Individual samples was differ in used basic material and manufacturing process. By the help of Voltametry was chosen sample with the best parameters. From the graph no. 2 is apparented that the best characteristics have the samples number 3 and 4. Extension of active surface of electrodes for electrolyzer was implemented by the same manufacturing process, which the sample with best parameters was created. In terms of economical was chosen samplne number 4.

Table 1 *Materials of electrodes, surfaces and manufacturing processes*

sample	basic material	created surface	comment
1	brass	Zn - Ni	Hull's cellule - 0,8 až 4 A/dm^2
2	nickel	Zn - Ni	Hull's cellule - 0,8 až 4 A/dm^2
3	nickel	Zn - Ni	Equable surface, 2,5 A/dm^2
4	brass	Ni + Zn - Ni	Equable surface, 1 A/dm^2 + 2,5 A/dm^2

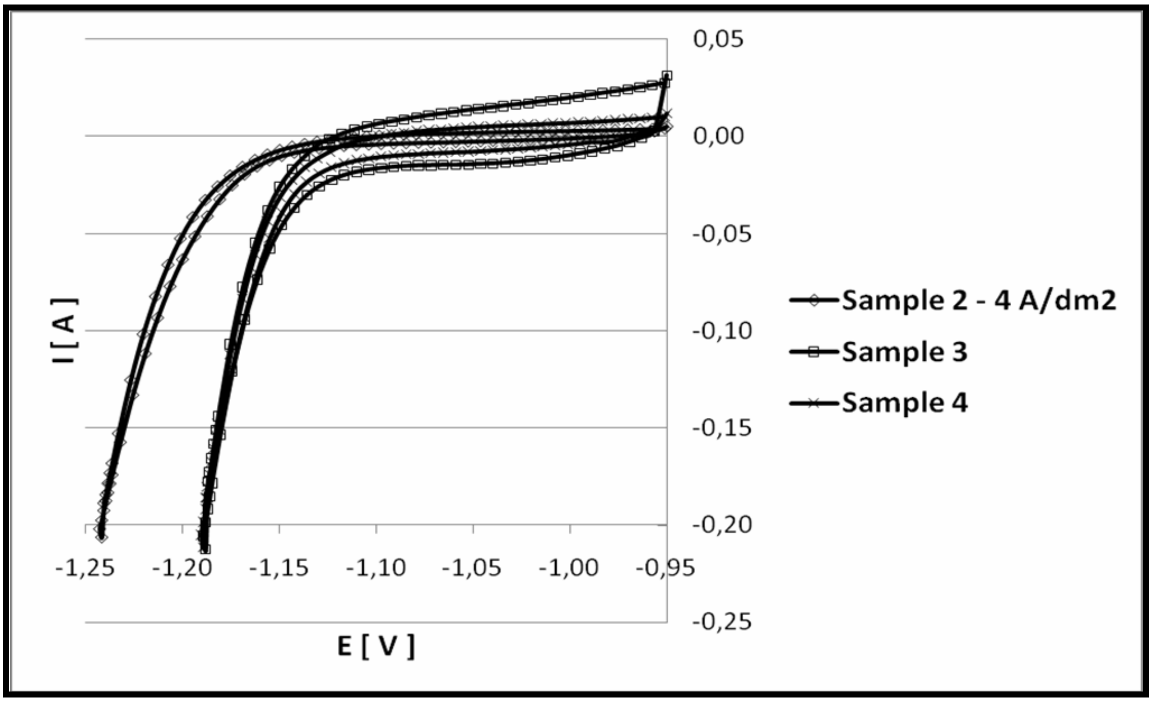

***Fig. 2** Polarization curves of 3 best samples, measured by voltametry*

Measurements were performed on a small electrolyzer with only two electrodes. To avoid mixing the resulting gases and creation of explosive mixtures we separate electrode spaces using membrane. We use membranes Ralex from MEGA company from Stráž pod Ralskem, particular type AMH5E-HD. It was first measured with the original electrodes, then with the new electrodes with extension of active surface. With using electrodes with extension of active surface supervened downtrend of electrolyzer voltage against original (only nickel) electrodes about 0,2 - 0,4V.

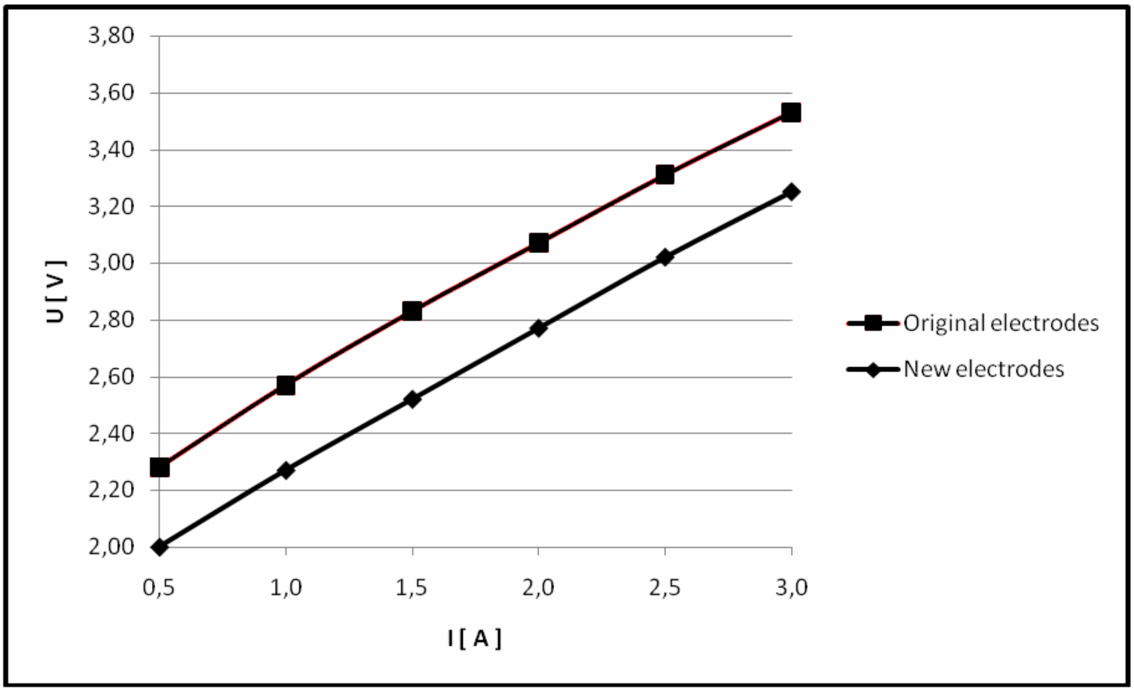

***Fig. 3** Electrolyzer voltage: confrontation of original and new electrodes with 6 mol KOH electrolyte*

Efficiency of electrolyzer determine as rate of theoretically used energy and really used energy. By using new electrodes with extended active surface in electrolyzer was his efficiency with identical conditions of measuring extended about 8,68% (counted for 5 mol KOH electrolyte, 0,5A). On this account, this method is proving as very perspective.

Table 2 *Efficiency of small electrolyzer - 5 mol KOH - 2 electrodes*

Electrodes	**I [A]**	**U [V]**	**t (10 cm^3) [s]**	**t (1 m^3) [h]**	**W_s [Wh]**	**W_t [Wh]**	**η_{el} [%]**
Original	0,5	2,28	150	4166,7	4750,0	2943,2	**61,96%**
New	0,5	2,00	150	4166,7	4166,7		**70,64%**
efficiency difference							**8,68%**

Conclusions

Purpose of this work was to create galvanic deposition of metals with electrocatalytic properties. This galvanic deposition will be used to prepare the high efficient electrodes for electrolysis cell for hydrogen production. It is clear, that we can create suitable surface for electrodes. Hence, the reduction of energy by their use is possible. Increased efficiency of elektrolyzer of 8.68% means in the case of large-scale use of elektrolyzer significant energy savings. Continuation of the work will be another increase of efficiency of electrolyzer and optimization of electrode processes. It was also found that exchange of the electrolyte during the electrolysis has a large influence on its efficiency.

Acknowledgements

This article was supported by the Ministry of Education, Youth and Sports, Czech Republic (project MSMT 0021630516).

References

1. VONDRÁK, J., BALEJ, J.: Influence of Mercury on Hydrogen Overvoltage on Solid Metal Electrodes I. Stationary Polarization Curves of Hydrogen Deposition on Pure and Poisoned Electrodes. Electrochim. Acta 15,1653(1970)
2. VONDRÁK, J., BALEJ, J., PASEKA, I.: Způsob výroby aktivních elektrod s nízkým přepětím. čs. pat. c. 125479, 15.12.1967
3. KNOTEK, T.: Diplomová práce, Ústav elektrotechnologie VUT, Brno 2007
4. KAŇA, O.: Tvorba elektrod pro elektrolyzér [Semestrální projekt]. Vysoké učení technické v Brně, FEKT, Rok obhajoby: 2008
5. VONDRÁK, J., SEDLAŘÍKOVÁ, M., BARATH, P.: Optimalizace a vývoj nového elektrolyzéru vody, Brno: Vysoké učení technické v Brně, zpráva grantu VaV SN/171/05 – příloha č. 4
6. BĚHAL, Ž.: Slitinová lázeň zinek/nikl SLOTOLOY ZN 80. Pokyny pro práci s lázňí. Rok 2006

AUTOMATIZED MEASUREMENT STATION FOR TESTING OF PHOTOVOLTAIC SYSTEM

R. Bilko, R. Lábus, P. Bača,

Department of Electrical and Electronic Technology, Brno University of Technology,
602 00 Brno

Corresponding author: Radek Bilko (xbilko00@stud.feec.vutbr.cz)

Introduction

The main objective of the project was to create the unique laboratory exercise for subject called Alternative energy resources. This laboratory exercise serves to analyzing of the photovoltaic system and determining of operational status of storage batteries and capacity loss of storage batteries in photovoltaic system simulated in various modes of operation. Created measurement station allows a better development of education especially for students of Master's studies, it helps students to improve their ability of orientation in question of photovoltaic systems. The conception of measurement station is discussed with the teachers to make provision for the requirements of students and also ensures the modernization of education.

The current status of the problem at issue

Photovoltaics has become one of the fastest growing fields. In terms of trends the importance of a photovoltaic system as a source of energy is constantly increasing due to perfecting of production technologies, while increasing the efficiency of solar panels and price lowering of the solar panels.

It offers solutions for the energy saving and environmentally sound utilization of alternative sources.

The solar system ensures the conversion of solar energy to electricity, and the further processed to maximize recovery, ie., which provides distribution of electricity, the conversion to such we need (change in voltage), storage (storage batteries), distribution (eg, into the grid) and end-use (appliance).

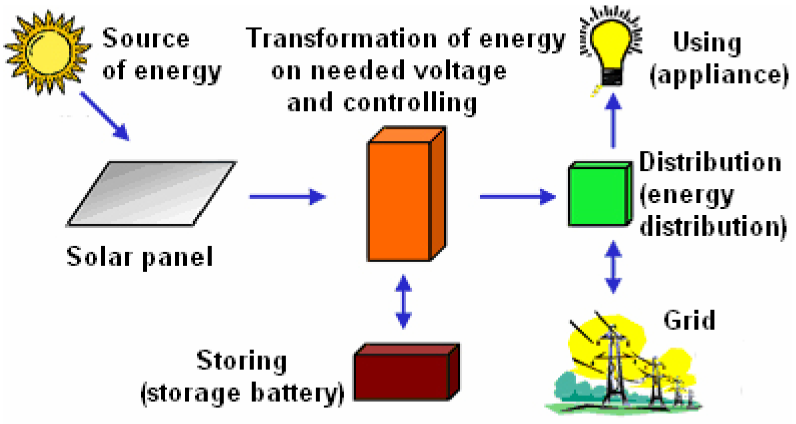

***Fig. 1** Complete solar system [1]*

According to the considered sample performance must combine solar cells into modules, panels and solar arrays (see Figure 2).

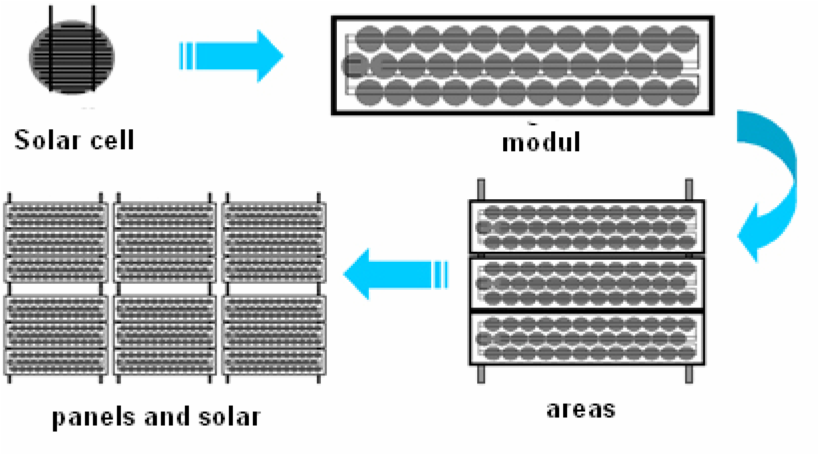

Fig. 2 *Solar cells, modulus, panels and solar areas [1]*

Desctription of measuring station

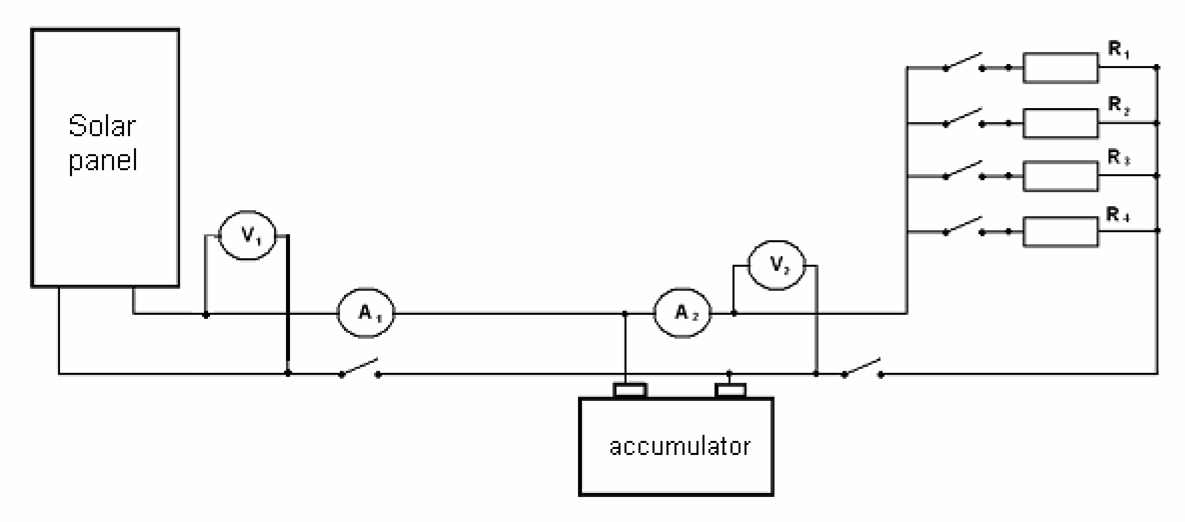

Fig. 3 *Overview diagram of measuring station wiring*

Automatized measurement station is compiled from three function blocks:

1. Solar panel with the pyranometr for ascertaining of intensity of incident solar radiation.
2. Accumulator to which stores and subscribes electric energy oneself.
3. Resistor set serves for inducing of different regime of endurance.

We designed the full automatic measuring station that is created by the digital multimetr for the measurement of voltage and amperage on the solar panel, storage battery and endurance. Multiplexer (L4421A by the company Agilent) serves to switching of voltage inputs. For controlling of endurance and disconnecting of storage battery or solar panel in achieving of limit affections of discharging or overcharging we used the wattage switching card (L4421A by the company Agilent). All the equipments of particular function blocks are performed in VEE 8.0 program.

Fig. 4 *Automatized measurement station*

Fig. 5 *Solar panels on the building roof*

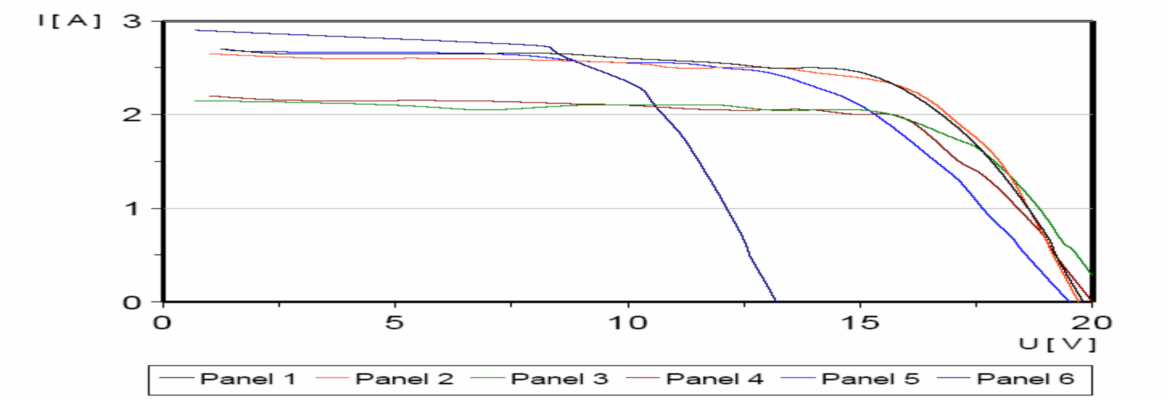

Fig. 6 *Voltage-current characteristics of solar pannels*

Measurement proceeded during highest solar activity sky was clean with minimum intensity variation. This conditions except the influence of negative atmospheric effects like clouds atc. Obtained characteristics for all panetls are shown on figure 6. In recent days long term measurement is run over on the automatized station. The goal is to simulate different types of loads and accumulator regimes with their description, and to find influence on affectivity of solar panels and accumulator power states.

Acknowledgment

Ministry of Education of Czech Republic, Project 2422/2009

References

1. http://science.howstuffworks.com,

DEPOSITING OF CARBON LAYERS FOR SUPERCAPACITORS

P. Dvořák, P. Stejskal

Faculty of electrical engineering and communication, Brno University of Technology,
602 00 Brno

Corresponding author: Petr Stejskal (xstejs08@stud.feec.vutbr.cz)
Phone: +420 720 323 484
Fax: +420 317 723 092

Introduction

Carbon based materials are commonly used in electrode substances of supercapacitors because of their low cost, chemical stability and relative high specific surface area (thousands m^2 per gram). There are many methods how to build up the carbon layers. This article treats one of them – the stencil printing. Similarly to the function of the solder paste in the process of surface mount technology, the material is printed through a stencil. This method guarantees the same thickness and area of the layer on the entire surface. The reproducibility of stencil printing is very good.

Experimental

Stencil printing is a very exact method of deposition. It has a problem with flatness of surface when is applied on large or oversize areas. It is caused by penetration of squeegee to volume of deposited material. Our stencil has (5 x 5) mm aperture and 200 µm thickness. At the figure 1 there is a photo of the stencil.

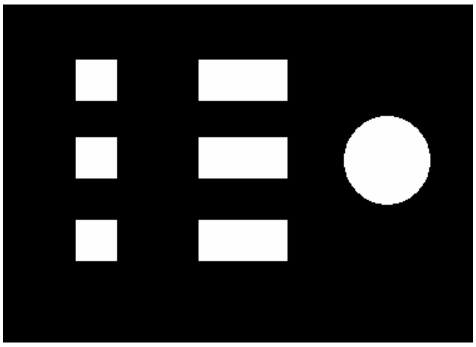

***Fig. 1** Photo of stencil*

The main part of the electrode in supercapacitors is carbon based material. Commercial available carbon black Vulcan XC72R was used for this experiment. Vulcan XC72R was heated and stirred in water with ethanol for 1 hour. The ratio of carbon, water and ethanol was 0.5 g : 50 ml : 10 ml. At the end 5 wt% PTFE was added as a binder. After 24 hours mixture was washed by distilled water and dried at 100 °C for 1 hour. The dried mixture was dilute by water (0.5g : 0.5 ml) and blended in a ultrasonic bath for 30 minutes before printing. Carbon paste was printed on nickel gauze and pressed by three different forces. Created electrodes were dried at 100 ^{o}C for 30 minutes.

Electrode properties were measured by the cyclic voltammetry in a three electrode cell in 0.5 M electrolyte of $LiClO_4$ and propylen carbonate. Lithium electrodes were used as reference and counter electrodes. The three electrode cell was placed in the dry box with argon atmosphere on the ground of lithium oxidation on the air.

Results and Discussion

Table 1 shows excellent reproducibility of screen printing process. Main result of this article is very good reproducibility of capacity of produced supercapacitors. Dispersion of capacity on the higher force is (2 – 5) F/g. The capacity was calculated from voltammograms by the formula.

$$C = 0,5 \cdot \Delta I / \alpha \qquad [F] \qquad (1)$$

where ΔI is a subtraction of the currents for one voltage and α is the scan rate. All results are in the table 1.
The highest specific capacity reached samples pressed by 4454 N. It could be caused by reduced resistivity between carbon black particles and also between carbon paste and nickel gauze.

Table 1 *Table of prepared samples.*

Force [N]	Weight of nickel gauze [g]	Weight of Electrode [g]	Weight of Printed Material [g]	Capacity of Electrode [F/g]
2227	0.044	0.047	0.003	63
2227	0.057	0.060	0.003	65
2227	0.070	0.073	0.003	71
3649	0.066	0.068	0.002	81
3649	0.052	0.054	0.002	84
3649	0.070	0.072	0.002	86
4454	0.079	0.081	0.002	147
4454	0.053	0.055	0.002	142
4454	0.064	0.066	0.002	144

Conclusions

Stencil printing has a good possibility for use in deposition of carbon layers because it has predefined same parameters of thickness in all area in this case. The influence of pressing force at specific capacity of electrodes was also shown.

Acknowledgements

This work was supported by the Ministry of Education (project MSM0021630516) and The Grant Agency of the Academy of Sciences of the CR (project KJB208130902).

References

1. B.E., Conway: *Elektrochemical Supercapacitors: Scientific Fundament and Technological Application, Kluwer Academic, New York, 1999, 698 s,ISBN 0-306-45736-9*
2. A.G., Pandolfo, A.F., Hollenkamp: Journal of Power Sources **157** (2006) 11–27.

RESEARCH OF THIN Ni-Zn ALLOY

T. Knotek, *J. Vondrák*

Faculty of electrical engineering and communication, Brno University of Technology, 602 00 Brno

Corresponding author: Tomáš Knotek (xknote06@stud.feec.vutbr.cz)

Abstract

Preparation of Ni-Zn alloys by electrodeposition and their electrochemical properties is described in this contribution. Zn component was extracted from the layers by HCl solutions for their activation. Electrocatalytic properties of the layers were estimated by the current – voltage curves in KOH solution. The best layer was selected on these bases.

Introduction

This work was created for better understanding to galvanic deposition of metals and electro catalytic properties of these depositions. This knowledge will by used to design best electrodes for electrolytic cell for hydrogen production.

Experimental

Ni-Zn alloys were electrodeposited, onto brass electrodes and nickel electrodes, using a commercial alkaline electrolyte (SLOTOLOY ZN 80 - produced by Dr.-Ing. Max Schlötter GmbH & Co.KG, SRN) of composition strictly identical to the industrial electrolyte, at 32 °C temperature. The chemical composition of the electrolyte was given in Table 1.

Table 1 *Composition of alkaline plating bath*

Compound	Concentration
NaOH	120 g l^{-1}
SLOTOLOY ZN 80	115 ml l^{-1}
Zinc	8 g l^{-1}

The working electrode area varied with the method of surface characterization. The plating cell was provided with an air bubbling. Parameters of galvanic deposition are given in table 2. The samples were after deposition immersed in hydrochloric acid (5% HCl, for 30s) for their activation consisting in dissolution of zinc from them.

***Table 2** Parameters of galvanic deposition*

Surface material	**Time [min]**	**T [°C]**	**I [A/dm^2]**
Brass	9	32	2,5
Brass	6	32	4
Nickel	9	32	2,5
Nickel	6	32	4

Then samples were tested with program GPES on device AUTOLAB (Eco Chemie). The supporting electrolyte was 1M KOH in distilled water. Measuring apparatus has three compartements for reference, counter and work electrodes. The samples were connected as work electrode, Saturated Calomel Electrode was connected as reference electrode and platinum electrode was connected as counter electrode. The device is shown in Fig. 1. Samples were tested in described way by means of cyclic voltammetry.

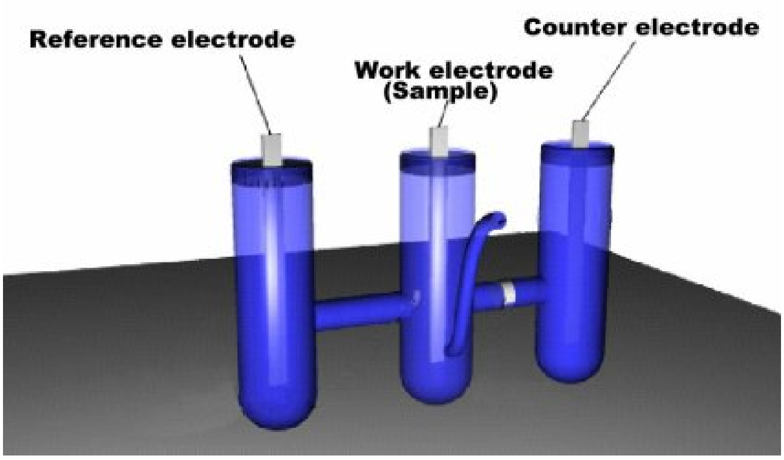

***Fig. 1** Connection diagram*

Results and discussion

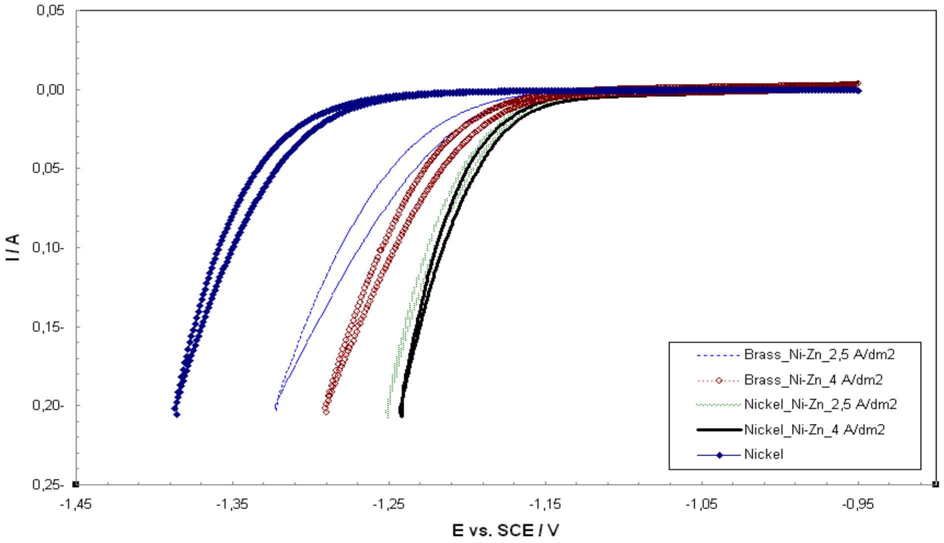

***Fig. 2:** Voltage-current curves*

How we can see in graph of all samples, the sample Nickel-ZnNi_4 is the most acceptable because the voltage of hydrogen evolution is the highest of them and the energy loss in the electrolytic cell would be lowest. The samples Nickel-Ni-Zn_2,5 and Nickel-Ni-Zn_4 have very similar curves and difference potential is about 0,01V. It is because of nickel surface. The samples with brass surface were bad. Difference potential between Nickel surface a Nickel_Ni-Zn_4 is about 0,14V.

Conclusion

Purpose of this work was to create galvanic deposits of metals with electro catalytic properties. This galvanic deposition will be used to create the best electrodes for electrolysis cell for hydrogen production. It is clear, that we can create suitable surface for electrodes. Hence, the reduction of energy requirement by their use is possible. Further, the starting preposition of activation by addition of zinc was proved successfully.

Acknowledgments

This work was supported by Grant Agency of Czech Republic (grant NO. MSM0021630516)

References

1. G. Vatankhah, J. Lessard, G. Jerkiewitz: Electrochimica Acta 48 (2003) 1613-1622
2. Barek J., Opekar F., Štulík K. Elektroanalytická chemie KAROLINUM
3. Regner A. Elektrochemické pochody v anorganickém průmyslu SNTL
4. Ramazan Solmaz, Gülfeza Kardas: Hydrogen evolution and corrosion performance of NiZn coating, received in revised form 9 December 2005; Dostupné online z www.sciencedirest.com.
5. Vladimír Krejčík: Povrchová úprava kovů I (Pro 2. ročník SOU), SNTL Praha 1987, 168 stran, 04-203-87
6. Vladimír Krejčík: Povrchová úprava kovů I (Pro 2. ročník SOU), SNTL Praha 1988, 312 stran, 04-229-88

STUDY OF HYDROGEN EVOLUTION ON PIGE AND HMDE ELECTRODES

K. Klosova[1], *P. Barath*[1,2,3], *L. Trnkova*[1]

[1]*Department of Chemistry, Faculty of Science, Masaryk University, Kotlarska 2, CZ-611 37 Brno, Czech Republic*
[2] *Institute of Electrical and Electronic Technology, Brno University of Technology, 602 00 Brno, Czech Republic*
[3] *Institute of Inorganic Chemistry of the ASCR, v. v. i., 250 68 Řež near Prague, Czech Republic*

Corresponding author: Peter Barath (barath@feec.vutbr.cz)

Abstract

Hydrogen evolution on a paraffin impregnated graphite electrode (PIGE) and hanging mercury drop electrode (HMDE) has been studied by linear sweep voltammetry (LSV) and elimination voltammetry with linear scan (EVLS). NaCl and Na_2SO_4 solutions at pH ranging from 2 to 4.5 have been used, containing either chloride or sulphate ions. LSV was performed at various scan rates using the step of 2 mV/s.

Introduction

The hydrogen evolution reaction (HER) is one of the most fundamental reactions in electrochemistry and has to be taken into account in many fields of technology. For example, in the case of electroplating, the hydrogen generation is an undesirable process, often causing porosity of deposits. On the other hand, hydrogen fuel cells are very promising in the area of power engineering and therefore the research on hydrogen evolution on various electrodes is of utmost importance. Even though Volmer-Heyrovsky mechanism of HER is generally accepted, all the processes participating in hydrogen evolution are not fully understood. A new electrochemical method - EVLS is considered prospective for the investigation of such processes. Therefore, the process of hydrogen evolution on two different electrodes (PIGE and HMDE) has been examined using LSV. Since LSV is a potential controlled electrochemical method and the obtained current is scan rate dependent, the measured data may be processed by EVLS. The principle of EVLS consists in eliminating and conserving various particular currents, of which the total recorded current is composed. The elimination process than provides further information on electrochemical mechanisms 1.

For the partial currents (diffusion current I_d, kinetic current I_k, charging current I_c) six elimination functions were derived as a linear combination of total currents measured at different scan rates. The most suitable elimination functions for our measurements are E1 and E4:

E1 (elimination of I_k with the conservation of I_d and display of 1.707 I_c):

$$f(I) = -3.414 I_{1/2} + 3.414 I \quad (1)$$

E4 (simultaneous elimination of I_k and I_c with the conservation of I_d):

$$f(I) = -11.657 I_{1/2} + 17.458 I - 5.828 I_2 \quad (2)$$

I is the reference voltammetric current, $I_{1/2}$ and I_2 are total voltammetric currents measured at one half and double of the reference scan rate.

The functions E1 and E4, which eliminate I_k, can be used for the expansion of an available electrode potential range, which is very significant for study of HER.

The experiments on hydrogen evolution has been conducted using two different solutions (NaCl, Na_2SO_4), containing either chlorine or sulphate. NaCl solution is also used for the production of chlorine and sodium hydroxide. The anode, on which the chlorine is evolved, is usually composed of graphite. Mercury or iron electrode is commonly used as the cathode, on which the hydrogen is evolved. During hydrogen evolution, NaOH cumulates at the vicinity of the negatively charged electrode due to the reaction:

$NaCl + H_2O \rightarrow 1/2Cl_2 + 1/2H_2 + NaOH$ (3)

If the cathode and anode compartments are not divided by a diaphragm, the hydroxyl ions can penetrate to the anode one and, apart from the chlorine evolution, hypochlorite ions are also produced.

In the case of the mercury electrode, sodium amalgam is produced according to the equitation:

$Na^+ + e + xHg \rightarrow NaHgx$ (4)

The electrolyte containing sulphate ions was composed of Na_2SO_4 solution. Oxidation of sulphate ions, resulting in the production of persulphate anions ($S_2O_8^{2-}$), is used among others for hydrogen peroxide manufacturing. The oxidation proceeds (for example on a platinum electrode) according to the reaction mechanism:

$SO_4^{2-} \rightarrow SO_4- + e$
$2SO_4- \rightarrow S_2O_8^{2-}$

Moreover, in acidic medium the persulphate anions are hydrolysed on hydrogen peroxide and sulphate. 5

Hydrogen evolution from NaCl and Na_2SO_4 solutions, containing boric acid, has also been observed during nickel electrodeposition on PIGE 6.

Experimental

Hydrogen evolution was investigated using three-electrode cell, which was composed of PIGE or HMDE (working electrode), Pt electrode (counter electrode), and Ag/AgCl/3M KCl (reference electrode). The equipment used for the measurements included Autolab Potentiostat 302N - EcoChemie and 663 VA Stand – Metrohm (Fig. 1). Nova 1.5 (Autolab) was used for controlling the experiments and data treatment. Microsoft Excel was employed during EVLS calculations.

The electrolytes used for the experiments consisted of 0.5M NaCl and 0.5M Na_2SO_4. The pH of the electrolytes was ranging from 2 to 4.5 and was adjusted by HCl (NaCl solution) or H_2SO_4 (Na_2SO_4 solution). The LSV curves were recorded at scan rates of 160, 80, 40, 20, 10 mV/s.

Results and discussion

A. PIGE:

It has been found that the process of hydrogen evolution differs in dependence on pretreatment of PIGE. The peak representing hydrogen evolution is shifted in the case of PIGE polished with an emery paper. Polished and unpolished PIGE behave as two different systems. The height of the peak does not only depend on the scan rate but also on the time left for the regeneration of the electrode, PIGE polishing, and on the pH (Fig. 1, 2). Peaks obtained at higher pH values are significantly smaller in comparison to lower pH values. The peak obtained using polished PIGE almost disappear at the pH higher than 3. If the electrode remains unclean of the previous reaction the peak is recorded even at higher values of pH. However, at the pH of 4.4 (the highest pH used for the experiments) none peak is visible regardless of the electrode. The diminishing peak at higher pH values has also been recorded during experiments carried out in Na_2SO_4 solutions (Fig. 3).

B. HMDE

The LVS using HMDE turned out to be very complicated due to the hydrogen bubbles affecting the mercury drop. In the case of successful measurement, the peak has been observed even at higher pH – 4.4 (Fig. 4).

The position of the peak was approx -1.1 - -1.2V in NaCl solutions and -1.4 - -1.5V in Na_2SO_4 solutions.

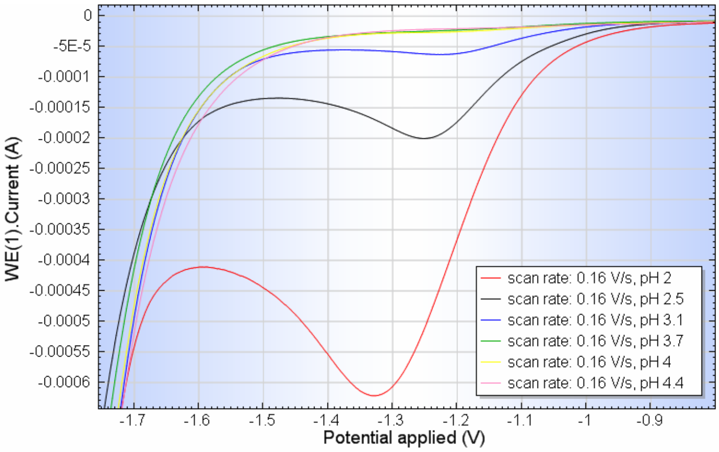

***Fig. 1** PIGE/0.5M NaCl, scan rate: 160 mV/s, LVS*

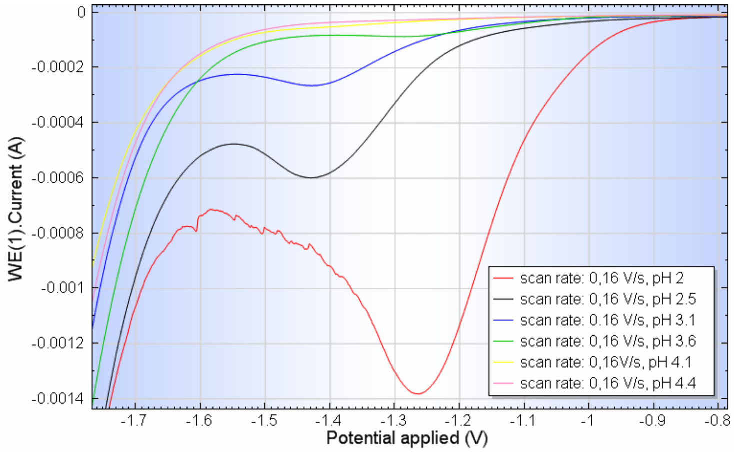

Fig. 2 *PIGE/0.5M Na_2SO_4, scan rate: 160 mV/s, LVS*

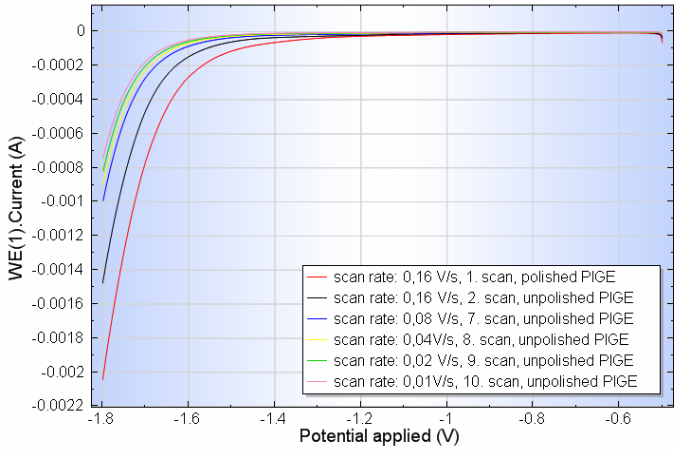

Fig. 3 *PIGE/0.5M Na_2SO_4, pH 4.4, LVS*

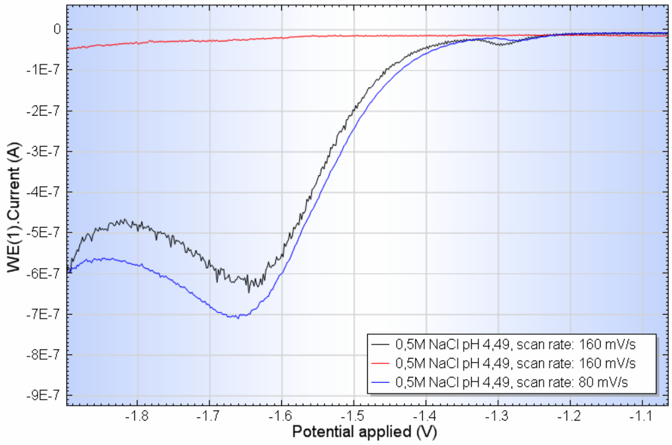

Fig. 4 *HMDE/0.5 M NaCl, pH 4.4, LVS*

Conclusion:

PIGE in chloride and sulphate electrolytes was used to obtain deeper insight in the mechanism of HER. Mercury electrode was used as the reference system.

Some differences in electrochemical behaviour of both electrolytes were observed. The specific adsorption of chloride anions on the surface of PIGE caused a shift of hydroxonium ion reduction potential to more negative values and a decrease of reduction current. In comparison to HMDE, voltammetric curves obtained using PIGE are more reproducible.

Acknowledgements

This work was supported by *INCHEMBIOL* (MSM 0021622412), BIO-ANAL-MED (LC06035), GACR (106/09/H035) and Ministry of Education, Youth and Sports, Czech Republic (MSM 0021630516 ČR).

References

1. L. Trnková, Elektrochemické eliminační metody, Chem. Listy 95, 518-527 (2001), pp 518-526.
2. L. Trnková, O. Dračka, J. Electroanal. Chem. 413 (1996) 123.
3. O. Dračka, J. Electroanal. Chem. 402 (1996) 18.
4. L. Trnková, R. Kizek, O. Dračka, Electroanalysis 12 (2000) 905.
5. Jiří Dvořák, Jiří Koryta, Vlasta Boháčková, Elektrochemie, Academia – Praha, 1975, page 416-417.
6. R. Oriňáková, M. Strečková, L. Trnková, R. Rozik, M. Gálová, Comparison of chloride and sulphate electrolytes in nickel electrodeposition on a paraffin impregnated graphite electrode, Journal of Electroanalytical Chemistry 594 (2006), 152-159.
7. M. Strečková, R. Oriňáková, R. Rozik, L. Trnková, M. Gálová, Helvetica Chimica Acta 89 (2006), 622-634.

10th ABAF

BRNO 2009

Advanced Batteries, Accumulators and Fuel Cells

Fuel Cells

CHARACTERISTICS OF METHYL CELLULOSE-NH_4NO_3-PEG ELECTROLYTE AND APPLICATION IN FUEL CELLS

N. E. A. Shuhaimi, N. A. Alias, M. Z. Kufian, S. R. Majid and A. K. Arof

Center for Ionics, University of Malaya, 50603, Kuala Lumpur, Malaysia

Corresponding author: A. K. Arof (akarof@um.edu.my)
Phone: +603-79674085
Fax: +603-79674146

We report the viability of methyl cellulose as a membrane in fuel cell. Methyl cellulose was used as polymer host, ammonium nitrate as salt and poly (ethylene glycol) as plasticizer. Conductivity measurement was carried out using electrochemical impedance spectroscopy. The room temperature conductivity of pure MC film is $(3.08 \pm 0.63) \times 10^{-11}$ S cm^{-1}. The conductivity was increased to $(2.10 \pm 0.37) \times 10^{-6}$ S cm^{-1} on addition of 25 wt. % NH_4NO_3. By adding 15 wt. % of PEG 200 to the highest conducting sample in MC-NH_4NO_3 system, the conductivity was further raised by two orders of magnitude to $(1.07 \pm 0.32) \times 10^{-4}$ S cm^{-1}. The highest conducting sample containing 15 wt. % PEG was used as membrane in PEMFC and was operated at room temperature. From voltage-current density characteristics, the internal resistance of the device was estimated to be 372 Ω and the short circuit current density ~30 mA cm^{-2}.

THERMAL STABILITY OF PROTON-CONDUCTING MATERIALS OF THE «BASIC POLYMER»-H_3PO_4 TYPE

O. Chervakov[1], M. Andriianova[1], E. Shembel[1,2], I. Maksyuta[1], V. Ryabenko[1]

[1]SHEI "Ukrainian State Chemical Technology University", 49005 Dnipropetrovs'k, Ukraine
[2]Enerize Corporation, Florida, USA

Corresponding author: O. Chervakov (chervakov@email.dp.ua)
Phone, Fax: +380 562 472 491

Introduction

Development of new technologies in the field of highly-efficient electro-chemical devices (fuel cells, solar batteries, gas sensors, lithium power sources, and the others) is impossible without development of the polymer materials with the increased complex of operational properties.

Investigations concerning creation of the membranes for fuel cells operational within the range of increased temperatures (120-150°C) are of specific interests. Utilization of the polymer membranes with a high ionic conductivity and stability in the specified temperature range allows to simplify significantly the fuel cell design and to increase the efficiency of its work.

Earlier, we proposed the synthesis method of cross-linked ammonium interpolymer complexes (AIPC) [1]. By their doping with orthophosphoric acid, there were produced the proton-conducting materials of the class of "basic polymer-inorganic acid" having the high ion conductivity (10^{-4}–10^{-2} S/cm) within the 20°C-150°C temperature range.

Estimation of the thermal stability of cross-linked AIPC and the proton-conducting materials on their basis under the condition of long high temperature effect (up to 150°C) was the aim of this work.

Experimental

Synthesis of the film materials based on AIPC was carried out during two stages. At the first stage the solution of for-interpolymer complex was produced by the joint condensation of epichlorohydrin homopolymer or the copolymer of epichlorohydrin with ethylene oxide and poly-4-vinylpyridine (molar ratio 1:1) in the medium of dimethylformamide at constant mixing and 40-50ºC temperature during 1.0-1.5 hours.

At the second stage, the solution of for-inter polymer complex cooled up to 20-25°C was poured out on a glass or fluoroplastic substrate. Then, the final condensation was carried out for 1.5-2.0 hours at 100-120ºC with the simultaneous removal of solvent up to obtaining the insoluble in water and the organic dissolvers of the space cross-linked film material.

The produced membranes based on AIPC (I) are characterized by the ion exchange capacity (IEC) of 3.7 meq/g and the conductivity at the level of $6.5 \cdot 10^{-6}$ S/cm in a dry condition.

Synthesis of the proton-conducting materials was realized by AIPC doping with the 50% solution of orthophosphoric acid. AIPC membranes in Cl-form (I), AIPC in $H_2PO_4^-$-form (II) and AIPC in $H_2PO_4^-$-form containing the surplus acid (III):

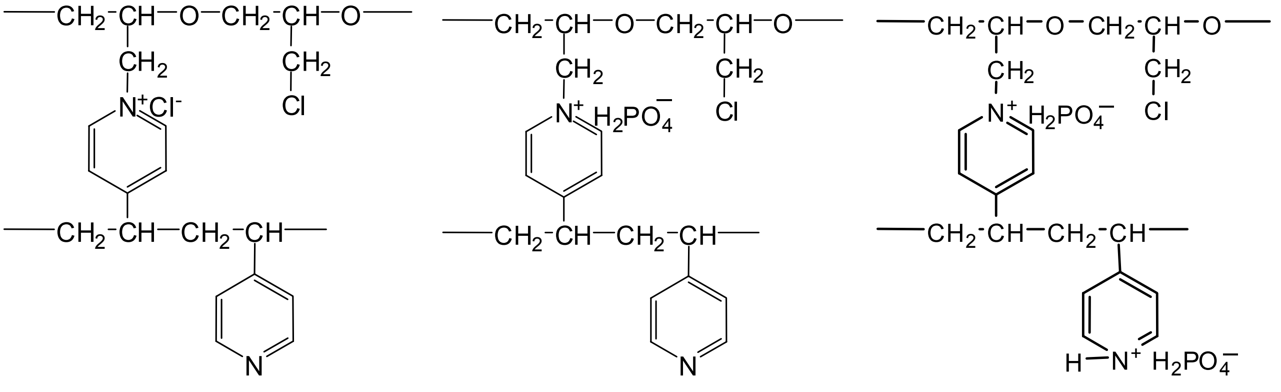

I II III

Fig.1 *Structure of AIPC in Cl^--form (I), in $H_2PO_4^-$-form (II) and in $H_2PO_4^-$-form, containing surplus acid (III).*

Table 1 *Properties of polymer proton-conducting membranes based on AIPC*

Compound	% H_3PO_4 in dry AIPC	Conductivity, $S \cdot cm^{-1}$ (at room temperature)		Mechanical strength, MPa	Elongation, %
		Dry membrane	After swelling in water		
I	–	$6.5 \cdot 10^{-6}$	$3.1 \cdot 10^{-4}$	9.6	58.0
II	19.8	$1.6 \cdot 10^{-5}$	$3.2 \cdot 10^{-3}$	39.4	16.9
III	54.1	$3.2 \cdot 10^{-2}$	$4.3 \cdot 10^{-2}$	0.8	52.2

Ionic conductivity was determined in a cell with platinum electrodes by impedance spectrometry within the frequency range from 1 Hz up to 100 KHz using a Voltalab system. The resistance of the membranes was determined by extrapolation of the $(1/(\omega * C)–R)$ dependence at high frequencies. Ionic conductivity was calculated using the following formula:

$$\sigma = \frac{l}{R * S},$$

where *l* is a thickness of the membrane (cm);

S is the membrane surface area (cm^2).

R is the resistance of membrane in Ohm.

FT-IR-spectrum of the membranes were plotted on the IR-spectrometer TENSOR-37 with the Fourier transformation ("BRUKER", Germany) within the range of the wave number of 650-4000 cm^{-1}.

Results and Discussion

In Fig.1 there are presented the data of the thermogravimetric analysis of AIPC membranes (I) and their complexes with orthophosphoric acid (II, III). As it is clear from Fig.1, AIPC (I) membranes are thermally stable up to 230°C. Introduction of orthophosphoric acid into the structure of AIPC (samples II, III) allows to increasing their thermal stability up to 260°C.

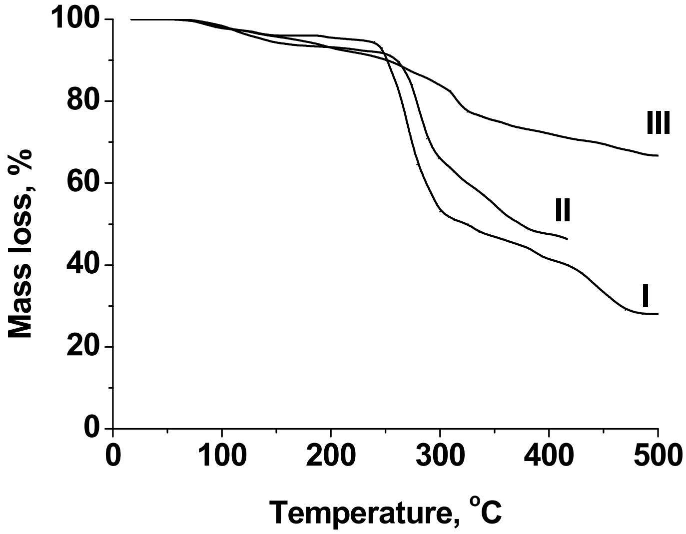

Fig. 2 *Thermogravimetric analysis of AIPC membranes*

As a result of carrying out our investigations it has been established that the long influence of high temperatures (120°C and 150°C during 24 hours results in the significant change of ionic conductivity and the strength properties of the synthesized materials (Table 2).

Table 2 *Properties of AIPC membranes after thermal treatment **

Compound	Temperature of treatment, °C	IEC, meq/g	Conductivity, S/cm	Mechanical strength, MPa	Elongation, %
I	-	3,7	$6.5 \cdot 10^{-6}$	9,6	58,0
	120	8,4	-	21.8	14.1
	150	9,1	-	29.6	15.1
II	-	-	$1.6 \cdot 10^{-5}$	39.4	16.9
	120	-	$6.8 \cdot 10^{-6}$	21.5	13.8
	150	-	$1.3 \cdot 10^{-6}$	19.3	13.1
III	-	-	$3.2 \cdot 10^{-2}$	0,8	52.2
	120	-	$5.5 \cdot 10^{-3}$	0,7	58,0
	150	-	$3.6 \cdot 10^{-4}$	0,6	60,0

* Time of thermal treatment - 24 hours.

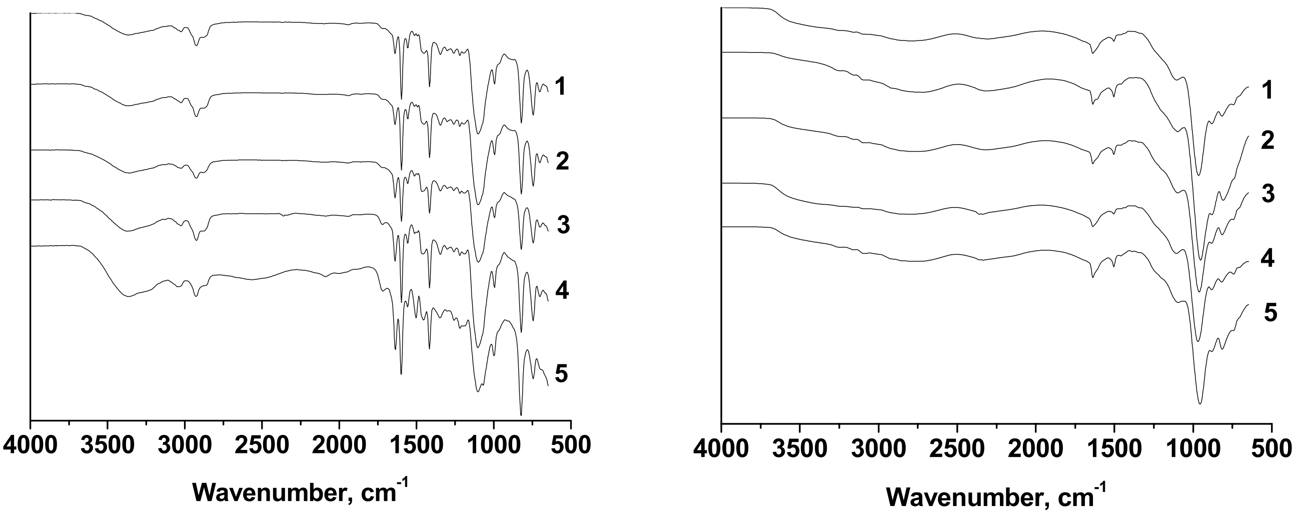

a

b

Fig. 3 *FT-IR-spectra of AIPC (I) in a Cl^--form (a) and AIPC (III) in $H_2PO_4^-$-form, containing the surplus of acid (b), after thermal treatment: 1 – AIPC (I or III) are without thermal treatment; 2 – at 120ºC during 5 hours; 3 – at 120ºC during 24 hours; 4 – at 150ºC during 5 hours; 5 – at 150ºC during 24 hours.*

By the data of IR-spectroscopy effect of the indicating temperatures results in decreasing the intensity of the oscillation peaks of free chloromethylic (670 cm^{-1} and 1270 cm^{-1}) and pyridine groups (1068 cm^{-1} and 819 cm^{-1}). At the same time the intensity of the oscillation peaks of pyridine groups (1640-1510 cm^{-1}) (Fig.3a) increases. This can be the warrant of the formation of additional cross-links in polymer matrix at the account of the interaction between free chlormethylic and pyridine groups. In this case the traces of polymer matrix destruction are not observed.

For the membranes of AIPC-H_3PO_4 (II, III) after thermal treatment, the certain decreasing of the strength properties is typical with temperature increasing. The observed high values of the relative elongation for AIPC (III) testify about the plasticizing effect of orthophosphoric acid relative to a polymer matrix (Table.2).

On the all spectra of AIPC (III) materials in the form of $H_2PO_4^-$containing the acid surplus (Fig.3b), and with standed at 120°C and 150ºC, there are present the oscillating peaks of the ions of PO_4^{3-}, HPO_4^{2-}, $H_2PO_4^-$, located within the range of 1100-950 $см^{-1}$ (peak at 965 cm^{-1} in Fig.3b). There are observed a certain decrease of the oscillating intensity of this peak after 24 hours at 150°C, that is conditioned by the ability of orthophosphoric acid for its degradation with simultaneous transition into a pyro- and then into poly-form [2]:

$$2H_3PO_4 \rightarrow H_4P_2O_7 + H_2O$$
$$H_4P_2O_7 \rightarrow 2HPO_3 + H_2O$$

In the connection with acid dehydration, the ion conductivity of AIPC (III), decreases up to $3.6\cdot10^{-4}$ S/cm (Fig.4, Table 2). However, after membrane immersion into water, the conductivity returns practically to the initial level, and is $1.2\cdot10^{-2}$ S/cm.

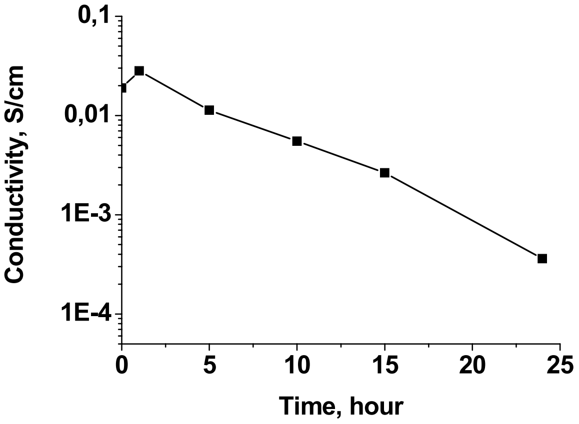

Fig. 4 *Ionic conductivity of AlPC-H_3PO_4 complexes (III) at room temperature as a function of storage time at 150ºC*

Conclusions

As a result of carried out work, the proton-conducting membranes based on the cross-linked AlPC-H_3PO_4 complexes are synthesized. It has been established that in a dry state they are characterized by the high enough ion conductivity on the level of $5.5 \cdot 10^{-3}$ S/cm (at 120°C) and $3.6 \cdot 10^{-4}$ S/cm (at 150°C). The obtained results allow to recommend the AlPC-H_3PO_4 complexes as high temperature polymer electrolyte membranes which can work up to 150°C.

References

1. Shembel E.M., Chervakov O.V., Meshri D., Andriianova M.V., Maksyuta I.M., Ryabenko V.V. Polymer Journal **31** (2009) 46.
2. Samms S.R., Wasmus S., Savinell R.F. J.Electrochem. Soc. **145** (1996) 1225.

PROTON CONDUCTING COMPOSITE MATERIALS BASED ON SULFONATED POLYAMIDES AND ZIRCONIUM PHOSPHATE

O. Chervakov[1], K. Gerasymenko[1], Yu. Gomza[2], Yu. Kobelchyk[1], I. Maksyuta[1],
E. Shembel[1], V. Vereschak[1], A. Hlopitskiy[1]

[1]SHEI "Ukrainian State Chemical Technology University", Dnipropetrovs'k, Ukraine
[2]Institute of Macromolecular Chemistry of National Academy Science of Ukraine, Kyiv, Ukraine

Corresponding author: *O.Chervakov (*chervakov@email.dp.ua)
Phone, Fax: +380 562 472 491

Introduction

Sulfonated polymers are widely used as a matrix for polymer electrolyte membrane (PEM) for fuel cells. The new generation of such type materials should have the following properties:

- ionic conductivity at level of 10^{-3}-10^{-1} S/cm in the wide temperature range;
- improved water retention at the temperature range above 100°C;
- high rates of mechanical strength and thermal stability;
- low cost.

One of the ways to improve operational characteristics of sulfonated PEM is a synthesis of composite material containing inorganic fillers. From all known fillers are attractive zirconium phosphate, which have a high ion exchange capacity (up to 13 meq/g) and high thermal stability. Phosphates, as well as many other zirconium derivatives, have a monomer or polymer structure, in amorphous or crystalline state. Depending on the degree of hydration, ion conductivity of zirconium phosphate can be higher than 10^{-3} S/cm [1]. In addition, they are able to hold firmly adsorbed water at temperatures up to 120ºC [2].

This work is devoted to the synthesis and study of properties proton conducting composite PEM (C-PEM) based on previously synthesized sulfonated polyamides (S-PA) [3,4] and zirconium phosphate (ZrP).

Experimental

C-PEM based on sulfonated polyamides (S-PA), and zirconium phosphate (ZrP) was obtained by the following methods: 2 g (0.0177 eq. NH-groups) aliphatic polyamide Ultramid B3201 (poly-ξ-caprolactam, Basf, Germany), dissolved in 12 ml of 99.7% formic acid. After this to the obtained solution has added 1.66 g (0.0088 mol) cresolsulfonic acid (KSA), 2.25 ml (0.0265 mol) 35% formalin, and 0.29 g of concentrated H_2SO_4. Molar ratio of reaction mixture NH: KSA: CH_2O = 1:0.75:1.5. In the resulting solution was added 0.4138 g (0.00128 mol) of zirconium oxychloride $ZrOCl_2 \cdot 8H_2O$ (estimating to obtain C-PEM contenting 10% zirconium phosphate). The resulting homogeneous solution is cast on the glass for the formation film material. Condensation performed at room temperature (10 hours) and additionally at 55ºC (1.5 hours). Then the resulting gel material is immersed for 24 hours in an aqueous solution of orthophosphoric and hydrochloric acid (10 wt.% H_3PO_4 + 13 wt.% HCl + 77 wt.% H_2O) for the transfer of zirconium oxychloride in phosphate on the scheme:

$$ZrOCl_2 + 2H_3PO_4 \xrightarrow{\text{HCl (Catalytic agent)}} Zr(HPO_4)_2 * H_2O + 2HCl$$

C-PEM on final step was washed by the distilled water for removing residual inorganic acid, and unreacted monomers. The operation is repeated until a neutral reaction of rinsing water the materials was. Dried at 60ºC for 6 hours C-PEM is opaque white film, which swelling in water.

Molecular and supramolecular structure of the polymer matrix, as well as the size and nature of the distribution zirconium phosphate in the C-PEM was determined by X-ray analysis. Curves of small-angle scattering of X-rays received in the vacuum chamber Kratky type in the emanation copper anode, which monochromatizated total internal reflection and nickel filter [5]. Measurement took place in a multiple step scanning scintillation detector in the range of scattering angles from 0.03 to 4.0°. This makes it possible to study the microheterogeneous filler formations with characteristic sizes, from 2 to 280 nm. Pre-treatment of small-angle scattering curves was carried out with using program FFSAXS [6].

Thermal stability of the synthesized polymers was determined by thermogravimetric analysis using Q1500D system Paulik-Paulik-Erdey (Hungary). Heating rate was 5ºC in minute. Samples of films dried 2 hours at the 60°C before analysis.

Proton conductivity of polymer electrolytes was determined by the impedance spectroscopy on the «Voltalab» device with computer control, use program of «Voltalab Master». The measurements were carried out in the plane-parallel cell with platinum electrodes in the frequency range from 0.001 to 100 kHz. Extrapolation hodograph $(1/(\omega*C)\text{-}R)$ in the high frequency resistance of the membranes at infinitely high frequency was determined.

Result and Discussion

Properties of film sulfonated polyamides (S-PA) and C-PEM based on them are show in Table.

Table 1 *Properties of S-PA and C-PEM on its basis*

№	Content of ZrP in C-PEM, %	Ionic conductivity, S/cm	IEC of C-PEM, meg/g	Water uptake, %
1	–	$4.9*10^{-3}$	3.0	54.3
2	5	$5,3*10^{-4}$	3,6	63,7
3	10	$1,5*10^{-3}$	4,3	68,3

Introduction of zirconium phosphate into membranes based on of S-PA leads to C-PEM with elevated rates of the ion exchange capacity (IEC), water absorption, but decreases the ionic conductivity. However, the conductivity increases significantly with increasing content of zirconium phosphate in the C-PEM.

According to the thermogravimetric analysis (Fig.1), with increasing content of inorganic filler the thermal stability of C-PEM slightly reduced. Nevertheless, the destruction of the membranes starts at temperatures above 230°C.

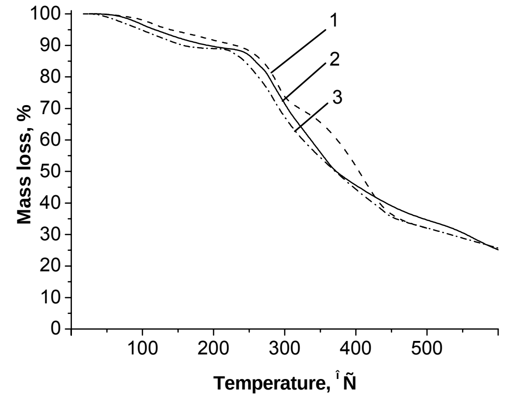

Fig. 1 *Data of therogravimetric analysis of polymeric materials:*
1 – S-PA; 2 – C-PEM (5% ZrP); 3 – C-PEM (10% ZrP).

By using a X-ray analysis, we determined molecular and supramolecular structure of synthesized S-PA and C-PEMs (Fig.2). It was established that a structure of obtained polymer matrix is similar to the typical segment polyurethanes. The material has lamellar type of structural organization. There are oligomeric aromatic fragments (products of condensation the KSA and formaldehyde) which connect long aliphatic macromolecules of the polyamides

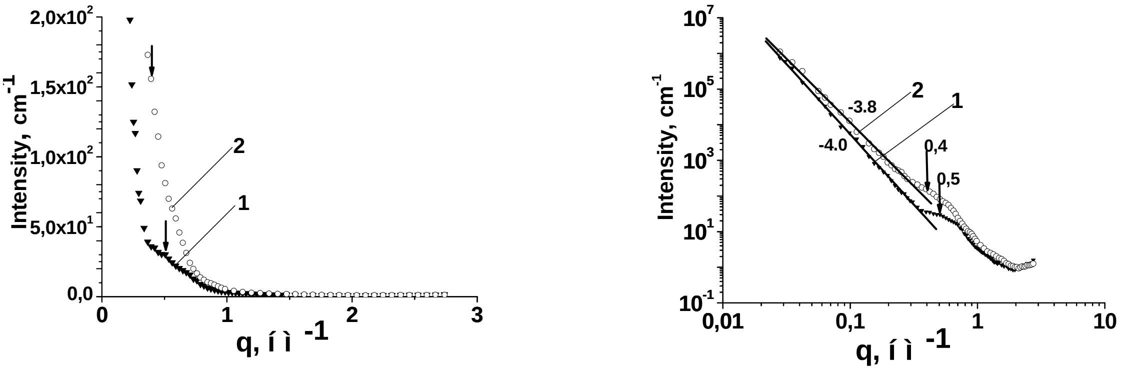

a b

Fig. 2 *Small-angle diffraction pattern researched materials in the conventional (a) and double logarithmic (b) coordinates: 1 - S-PA and 2 - C-PEM (10% ZrP).*

According to calculations the length of aromatic fragments is ~6 nm, that satisfies of amount elementary links of aromatic oligomers n=12-13 (see Fig.3).

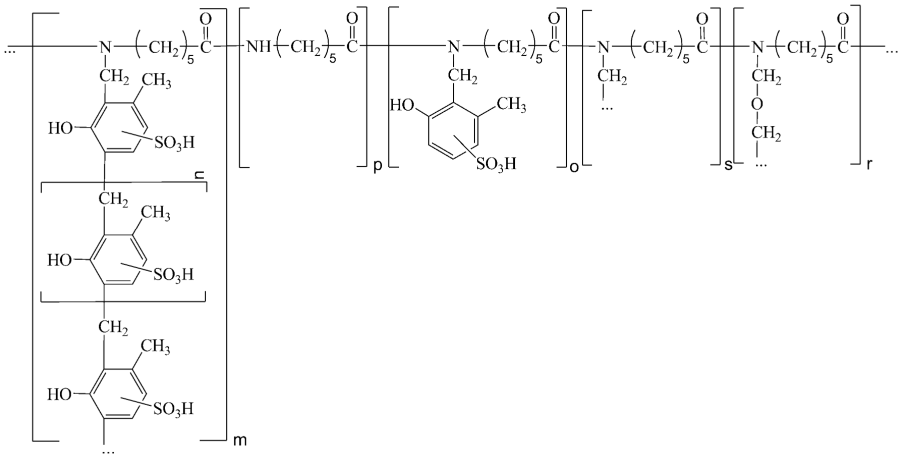

***Fig. 3** Chemical structure of polymeric matrix – sulfonated polyamide (S-PA)*

All oligomers chemically linked with polyamide matrix. C-PEM do not dissolve in any of the known organic solvents.

Supramolecular structure of the polymer matrix C-PEM is an amorphous system with distributed it «quasi-crystalline» domains (Fig.4). The domains are composed include folded lamellas (2.1), which contain oligomer cresolsulfonic acid fragments, and bar-to-bar layers with less ordered parts of aliphatic polyamides (2.2). Domains size is about 60-80 nm.

Zirconium phosphate evenly distributed throughout the volume of C-PEM.

The particles with size 1-2 nm located in the bar-to-bar interlayer of «quasi-crystalline» domains. The larger particle with size up to 280 nm are located in amorphous zones of polymer matrix.

***Fig. 4** Conceptual supramolecular structure of C-PEM based on S-PA and ZrP, where:*
1 - amorphous parts of the polymer matrix;
2 - «quasi-crystalline» domains;
3 - nanoparticles of ZrP.

Conclusions

As a result of the work, were obtained C-PEM based on inexpensive sulfonated polyamide matrix and zirconium phosphate. The proposed technology makes possible to obtain composite materials with evenly distributed zirconium phosphate in the volume polymer matrix. Rather high conductivity (10^{-3} S/cm) and thermal stability (up to 230ºC) allows for use such in electrochemical devices of various application.

References

1. G. Alberti, M. Casiola: Annual Revue Material Research. **33** (2003) 129.
2. S.V. Wilson, K.I. Petrov: Zirconium. Chemical and physical methods of analysis, Moskou, Atomizdat, 1960, page 213 (in Russ.).
3. Pat. 0064831 United States MKV7 S08G 69/00 Proton-conducting polyamide polymer membrane and method for production / Oleg Chervakov, Elena Shembel, Yu. Kobelchuk, Konstantyn Gerasymenko.- № 11/891, 548 claimed. 11.08.2007, publ. 13.03.2008.
4. E. Shembel, V. Redko, V. Khandetskyy, O. Chervakov, Y. Kobelchuk, V. Ryabenko, I. Maksuta, M. Andriianova, K. Gerasimenko, A. Markevich, D. Meshri: 3rd Annual Conference - FUEL CELLS DURABILITY & PERFORMANCE 2007 Miami, USA (2007) 301.
5. Yu.S. Lipatov, V.V. Shilov, Yu.P. Gomza, N.E. Kruglyak. Radiographic methods for the study of polymers. – Kiev, Nauk. dumka, 1982, page 296 (in Russ.).
6. Vonk CG, FFSAXS's Program for the Processing of Small-Angle X-ray Scattering Data (Geieen: DSM: 1974).

LYOTROPIC LIQUID CRYSTALS – MEDIUM FOR PREPARATION OF HIGHLY ORGANISED MESOPOROUS MATERIALS

P. Barath[1,2]*, T. Uhlířová*[1]*, J. Reiter*[1]

[1] *Institute of Inorganic Chemistry of the ASCR, v. v. i., 250 68 Řež near Prague, Czech Republic*
[2] *Institute of Electrotechnology, Technical University of Brno, 602 00 Brno, Czech Republic*

Corresponding author: Jakub Reiter (reiter@iic.cas.cz)
Phone: +420 266 172 198
Fax: +420 220 941 502

Introduction

A novel approach to preparation of mesoporous metals and oxides reported in recent years [1-5] has involved electrodeposition from lyotropic liquid crystals (LLCs). The ability of several non-ionic surfactants to form self-assembled liquid crystalline phases on addition of aqueous solutions or pure water [6, 7] results in a facile synthesis of a variety of dimensionally variable templates in which the electrodeposit morphology is the inverse of the template.

The liquid crystal structure is determined by the system composition, surfactant type and temperature. For the application of LLC in the nanotechnology, the hexagonal phase is the most important one due to its characteristic dimension less than 100 nm.

The regular deposited structure provide very high surface area in comparison with the smooth sample surface prepared by conventional electrolytical method. The electrode surface with highly organised structure is much better accessible for the molecules of gaseous or liquid compounds. This effect is strongly welcomed in the technology of fuel cells, where high catalytic activity of the material is expected.

Our recent work is aimed at the preparation of mesoporous catalysts for the application in low-temperature H_2-O_2 fuel cells. In this area, the main task is to substitute expensive materials with more affordable components such as nickel or manganese oxide [9], or as in the case of platinum, to minimize the total amount of the catalyst with achieving comparable catalytic activity.

Experimental

The lyotropic liquid crystal was prepared from Brij® 56 (poly(ethylene glycol)hexadecyl ether; Fluka) and aqueous solution of the precursor. The weight ratio surfactant – aqueous solution was 55 – 45 wt. %.

a) for nickel 0.2M $(CH_3COO)_2Ni$, 0.5M CH_3COONa, 0.2M H_3BO_3;
b) for platinum 1.9M H_2PtCl_6;
c) for manganese oxide 0.1M $(CH_3COO)_2Mn$, 0.1 Na_2SO_4.

The electrochemical measurements were performed using potentiostat-galvanostat PGSTAT 30 (Eco Chemie, Holland). The catalysts were deposited potentiostatically on a glassy carbon or gold electrode (∅ 3 mm) at 30 °C. Studied materials were also electrodeposited directly from the aqueous solutions under the same conditions. The electrochemical investigation of prepared materials was done on a rotating disc electrode RDE; Metroohm) and aimed mainly at measurements of the hydrogen oxidation reaction (HOR) – nickel and platinum, and oxygen reduction reaction (OOR) – manganese oxide.

Results and Discussions

In our previous research, we found out, that the areas of the oxidation peak of nickel are in ratio 8.9 : 1 in favour of the mesoporous sample. The oxidation also occurs at lower potential and both oxidation and reduction peaks are sharper, what can be explained by its higher reactivity. The voltammetrical measurements done at higher scan rates (up to 100 $mV.s^{-1}$) showed rapid charge transfer and fast transport to the mesoporous surface.
Fig. 1 presents linear voltammograms of deposited nickel in Ar– and H_2–saturated 1M KOH solution. Our first results of the measurement on a rotating disk electrode showed distinctive catalytic activity, when the current corresponding to hydrogen oxidation is increasing with increasing speed of rotation.

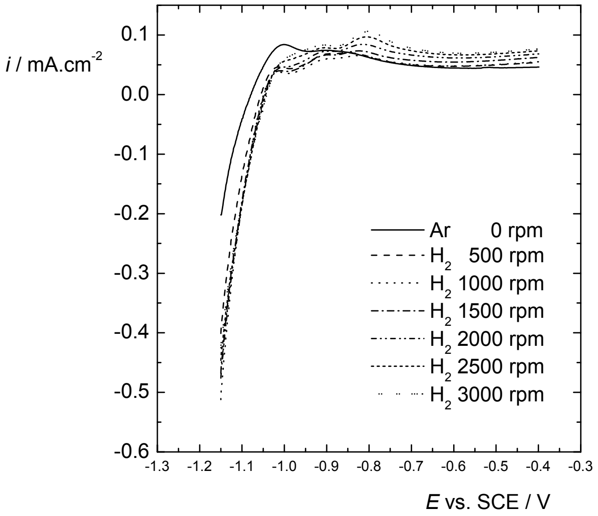

Fig. 1 *Linear voltammograms of nickel deposited potentiostatically from LLC at –0.9 V vs. SCE with a charge density of 0.7 $C.cm^{-2}$ measured in 1M KOH at 60°C (scan rate 10 $mV.s^{-1}$).*

This research is in progress together with the measurements of nickel catalyst deposited on graphite paper.

Acknowledgements

This work was supported by the Academy of Sciences (Research Plan AV0Z40320502), by The Grant Agency of the Academy of Sciences (grant KJB200320801) and the Ministry of Education, Youth and Sports, Czech Republic (project MSMT LC523).

References

1. G.S. Attard, J.C. Glyde, C.G. Göltner, Nature **378** (1995) 366.
2. G.S. Attard, M. Edgar, C.G. Göltner, Acta Mater. **46** (1998) 751.
3. A.H. Whitehead, J.M. Elliott, J.R. Owen, J. Power Sources **81-82** (1999) 33.
4. P.N. Bartlett, P.N. Birkin, M.A. Ghanem, P. de Groot, M. Sawicki, J. Electrochem. Soc. **148** (2001) C119.
5. J.M. Elliott, G.S. Attard, P.N. Bartlett, N.R.B. Coleman, D.A.S. Merckel, J.R. Owen, Chem. Mater. **11** (1999) 3602.
6. G.S. Attard, P.N. Bartlett, N.R.B. Coleman, J.M. Elliott, J.R. Owen, Langmuir **14** (1998) 7340.
7. J.M. Elliott, J.R. Owen, Phys. Chem. Chem. Phys. **2** (2000) 5653.
8. P.A. Nelson, J.M. Elliot, G.S. Attard, J.R. Owen, Chem. Mater. **14** (2002) 524.
9. J. Vondrák, B. Klápště, J. Velická, M. Sedlaříková, J. Reiter, I. Roche, E. Chainet, J.F. Fauvarque, M. Chatenet: J. New Mat. Electrochem. Syst. **8** (2005) 209-212.

POLY(VINYL ALCOHOL) BASED POLYMER ELECTROLYTE MEMBRANES FOR PASSIVE DIRECT METHANOL FUEL CELL

Mitsuru Higa, Mikinori Sugita, Shin-ichi Maesowa, Nobutaka Endo

Graduate School of Science and Engineering, Yamaguchi University,
2-16-1 Tokiwadai, Ube 755-8611 Japan

Corresponding author: Mitsuru Higa (mhiga@yamaguchi-u.ac.jp)
Phone: +81-836-85-9203,
Fax: +81-836-85-9201

Introduction

A direct methanol fuel cell (DMFC) using polymer electrolyte membranes (PEMs) are one of the most attractive power sources due to their stable operation at a low temperature, the high energy generation yield and energy density, the simplicity of system [1,2]. PEMs for DMFC have been developed in order to reduce methanol crossover as well as to reach high proton conductivity. In this study, PEMs were prepared from a poly(vinyl alcohol) based polymer shown in Fig.1, and their performances for a passive type DMFC were examined.

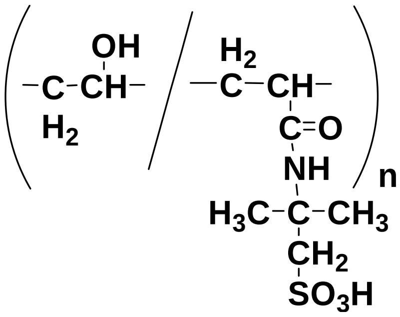

***Fig. 1** Chemical structure of a polyanion, AP-X.*

Experimental

An aqueous solution of a mixture of PVA and poly(vinyl alcohol-co-2-acrylamido-2-methylpropane sulfonic acid) (AP-4) was cast on a plastic plate and dried over a hot stage at 50 °C for 24 h to afford a self-standing membrane. The molar percentage of the proton exchange groups in the obtained PEMs was controlled by changing the PVA/AP-X ratio in the casting solution. The PEMs obtained were annealed at 180 °C for 30 min, and then were cross-linked chemically by immersing them in a cross-linking solution of mixed glutaraldehyde and Na_2SO_4 or acetone solutions at 25 °C for 24 h to control their water content [3].

Membrane-electrode assemblies (MEAs) for DMFC were prepared from the PEM, Pt-Ru/C and Pt/C electrodes using Nafion solution as an ionomer and binder. Single cell performance was measured by using a passive DMFC with the MEA changing methanol solution in the fuel. Cell voltage versus current density response was measured galvanostatically by incrementally increasing the current from open circuit and measuring the cell voltage.

Results and Discussion

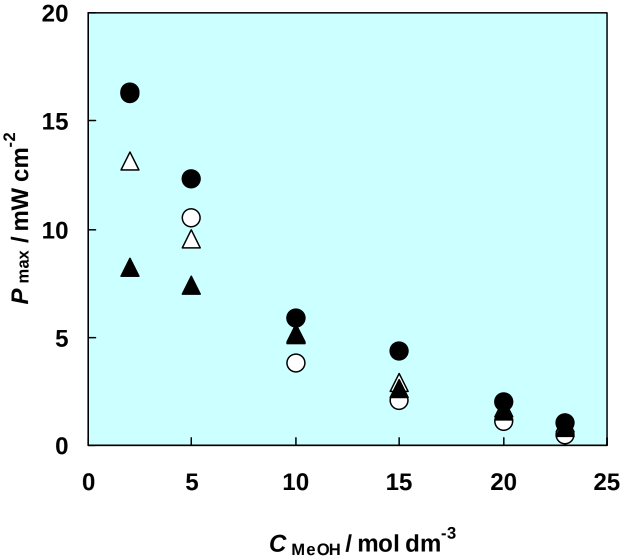

Fig. 2 *Performances of the passive DMFC as a function of methanol concentration, C_{MeOH}, in the fuel. Measurement temperature: 60°C. Amount of catalyst: 4 mg cm^{-2}. Binder: Nafion® solution. Sample PEM: solid circles, AP-4 cross-linked with Na_2SO_4/GA solution; solid triangles, AP-4 cross-linked with acetone/GA solution; open circles, AP-4 without chemical cross-linking; open triangles, Nafion®117.*

Fig. 2 shows maximum power density (P_{max}) of the passive DMFC test cell as a function of methanol concentration in the fuel (C_{MeOH}). P_{max} of all the MEAs decreases with increasing methanol concentration. One of the reasons for the decrease in the P_{max} will be due to the decrease in OCV of the test cell, whose data are not shown here. The MEA with AP-4 PEM cross-linked Na_2SO_4/GA solution has highest P_{max} in all the MEAs at the all methanol concentration and has 1.5 times higher value than that with Nafion® 117.

Conclusions

PEMs for DMFC were prepared from PVA and a PVA-based polyanion changing their cross-linking conditions. The single cell performance shows that the PEMs have higher performance than Nafion® 117 for passive DMFC. Hence, PVA-based PEMs are potential candidates for DMFC applications.

Acknowledgements

This works was supported by Electric Technology Research Foundation of Chugoku, the Mazda Foundation, the UBE Foundation, Kurita Water and Environmental Foundation (No. 20320), and the Salt Science Research Foundation, No. 0612, No. 0709 and No. 0810.

References

1. Kim, D. S., Park, H. B., Rhim, J. W., Lee, Y. M., *J. Membr. Sci.*, **240** 37-48 (2004).
2. Ren, X., Wilson, M. S., Gottesfel, S., *J. Electrochem. Soc.,* **143** L12-L15 (1996).
3. Higa, M., Sugita, M., Maesowa, S., Endo, N., *Electrochimica Acta*, (2009) in press.

CONDUCTIVITY OF CARBON MATERIALS FOR ALTERNATIVE ENERGY SOURCES

J. Tichý[1], V. Novák[1], P. Barath[1,2]

[1] *Institute of Electrical and Electronic Technology, Brno University of Technology,*
602 00 Brno, Czech Republic
[2] *Institute of Inorganic Chemistry of the ASCR, v. v. i., 250 68 Řež near Prague,*
Czech Republic

Corresponding author: Peter Barath (barath@feec.vutbr.cz)

Abstract

This work deals with measuring conductivity of carbon materials for use in electrochemical energy sources. Object of this work was prepared electrodes with carbon materials and investigate their electrical properties.

Introduction

This work was created to select optimal carbon materials for use in electrochemical energy sources, especially fuel cells and Ni-Cd batteries. This knowledge will be used to make better electrodes for fuel cells and Ni-Cd batteries.

Experimental

The first part was the creation of samples. The carbon samples in powder form mixed with H_2O and IPA were deposited on a steel grid, by the pressure and heat for about 30min. We can see samples with their non-electric parameters in Table 1.

***Table 1** Non-electric parameters of measured electrodes*

Material	weight of empty grid [g]	weight of grid with the material [g]	weight of the material [g]	resistance of the sample [Ω]	active surface of the electrode [m^2]	electrode thickness [m]
Chezacarb A	0,229	0,246	0,017	3,50	0,00010	0,0007
Chezacarb B	0,212	0,224	0,012	6,50	0,00010	0,0007
Chezacarb HS 9,4% PTFE + β-$Ni(OH)_2$	0,132	0,141	0,009	6,30	0,00005	0,0005

Second part was measuring samples using potentiostat PGSTAT12 plus FRA and later NOVA 1.5. software (Ecochemie). The electrolyte was 1M KOH in distilled water. There were three electrodes in measuring cell: referent electrode (REF) Hg-HgO, counter electrode (CE) Pt and working electrode (WE) which was the measured sample. Samples were tested by Frequency response analysis (FRA) measuring process.

Results and Discussion

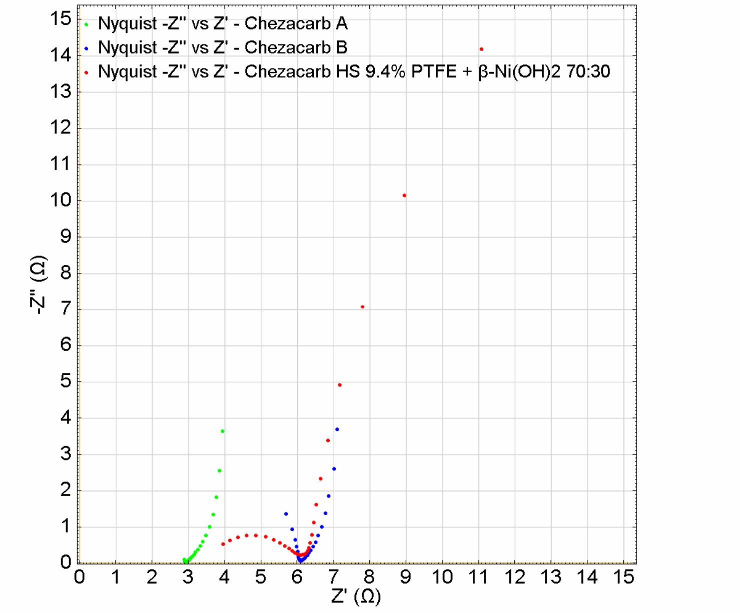

***Fig. 1** Nyquist diagram of measured electrodes*

The best conductivity was found by the material Chezacarb SH 9,4% PTFE + β-$Ni(OH)_2$ as we can see in Table 2. From pure carbon materials has Chezacab A better conductivity than Chezacarb B.

***Table 2** Conductivity of measured materials*

Material	conductivity of the electrode [$S.m^{-1}$]	**conductivity per gram of material [$S.m^{-1}/g$]**
Chezacarb A	2,000	**117,647**
Chezacarb B	1,077	**89,744**
Chezacarb SH 9,4% PTFE + β-$Ni(OH)_2$	1,587	**176,367**

Conclusions

Purpose of this work was to find out the conductivity of carbon based materials. The best measured materials will be used to create electrodes for fuel cells or batteries. Pure carbon materials are suitable for fuel cells, materials with β-$Ni(OH)_2$ are used in Ni-Cd and Ni-MH batteries.

Acknowledgements

This work was supported by Ministry of Education, Youth and Sports, Czech Republic (project MSMT 0021630516)

References

1. Tichý, J.: Bakalářská práce: Uhlíkové materiály pro alternativní zdroje energie. Brno: Vysoké učení technické v Brně, Fakulta elektrotechniky a komunikačních technologií, 2009.
2. Barath, P.: Disertační práce: Palivové články H_2-O_2 s iontoměničovou membránou anexového a bipolárního typu. Brno: Vysoké učení technické v Brně, Fakulta elektrotechniky a komunikačních technologií, 2008

THE DEVELOPMENT OF ELECTRODE MATERIALS FOR PEM FUEL CELL

T. Kazda[1]*, V. Novák*[1]*, P. Barath*[1,2]

[1] Institute of Electrical and Electronic Technology, Brno University of Technology,
602 00 Brno, Czech Republic
[2] Institute of Inorganic Chemistry of the ASCR, v. v. i., 250 68 Řež near Prague,
Czech Republic

Corresponding author: Peter Barath (barath@feec.vutbr.cz)

Abstract

This work deals with creating a mixture of carbon deposited platinum. Furthermore measurement of these mixtures with using the methods Impedance Spectroscopy and Linear scan voltametry and then compare the identified characteristics of follows the measured samples. [1-8]

Introduction

The work was created to detect the difference in the properties of different carbon materials with deposited platinum. The results observed from this measurement will be further used to produce better working electrodes for fuel cells.

Experimental

As a first step, the samples were made from carbon materials CHEZACARB A and CABOT VULCAN GP-3893 which was deposited platinum. Carbon materials were milled and mixed in a distilled water and IPA, in this suspension was subsequently added intended amounts of acid H_2PtCl_6 and mixed. The sample was then inserted into the oven heat to 400°C.

Tab. 1 *used carbon and representation H_2PtCl_6 to their weight*

Used carbon	Amount [mg]	H_2PtCl_6 [mg]	Temperature [°C]	Annealing [min]	Mass ratio [%]
VULCAN GP 3893 milled	1000	200	400	30	20
CHEZACARB A milled	500	100	400	30	20

From the samples were taken always 25mg electrode matter for the preparation of ink to which was added micropipette PTFE emulsion. Subsequently, they were taken 4μl suspension and the application of the adapter RDE and dried. After drying was some of electrode application slight amount Ionomer.

***Tab. 2** List and the procedure for a mixture of the electrode*

Designation of sample	Designation of a mixture	Used quantities [mg]	H_2O [ml]	IPA [ml]	PTFE [μl]	Ionomer [μl]
I	VULCAN GP 3893 milled 20%Pt	25	0,6	0,3	4	3
II	VULCAN GP 3893 milled 20%Pt	25	0,6	0,3	0	3
III	VULCAN GP 3893 milled 20%Pt	25	0,6	0,3	4	0
IV	CHEZACARB A milled 20%Pt	25	0,6	0,3	4	3
V	CHEZACARB A milled 20%Pt	25	0,6	0,3	0	3
VI	CHEZACARB A milled 20%Pt	25	0,6	0,3	4	0

The final part has been deposited as follows measure samples using potenciostat Autolab attached to RDE and an assessment of the program Nova. Using the three-electrode involvement with the current electrode (CE) used platinum and calomel electrodes (Hg-HgO) was used as reference electrode (RE). Working electrode (WE) formed rotating adapter with deposited sample. All samples measured at the RDE were measured in 1M KOH solution.

Results and Discussions

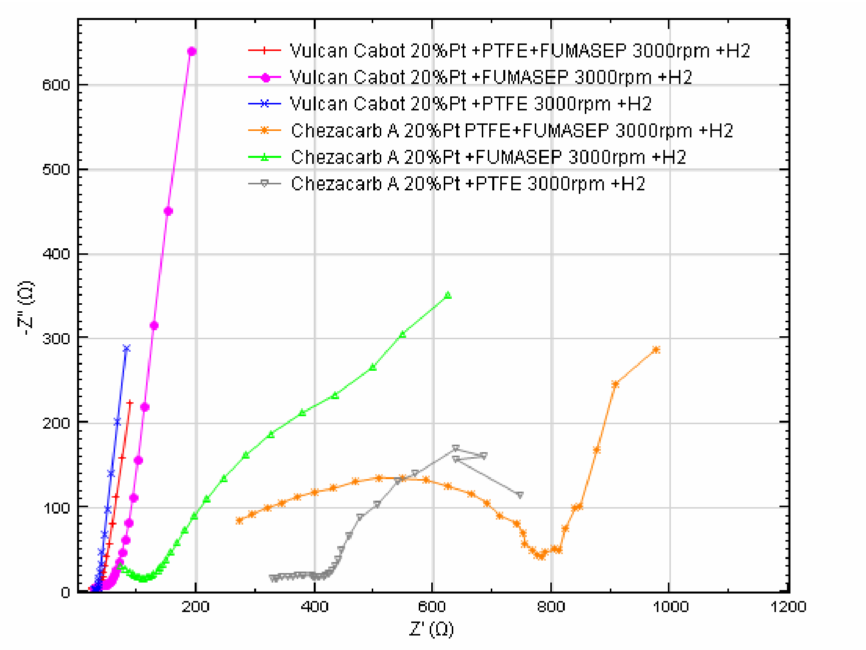

***Fig.1** Impedance spectroscopy comparison of all samples 3000ot +H_2 -1V*

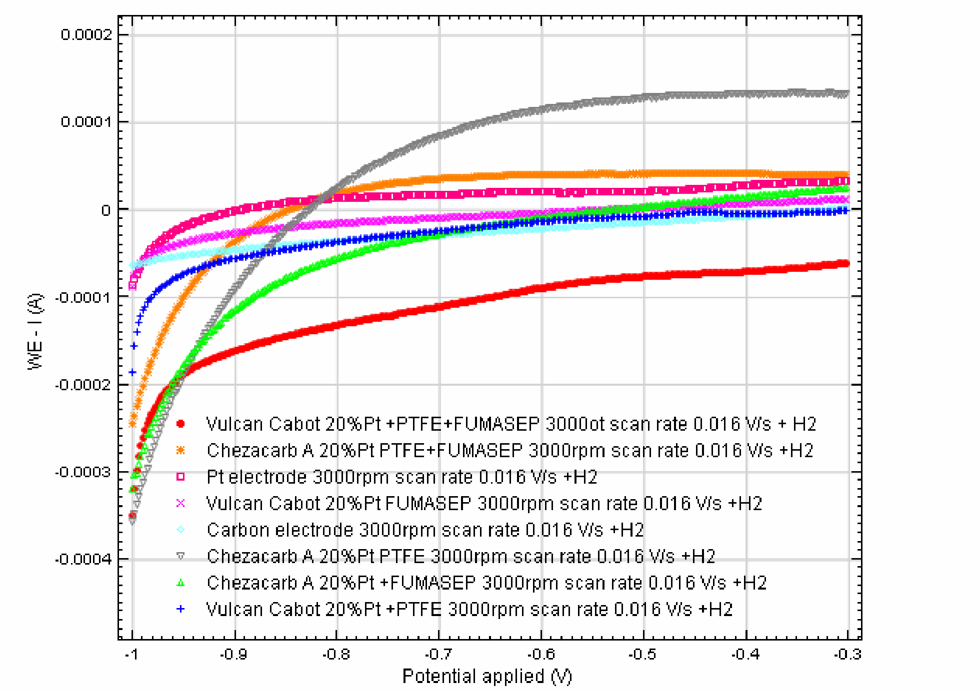

Fig.2 *LSV compare all samples with platinum and carbon electrodes 3000ot +H_2 scan rate 0,016*

From chart No.1 we see that the highest values of conductivity in the potential of-1V reached with the electrode material used carbon type Vulcan Cabot, closest to their conductivity values of a group of electrode materials using Chezacarb A the sample was addition deposition monomer. From chart No.2 is evident in the overall comparison of the speed of development of electrode materials that is most close to clean platinum electrode samples of type Chezacarb A.

Conclusions

The aim of the project was to create and measure the electrode materials and to determine their suitability for use in fuel cells. The most appropriate material according to the results obtained using carbon material type Vulcan Cabot with a good value of conductivity and an acceptable rate of speed development. These electrode materials will be further used and measured in the experimental fuel cells.

Acknowledgements

This work was supported by the Ministry of Education, Youth and Sports, Czech Republic (project MSMT 0021630516).

References

1. Miroslav Březina a kolektiv, Katalytické děje v elektrochemii, Academia-Praha 1979
2. Ch. N. Satterfield, Heterogenous catalysis in practice, McGraw-Hill Book Company 1980
3. M. M. Taqui Khan, A.E. Martell, Homogenous Catalysis by Metal Komplex, ACADEMIC PRESS 1974
4. P.N. Rylander, Catalytic Hydrogenation over Platinum Metals, London 1967
5. J. Klikorka, Úvod do preparativní anorganické chemie, Praha 1987
6. E.R. Technology of chemical and materiále for Electronics, Society of chemical industry, 1984
7. Pozio, L. Giorgi, E. Antolini, E. Passalacqua, *Electrochim. Acta*, **46**, 555 (2000).
8. S. - U. Rahman, M. A. Al-Saleh, A. S. Al-Zakri, S. Gultekin, *J. Appl. Electrochem.*, **27**, 215 (1997).

10th ABAF

BRNO 2009

Advanced Batteries, Accumulators
and Fuel Cells

:-)

HYBRIDE FUEL CELL-LITHIUM BATTERY POWER SOURCES FOR ADVANCED BROOM TRANSPORT

R. B. Weasley[1], E. McMillan[2], A. Dippet[1]

[1] Hogsmeade University, 25 Castle Avenue, Gorebridge
[2] Muggle Institute of Science, Aberdour Road, KY11 4PB Dunfermline, United Kingdom

Corresponding author: Armando Dippet
Phone: +44 (0) 1225 383899
Fax: +44 (0) 1225 386108

Safety and depreciation of air traffic have been generating a lot of attention for scientists. The latest news of Boeing[1] company has shown possibility to use combination fuel cell and Li-ion batteries as a generator of flight (see Fig. 1). The advantage of this combination is a constant taking-in electric energy from fuel cells during the flight and short-term taking-in from Li-ion batteries during airplane taking-off.

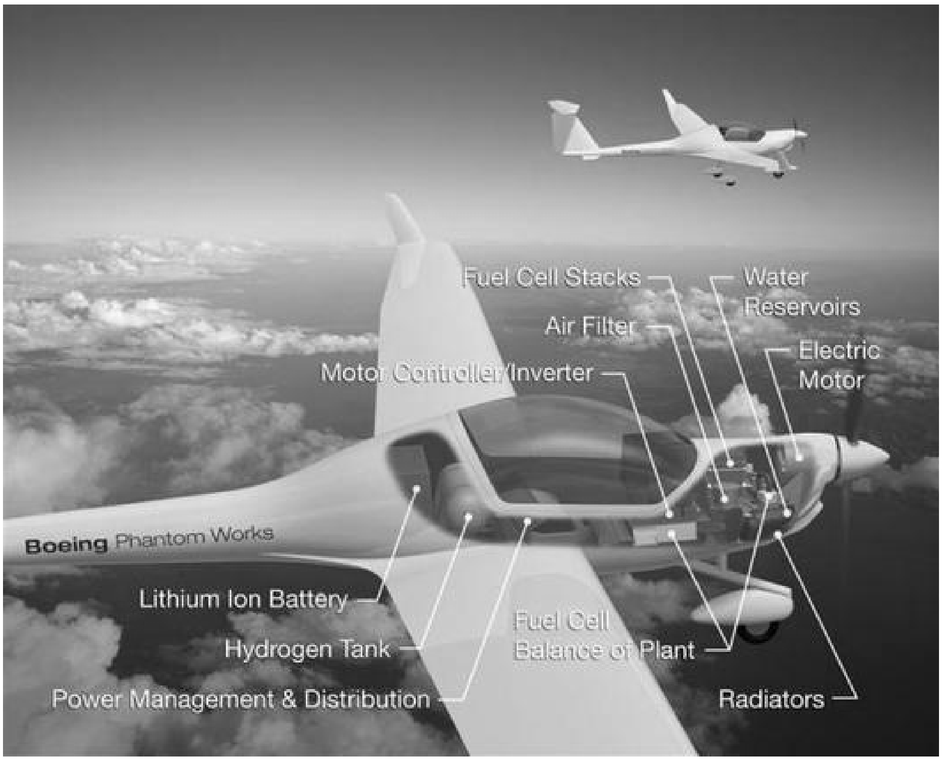

Fig. 1 *Scheme of the Boeing Phantom Works*

Our research of analogous hybrid source of energy for new type light long-flying broom for one or two passengers[2] respectively, is based on already mentioned Boeing company advancement. We have laid stress on decrease of consumption and increase of safety indeed.

Results of pilot project within 8-FP „Advanced technologies for automotive, air and transport industry“ will be presented. In this project many institutions have been engaged till Air Liquide Ireland performed the detailed design and assembly of the onboard fuel system and the refueling station; the Electronic Engineering Division of the Muggle Institute of Science (School of Industrial Engineering) collaborated in the design and construction of the power management and distribution box; post-integration bench testing is being conducted in a facility that belongs to the Hogsmeade University. Recently we are seeking for company that will provide a test pilot and facilities for flight tests.

Acknowledgements

We appreciate the support by The European Muggle Researcher´s Mobility Portal (J.O.A.N. 43555-06/09).

References

1. http://www.boeing.com/news/releases/2008/q2/080403a_nr.html (downloaded August 1st, 2009).
2. http://www.etsy.com/shop.php?user_id=6413104&order=&section_id=&page=5(downloaded August 5th 2009).

INFORMATION ABOUT THE ELECTROCHEMICAL SOCIETY

Introduction

ABAF 2009 is co-sponsored by the Electrochemical Society, Inc (ECS). ECS was founded in 1902 as an international nonprofit, educational organization concerned with a broad range of phenomena relating to electrochemical and solid state science and technology. The Electrochemical Society has about 8,000 scientists and engineers in over 75 countries worldwide, who hold individual membership, as well as roughly 100 corporations and laboratories, that hold corporate membership. ECS objectives are:

- to advance the theory and practice of electrochemistry, solid-state science, and allied subjects;
- to encourage research and dissemination of knowledge in these fields; and
- to assure the availability of adequate training and education of fundamental and applied scientists and engineers in these fields.

First founded as the American Electrochemical Society in 1902, the name of the Society was changed to The Electrochemical Society already in 1930 to more accurately reflect its international activities and membership. Presently, more than 50 % of members reside outside USA. ECS has grown and continued to respond to the changing technical needs and interests of its members; and in 2000, adopted the official acronym of ECS, to encompass long tradition of advancing the theory and practice of both solid-state and electrochemical science and technology. ECS continues to disseminate information through individual membership, corporate membership, student services, technical journals, a quarterly news magazine, books, technical meetings, and awards; and to provide networking contacts through ECS’s thirteen Divisions. Geographically, members can also associate with Sections. For example, most members in Europe will be members of the European Section.

ECS bridges the gaps among academia, research, and engineering—bringing together scientists from around the world for the exchange of technical information. This unique blend provides an unparalleled forum for the integration of these areas of science and technology. The ECS staff can provide support to you in learning more about ECS and its many activities.

The Society actively recruits students and gives them the opportunity to get organized in student chapters. One of the active chapters is also in Brno, the site of this year's ABAF meeting. Student membership can be obtained at a discount.

ECS maintains digital library of its collection of publication. Access to the library, with certain number of downloads, is part of the membership package.

Full information can be obtained at www.electrochem.org.

(contributed by Petr Vanýsek, pvanysek@niu.edu)

ABOUT BOCHEMIE, A.S.

Mission

To meet the needs of its customers, particularly in the following areas: disinfection, protection of wood, materials for accumulators and metal surface treatment BOCHEMIE provides its customers with comprehensive solutions to their problems through its products, services and related equipment and user know-how.

Profile

BOCHEMIE A.S. (joint-stock company) PERFORMS ITS BUSINESS ACTIVITIES in five primary production branches: disinfection, consumer goods, protection of building materials against biological corrosion, surface finishing of metals and production of accumulator masses and other materials for manufacturers of accumulators. Approximately half of the production is exported to foreign markets. The major sales territories include countries of Central and Western Europe, USA and Eastern Asia.

BOCHEMIE A.S. keeps the leading position on the Czech market in the area of disinfection, which includes product lines for medicine and food industry, agriculture and institutions; the company also enjoys a significant position in Slovakia, where it is ranked third.

As for consumer goods we succeeded in keeping the leading position of SAVO product line on the Czech and Slovak market of liquid cleaners and bleaching agents.

BOCHEMIE A.S. is a leader on the building market in Czech Republic and Slovakia with its line of fungicidal and insecticidal products for protection of wood and masonry. We are also a leading company on the market of „hobby“ fungicides in Bulgaria.

Activities connected with production of materials designed for steel treatment are of a high export potential. Progressive, environment-friendly and universal pickling technology FEROPUR is a leader on the narrow segment of the stainless steel long products market.

BOCHEMIE A.S. is one of the world’s most important suppliers of raw materials and technologies for alkaline accumulators. Bochemie doesn’t forget about developing new more effective materials designated for this segment. The company has approximately one-fifth share on the worldwide market of these commodities.

BOCHEMIE A.S. is the holder ISO 9001:2001 certificate and Responsible Care certificate as well.

BOCHEMIE A.S. aims for the protection of environment, working environment, decreasing the release of dangerous substances and increasing the security against accidents.

NOVA-LAB

Martijn van Dijk
Eco Chemie BV
Kanaalweg 29G, 3526 KM Utrecht, The Netherlands
Corresponding author: Martijn van Dijk
Phone: +31 30 2893154 Fax: +31 30 2880715
Email: martijn@ecochemie.nl
WWW: www.ecochemie.nl

Distributor: *NOVA-LAB s.r.o.*
Phone: +420777 58 00 63
Email: barath@nova-lab.cz
WWW: www.nova-lab.cz

Founded in 1986 and since 1999 a member of the Metrohm group of companies, Eco Chemie designs and manufactures state of the art Autolab series of instrumentation and software for electrochemistry and biochemistry. ISO 9001:2000 certified, Eco Chemie has been setting the benchmark in electrochemical research instrumentation for almost two decades. With our background and knowledge in electrochemistry and biochemistry and our worldwide distributor network, our mission is to serve the research community worldwide by supplying modern, affordable instruments, software and accessories. The Autolab instruments serve a wide range of industries and research applications. Ever since the foundation everyone within the company has been dedicated to the development, production and testing of Autolab electrochemical instruments and their software. This focus coupled with the flexibility of the company resulted in the finest range of potentiostats/galvanostats available today.

The flexibility of Eco Chemie is reflected in the modularity of the Autolab instruments. Potentiostat range from 12 to 100 V output voltage with the possibility to add a variety of modules throughout the lifetime of the instrument.

Some of the popular modules include:

- FRA2 (Module for impedance spectroscopy, for battery and corrosion research)
- BA (Bipoteniostat and Array, second working electrode in combination with other techniques like; Scanning Electro Chemical Microscope, Scanning Tunneling Microscope and Raman)
- ADC10M (Fast sampling module, scan rates up to 250 kV/s in combination with
- SCAN250 true analog sweep generator)
- ECD (Low current amplifier, current ranges from 10 pA to 100µA)
- MUX (Multiplexing module, possibility of measuring a maximum of 96 complete electrochemical cells or 256 working electrodes in sequence)
- BOOSTER 10A/20A (Current booster)

The Autolab instruments can be controlled by two different software packages:
General Purpose Electrochemical Software for all common DC electrochemical techniques and the Frequency Response Analyzer software for impedance spectroscopy (in combination with the FRA2 module). The combination of the Autolab hard- and software gives the user an unrivalled instrument to perform a wide range of electrochemical experiments. Fundamental electrochemistry, corrosion and battery & fuel cell research are easily achieved with Autolab systems.

Rastrovací hrotové mikroskopy Agilent Technologies

Společnost H TEST a.s. rozšířila svoji nabídku testovacích systémů i o produkty divize Agilent Materials Sciences Solutions tj. AFM (Atomic Force Microscopy)/SPM (Scanning Probe Microscopy) rastrovací mikroskopy.
Zásadní výhodou technologie AFM oproti elektronovým mikroskopům je, že měřené vzorky nemusí být vodivé! S technologií AFM lze dosáhnout rozlišení až v řádu jednotek nanometrů.

Systémy Agilent se uplatní v:

- **elektrochemii**
- **nanolitografii**
- **aplikacích s polymery**
- **biotechnologiích**
- **medicíně**

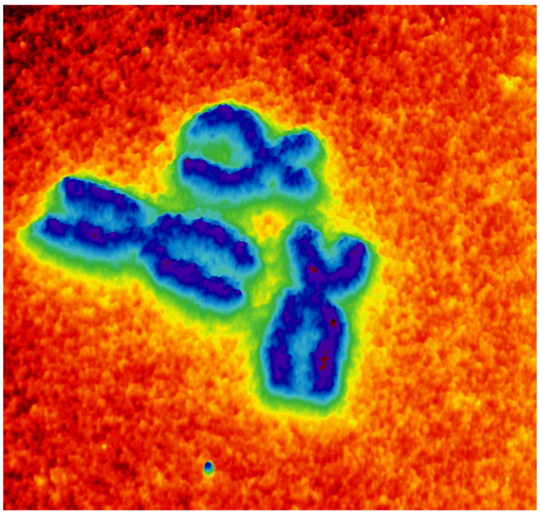

Série 5500 AFM/SPM
AFM mikroskop Agilent 5500 je vrcholný víceúčelový výzkumný mikroskopický systém pro AFM a SPM. Modulární koncepce této série dovoluje jednoduchou integraci stojanu pro velké vzorky až 150 x 200 mm (LS), invertovaného mikroskopu (ILM), scannerů pro malé i velké zobrazované plochy, adaptérů pro uchycení vzorků, soupravy pro elektrochemii nebo video mikroskopu.

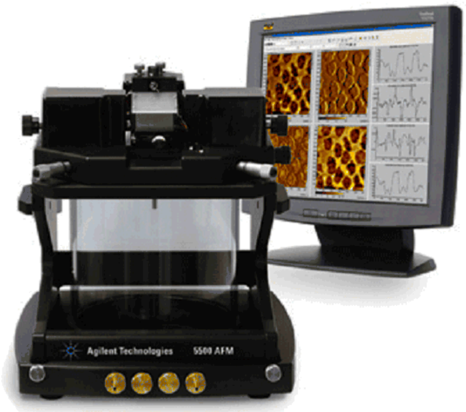

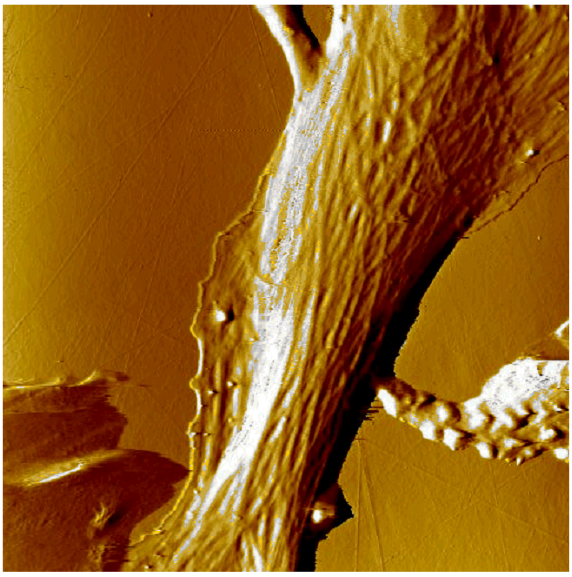

Série 5100 AFM/SPM
AFM mikroskop Agilent 5100 je vhodný pro uživatele, kteří nepotřebují plnou funkčnost vrcholného modelu Agilent 5500, a přesto vyžadují možnost plné kontroly prostředí, ve kterém se nachází měřený vzorek. Pro plnou kontrolu prostředí, ve kterém se nachází měřený vzorek, je k dispozici volitelná hermeticky uzavřená komora a teplotně regulovaný adaptér pro uchycení vzorků.

- Velikost vzorku 20 mm x 20 mm
- Kontrola teploty a prostředí

Série 5400 AFM/SPM
Nový AFM mikroskop Agilent 5400 AFM/SPM je velmi přesný, univerzální přístroj za dostupnou cenu, určený zejména pro oblast vzdělávání a výzkumu a představuje tak ideální možnost zpřístupnění AFM technologie širokému spektru potenciálních uživatelů. Mikroskop je dodáván s podklady pro výuku AFM včetně vzorků pro experimenty.

- Velikost vzorku 20 mm x 20 mm
- Kontrola teploty

Kontaktní informace:

H TEST a.s.
Na okraji 44B
16200 Praha 6
Tel: 235 365 207, 204
Fax: 235 363 893
E-mail: info@htest.cz

www.htest.cz
www.agilent.com/find/nanotech

H/test®
Agilent Technologies
Authorized Distributor

RESISTIVITY MEASURING WORKPLACE FOR BULK MATERIALS

J. Vognar[1], J. Vondrák[1,2], V. Novák[1]

1 Department of Electrotechnology FEEC BUT, Údolní 53, 602 00 Brno, CZE
2 Institute of Inorganic Chemistry of the ASCR, v.v.i.,250 68 Řež, CZE

Corresponding author: J. Vognar (jirikv@email.cz)

Introduction

This thesis is focused on construction resistivity measuring workspace for bulk materials. Resistivity will be measured according to the pressure. Sample resistance was measured by four-wire method. It was also necessary to measure the volume (height) of the sample and applied pressure. Measured material was ground and unground form of carbon black.

Experimental

Resistivity (conductivity) is a property of a material, which descrives its using as a conductor. For resistivity calculation next formula is used:

$$\rho = \frac{R \cdot S}{l} = [\Omega \cdot m] \qquad (1)$$

where R is measured resistance, S is conductive surface and l is heigh of the sample.

Measuring aparatus

Basic requierements to get reasonable results are:

- great resistance of a material from which measuring aparatus has been made.
- toughness of aparatus material to get no deformation during pressing
- accuracy positioning of the aparatus in a presser. Press will be distributed through all surface of the sample uniformly
- minimal resistance of wires and contacting places for measuring through 4-wire method

Maesuring aparatus is made from alkalic polyamide PA-6. Its toughness is 84 (D shore scale), stregness in press is 95-120 MPa and resistivity is 5.10^{15} Ω.cm. Using turning machine a cylinder and two clicks have been carved out. Diameter of clicks, which will press a sample inside the cylinder, is same inner diameter of cylinder and it is 26,8 mm.

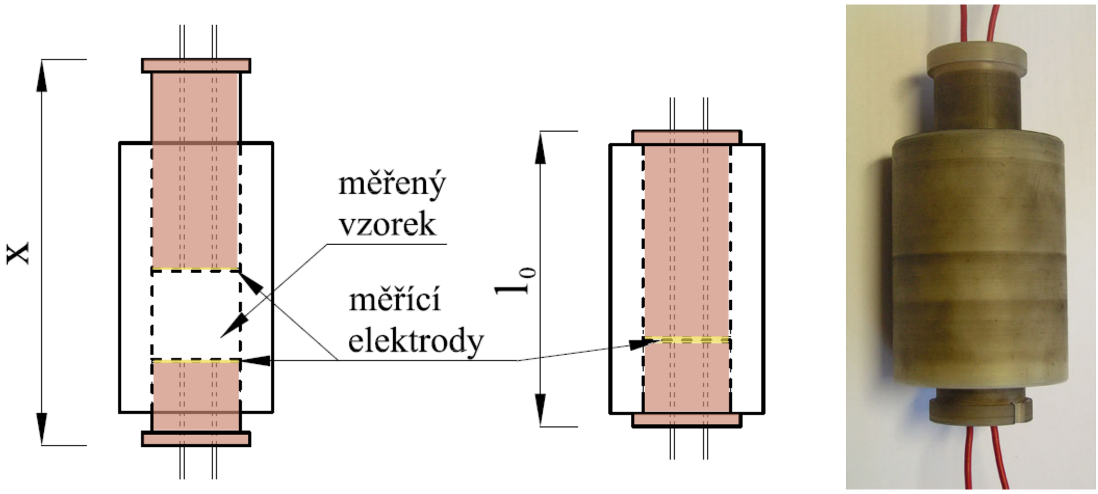

Fig. 1 *a)Measuring piston (front view) with a measured sample b) Measuring piston without sample c) Real piston*

Principle of a press measuring piston is seen on figure 1. For calculation of the resistivity is need to measure heigh of the sample a its resistance (diameter of the electrodes is constant). An example of the calculation:

$$\rho = \frac{R \cdot \frac{\pi \cdot d^2}{4}}{x - l_0} = \frac{10 \cdot 10^{-3}\Omega \cdot \frac{\pi \cdot \left(2{,}68 \cdot 10^{-2}\right)^2 m^2}{4}}{\left(1{,}305 \cdot 10^{-1} - 1{,}237 \cdot 10^{-1}\right)m} = 8{,}296 \cdot 10^{-4}\Omega \cdot m \qquad (2)$$

where *R* is measured resistance, *d* is diameter of the electrode, *x* is height of the piston with sample inside and l_o is heigh of the piston without the sample.

Presser, in which is maesuring piston placed, is equiped with barometer. Barometer measuring in metric ton units p_{MT} [t]. For recompute to Pascal units next formula has been used:

$$p = \frac{F[N]}{S[m^2]} = \frac{p_{MT}[t] \cdot 10^{-3} \cdot g[m \cdot s^{-2}]}{S[m^2]}[Pa] \qquad (3)$$

where *S* is surface under pressure, *F* is force inside the press computed from p_{MT} and acceleration of gravity *g*.

Description of 4-wire measuring method

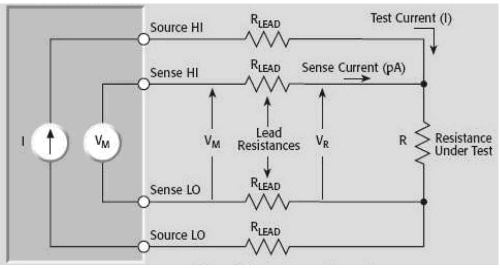

Fig. 2 *Circuit scheme for 4-wire measuring of resitance [2]*

Testing current (I) passes through measured sample (R) using first couple of wires. Simulatenously is measured voltage on second couple of wires. Multi-wired wires has been choose for a better and more superior soldering. According to that the wires are connected together on the chemically goldened copper electrode is loss of the voltage neglectable. Measured voltage V_M is measured with minimal difference to sample voltage V_R. With this method is reached higher accuracy of the measurement than using 2-wire method [2].

Measurements errors

Measurements were influenced by errors. The most influence had height of sapmle measurement using caliper with accuracy 0.01mm. Another errors come though the press measurement. The presser had only analogue scale with resolution of tenth of tons. This lower resolution influence measuruments for lower presses to 1 metric ton. Microohmmeter TESLA BM 591 measuring resitance with error 0,25% ± 2 dig (U=1V and f=100Hz). For next experiment will usefull to find device, which can measure with accuracy to tenths of miliohms [3].

Measured resistivities

As materials for measuring resistivity composit carbon black Chezacarb A has been used in milled and unmilled form. Measured results can be seen on firure 3.

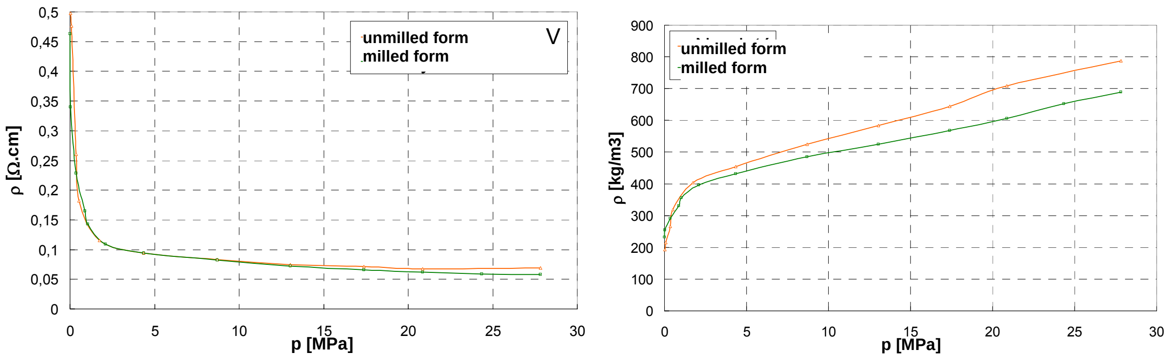

Fig. 3 *a)Dependance of resistivity of carbon black Chazacarb A on press b) Dependance of density of carbon black on apllied press*

Results ond disscusion

Functionable workplace for measuring resistivity of bulk material has been made. Results can be seen in figure 3 and it can be concluded that resistivity decreases with rising pressure. Milled carbon black has due to theoretical theorems lower resistivity than unmilled one and its density is lower at the same apllicated pressure. By pressure around 2 MPa resistivity rapidly lowers, from 0.5 Ω.cm to 0.1 Ω.cm. After 2 MPa to higher pressures were resistivity around 0.1-0.05 Ω.cm. In Further measurements will be eliminated factors, which causes errors.

References

1. KUCHARČÍK, J. *Uhlíkové materiály pro elektrody palivových článků.* Brno: Vysoké učení technické v Brně, Fakulta elektrotechniky a komunikačních technologií, 2009. 28 s. Vedoucí semestrální práce Ing. Jiří Vognar.
2. *Low Level Measurements Handbook : Precision DC Current, Voltage, and Resistance Measurements*. 2004. 247 s. 6th edition. Dostupný z WWW: <https://www.keithley.com/servlet/Data?id=9538>.
3. *TESLA Automatický měřič RLCG BM 591*. Brno, 1980. 73 s.

TOTAL CHARGE PASSED ON THE SURFACE AND DISTRIBUTION INTERNAL RESISTANCE OF LEAD-ACID ACCUMULATOR ELECTRODES

R. Lábus, R. Bilko, P. Křivík

Department of Electro technology, Technical University, 602 00 Brno, Czech

Corresponding author: Radek Lábus (xlabus00@stud.feec.vutbr.cz)

Abstract

Total charge passed on the surface and distribution internal resistance of lead-acid accumulator electrodes in the course of discharge was determined mathematically by using the equivalent circuit method. Target of this work is limitation of degradation mechanisms of lead-acid cells, that is presented by distribution of the internal resistance and the charge passed. The results are presented in the form of 3-D diagrams for different states of discharge.

Keywords: lead-acid cells, internal resistance, charge passed, grid design

Introduction

As a continuation of our past research work on the modelling of current distribution on the surface of standard lead-acid battery [1] plate electrodes and a cylindrical type VRLA cell [2] in the course of discharge for various configurations of the current tabs, we used a similar model also for 3-D modelling of internal resistance distribution and charge passed on the surface of standard lead-acid battery. Cell electrodes with position of current tabs are shown on top in Fig. 1. We have shown that our method can successfully be applied in the case of current distribution over the electrode surface in a lead-acid cell [1].

Method of calculation

The mathematical model was based on an electrical equivalent circuit similar to that used by previous authors [1, 2]. It is assumed that the positive and negative grids have equal numbers of meshes of equal forms, thus corresponding, in the geometrical sense, to each other.

The internal resistances, R_{vk}, between the cell elements depend on the discharge current, I, and on the charge passed, Q. The course of this functional dependence was determined on a laboratory cell for various discharge currents. The values of R_{vk} involving the electrolyte resistance, contact resistance between the lead grid and the active mass and the active mass resistance were fitted by the following exponential function by using the least squares method (1):

$$R_{vk} = 0.32 + 4.2Q + 2.6 \times 10^{-5} \exp (730Q + 100I - 14) \qquad (1)$$

After application of the first and second Kirchhoff laws to nodes and loops of the whole equivalent circuit, we obtain a system of linear equations whose solution gives the sought distribution of local potentials and currents. To take into account the system changes with the time, the calculations were carried out in many steps as described in [1].

The results of the calculations of the internal resistance and charge passed distribution over the electrode surface are shown in the form of 3-D diagrams in figs. 1 – 2.

Analysis

Results from fig.1 - during discharge internal resistance dramatically increases as far as from 80 % of discharge.
The active mass is mostly exploited at current tabs especially on positive electrode (positive electrode has bigger resistance than negative electrode). At the end of discharge rate of R_{max}/R_{min} = 2.57.
Results from fig.2 - charge passed is increased equally during discharge. In half of discharge exploitation of charge passed increased on electrodes surface unevenly, especially active mass near current tabs (similarly as internal resistance on positive electrode) is exploited. At the end of discharge non-uniformity of exploitation of charge passed on electrodes surface is decreasing, even if at the end of discharge the active mass nearly current tabs is more exploited than in other regions of active mass (Q_{max}/Q_{min} = 1.09).

Conclusions

Mathematical model was created for recognition of internal resistance and charge passed distribution. Target of this work was limitation of degradation mechanism of lead-acid cells that is presented by distribution of internal resistance and charge passed. Unequally distribution of internal resistance and charge passed affected lay-out of current tabs located at opposite ends of the plate electrodes.

Acknowledgement

This work was supported by:
The Research Project CZ No. MSM0021630516
ALABC (Project No. C2.2)

References

1. Petr Král, Petr Křivák, Petr Bača, Milan Calábek, Karel Micka: Current distribution over the electrode surface in a lead-acid cell during discharge, Journal of Power Sources, 105, 2002, s. 35-44.
2. Petr Křivák, Petr Bača, Milan Calábek, Karel Micka, Petr Král. Current distribution over the electrode surface in a cylindrical VRLA cell during discharge. Journal of Power Sources, 2006, 154, 2006, s. 518-522. ISSN: 0378-7753.

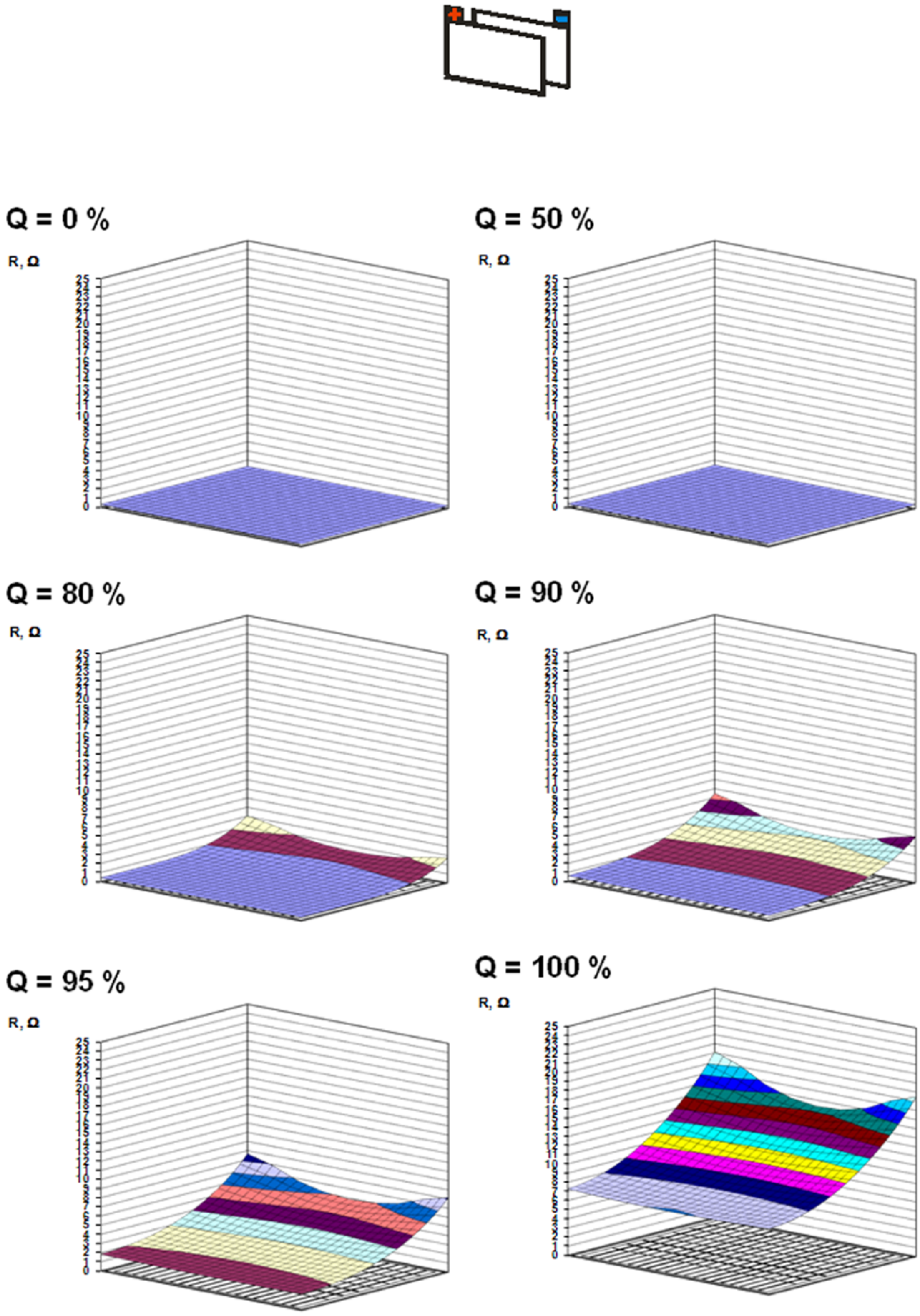

Fig. 1 *Internal resistance distribution over the plate electrode surface at increasing state of discharge, Q, from 0 to 100%.*

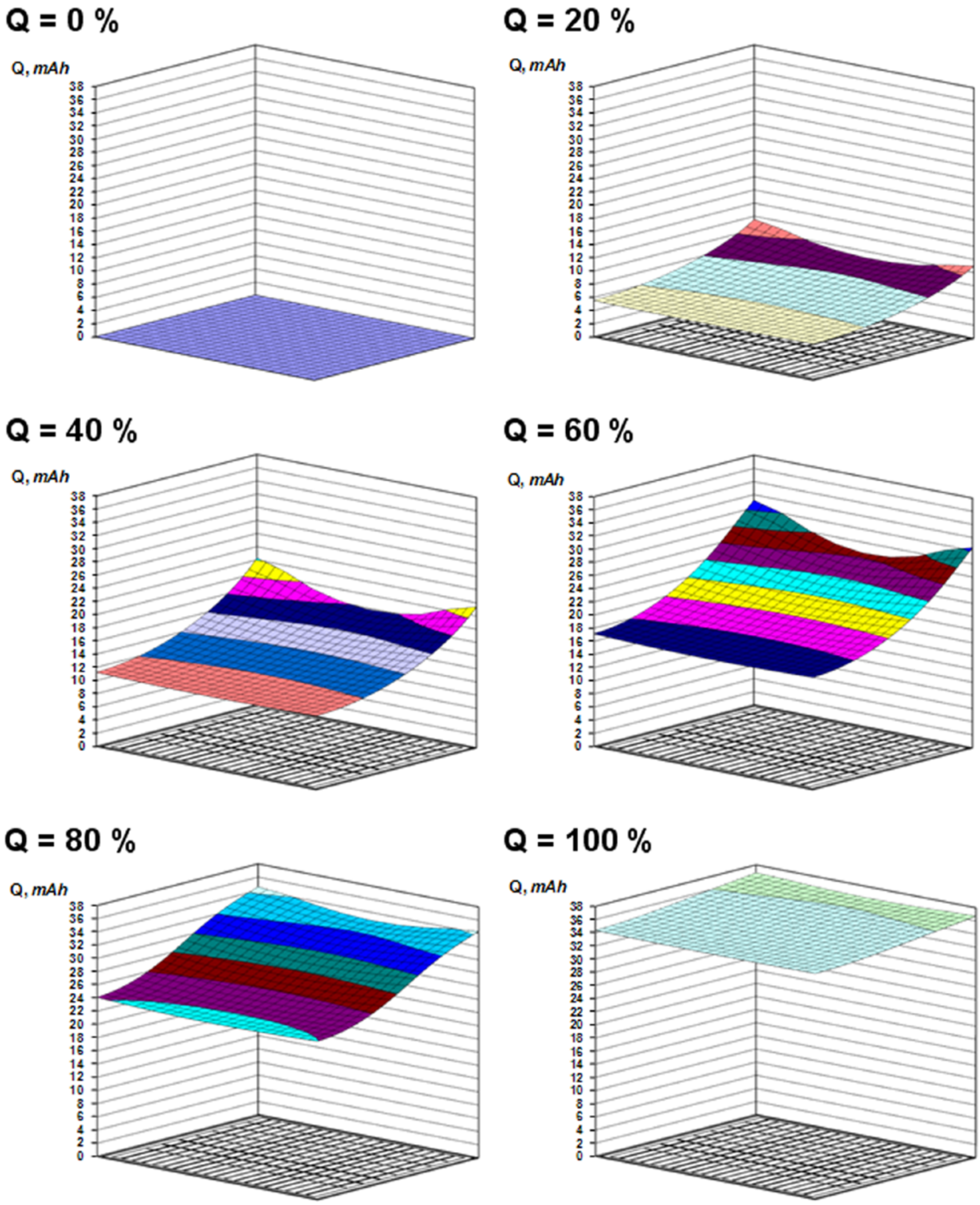

Fig. 2 *Charge passed distribution over the plate electrode surface at increasing state of discharge, Q, from 0 to 100%.*

QUANTUM-CHEMICAL MODELING OF REACTION OF GAMMA - BUTYROLACTONE DECOMPOSITION ON Li-ELECTRODE SURFACE

G.Z. Tulibaeva, O.V. Yarmolenko, A.F. Shestakov

Institute of Problems of Chemical Physics of the Russian Academy of Sciences,
142432. Chernogolovka, the Moscow region, Semenov av., 1, Russian Federation

Corresponding author: Tulibaeva G.Z. (galia@icp.ac.ru)
Phone: +7(496)5225625

Introduction

Rechargeable lithium batteries are rather perspective chemical power sources. But there are a number of the problems caused by deterioration of Li/electrolyte interface with time. First, at cycling in organic electrolytes side reactions of corrosion of lithium metal and decomposition of electrolyte components with gassing are possible that results to decapsulation of case of power sources and even to explosion. Second, on Li-electrode surface dendrite formation is probably that can result in a short circuit.

The problem of passivation of lithium anode surface in organic electrolytes has arisen from the first works on formation of lithium power sources (LPS). Thermodynamic calculations show principal opportunity of passing of reduction reaction by lithium of aprotic polar solvents used in LPS [1-2]. For number of solvents (propylene carbonate, ethylene carbonate) process of interaction with lithium and composition of surface layers are investigated sufficiently in detail. From that angle out gamma-butyrolactone **(GBL)** is less investigated.

Interaction GBL with alkali metals was earlier studied. It is reported [1] that at lithium cutting into GBL the short pulse of gases is observed only, and then the surface is passivated. The composition of surface compounds formed at interaction of lithium surface with wet GBL in absence of gassing is underlined [2]. The main product of interaction is organic salt $LiO(CH_2)_3COOLi$.

By us it has experimentally been shown, that 1M solution $LiClO_4$ in GBL decays on lithium anode at water content 0.2 wt. % [3-4]. The electrolyte decomposition was not observed at low water concentration. At current densities > 1.0 mA/cm^2 gases H_2, CO and CO_2 in comparable quantities and 5 hydrocarbons gas: CH_4, C_2H_4, C_2H_6, C_3H_6, C_3H_8 are generated. For understanding of the basic features of the gassing mechanism quantum-chemical modeling interaction GBL with lithium surface is carried out.

The theoretical analysis of the GBL decomposition mechanism

Experimental data indicate strong influence of current density both on speed of gassing and on composition of electrolysis products. It is known also that there is some limit for current density since which fast growth of dendrites on lithium surface is occurs. It allows to make a conclusion that in a deposition process of Li atoms on the electrode during the initial moment of time nonequilibrium structures are formed. Further they have time to relax and form equilibrium Li-layer but only at small current densities. In this case it is possible to think that on Li-surface there are not active centers and consequently gassing not occurs. These nonequilibrium structures can be represented as various roughnesses on Li-surface. Clearly their structural characteristics will be determined by a ratio of settling rate of Li atoms on an electrode surface and their surface diffusions. Consequently characteristics will differ at various current densities. It is possible to assume occurrence of the greater nonequilibrium, so also the greater activity of the surface centers with growth of current density.

The information on thin details of surface structure of the growing lithium anode is necessary for understanding of the reasons of change of gas composition. It is receive inconveniently. Therefore, it is possible to put a task only about understanding of the basic features of interaction of a solvent molecule – GBL with Li-surface. For this purpose it was used cluster Li_{20} for active centers modeling on a surface. Quantum-chemical studying interaction of molecule GBL with lithium cluster Li_{20} has been carried out by method of density functional. The not empirical I functional PBE [5] and extended basis H [6s2p/2s1p], C, O [10s7p3d/3s2p1d], Li [10s7p3d/4s3p1d] were using. All calculations are carried out by program complex the PRIRODA [6]. This approach allows well describing structure and relative energies of molecule GBL [8] and isomers of cluster Li_6 for which the data of high-accuracy calculation [7] are known.

The cluster Li_{20} in the basic state has irregular structure of symmetry C_{2v} (fig. 1) which is not a fragment of geometrical lattice Li. The designed geometrical parameters correspond to the literary data [9].

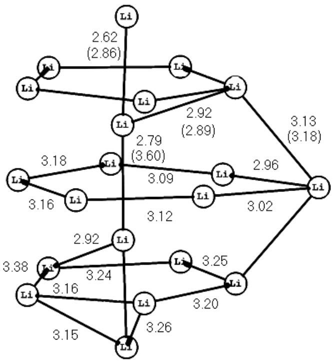

Fig. 1 *Structure of Li_{20} cluster*

At interaction Li_{20} with one molecule GBL it was not possible to find out formation of intermediate adsorptive complexes with preservation of integrity of molecule GBL. At geometry optimization of system Li_{20} + GBL the structure of chemisorbed complex with cleavage C-O bond (fig. 2a) is formed with a gain of 66.7 kcal/mole. That is decomposition reaction GBL begins at joining to lithium cluster on an C-O bond of carbonyl group. The further transformation structures (fig. 2a) with more penetration of a carbonyl group in surface layer of lithium cluster (fig. 2b) also proceeds with a energy gain (17.9 kcal/mole). In the given complex only three methylene links do not participate in interaction with lithium atoms. This structure fragment C_3H_6 can be considered as base for C_3-hydrocarbons. However, the decomposition reaction of a complex (fig. 2b) with formation of propylene and cluster $Li_{20}CO_2$ demands power expenses. Since 1-3 hydrogen shifts is required for transformation trimethylene fragment in propylene at single-stage formation C_3H_6. It should be carried out simultaneously with cleavage strong C-O and C-C bonds. Therefore such reaction will have rather high activation barrier. This conclusion corresponds to the experimental fact that gassing is not observed at minimally possible water content (up to 10^{-2} wt. %).

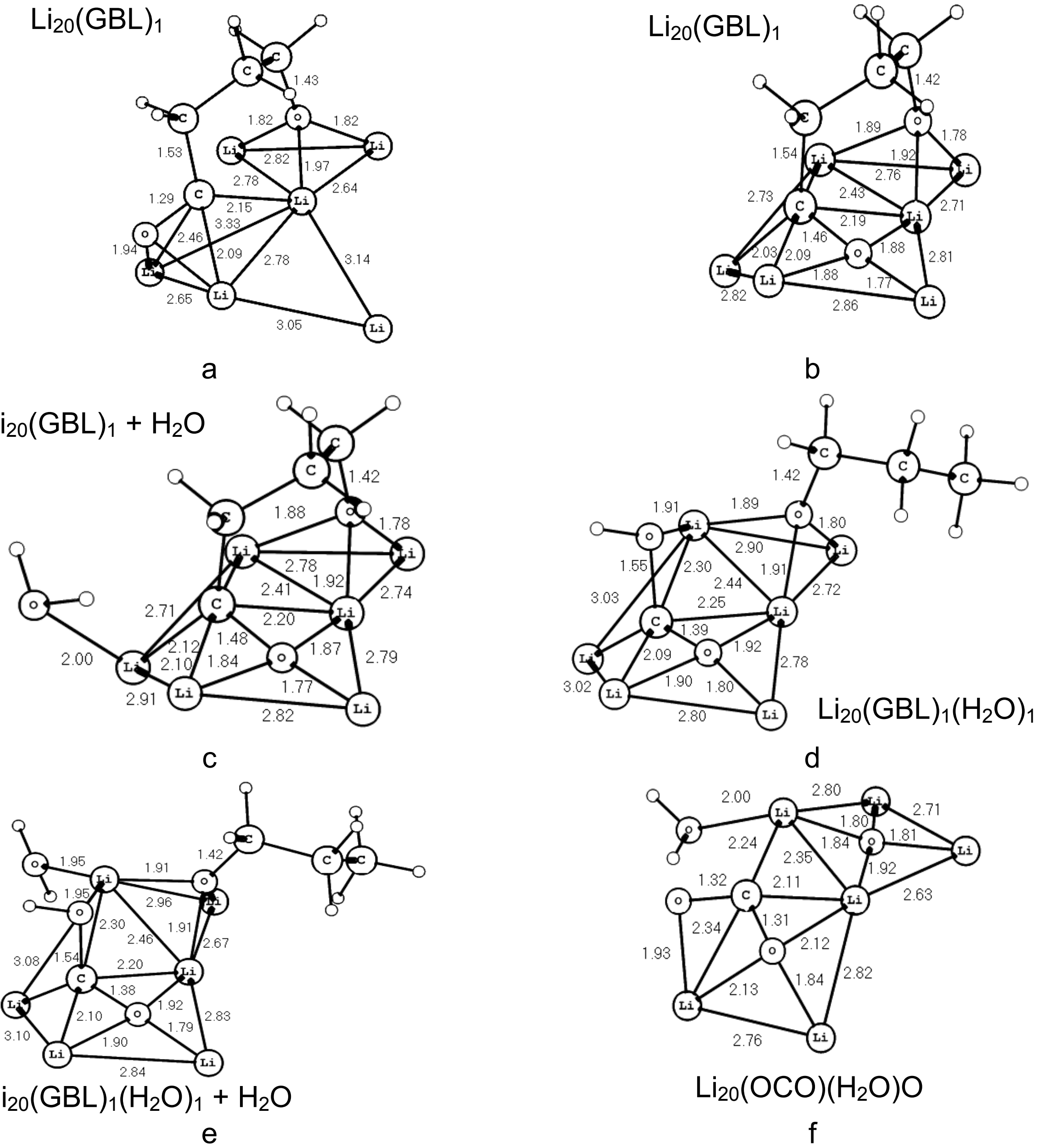

***Fig. 2. a, b**) Fragments of $Li_{20}(GBL)_1$ isomers structure; **c, d**) fragments of $Li_{20}(GBL)_1(H_2O)_1$ isomers structure; **e**) fragment of $Li_{20}(GBL)_1(H_2O)_2$ structure; **f**) fragment of $Li_{20}(OCO)(H_2O)$ structure. Lengths of bond are specified in Å.*

At interaction of lithium surface with a water molecule at the first stage an adsorption of a molecule of water on next atom Li is occurs with a gain 15.2 kcal/mole (fig. 2c). At the following stage there are formation C-H bonds with simultaneous cleavage O-H and C-C bonds (fig. 2d). This reaction is close to thermoneutral and gain is 2.9 kcal/mole. Activation energy of such reaction should be medium value. The adsorption of the following molecule of water (fig. 2e) also is energetically favorable and results in decreasing energy of system on 22.3 kcal/mole. Decomposition of this superficial complex with formation of propane results in big energy gain (70.3 kcal/mole) (fig. 2f). As this reaction very much exothermal it is necessary to expect small activation energy. It is interesting, that at transformation of molecule GBL into propane with participation of water simultaneously there is a formation of molecule CO_2 in chemisorbed condition. At hydrolysis of such superficial complexes in products it should be observed CO_2 which is found out experimentally. The occurrence CO, apparently, is connected to formation of propylene. From the formal point of view it is possible to count that in this process two atoms H pass not on C_3- fragment GBL but on CO_2- fragment. In this case propylene, CO and H_2O are formed. As to formation of alcohols which have been found out in mass spectrums in case of isopropanol it is the hydrated form of propylene, and methanol – a product of reduction CO on surface Li. As there is hydrogen at apparent quantities in gas phase it is clear that along with reactions of H_2 formation from chemisorbed atoms H there should be also reactions with chemisorbed fragments of GBL molecule.

Conclusions

Quantum-chemical modeling of interaction of molecules of gamma-butyrolactone with lithium surface is carried out. The conclusion is made that an incipient state of decomposition reaction of GBL is formation of superficial Li-organic compound. It is hydrolyzed in the subsequent reactions with water and with evolution of hydrocarbons, CO_2, CO, H_2.

References

1. I.A. Kedrinskii, V.E. Dmitrenko, I.I. Grudyanov: *Litievye istochniki toka*. Energoizdat, Moscow 1992, 240 p.
2. D. Aurbach “The Role of Surface Films on Electrodes in Li-Ion Batteries” in “Advances in Lithium-Ion Batteries” (W.A.Schalkwijk and B. Scrosati, ed.). Kluwer Academic/ Plenum Publishers, New York 2002. P. 7-78.
3. N.I. Shuvalova, G.N. Petrova, G.Z. Tulibaeva, O.V. Yarmolenko, O.N. Efimov: 10th international conference “Basic problems of energy conversion in lithium electrochemical systems“. June 23-27, 2008, Saratov, Russia, p.222-224.
4. O.V. Yarmolenko, G.Z. Tulibaeva, G.N. Petrova, N.I. Shuvalova, O.N. Efimov: 9th International Meeting “Fundamantal problems of solid state ionics” June 24-27, 2008, Chernogolovka, Russia, p.204.
5. Perdew, K. Burke, M. Ernzerhof: Phys. Rev. Lett., **77** (1996) 3865.
6. D.N.Laikov: Chem. Phys. Lett., **281** (1997) 151.
7. B. Temelso, D. Sherrill: J. Chem. Phys., **122** (2005) 064315.
8. R.J. Papoular, H. Allouchi, A. Chagnes, A. Dzyabchenko, B. Carre, D. Lemordant, V. Agafonov: Acta Cryst. B, **61** (2005) 312.
9. J.K.V. Jovan, R.G. Shridhar: J. Chem. Phys., **129** (2008) 164314.

Title: Advanced Batteries Accumulators and Fuel Cells – 10th ABAF

Edited: Jiří Vondrák
Vítězslav Novák

Publishing Office: Vítězslav Novák

Deadline: August 7th 2009

Publisher: Brno University of Technology
Faculty of Electrical Engineering and Communication
Department of Electrotechnology

Press: Akademické centrum GEPARD International, s.r.o.
Purkyňova 95a, 612 00 Brno

Year: 2009

Number of Copies: 90

ISBN 978-80-214-3943-6